UNIVERSITÀ DEGLI STUDI FIRENZE

DOTTORATO DI RICERCA IN FISICA E ASTRONOMIA

CICLO XXXII

COORDINATORE Prof. Raffaello D'Alessandro

Isotopic fractionation study towards massive star-forming regions across the Galaxy

Settore Scientifico Disciplinare FIS/05

Dottorando
Dott.ssa Laura Colzi

(firma)

Tutori
Dott. Francesco Fontani

(firma)

Prof. Guido Risaliti

(firma)

Coordinatore
Prof. Raffaello D'Alessandro

(firma)

Anni 2016/2019

Ai miei genitori

CONTENTS

ABSTRACT

Nowadays there is evidence supporting the idea that our Sun was born in a stellar cluster including also high-mass stars (stars with more than 8 $M_\odot$). For this reason the study of the chemical content of massive star-forming regions can give us important information about the chemical heritage of our Solar system. One of the most important tools to investigate our chemical history is to measure the isotopic fractionation. This is the process that distributes the less abundant stable isotopes of an element in different molecular species. Pristine Solar system materials, like comets and carbonaceous chondrites, present very different hydrogen and nitrogen isotopic ratios (D/H~10^{-4} and ^{14}N/^{15}N~50–200) with respect to those measured for the proto-Solar nebula, in which our Sun was born (D/H~2×10^{-5} and ^{14}N/^{15}N=441). In particular, the proto-Solar nebula corresponds to the cloud of gas and dust that, due to gravitational collapse, formed the Sun at its center. This difference indicates that the isotopic values have been altered due to physical/chemical processes during the formation of the Sun. Low- and high-mass star-forming regions also present a variety of isotopic ratios, with a lower enrichment of the heavier isotopes with respect to the one present in pristine Solar system materials. Nowadays observations and theoretical works about hydrogen fractionation agree about the processes that enrich deuterium with respect to hydrogen during star-formation. These processes are related to the cold phases of star-forming regions, where the CO freeze-out on grain surfaces and, because of this, gas-phase molecules are enriched in deuterium. However, it is not the same for nitrogen fractionation. Chemical models are not able to reproduce all the observed ^{14}N/^{15}N ratios for the different molecules and in the different physical conditions of the observed targets.

In this thesis work I have contributed by studying more in detail the nitrogen fractionation processes following different approaches. First, I have studied the ^{14}N/^{15}N ratio of a sample of 27 massive star-forming regions for HCN and HNC with single-dish observations (encompassing regions of ~0.5 pc). I have searched for a trend of the ^{14}N/^{15}N ratio with the evolutionary stage (high-mass starless cores, high-mass protostellar objects, and ultra compact HII regions), and, with observations of DNC, I have derived the D/H ratio, and its possible correlation with N-fractionation. In a second work, I have derived the ^{14}N/^{15}N ratios for HCN and HNC as a function of the Galactocentric distance, to compare with Galactic chemical evolution (GCE) models (in a large sample of 87 massive star-forming regions). Besides, I have studied the N-fractionation of individual intermediate- to high-mass star-forming regions at core scales. In particular, I have studied high angular resolution observations of the massive star-forming protocluster IRAS 05358+3543, resolving for the first time the spatial distribution of the ^{15}N-isotopologues of N_2H^+ at core scales (~0.05 pc of resolution). Finally, I have performed a theoretical study of C-fractionation implementing a gas-grain chemical network with the ^{13}C molecular species. In particular, I have studied the contribution of new low-temperature isotopic-exchange reactions, and a detailed parameter space exploration to study the ^{12}C/^{13}C ratio for different densities and temperatures to compare with some observed values.

The main findings and conclusions of this thesis are:

- **Hydrogen and nitrogen fractionation of HNC are independent.**
  The H/D and $^{14}N/^{15}N$ ratios for HNC in a sample of 27 high-mass star-forming regions have been studied and I have concluded that the two isotopic fractionation ratios are independent. This is in agreement with the possible anti-correlation found by Fontani et al. (2015b) for N_2H^+ towards the same sample of sources, and with the results of the chemical model performed by Wirström et al. (2012).

- **Nitrogen fractionation is not dependent on the evolutionary stage.**
  In addition to the HNC/H^{15}NC, I have also derived the HCN/HC^{15}N column density ratios. I have derived no large spread of $^{14}N/^{15}N$ values around the PSN one (441) for both HNC and HCN, and no difference between different evolutionary stages. A similar result was already found also by Fontani et al. (2015b) for N_2H^+ towards the same sample of sources, and agrees with the predictions of the chemical model of Roueff et al. (2015). Our findings support that most of the important low-temperature isotopic-exchange reactions present a barrier and could not occur, maintaining the $^{14}N/^{15}N$ ratios very similar to the assumed initial condition ($^{14}N/^{15}N$=441). Thus, the processes that enriched the ^{15}N during the Sun formation should be searched at different spatial scales, probably smaller than those resolved with a single-dish radiotelescope (~0.5 pc).

- **$^{14}N/^{15}N$ Galactocentric behaviour and its consistency with Galactic chemical evolution models.**
  I have derived a new $^{14}N/^{15}N$ Galactocentric trend with a large sample of 87 massive star-forming regions. I have performed a linear regression fit and a parabolic analysis to the $^{14}N/^{15}N$ ratios found as a function of the Galactocentric distance. The linear positive trend found with the first analysis is consistent with the prediction of GCE models (Romano et al. 2017; Romano et al. 2019) up to 8 kpc. These models predict a linear positive trend up to 8 kpc because of the introduction of novae outbursts as the main mechanism to produce ^{15}N. Then, after 8 kpc predict a flattening trend because of the stellar yields that they assume for low-metallicity massive stars. The entire predicted trend exactly reproduces the parabolic analysis done on our data. The average observed trend could be explained with the GCE of the $^{14}N/^{15}N$ ratio, and the spread of values found at each distance is probably due to chemical fractionation processes within the molecular clouds.

- **The new local ISM $^{14}N/^{15}N$ ratio.**
  The new linear positive trend allowed us to find a new local ISM $^{14}N/^{15}N$ value: 375±60. This was evaluated from the linear regression fit at a Sun distance from the Galactic center of 8.4 kpc, as derived by Reid et al. (2014). This new value approaches the PSN $^{14}N/^{15}N$ of 441, with respect to previous estimates, and is consistent with the nowadays local value predicted by GCE models.

- **N-fractionation of N_2H^+ is a local effect in the high-mass star-forming region IRAS 05358+3543.**
  To investigate more in detail the processes that could enrich ^{15}N during the star-formation process, I have studied the spatial distribution of ^{15}N-isotopologues of N_2H^+ towards the high-mass star-forming region IRAS 05358+3543, with high angular resolution NOEMA Interferometer observations. The angular resolution of

$3''$ allowed us to resolve spatial scales of ~0.03 pc given the distance of the source (1.8 kpc). The continuum emission is resolved in four cores: a high-mass protostellar object, a starless core, a core in an evolutionary stage intermediate between starless and protostellar, and a core (detected for the first time in this work) whose nature is not clear yet. The overall structure of the integrated N_2H^+(1–0) emission, and that of $^{15}NNH^+$(1–0) and $N^{15}NH^+$(1–0) consists of three main cores, in agreement one with each other. These cores are shifted with respect to the continuum peak, especially towards the protostellar object, probably because of the star-formation activity that destroys N_2H^+. The $^{14}N/^{15}N$ ratios found are of about 100-200 towards the dense cores, and higher (>250) towards the diffuse envelope in which the cores are embedded. The main result of this work is that the N-fractionation of N_2H^+ is a local effect. This is in agreement with the model proposed by Furuya and Aikawa (2018). In fact, the isotope-selective photodissociation of N_2 leads to higher values of $^{14}N/^{15}N$ for N_2H^+, with respect to an initial one in the diffuse regions of a molecular cloud.

- **Carbon fractionation: the importance of new low-temperature isotopic-exchange reactions.**
  Since some of the $^{14}N/^{15}N$ ratios derived in the previous works strongly depend on the assumed $^{12}C/^{13}C$, I have studied how this ratio can vary in environments similar to those studied, and how this can influence the results. I have implemented a gas-grain chemical model with new carbon fractionation reactions. The same low-temperature isotopic-exchange reactions used in the chemical model by Roueff et al. (2015) have also been included. In particular, I have found that the reaction $^{13}C + ^{12}C_3 \rightleftharpoons C + ^{13}CC_2$, included for the first time in our chemical network, is important for gas temperature <27 K, leading to $^{12}C/^{13}C$ ratios lower than the nominal initial value of 68. This result is a consequence of the time scales when this reaction is still efficient and when most of the atomic carbon is already transformed into CO.

- **Carbon fractionation: density and temperature space exploration.**
  I have performed a detailed analysis of C-fractionation for the nitrile-bearing species CN, HCN and HNC, for different densities and temperatures. With this analysis some of the observed $^{12}C/^{13}C$ ratios towards low-mass star-forming regions, lower than the local ISM value of 68, are reproduced. Finally, I have used the parameter space exploration to search for the predicted $^{12}C/^{13}C$ in regions with the densities and kinetic temperatures similar to those observed in the first sample of 27 high-mass star-forming regions. The derived $^{12}C/^{13}C$ for HCN and HNC differ by factors between 0.8–3.7 compared to the value of 68 assumed for the local ISM, using the Galactocentric dependence. This result highlights the importance of a proper derivation of the $^{12}C/^{13}C$ ratio in order to study the $^{14}N/^{15}N$.

<div align="right">

1

</div>

<div align="right">

INTRODUCTION

</div>

1.1. STAR FORMATION PROCESS

The interstellar medium (ISM) is the matter (gas 99%, dust 1%) distributed in the space between the stars. Hydrogen (H) is the most abundant element of the ISM, and its physical/chemical state defines the ISM phases: the ionised phase, in which H is atomic ionised, the neutral phase, in which H is neutral atomic, and the molecular phase, in which H is neutral molecular (H_2). Star formation is the set of physical processes that forms stars from the material of the ISM. In particular, molecular clouds are the places where stars are born. The largest molecular clouds are called Giant Molecular Clouds (GMCs), with typical densities of 10^2–10^3 cm^{-3}, diameters greater than 25 pc, average temperatures of 10 K and masses of about 10^5 M$_\odot$ (e.g. Murray 2011). Turbulence, gravity and magnetic field give rise to dense cores of different mass and size through the fragmentation process inside a large GMC. Cores have typical sizes of 0.02–0.2 pc, masses of ~0.5–5 M$_\odot$ and densities $>10^4$ cm^{-3} (e.g. Williams et al. 2000; Bergin and Tafalla 2007).

 The standard theory of the formation of an isolated low-mass star[1] is based on the gravitational collapse of a single low-mass core (Shu et al. 1987; Shu 1991; Shu et al. 1993) through 3 main phases that are summarised in Fig. 1.1:

1. A single core contracts quasi-statically and isothermally until it reaches an unstable configuration (*pre-stellar phase*). The time spent in this phase is ~5×10^6 yr;

2. The core can gravitationally collapse giving rise to a central protostar that accretes material from the parental cloud, and at the same time contracts onto itself becoming more and more dense and hot. If no other forces exist to oppose collapse, the core will collapse under its own gravity in a "free-fall time". This time is defined as:

$$t_{\text{ff}} = \left(\frac{3\pi}{32G\rho} \right)^{1/2}, \tag{1.1}$$

where ρ is the average mass density of the core. Magnetic field and turbulence are also important and provide additional support to cloud material against the gravitational collapse. Without entering into details (since it is not the subject of this thesis),

---

[1] Star with a mass similar to or lower than our Sun.

if the core has a slight amount of initial rotation, the conservation of angular momentum during the collapse produces curved infall trajectories, giving rise to a disc-like structure. In this phase (*protostellar phase*), the protostar dissipates also a significant fraction of its angular momentum, into the surrounding environment, through bipolar outflows. The time of the accretion phase is $t_{\mathrm{acc}} = \frac{M_*}{\frac{dM}{dt}} \sim 10^5$ yr, where M_* is the protostellar mass and $\frac{dM}{dt}$ is the accretion rate of the gas to the center of the core;

3. After the accretion is finished, the "naked" protostar goes on contracting (*pre-main sequence* or "*T-Tauri*" *phase*). The total contraction time of the protostar is the Kelvin-Helmholtz time, $t_{\mathrm{K-H}} = \frac{GM_*^2}{R_* L_*}$, where R_* is the protostellar radius and L_* is its luminosity. At the end of this time the star reaches an internal temperature that is sufficient to ignite hydrogen and hence to reach the Zero Age Main Sequence (ZAMS). The duration of this phase is $t_{\mathrm{K-H}} \sim 10^6$–$10^7$ yr.

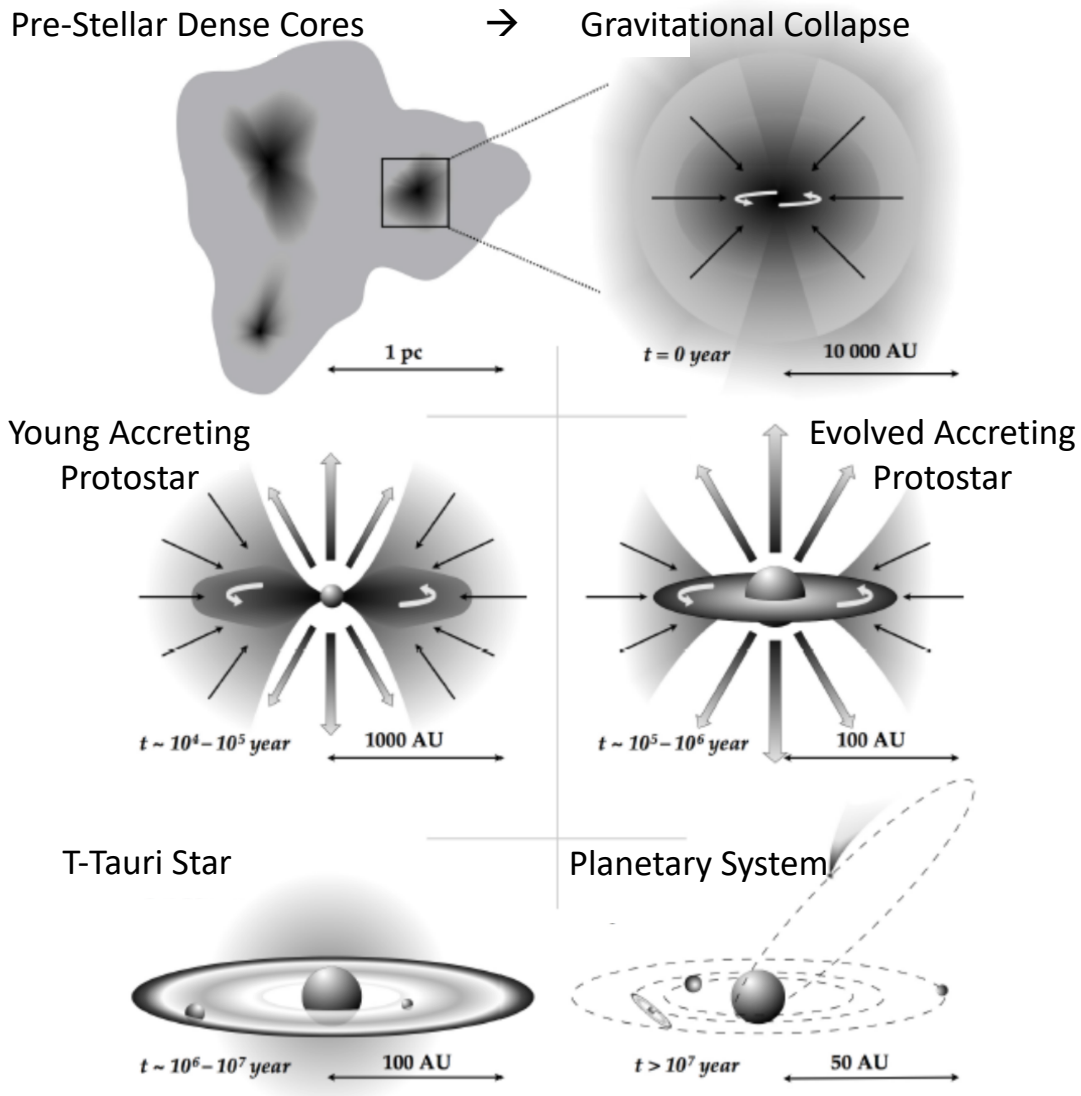Fig. 1.1: Evolutionary stages for the formation of low-mass stars, adapted from Frieswijk (2008).

1.1.1. THE CHALLENGE OF HIGH-MASS STAR FORMATION

High-mass stars (or massive stars) have masses M>8M$_\odot$ and main sequence (MS) spectral types[2] from B3 to O2 (OB stars). Although massive stars make up less than 1% of the stellar population in the Milky Way (integrating the initial mass function by Kroupa 2001), they play a central role in many astrophysical processes, such as shaping the ISM, regulating star formation, and ultimately governing the evolution of their host galaxies (Kennicutt 2005). However, to date, understanding massive star formation remains a challenge.

The scenario presented above for the formation of low-mass stars is not applicable for massive stars. In fact, the standard theory cannot be applied to stars more massive than 8 M$_\odot$ because for these stars the accretion timescale is longer than the rapid Kelvin-Helmholtz, or contraction, timescale[3]. Therefore, when the star arrives on the ZAMS, and the hydrogen starts to burn, the accretion from the surrounding gas continues. Then, a necessary condition to form a massive star (with mass M_*), is that the acceleration of a unit mass, dm, at a radius r, due to gravity, $\frac{GM_*}{r^2}$ must exceed the outward-directed radiative acceleration of the accreting gas, $\frac{\kappa L}{4\pi r^2 c}$. In the last expression κ is the opacity of the accretable material for ultraviolet (UV) radiation, L is the protostellar luminosity given by the sum of the intrinsic luminosity and the luminosity emitted from the dissipation of kinetic energy of the accreting material, and c is the speed of light. Therefore:

$$\frac{\kappa L}{4\pi r^2 c} < \frac{GM_*}{r^2}, \tag{1.2}$$

which translates into (Wolfire and Cassinelli 1987; Yorke 2004):

$$\kappa < \kappa_{\text{crit}} = 130 \; cm^2 g^{-1} \Big[\frac{M_*}{10M_\odot}\Big]\Big[\frac{L_*}{1000L_\odot}\Big]^{-1}. \tag{1.3}$$

Given typical values of the opacity of dusty ISM ($\kappa \sim 100$ cm^2 g^{-1}), the Eq. (1.3) is not satisfied for MS stars more massive than ~ 5 $M_\odot$ and luminosity of 10^4 $L_\odot$, for which $\kappa_{\text{crit}} \sim 10$ cm^2 g^{-1}. With more refined models one finds that the limit at which Eq. (1.3) is satisfied is at about 8 $M_\odot$. Therefore, for such stars, the net force on dusty ISM is directed away from the star, and accretion cannot continue to allow the growth above 8 $M_\odot$. This effect is known as the radiation pressure problem.

PROPOSED SOLUTIONS

To solve this problem at least one of these conditions must be satisfied:

- the radiative acceleration ($\propto$ L$_*$) must be reduced;
- the gravitational force ($\propto$ M$_*$) must be increased;
- the opacity of dusty ISM must be reduced.

In the last decade several works have shown that in theory is possible to overcome the radiation pressure problem and gather enough mass to build up a massive star. In the review of Tan et al. (2014), two main alternative theories are presented: *i)* the core accretion, *ii)* the competitive accretion.

---

[2] Spectral types are identified by different letters (O, B, A, F, G, K and M) that are used to characterize stars according to their mass and temperature, from the most massive and hottest to the least massive and coldest.
[3] For a high-mass star the $t_{\text{KH}} \sim 10^4$ yr is shorter than the $t_{\text{acc}} \sim 10^5$ yr.

i) *Core accretion*: it is a "scaled-up" version of low-mass star-formation (Fig. 1.1), char-
   acterised by higher accretion rates and non-spherical geometry. However, this sce-
   nario presents some problems as the theory assumes the existence of turbulent mas-
   sive cores[4] that have prevented fragmentation during their formation. Radiative feed-
   back from the star or magnetic fields are thought to inhibit fragmentation (e.g. Hosk-
   ing and Whitworth 2004). However, several observations and simulations did not find
   turbulent massive condensations, but smaller and lower-mass fragmented objects
   (Pillai et al. 2011; Duarte-Cabral et al. 2013; Palau et al. 2013; Fontani et al. 2016;
   Fontani et al. 2018a), although a few recent massive starless core candidates possi-
   bly non-fragmenting have been proposed (e.g. Cyganowski et al. 2014; Nony et al.
   2018).

ii) *Competitive accretion*: this theory relies on the fact that nearly all massive stars are
    formed in clusters together with low- and intermediate-mass stars (Lada and Lada
    2003). Therefore, the stellar cluster environment may influence the massive star for-
    mation process. Numerical simulations have shown that the gravitational fragmenta-
    tion of a molecular cloud produces fragments of gas and dust that collapse and form
    a low-mass star cluster (Bonnell et al. 2004). The overall potential well, created by the
    low-mass star cluster, funnels gas down to the potential center producing a global
    infall of material. Some of the stars accumulate the majority of gas and will become
    massive stars.

Testing the theories presented above with observations is challenging for several rea-
sons: being at distances $\gtrsim$1 kpc massive star-forming regions have small angular sizes, they
are few with respect to low-mass stars, and they are usually embedded in crowded environ-
ments (e.g. Zinnecker and Yorke 2007; Tan et al. 2019). Nevertheless, investigations of the
natal environment of massive stars provide clues for a better understanding of its physical
and chemical properties and of the star formation process itself.

PHASES OF MASSIVE STAR FORMATION

For the reasons discussed above, for massive stars there is not an equivalent classifica-
tion scheme like that described for low-mass stars (Fig. 1.1). Motte et al. (2018) intro-
duce the most likely evolutionary scenario for high-mass star formation, which is sum-
marised in Fig. 1.2. This scenario is based on observational constraints and follows the
competitive/clump-fed scenario. The different phases that they propose are described as
follow:

1. Massive stars form in molecular complexes hosting massive clouds and OB star clus-
   ters (i.e. where main sequence massive stars are already present). Parsec-scale clouds
   called ridges or hubs are the sites in which high-mass star-formation is preferred to
   occur. In particular, ridges are high-density filaments ($n >10^5$ cm^{-3}, diameter d of
   ~5 pc) forming clusters of high-mass stars (e.g. Nguyen-Lu'o'ng et al. 2013), while
   hubs are more spherical and smaller clumps (d ~1–3 pc), forming at most a couple
   of massive stars (e.g. Didelon et al. 2015).

---

[4]   The typical sizes and masses of these objects are ~0.2 pc and 100 M$_\odot$, respectively. Based on the size,
in the literature sometimes they are called *clumps* rather than *cores*. Therefore, we note that although the
nomenclature of this theory refers to the term *core*, their initial condensations are indeed *clumps*.

2. Ridges are fragmented in IR-quiet massive dense cores (MDCs) of 0.1 pc ($n > 10^5$ cm^{-3}, T<20 K), which host several low-mass pre-stellar cores. These objects are also considered as IR-dark clouds (IRDCs) since they do not emit strongly in the IR. IR-dark features are also seen in silhouette against the bright IR galactic background (e.g. Teyssier et al. 2002; Butler and Tan 2009), and are bright in the mm, with typical T~10–20 K and $n \gtrsim 10^4$ cm^{-3} (e.g. Rathborne et al. 2006; Ragan et al. 2009).

3. The low-mass pre-stellar core accretes material from the parental clump. This accretion is generated by the global collapse of ridges that creates flow streams and increase the MDCs mass. This gas inflow accretes onto a high-mass protostar at MDCs centers.

4. After about 10^5 yr, on 0.01 pc scales, one massive protostar or a close binary system forms at the center of MDCs. Observationally, during the accretion, the low-mass protostellar cores become IR-quiet high-mass protostars. In this phase collimated jets and molecular outflows from the star might appear.

5. Then, high-mass protostars become IR-bright for stellar embryos larger than 8 M$_\odot$, which are similar to the low-mass protostellar objects but with higher densities and temperatures ($n \gtrsim 10^6$ cm^{-3}, T$\gtrsim$20K).

6. Finally, when the hydrogen burning starts, the generated UV radiation ionises the surrounding hydrogen forming a hypercompact (r≤0.01 pc) HII region, that progressively expands to ultracompact HII regions (UC HII r≤0.1 pc) and finally becomes a classical HII region (1-10 pc).

GROSS EVOLUTIONARY CLASSIFICATION FOR MASSIVE STAR FORMATION

Due to the short evolutionary timescales, and the possible overlaps between the processes described above, the phases presented in Fig. 1.2 can be divided empirically into three gross phases, as proposed by Beuther et al. (2007a):

(i) **High-Mass Starless Cores (HMSCs)**: these objects are in a phase immediately before the collapse or at an early stage of the collapse. HMSCs put together phases 2 and 3 of Fig. 1.2.

(ii) **High-Mass Protostellar Objects (HMPOs)**: these are similar to the low-mass protostellar objects but with higher densities and temperatures ($n \gtrsim 10^6$ cm^{-3}, T$\gtrsim$20K). In this phase collimated jets and molecular outflows from the star might appear. HMPOs put together phases 4 and 5.

(iii) **UC HII regions**: these objects are already ZAMS stars still embedded in the natal cloud, and are part of phase 6 above. The pressure enhancement, due to the heating produced by the ionising radiation, produces an expansion of the hypercompact HII region, forming the so-called UC HII regions (r~0.1 pc).

This classification, shown in Fig.1.3, is the one that has been used in this thesis, in particular in the works described in chapters 2 and 3.
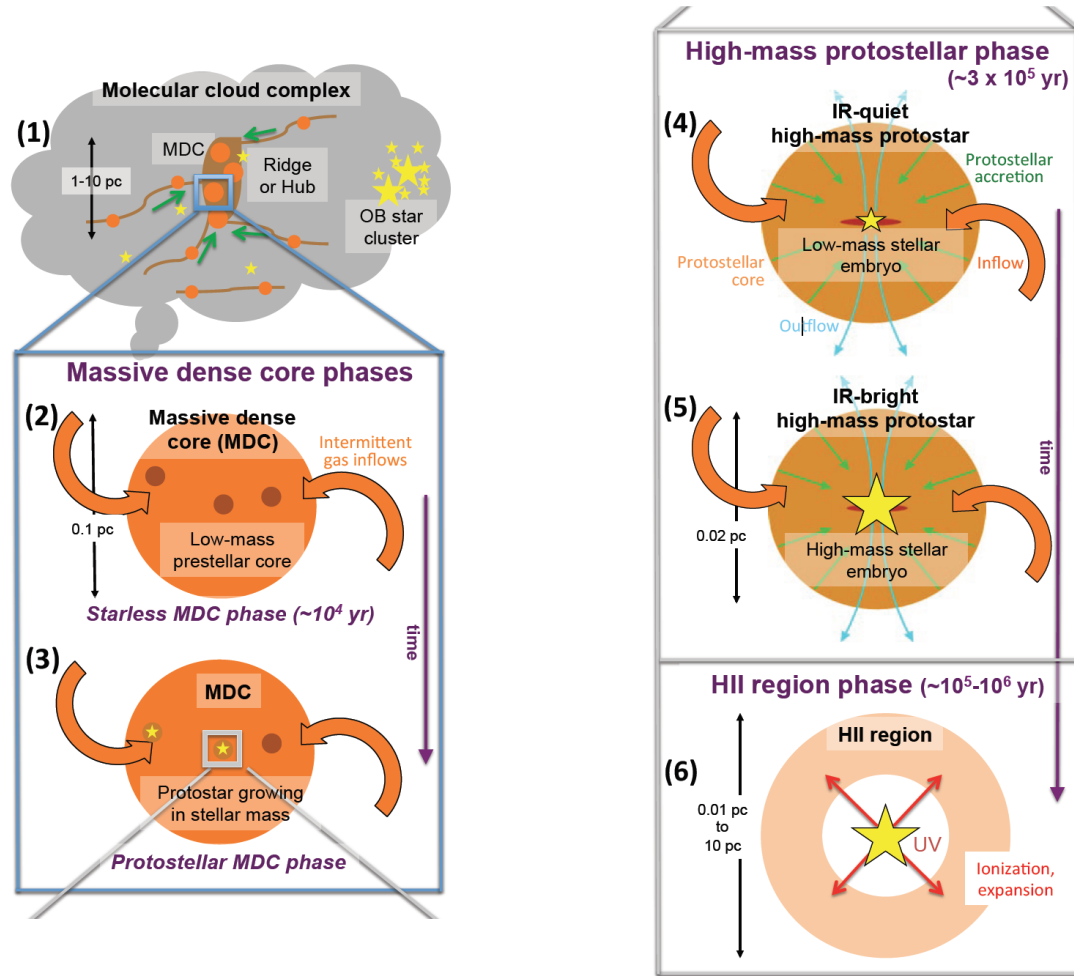
Fig. 1.2: Scheme of the evolutionary stages for the formation of massive stars, taken from Motte et al. (2018).

1.2. THE IMPORTANCE OF HIGH-MASS STAR-FORMING REGIONS FOR THE SOLAR SYSTEM FORMATION

Nowadays, there is growing evidence that stars, including our Sun, do not form in isolation, but in rich clusters (e.g. Lada and Lada 2003). Adams (2010) discuss in his review the birth environment of the Sun from the extant properties of our Solar system. In particular, one of the physical processes that influenced the forming Solar system can be inferred by the presence of short-lived radioactive species in meteorites. Short-Lived Radionuclides (SLRs) are those with half-lives less than about 10 Myr. From the relative abundance of the daughter species in meteoritic samples it can be inferred how much time it takes from their production and their incorporation into the early Solar system. These measurements indicate that only a short time (~1 Myr) could have elapsed between the production of short-lived species and their subsequent incorporation into the early Solar system material. Supernova explosions provide one possible source of these radioisotopes. One example SLR is ^{26}Al, which has a half-life of 0.72 Myr and decaying creates ^{26}Mg, the amount of which is measurable in meteoritic samples. However, more recent works show that the ^{26}Al distribution in the early Solar system seems to have been heterogeneous (e.g. Liu et al. 2012). This
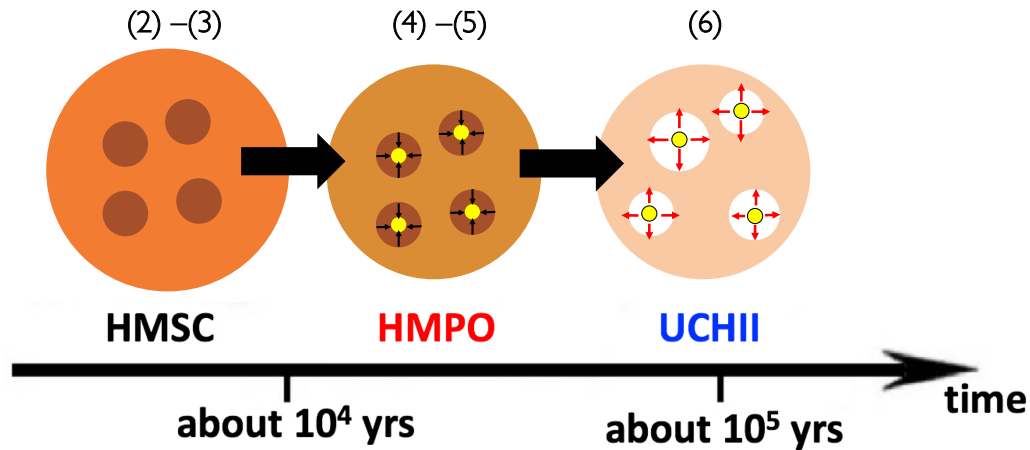
Fig. 1.3: Scheme of the gross evolutionary classification for high-mass star-forming regions, adapted from Beuther et al. (2007a). The numbers in the top represent the phases proposed by Motte et al. (2018) and described in the text.

suggests that the ^{26}Al is most likely produced from the wind of massive stars, and not from a single supernova explosion. Gounelle and Meynet (2012) proposed that ^{26}Al originated in a wind-shell around a massive star which, after several Myr, reaches large densities and becomes gravitationally unstable, giving rise to a second star generation. The presence of ^{26}Al in the early Solar system is also important to explain the bulk of the water that we expect during the formation of planetesimals. In fact, the decay heat from this SLR should have been sufficient to power the interior evolution of these bodies. Lichtenberg et al. (2019) use numerical models of planet formation to show that a planet's bulk water fraction is anti-correlated with initial ^{26}Al levels. The heat generated by the decay of this element rapidly dehydrates planetesimals before their accretion onto larger protoplanets. This would allow to form *dry* terrestrial planets like our Earth. Another SLR found in pristine Solar system material is the ^{60}Fe, the abundance of which could be explained only by the presence of, at least, two supernovae, as proposed by Portegies Zwart (2019). In fact, one is necessary to deliver the ^{60}Fe, and the other to preserve it in the proto-Solar disc.

Although some SLRs could be explained also by internal processes connected to the forming Sun itself (e.g. ^{10}Be, Gounelle et al. 2001), the processes mentioned above indicate that the forming Solar system was not in a peaceful, quiescent environment, but in the middle of a rich cluster including massive stars, some of which could have been exploded as supernovae. All of these arguments, thus, suggest that data from meteorites can be interpreted by both an external and internal enrichment mechanism into the early Solar system.

Another physical process that influenced the Solar system formation, discussed by Adams (2010), is the dynamics of the birth cluster that could have affected stars and planets formation. In fact, the observed planetary orbits indicate that no passing stars have made disruptive encounters with the Solar system after the giant planets were formed. However, the orbit of the dwarf planet Sedna can be explained only with a close encounter, at a distance of 400-800 au. This information constrains the stellar density n_* of the Solar system birth environment, in residence time t in that region, to be of the order of $<n_* t> \sim 80000$ pc^{-3} Myr. Since $n_* \sim 100$ pc^{-3} is a mean typical stellar density, the Solar system must have

lived in its birth cluster for a few hundred million years. In this case, only large bound clusters, with a number of membership $N > 1000$ are expected to live that long (e.g. Kroupa 2001). The other possibility is that the Sun lived in a higher density environment.

The last point discussed by Adams (2010) is the possible external UV radiation field experienced by the young Sun, and provided by the cluster which could have played a role in shaping the proto-Solar nebula (PSN), in which our Sun was born. The far-UV (FUV) fluxes are expressed in units G_0, and $G_0 = 1$ corresponds to the flux in the solar neighbourhood $F_{\text{FUV}} = 1.6 \times 10^{-3}$ erg s^{-1} cm^{-2} (Habing 1968). An external FUV with $G_0 \approx 10^4$ is necessary to photoevaporate the early Solar nebula beyond about 30 au and to explain the low amount of gas in ice giant planets, like Neptune and Uranus. This value is beyond the peak of the distribution for young clusters in the solar neighbourhood. This means that the birth cluster must be larger than the clusters in the neighbourhood of the Solar system, with $N \geq 1000$.

A possible scenario that puts together these three points, for example, requires a cluster with at least $N \geq 1000$, in order to produce a 25 M$_\odot$ star. This star could enrich the Solar system of the short-lived radioisotopes through its wind, and is able to explain both the possible external UV radiation $G_0 \leq 10^4$ and the present planet orbits (see Fig. 1.4).
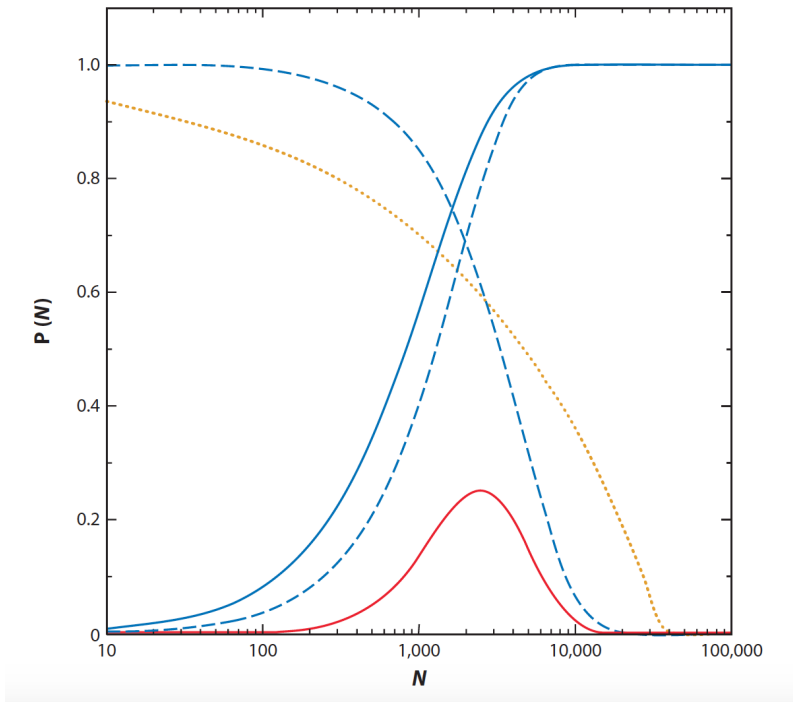
Fig. 1.4: Probability distributions for a cluster of membership size N as a function of N. In particular, the solid blue curve is the probability to produce a supernova with progenitor mass $M_* \geq 25$ M$_\odot$. The dashed blue curves represents the probability of a close encounter with a distance less than 400 au (to produce Sedna), but no encounters at a distance < 225 au in order to preserve the planetary orbits. The dotted orange curve is the probability to have an external FUV with $G_0 \leq 10^4$. Finally, the red solid line is the joint probability distribution with $<N> = 4300 \pm 2800$. Taken from Adams (2010).

Other evidence that our Sun was born in a cluster containing massive stars comes also from the works made by Taquet et al. (2016) and Drozdovskaya et al. (2018). In particular, Taquet et al. (2016) investigated the chemical and physical origin of O_2 using astrochemical models, and compared these results with the gas-phase O_2 recently observed in the coma of comet 67P/Churyumov-Gerasimenko (hereafter 67P, Bieler et al. 2015) by

the *Rosetta* spacecraft. The main result that they obtained is that the molecular oxygen is mainly formed in dark clouds for higher densities ($\gtrsim 10^5$ cm^{-3}) and moderate temperatures (≈ 20 K) with respect to those commonly considered as Solar system progenitor. In fact, this is the typical temperature of a high-mass starless core (HMSC, e.g. Fontani et al. 2011), and is hotter than that of isolated low-mass pre-stellar cores (<10 K, e.g. Keto and Caselli 2010). Furthermore, Drozdovskaya et al. (2018), searched for S-bearing species at a distance of 60 au from the proto-Sun analogous low-mass protostar IRAS 16293-2422 B (hereafter 16293B), and compared these results with data on comet 67P. They show that 16293B contains much more OCS than H_2S in comparison with 67P. A possible explanation is a a relatively warmer birth cloud of our Solar system, with respect to 16293B.

In summary, the detailed study of the physical and chemical conditions of high-mass star-forming regions is important not only to understand the formation of massive stars, but also because they probably are the cradle in which our Solar system was born.

1.3. ASTROCHEMICAL PROCESSES IN THE INTERSTELLAR MEDIUM

Before discussing in detail the main topic of this thesis, let us briefly review the main processes that lead to the formation of molecules in the ISM. Molecules can form both on ice mantles of grains and through gas-phase reactions. In particular, in the gas phase, a chemical reaction can occur spontaneously if the variation of the Gibbs free energy, ΔG, is lower than zero. G is a state function used in thermodynamics that represents the free energy (U) of the isothermobaric reactions, i.e. those during which pressure (P) and temperature (T) remain constants. So, given that $G = H - TS$, with the enthalpy $H = U + PV$ and the entropy S:

$$\Delta G = \Delta H - T\Delta S = \Delta U + R_g T \Delta N + T\Delta S, \tag{1.4}$$

in which it is assumed a constant T during the reaction, and that the gas follows the ideal gas law $PV = \mathcal{N} R_g T$ ($\mathcal{N}$ moles number, and R_g ideal gas constant). Considering that the typical temperatures in the ISM are low (~ 10 K), the second and the third terms are negligible with respect to the first one. So, the condition to have $\Delta G \leq 0$ is $\Delta U \leq 0$, i.e. the internal energy of the reaction products must be less than the internal energy of the reactants. This means that the energy is transferred to the environment in which the reaction occurs (exothermic reaction).

During a reaction, before the formation of the products, there is an intermediate state in which some bonds are broken, but the final ones of the products are still not formed. In this state, the system possesses an amount of extra energy with respect to the rest internal energy of the reactants called "activation energy", because it is also the energy that needs to be provided to the reactants to activate the reaction (Fig. 1.5).

For example, in the reaction

$$C + H_2 \rightarrow CH + H, \tag{1.5}$$

the H_2 bond energy is 4.48 eV, while that of CH is 3.47 eV: the reaction is endothermic (see right panel of Fig. 1.5), i.e. requires from the environment 1.01 eV to be spontaneous. Then, since 1 eV corresponds to 11.6×10^4 K, at the typical temperature of the ISM (10–100 K) this reaction is not spontaneous.
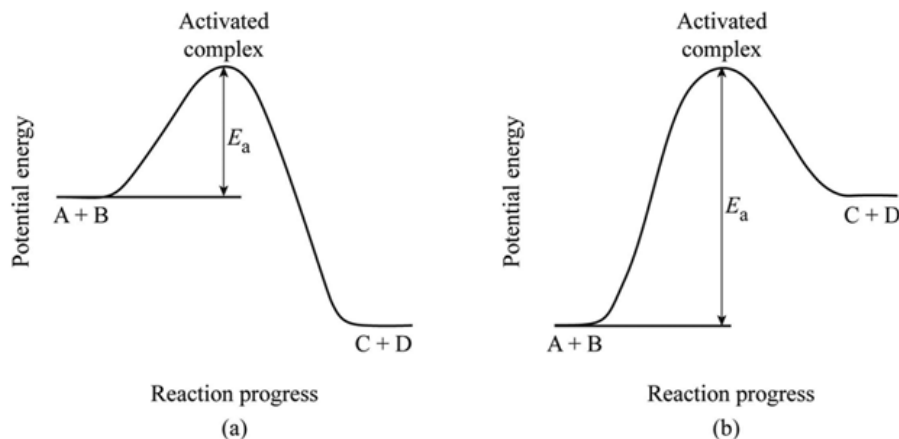
Fig. 1.5: Energy scheme of a reaction as a function of the reaction coordinate. Here the activation energy is noted by E_a. *Left panel*: exothermic reaction. *Right panel*: endothermic reaction.

1.3.1. GAS-PHASE CHEMISTRY

Gas-phase reactions can be divided into different categories. Reactions such as photodissociation, dissociative recombination, and collisional dissociation are bond-destruction processes that fragment species into smaller ones. Other reaction types are, for example, ion-molecule reactions, charge-transfer reactions, and neutral-neutral reactions.

A general chemical reaction

$$A + B \xrightarrow{k} C + D, \tag{1.6}$$

is associated with his rate coefficient, k, which is a measure of the efficiency of the reaction. Generally, this coefficient is given in the form of a modified Arrhenius equation:

$$k = \alpha \left(\frac{T}{300K} \right)^{\beta} \exp\left(\frac{-\gamma}{T} \right), \tag{1.7}$$

where β is a possible dependence on the temperature of the reaction and γ is the possible activation energy. This is a general formula used for most of the gas-phase reactions, but some reaction types are parametrized differently. We will discuss some of them later in this chapter and in chapter 5. k is also called capture-rate coefficient ($k_{capture}$), from the theory for barrierless reactions (e.g. Georgievskii and Klippenstein 2005). For a reaction like (1.6), the corresponding rates of formation and destruction of a species are

$$\frac{dn(C)}{dt} = k n(A) n(B), \tag{1.8}$$

and

$$\frac{dn(A)}{dt} = -k n(A) n(B), \tag{1.9}$$

respectively, where $n(i)$ is the number density of species i in cm^{-3}. The total rate of change in the number density of species X is thus given by

$$\frac{dn(X)}{dt} = \text{formation terms} + \text{destruction terms.} \tag{1.10}$$

For a reaction system with forward and reverse reactions,

$$A + B \underset{k_r}{\overset{k_f}{\rightleftharpoons}} C + D, \tag{1.11}$$

the equilibrium coefficient $K(T)$ is defined by the relation

$$K(T) = k_f / k_r, \tag{1.12}$$

where k_f and k_r are the forward and reverse rate coefficients, respectively.

The equilibrium coefficient $K(T)$ is defined by the equation (McQuarrie 1976):

$$K(T) = k_f / k_r = \left[\frac{m(C)\,m(D)}{m(A)\,m(B)} \right]^{3/2} \frac{q(C)\,q(D)}{q(A)\,q(B)} \exp(\Delta E_0 / k_B T), \tag{1.13}$$

where $m(...)$ are the masses of molecules, $q(...)$ are the internal molecular partition function, and ΔE_0 is the zero-point vibrational energy difference between the reactants and the products[5]. This latter is positive if the reaction is exothermic. Moreover, k_B is the Boltzmann constant, and T is the temperature. The partition functions are given by

$$q(T) = \sum_i g_i \exp(-E_i / k_B T), \tag{1.14}$$

where g_i is the spin degeneracy of the level i and E_i is the energy of the ith state. If there is no coupling, the partition functions can be factored in the three therms corresponding to the electronic, vibrational and rotational-nuclear spin terms.

A simplified expression for $K(T)$, equivalent to (1.13), is

$$K(T) = f(B, m) \exp(\Delta E_0 / k_B T), \tag{1.15}$$

in which the factor f is called "symmetry factor" and depends on the rotational constants, B, of molecules involved in the reaction, masses and symmetries of the reactants and products (e.g. Terzieva and Herbst 2000).

1.3.2. TYPE OF REACTIONS

Two of the main type of reactions that could occur in the ISM are the neutral-neutral and the ion-neutral ones (e.g. Tielens 2005). The property that distinguishes them is the rate of two-body collisions, k_{AB}. If particles B are characterised by a velocity distribution relative to particles A, $f(v)$, then

$$k_{AB} = \int_0^\infty v f(v) \sigma_{AB}(v)\, dv \quad \mathrm{cm^3 s^{-1}}, \tag{1.16}$$

where $\sigma_{AB}(v)$ is the collisional cross-section. If particles B follow the Boltzmann energy distribution, then the velocity distribution is the Maxwell one:

$$f(v) = 4\pi v^2 \left(\frac{\mu}{2\pi k_B T} \right)^{\frac{3}{2}} \exp\left(-\frac{\mu v^2}{2 k_B T} \right), \tag{1.17}$$

---

[5] The zero-point energy (ZPE) is the lowest possible energy that a quantum mechanical system may have. In our case, the systems are the single molecules, and their ZPE is defined as the lowest quantum energy level.

where T is the gas kinetic temperature, μ is the reduced mass of the reactants, and v is the relative velocity. Thus, substituting in eq. (1.16),

$$k_{AB} = 4\pi\left(\frac{\mu}{2\pi k_B T}\right)^{\frac{3}{2}} \int_0^\infty v^3 \exp\left(-\frac{\mu v^2}{2 k_B T}\right) \sigma_{AB}(v)\, dv. \tag{1.18}$$

For different reactions, σ_{AB}, and hence k_{AB}, is different:

- **neutral-neutral reactions**: the collision of the two particles can be approximated as that of two rigid spheres. In this case the cross-section is given by the geometric area defined by the distance between the sphere centres, $\sigma_{AB} = \pi(r_A + r_B)^2$, and then taking A = B = hydrogen with mass m_H, equation (1.18) becomes:

$$k_{AB} = 1.81 \times 10^{-10}\left(\frac{T}{10^2 \text{K}}\right)^{\frac{1}{2}}\left(\frac{m_H}{\mu}\right)^{\frac{1}{2}}\left(\frac{r_A + r_B}{2\text{Å}}\right)^2 \quad \text{cm}^3\text{s}^{-1}; \tag{1.19}$$

- **ion-neutral reactions**: in this case the spherical approximation is not valid. The two particles react also at large distance through the electrostatic attraction between the ion and the dipole moment induced on the neutral particle. The cross section could be described by $\sigma_{AB} = \pi b_0^2$, where b_0 is the limit cross distance, beyond which there is no collision (Duley and Williams 1984). One can demonstrate that b_0 is a function of the polarizability of the neutral species, α, and then (1.18) becomes:

$$k_{AB} = 2.34 \times 10^{-09} q\left(\frac{\alpha}{\mu}\right)^{\frac{1}{2}} \quad \text{cm}^3\text{s}^{-1}, \tag{1.20}$$

where α is in cubic angstroms, μ is in atomic mass units (amu), and q is the electronic charge in unit of 4.80×10^{-10} esu, that is the c.g.s. expression for the elementary charge. This rate coefficient is also called "Langevin rate", k_L (e.g. Tielens 2005), and to a first approximation it is independent on the temperature. At high temperatures, the rapid rotation of neutral species over various directions generate an average value of zero for the dipole moment. However, the latter is not zero at low temperatures since neutral species rotate slowly. Complex dependences on the temperature have been proposed and, for example, for ion-neutral reactions with a dipole moment it can be used the Su-Chesnavich capture approach (e.g. Woon and Herbst 2009 and Wakelam et al. 2012). In particular, the rate for these reactions is expressed in terms of the Langevin rate using two formulas, one for lower and one for higher temperatures. The temperature ranges will depend on the parameter x, defined as:

$$x = \frac{\mu_D}{\sqrt{2\alpha k_B T}}, \tag{1.21}$$

where μ_D is the dipole moment in units of Debye (1 D = 10^{-18} statC cm). The rate coefficient is then expressed as follows:

$$k_{AB} = \alpha k_L\left(0.62 + 0.4767\gamma\left(\frac{300}{T}\right)^{1/2}\right) \quad \text{if } x \geq 2, \tag{1.22}$$

$$k_{AB} = \alpha k_L\left(1 + 0.0967\gamma\left(\frac{300}{T}\right)^{1/2} + \frac{\gamma^2}{10.526}\frac{300}{T}\right) \quad \text{if } x < 2, \tag{1.23}$$

where α, in this case, is the branching ratio of the reaction, while γ represents the value of x at 300 K.

From what described above, at low temperature the ion-neutral reaction k_{AB} is constant (because temperature-independent), while for neutral-neutral reactions decreases. This is the reason why ion-neutral reactions are the most probable to occur in the molecular clouds, where often temperature is as low as 10 K.

BASICS OF CARBON, OXYGEN, AND NITROGEN CHEMISTRY

The most abundant molecular ion of the ISM is H_3^+, formed by the following reactions:

$$H_2 + c.r. \rightarrow H_2^+ + e^- + c.r., \tag{1.24}$$

and

$$H_2^+ + H_2 \rightarrow H_3^+ + H. \tag{1.25}$$

This very abundant ion triggers many ion-neutral reactions. In fact, it can easily donate a proton and allows the formation of bigger and bigger molecules.

For example, oxygen (O) chemistry starts from reactions shown in Fig. 1.6, and in particular with a proton transfer from H_3^+ to the neutral oxygen. Oxygen leads to the formation of water, H_2O, a molecule important for life on Earth. The formation of organic molecules and hydrocarbons from atomic carbon follows a similar path (see the bottom-right panel in Fig. 1.6), starting from neutral atomic carbon that reacts with H_3^+. Note that in diffuse clouds the OH^+ and CH^+ ions can also form starting from O^+ (that forms from $O + H^+$) and C^+ (that is the dominant form of carbon in diffuse clouds), respectively. In fact, the O^+ and C^+ ions react with H_2 forming OH^+ and CH^+ (for more details see Yamamoto 2017). However, nitrogen (N) chemistry do not start with the reaction

$$N + H_3^+ \rightarrow NH^+ + H_2, \tag{1.26}$$

given that it is endothermic. This chemical network starts with the neutral-neutral reaction

$$CH + N \rightarrow CN + H, \tag{1.27}$$

and can form molecules such as HCN, N_2H^+ or NH_3 (Fig. 1.6).

1.4. ISOTOPIC FRACTIONATION IN THE CONTEXT OF STAR FORMATION

Isotopic fractionation is the set of processes that distributes different isotopes[6] of an element in molecular species. The study of the isotopic fractionation during the different phases of star formation is a powerful tool to understand how the chemical content can be transferred from the initial molecular clouds to planetary systems. However, the processes by which it proceeds during star formation are not well understood and are a highly debated topic in the astrochemistry field. In this section the state-of-the-art of isotopic fractionation of hydrogen and nitrogen, and their link with the chemical complexity at different phases of star formation, is presented.

---

[6] Isotopes are variant of a chemical element which differ in the number of neutrons.
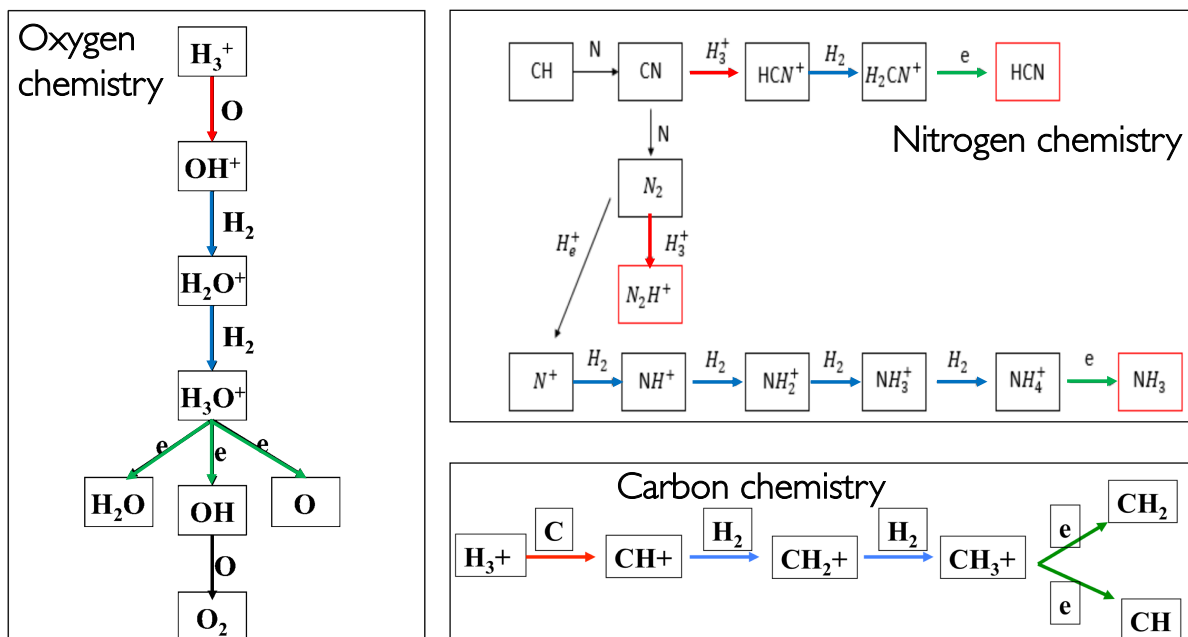
Fig. 1.6: Carbon, nitrogen, and oxygen chemical networks. The red arrows represent the proton transfer reactions, the blue arrows represent the hydrogen abstraction reactions, and the green arrows are the dissociative recombination reactions with electrons. Adapted from Duley and Williams (1984).

1.4.1. THE EVOLUTION OF CHEMICAL COMPLEXITY DURING STAR FORMATION

CHEMICAL COMPLEXITY IN LOW-MASS STAR-FORMING REGIONS

Star formation and molecular complexity evolve closely together. In fact, a rich chemistry has been observed during the different phases of star formation (Fig. 1.7). Recalling the main phases of Sun-like star formation, they can be described also from a chemical point of view (Caselli and Ceccarelli 2012):

- **Pre-stellar cores.** At the low temperatures (~10 K) of this phase, the gas-phase chemistry is dominated by ion-neutral reactions, as discussed in Sect. 1.3. Atoms and molecules can directly react in gas-phase, and if the gas temperature allows to overcome the activation energies of exothermic reactions, more complex chemistry progresses. Moreover, if the density is high enough ($\geq 10^6 cm^{-3}$) and the temperature is ≤ 10 K, molecules and atoms in the gas-phase freeze-out[7] onto the cold surfaces of sub-micron size dust grains. H atoms have high mobility on dust surfaces, and this allows the hydrogenation of atoms and CO (the molecule most abundant in the ISM, after H_2). In this way molecules such as water (H_2O), formaldehyde (H_2CO) and methanol (CH_3OH) can be formed efficiently on the surface of dust grains. It has been observed that also more complex organic molecules (e.g. CH_3OCH_3) are already formed in these initial phases of star formation (e.g. Bacmann et al. 2012; Vastel et al. 2014; Jiménez-Serra et al. 2016).

---

[7]   The adsorption of species onto dust grain surfaces.
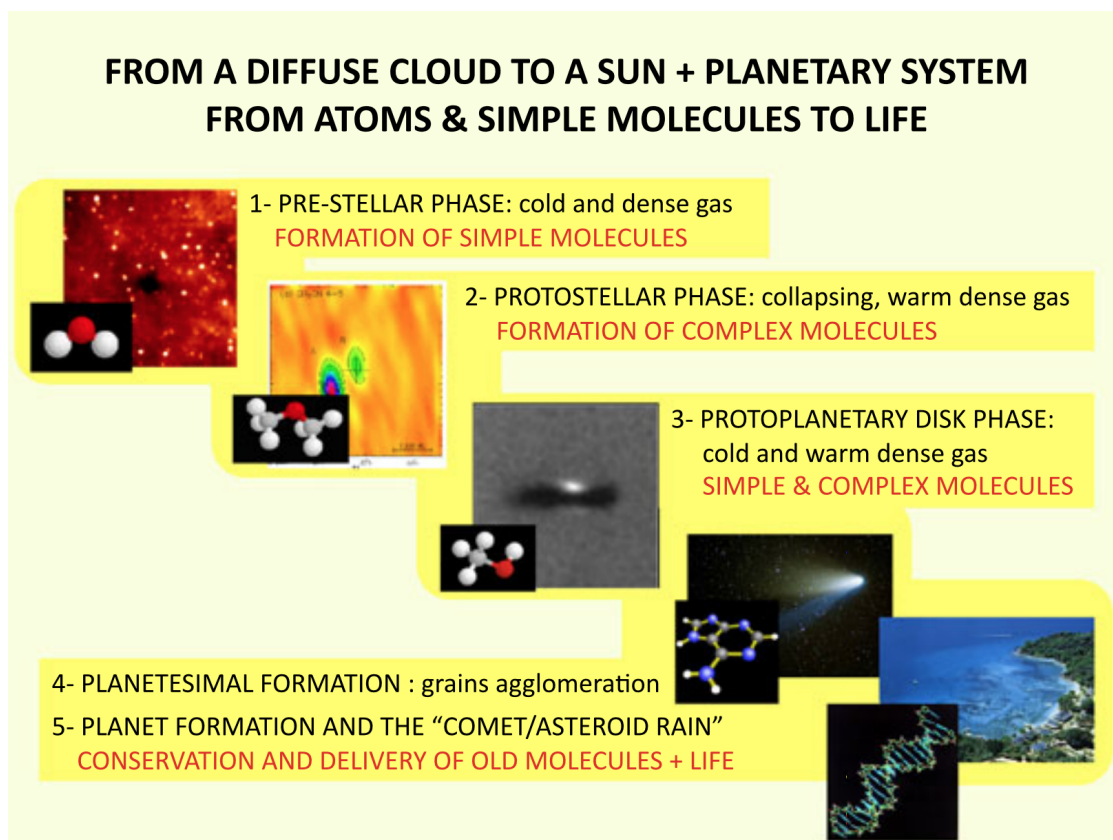
Fig. 1.7: Simplistic view of the evolution of chemical complexity, hand in hand with phases of Sun-like star formation. Taken from Caselli and Ceccarelli (2012).

- **Protostellar envelopes.** In this phase the temperature increases and when the envelope reaches the mantle sublimation temperature, the molecules formed onto ice surfaces sublimate. Here they can react and form more complex molecules. Moreover, collimated jets and molecular outflows are present and, when impacting the quiescent gas of the birth molecular cloud, create shocks that partially sputter the ice mantles and refractory materials of grains, injecting molecules into the gas phase.

- **Protoplanetary discs.** In the colder inner substrates of the disc, molecules formed during the protostellar phase freeze-out onto ice mantles, and could still preserve a part of the composition of the pre-stellar phase. The process of "conservation and heritage" begins.

- **Planetesimal formation.** While the grains glue together forming pebbles and planetesimals, part of the icy grain mantles is preserved. Thus, part of the chemical history of the first phases of star formation is conserved in the building blocks of the Solar System rocky bodies.

- **Planet formation and the comet/asteroid rain.** Comets and asteroids that arrive onto the primitive Earth also release the heritage conserved in the ice trapped in planetesimals and rocks.

CHEMICAL COMPLEXITY IN HIGH-MASS STAR-FORMING REGIONS

In high-mass star-forming regions the chemistry evolves similarly to the low-mass star-forming ones. Recalling the three main evolutionary stages described in Sect. 1.1.1 and Fig. 1.3, the chemical evolution could be described as follows (e.g. Bisschop et al. 2007; Beuther et al. 2009):

- **HMSCs**: mostly simple molecules (like CO, N_2H^+, HCN, HNC, CN) form during this phase, as in the low-mass case. Moreover, the chemical complexity grows on dust grains thanks to the freeze out of molecules into ice mantles. Most saturated and complex species, such as H_2CO, CH_3OH, C_2H_5OH, $HCOOCH_3$, and CH_3OCH_3, probably result from a "first generation" chemistry in ices, likely dominated by surface chemistry.

- **HMPOs**: some of the species formed in ice mantles desorb thanks to the higher temperatures (>20 K) during this phase. Moreover, extended outflows and shocks sputter the mantles and refractory materials of grains directly in the gas phase. These objects are also characterised by H_2O and methanol masers (e.g. Moscadelli et al. 2017; Sanna et al. 2018);

- **UCHIIs**: this phase is characterised by ionised hydrogen (H^+), and a high electronic density ($n_e \geq 10^4$ cm^{-3}). These regions are traced, for example, by the free-free radiation (or thermal bremsstrahlung) at cm wavelengths. Moreover, the central envelope is chemically enriched as the HMPO phase (e.g. Bisschop et al. 2007; Fontani et al. 2007).

1.4.2. THE HERITAGE OF THE SOLAR SYSTEM

A powerful tool to understand the chemical heritage from the earliest to the latest phases of the Solar system formation is the study of isotopic anomalies, in particular those measured for D/H and ^{14}N/^{15}N. In fact, the isotopic values of hydrogen, nitrogen and oxygen derived for the proto-Solar nebula differ by a factor of ~2 with respect to those measured in comets and carbonaceous chondrites[8], which represent the pristine Solar system material. This indicates that the isotopic values have been altered due to physical/chemical processes during the formation of the Sun. Isotopic anomalies could also give important information about the Galactic environment in which our Sun was born. For example, the anomalous ^{18}O/^{17}O in meteorites (5.2±0.2, Wouterloot et al. 2008) with respect to the Galactic value (4.1±0.1, Young et al. 2011) is another proof of injection of material from a type II supernova exploded near the Solar system just before its birth.

In this thesis I will focus on the isotopic fractionation of nitrogen, hydrogen, and carbon in star-forming regions.

---

[8] They are a class of chondritic meteorites and include some of the most primitive material. Chondritic meteorites are stony meteorites that have not been modified due to the melting or differentiation of the parent body.
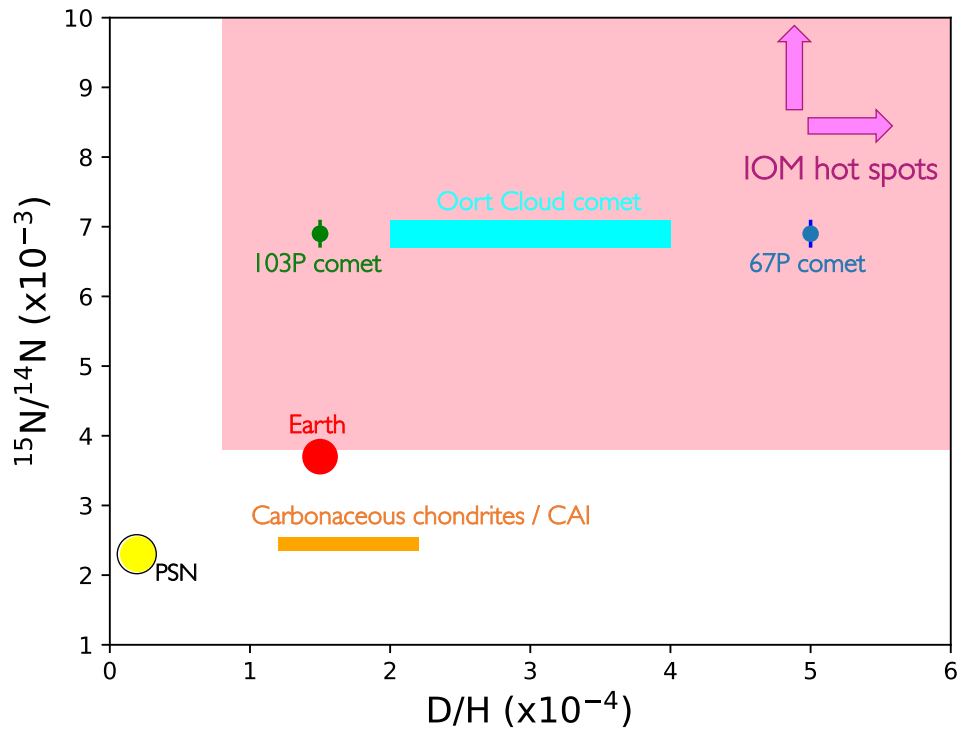
Fig. 1.8: $^{15}N/^{14}N$ vs D/H in comets, chondrites, hot spots in the IOM of meteorites, Earth and PSN.

DEUTERIUM IN PRISTINE MATERIALS

The D/H ratio for the PSN was estimated to be $(2.1\pm0.5)\times10^{-5}$ (Geiss and Gloeckler 1998). Different values of the D/H ratio have been estimated in comets: in the Jupiter-family comet 67P, the D/H ratio measured in H_2O is about 5×10^{-4} (Altwegg et al. 2015), approximately three times that of Earth's oceans (1.5×10^{-4}). However, results from *Herschel* have shown D/H$\sim1.5\times10^{-4}$ in another Jupiter-family comet, 103P/Hartley (Hartogh et al. 2011), which is the same as in the Earth oceans. Other measurements are from the Oort Cloud comets, where the HDO/H_2O ratio has been measured to be $\sim3\times10^{-4}$ in C/1996 B2 (Bockelée-Morvan et al. 1998), $\sim4\times10^{-4}$ in 8P/Tuttle (Villanueva et al. 2009), and in C/2009 P1 it is 2×10^{-4} (Bockelée-Morvan et al. 2012).

Deuterium enrichment in Earth's oceans with respect to the PSN value has been investigated and two theories were proposed. The first theory suggested that water is delivered to Earth from comets during the Late Heavy Bombardment (Gomes et al. 2005). This theory was encouraged by the *Herschel* measurement toward the comet 103P/Hartley that presents the same H/D value than that of the terrestrial oceans. The second theory is based on the possibility that the Earth was partly built from water-rich planetesimal from the outer zone (Morbidelli et al. 2000). The HDO/H_2O measured in carbonaceous chondrites is in agreement with this theory (see Fig. 1.8).

Deuterium enrichment has also been observed in HCN, in the comet C/1995 O1 (Meier et al. 1998), and it is 10 times larger than the water D-enrichment. This difference is one of the hints that different chemical formation pathways could occur for the two different species.

In carbonaceous chondrites, values of D/H~1.2-2.2×10^{-4} in hydrous silicates were obtained (Robert 2003), and are very similar to that of the terrestrial oceans. Furthermore,

very high D/H ratios of $\sim 10^{-2}$ have been found in small regions in insoluble organic matter (IOM) of meteorites (Remusat et al. 2009); these regions are called "hot spots". In addition, interplanetary dust particles (IDPs) presents very variable values, from D/H$\sim 8 \times 10^{-5}$ up to $\sim 10^{-2}$. The values described above are shown in Fig. 1.8.

^{15}N IN PRISTINE MATERIALS

The ^{14}N/^{15}N ratio measured for the PSN is about 441 (Marty et al. 2010). A ^{14}N/^{15}N ratio of 139±26, from HCN, was estimated in the comet 17P/Holmes after an outburst (Bockelée-Morvan et al. 2008). Manfroid et al. (2009) estimated a mean value of ^{14}N/^{15}N=148±6 from CN in 18 comets. Fig. 1.9 summarises ^{14}N/^{15}N measured in comets from HCN, CN, and NH$_2$. The values found in different comets are similar, with an average value of ^{14}N/^{15}N=144±3.

Different values of ^{14}N/^{15}N were estimated in the carbonaceous chondrite Isheyevo: ~ 424 in an osbornite-bearing calcium-aluminium-rich inclusion (CAI) (Meibom et al. 2007), and from 44 up to 264 (van Kooten et al. 2017) in lithic clasts. In the latter the maximum value is similar to the typical one derived in the terrestrial atmosphere (TA), as derived from N$_2$, ~ 272 (Marty et al. 2009). The ^{15}N-enrichment in the terrestrial atmosphere, as well as that in other rocky planet atmospheres (e.g. Mars), is still not well understood. This value could be linked to the history of asteroids fallen to the Earth, or to a secondary atmospheric processing (Marty et al. 2009). Measurements in carbonaceous chondrites are made in specific parts of the objects, as described above, while measurements in comets refer to average values in cometary comae. For these reasons, the values obtained from extraterrestrial material studied on Earth could be different from observations of comets. At the same time, different values from different parts of the same chondrite are measured, and this indicates that different parts of a chondrite are formed during different times of star formation. Meibom et al. (2007) infer that the carbon-bearing titanium-nitride (osbornite) in the Isheyevo CAI formed by gas-solid condensation, started in a high-temperature (~ 2000 K) inner region (< 0.1 AU) of the PSN, where all solids were initially evaporated and the gas homogenized. Under such high-temperature conditions, little isotopic fractionation is expected between gas and solids, and the nitrogen isotopic composition of osbornite in the Isheyevo CAI must be representative of the Solar nebula. In fact, winds associated with bipolar outflows, or turbulent transport of the hot inner nebula (silicate) dust, may have carried small refractory particles out to colder zones where CAIs were incorporated during protoplanet formation. van Kooten et al. (2017) infer, from isotope data of Isheyevo lithic clasts, that these variations in N isotopes are consistent with the accretion of multiple organic precursors and subsequent alteration by fluids with different (isotopic) compositions, taking place in more evolved stages of protoplanetary formation than the enrichments in CAI.

All of these values are different than those measured for the PSN, as summarised in Fig. 1.8, suggesting that at some point of the Sun formation D- and ^{15}N-enrichment processes occurred. One possibility is a direct heritage of the chemical complexity from the pre-stellar core phase or the protoplanetary disc phase. For this reason observations of H- and N-fractionation in these phases are really important to understand D- and ^{15}N-enrichments in pristine Solar system materials, and also in our Earth.
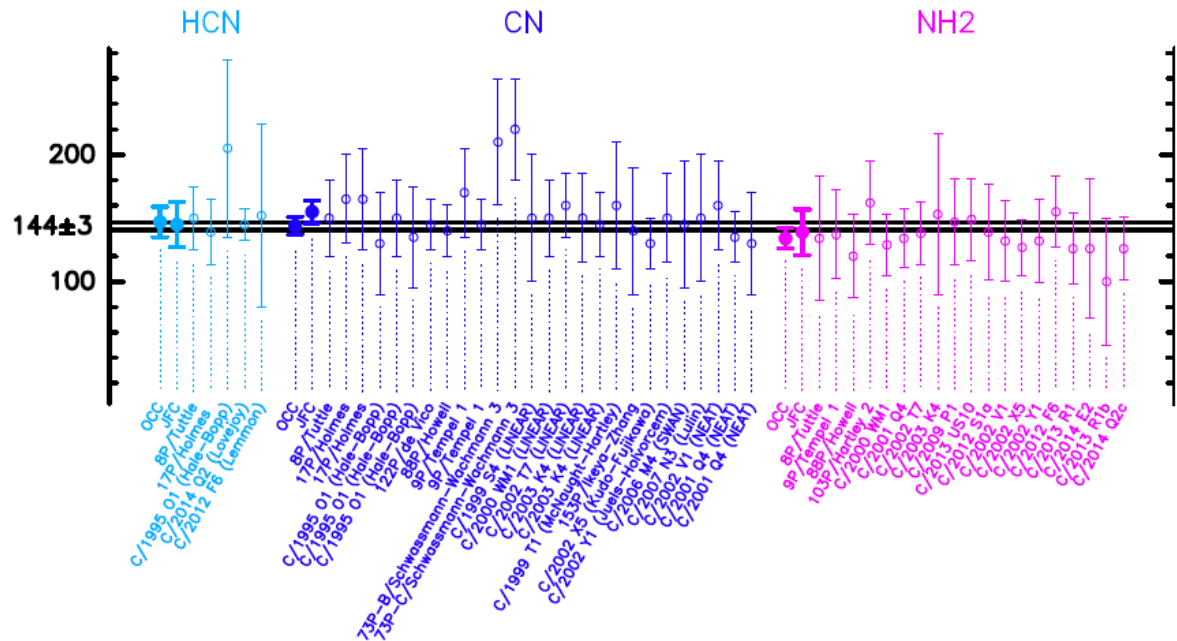
Fig. 1.9: Compilation of all $^{14}N/^{15}N$ ratios measured in comets. Taken from Hily-Blant et al. (2017).

1.4.3. DEUTERIUM ENRICHMENT DURING STAR FORMATION

How the D/H ratio changes in different phases of star formation in the ISM was highly debated in past years. Nowadays there is a common opinion on the main process that enhances or decreases deuterium in molecules in molecular clouds. In this section the general idea, based both on theoretical and observational results, is reviewed.

D-FRACTIONATION IN LOW-MASS STAR-FORMING REGIONS

Low-mass pre-stellar cores present densities that go from $\sim 10^3$ cm^{-3} in the outer part, to about $\sim 10^7$ cm^{-3} in the inner 1000 au[9]. Between 7000 and 15000 au the gas density is about 10^4 cm^{-3} and the temperature ~ 10 K. In this region classical dark-cloud chemistry is at work with a high probability of ion-molecule reactions that dominate the carbon chemistry and create CO. Less important but probable are also neutral-neutral reactions that start the transformation of nitrogen atoms into nitrogen-bearing molecules, N_2, N_2H^+, and NH_3. First carbon and nitrogen chemistry are summarised in Fig. 1.6. Moreover, in the inner 7000 au the density increases to $\sim 10^5$ cm^{-3} and the temperature drops below 10 K. In these regions carbon-bearing species like CO, tend to disappear from the gas-phase and to be adsorbed onto dust grain surfaces. Freeze-out is a consequence of both low temperature and high-density environments. In fact, thanks to the high densities ($\sim 10^5$ cm^{-3}) there is a high probability that gas particles impact on dust grains. Thus, once species land on grain surfaces, they cannot thermally evaporate since their binding energies, E_B, are higher than 1000 K and the thermal evaporation rate is $\propto$ exp[$-E_B/k_B T$]. However, there is the possibility that a small fraction of the adsorbed species can return in the gas-phase via desorption

---

[9]   These values of density and distance refer to those derived by Keto and Caselli (2010) for the pre-stellar core L1544. We note that this might not apply for other low-mass star-forming regions, even thought the general structure is likely to be similar.

caused by cosmic-rays impact into the grain surface, or photodesorption due to the FUV field produced by cosmic-ray impacts with H_2 molecules.

In the dense and low-temperature environment of pre-stellar cores, where ion-molecule reactions are favoured, chemical fractionation occurs, as described by Herbst (2003) starting from the reactions:

$$H_3^+ + HD \rightleftharpoons H_2D^+ + H_2 + 232K, \tag{1.28}$$

$$CH_3^+ + HD \rightleftharpoons CH_2D^+ + H_2 + 390K, \tag{1.29}$$

$$C_2H_2^+ + HD \rightleftharpoons C_2HD^+ + H_2 + 550K. \tag{1.30}$$
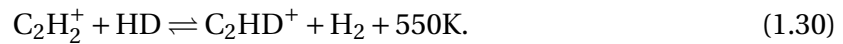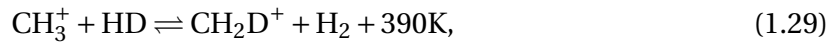
These reactions are called isotopic-exchange reactions and are caused by a thermodynamic effect in which the reaction has a preferred direction owing to exothermicity caused by a difference in the zero point energies between reactants and products. Reaction (1.28) produces an enhanced H_2D^+/H_3^+ abundance ratio for temperatures lower than ~20 K (since the reaction from right to left is very inefficient) and when H_2 is mainly in the para form (anti-parallel H spins, e.g. Pagani et al. 1992; Walmsley et al. 2004). Moreover, in dense cores CO freezes out onto dust grains (e.g. Caselli et al. 1999). Since reaction with CO is the main destruction pathway of H_3^+ and H_2D^+, these two species remain abundant. Then, the high H_2D^+/H_3^+ is propagated to other molecules that react with the two ions. The grain surface chemistry on icy material during the early cold phase is also expected to play an important role for the deuteration of neutral species such as water (H_2O), formaldehyde (H_2CO), methanol (CH_3OH), and complex organic molecules (e.g. Cazaux et al. 2011; Taquet et al. 2012; Chacón-Tanarro et al. 2019). The reason is that the enhanced abundances of the deuterated forms of H_3^+ (H_2D^+, D_2H^+, D_3^+) produce enhanced abundances of D atoms in the gas-phase upon their dissociative recombination with electrons. The enhanced D abundance causes D/H ratio up to ~0.1, so that molecules on the surface of dust grains (in particular CO) can be deuterated, to produce singly and doubly deuterated water and formaldehyde as well as singly, doubly, and triply deuterated methanol (e.g. Caselli and Ceccarelli 2012; Ceccarelli et al. 2014).

From an observational point of view, as a proof of the importance of reactions (1.28), (1.29) and (1.30), the ground state line of *ortho*-H_2D^+ was detected towards the starless core L1544 in the Taurus Molecular Cloud by Caselli et al. (2003). Fig. 1.10 shows the continuum map of this pre-stellar core, and the inner densest part is the one in which the deuteration of molecules occurs as explained above. Moreover, Vastel et al. (2004) detected the D_2H^+ ion in LDN 1689N, providing strong observational support for the D-fractionation theory.

Roueff et al. (2005) presented a steady-state model of the gas-phase chemistry for pre-stellar cores, including passive depletion on dust grains and multiply deuterated species. They compared the results of this model with observations of NH_2D, ND_2H, and ND_3 towards 5 pre-stellar cores. They obtained ND_3/NH_3 ratios between 2×10^{-4} and 1–2×10^{-3}, which imply an enhancement factor of 11–12 order of magnitude over the cosmic D/H value. Their model predicts that high densities and high C and O depletion yield to an enhancement of the relative abundance of deuterated ammonia isotopologues, in agreement with observations (see also Gerin et al. 2006).
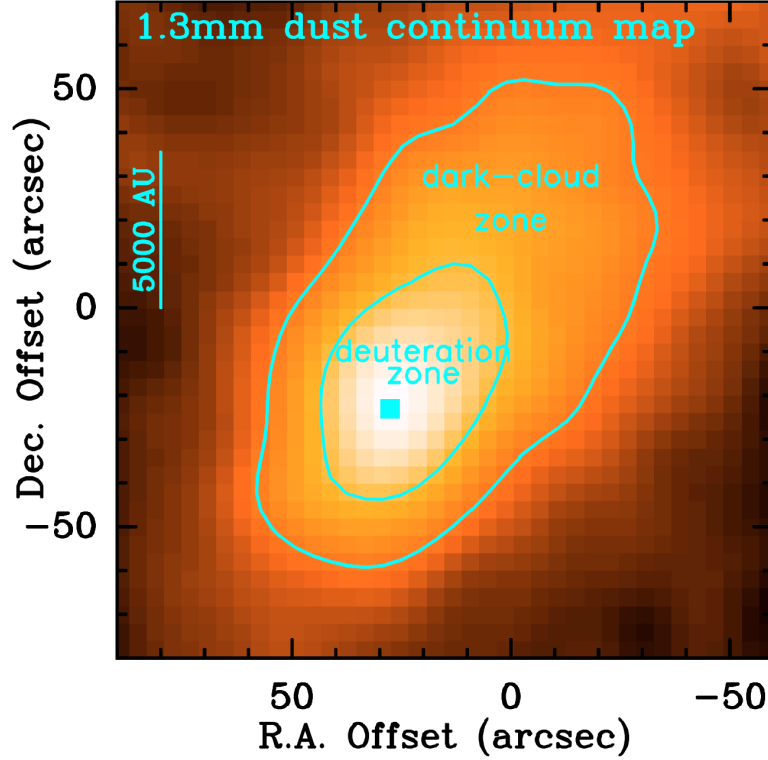
Fig. 1.10: The color scale represents the 1.3 mm dust continuum emission map obtained with the IRAM 30m radiotelescope by Ward-Thompson et al. (1999) towards the pre-stellar core L1544. Cyan contours indicate the two zones in which chemistry could be divided: the inner part is the one in which deuteration of molecules is enhanced. Image taken from Caselli and Ceccarelli (2012).

Crapsi et al. (2005) observed N_2H^+ and N_2D^+ towards a sample of 31 low-mass starless cores finding that the $N(N_2D^+)/N(N_2H^+)$ ratio is larger in the cores closest to the gravitational collapse. Emprechtinger et al. (2009) found also that $N(N_2D^+)/N(N_2H^+)$ ratio could be used as an evolutionary tracer for young protostars still embedded in their cold envelope. They derived that $D_{\mathrm{frac}}(N_2H^+)=N(N_2D^+)/N(N_2H^+)$ decreases with the protostar evolution. Moreover, Caselli et al. (2008) found, from observations of a sample of 10 starless cores and 6 protostellar cores, that the *ortho*-H_2D^+ is on average more abundant towards the starless cores than in the protostellar sources.

Recently, Redaelli et al. (2019) performed a detailed non-local thermodynamic equilibrium (non-LTE) analysis of N_2H^+, N_2D^+, $HC^{18}O^+$, and DCO^+ across the whole L1544 core. They found that N_2H^+ is more deuterated than HCO^+ (D/H=26% and 3.5%, respectively), as a consequence of the fact that N_2H^+ is less affected by depletion. Therefore, N_2H^+ appears in gas-phase when CO is already depleted and H_2D^+ is already abundant.

D-FRACTIONATION TOWARDS MASSIVE STAR-FORMING REGIONS

Can the results described above be applied to the high-mass regime? As already said, the theory of massive star-formation is still not well-understood and, moreover, the observations are challenging since these regions are at large distances (>1 kpc), and hence they have small angular sizes. Moreover, clustered environments make observations of the process challenging. However, in the last decade many studies have been performed to check

if the chemical properties observed in the earliest stages of low-mass stars are also valid for high-mass star-forming regions. In this section I will go through the main papers that studied, until now, the problem of deuterium fractionation towards these regions.

Fontani et al. (2006) observed N_2H^+ and N_2D^+ towards 10 high-mass protostellar candidates, selected from the samples described by Molinari et al. (1996) and Sridharan et al. (2002). These molecules were chosen since they can form only in gas-phase, and then they are appropriate to trace deuteration occurring through gas-phase chemistry. They found $D_{frac}(N_2H^+)$ between ~0.004 and ~0.02, with an average value of 0.015, 3 orders of magnitude higher than the PSN value, and quite close to the values found by Crapsi et al. (2005) in a sample of low-mass starless cores.

Fontani et al. (2011) expanded the previous work observing with the IRAM 30m telescope N_2H^+ and N_2D^+ towards 27 high-mass star-forming cores divided into different evolutionary stages of the massive star-formation process, already described in Sect. 1.2: high-mass starless cores (HMSCs), high-mass protostellar objects (HMPOs) and UC HII regions. They found a high N_2D^+ detection rate (>65%) towards each evolutionary stage, meaning that deuterated gas is present at every stage of massive star formation. The main result is that HMSCs have an average $D_{frac}(N_2H^+)$ of ~0.26, while HMPOs and UC HIIs have an average $D_{frac}(N_2H^+)$ of ~0.037 and ~0.044, respectively: the difference between HMSCs and both HMPOs and UC HIIs is statistically significant, and shows that $D_{frac}(N_2H^+)$ decreases by an order of magnitude from the starless to the protostellar phases in both low- and high-mass star-forming cores.

Sakai et al. (2012) measured for the first time the D-fractionation for HNC in a sample of 18 massive cores including IRDCs and HMPOs. They found that $D_{frac}(HNC)$ in the starless cores is only marginally higher than that measured in the protostellar cores. This could be explained by the faster destruction processes of N_2D^+ than those of DNC. In fact, N_2D^+ can recombine quickly with CO or electrons, while DNC has to be destroyed by ions, like HCO^+, through much slower (10^4–10^5 yr) chemical reactions. In particular, chemical calculations show that the N_2D^+/N_2H^+ ratio is ~0.1 during the cold pre-stellar phase and drops quickly to ~0.01 after the protostellar birth since it is very sensitive to the temperature growth (Fontani et al. 2014, right panel of Fig. 1.11).

To allow for a consistent observational comparison between the deuterated fraction of N_2H^+ and HNC, Fontani et al. (2014) observed the D-fractionation of HNC towards a subsample of the sources used in Fontani et al. (2011). They found for the HMSCs an average $D_{frac}(HNC)$~0.012, and for the HMPOs and UC HII very similar average values of ~0.009 and ~0.008, respectively. This supports the results by Sakai et al. (2012), that $D_{frac}(HNC)$ does not change significantly going from the colder phase to the active star formation phases. Thus, there is a clear different behaviour between $D_{frac}(HNC)$ and $D_{frac}(N_2H^+)$ in high-mass star-forming cores. In particular, the first is less sensitive to a temperature rise and the second is more suitable to identify HMSCs: $D_{frac}(N_2H^+)$ of ~0.2–0.3 should signpost good candidate massive pre-stellar cores. A similar result has been found more recently by Imai et al. (2018) towards a sample of young protostars with a strong accretion and more evolved objects that have already accreted their final mass, still embedded in their cold envelope.

However, N_2H^+, HNC and their deuterated isotopologues can form mainly (HNC, DNC) or solely (N_2H^+, N_2D^+) in the gas phase. Other important molecules, like NH_3, CH_3OH and their deuterated forms, can be produced on dust grain surfaces, and theoretical models
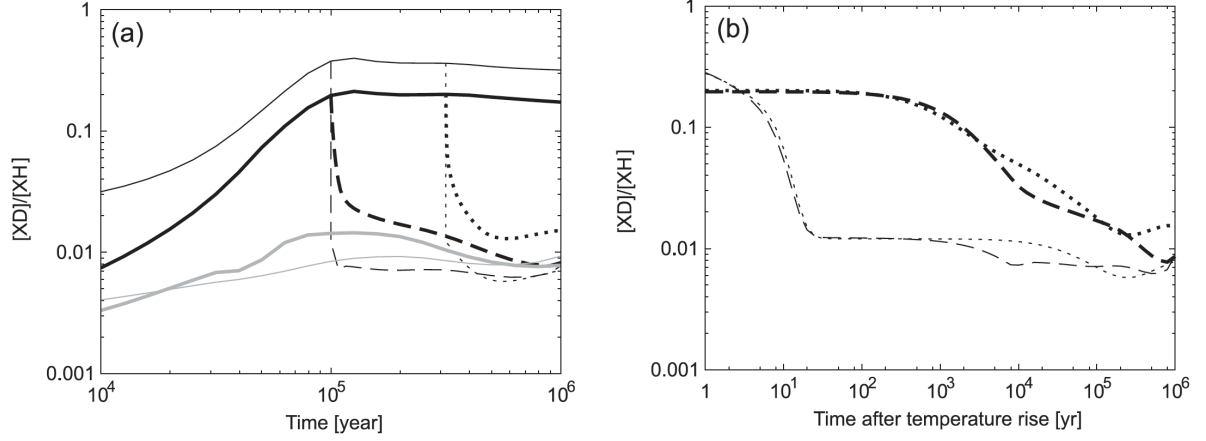
Fig. 1.11: Chemical model calculation of the time dependence of DNC/HNC (thick lines) and N_2D^+/N_2H^+ (thin lines) made by Fontani et al. (2014). *Panel (a):* the constant temperature cases are the solid black (10 K) and the solid grey (30 K) lines. The other lines represent the cases in which the temperature rises from 10 to 30 K at an age of 1×10^5 yr (dashed) or 3×10^5 yr (dotted). *Panel (b):* same as left panel but the time starts when the temperature increases from 10 to 30 K.

show that their D_{frac} could be different than that of gas-phase species, especially during the protostellar phase in which grain mantles evaporate. Fontani et al. (2015a) investigated the role of surface chemistry through observations of ammonia, methanol and their deuterated species (NH_2D, CH_2DOH, CH_3OD).The main conclusion of this work is that N_2D^+/N_2H^+ is the only ratio which shows a statistically significant decrease from HMSCs to HMPOs. Recently, Ospina-Zamudio et al. (2019) investigated the deuteration of methanol towards the high-mass star-forming region NGC7538-IRS1. Their study showed that the fractionation degree of deuterated methanol is low in this source ~1–3×10^{-4}, and a CH_2DOH/CH_3OD relative abundance of 3.2±1.5. These results are consistent with the hypothesis that deuterium fractionation of methanol proceeds in the ice during the early cold pre-stellar phase through the statistical addition of H and D atoms to CO molecules (e.g. Faure et al. 2015; Bøgelund et al. 2018).

Even though the CO depletion is expected, in theory, to be lower in high-mass star-forming regions, because they are warmer since the early phases, observations show that CO depletion is also efficient for these objects. To estimate the CO depletion, a factor called CO depletion factor (f_D) is commonly used. It is defined as the ratio between the expected abundance of CO relative to H_2 (derived taking into account the atomic carbon and oxygen abundances with distance to the Galactic center) and the observed value. For example, Fontani et al. (2012) and Sabatini et al. (2019) found f_D of ~10 or more, i.e. even larger that in low-mass pre-stellar cores, towards the innermost regions of IRDCs. Moreover, Giannetti et al. (2014), using observations of the ATLAS survey towards massive clumps, found that CO depletion in these clumps seems to behave as in the low-mass regime, with less evolved clumps showing larger values for the depletion than their more evolved counterparts, and increasing for denser sources.

1.4.4. Nitrogen fractionation in the ISM

First chemical models

The possibility of nitrogen isotopic fractionation in interstellar clouds was discussed for the first time by Terzieva and Herbst (2000). In cold dense environments the only source of fractionation was expected to be isotope-exchange reactions, as already explained for deuterium fractionation. Adams and Smith (1981) studied in laboratory the system

$$N_2H^+ + {}^{15}NN \rightleftharpoons {}^{15}NNH^+ + N_2. \tag{1.31}$$
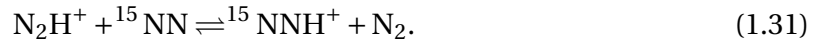
They found that the forward reaction is the exothermic direction, but that the exothermicity is small and expected to lead a small amount of fractionation in clouds with a temperature lower than 10 K. Thus, Terzieva and Herbst (2000) decided to theoretically study a variety of possible ion-molecule isotopic exchange reactions involving abundant N-containing species. Their study was based on a statistical mechanical approach to derive the rate coefficients (see Sect. 1.3). They considered fractionation from molecular, neutral and ionised atomic nitrogen, and derived the exothermicity for all of the cases. They set the forward reaction rate coefficient to be equal to a fraction of the Langevin collisional rate ($k_L = 8.1 \times 10^{-10} \mathrm{cm}^{-3}\mathrm{s}^{-1}$). They modelled a system with a number density n_H of 2×10^4 cm^{-3}, a cosmic-ray ionisation rate ζ for H_2 of 1.3×10^{-17} s^{-1}, and temperatures from 10 K up to 40 K. The main finding of this work was that exchange reactions between ^{15}N atoms and N-containing ions are the main contributors to N-fractionation. However, they did not find a large amount of fractionation between different molecules.

Charnley and Rodgers (2002) showed that, as for D-fractionation, gas-grain effects could lead to significant ^{15}N-fractionation. In fact, under normal interstellar conditions, N_2 is the dominant form of nitrogen, and ^{14}N and ^{15}N are continuously cycled in gas-phase through the sequence

$$N_2 \xrightarrow{He^+} N \xrightarrow{OH} NO \xrightarrow{N} N_2, \tag{1.32}$$

that cycles nitrogen between atomic and molecular form (see also Fig. 1.12).

The first step of this cycle produces also N^+, which reacts with molecular hydrogen and leads to ammonia. When O/C-bearing molecules freeze out on ice mantles, there is insufficient OH to drive the above cycle. This leads to more nitrogen atoms in each of the isotopic forms. Charnley and Rodgers (2002) considered the effect in the context of dense pre-stellar cores adopting a gas density of 10^7 cm^{-3} and a temperature of 10 K. They found that most of the atomic ^{15}N goes in N_2H^+ through the reactions

$$N_2H^+ + {}^{15}N \rightleftharpoons {}^{15}NNH^+ + N, \tag{1.33}$$

and

$$N_2H^+ + {}^{15}N \rightleftharpoons N^{15}NH^+ + N. \tag{1.34}$$
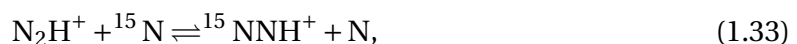
Moreover, when the electronic dissociative recombination of ^{15}NNH$^+$ and N^{15}NH$^+$ is efficient, this excess of N-fractionation reflects into an enhanced abundance of ^{15}N^{14}N, which, subsequently, could cause an excess of ^{15}N$^+$ through the first step of the cycle shown in (1.32). The excess of ^{15}N$^+$ leads to fractionation of ^{15}NH$_3$, which then depletes onto ices. The main nitrogen isotopic-exchange reactions used in their chemical network are schematised in Fig. 1.13.
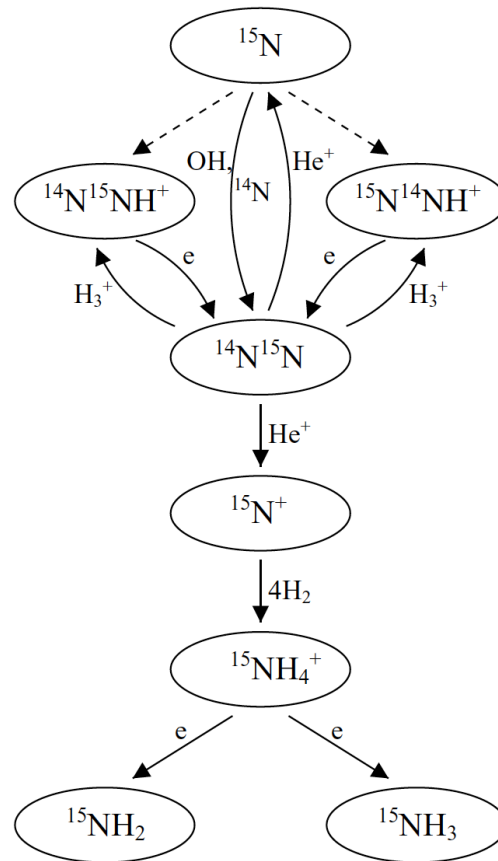
Fig. 1.12: Main gas-phase reactions involving nitrogen included in Charnley and Rodgers (2002) and Rodgers and Charnley (2008a) chemical networks.

Rodgers and Charnley (2008a) revised their chemical model to take into account new experimental results for the branching ratio of the dissociative recombination of N_2H^+:

$$N_2H^+ + e^- \rightleftharpoons N_2 + H \quad (1-f), \tag{1.35}$$

$$N_2H^+ + e^- \rightleftharpoons NH + N \quad (f). \tag{1.36}$$
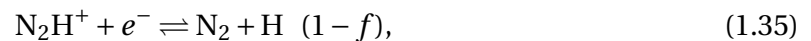
They considered values for f=0, 0.02 and 0.05 (Molek et al. 2007). Moreover, they also tracked the $^{14}N/^{15}N$ in different monolayers of ammonia ice on grain surfaces. With these updates they could recover the results of the earlier work in dense, CO-depleted gas at 10 K, finding that the uppermost layers, which accrete later, have the largest ^{15}N-enrichments.

However, these models can not reproduce the CN abundances derived towards the pre-stellar cores L1544 and L183 ($\sim 2 \times 10^{-9}$, Hily-Blant et al. 2008). Rodgers and Charnley (2008b) reassessed the ^{15}N chemistry to shed light to these new observational evidences. They found that enhanced ^{15}N in nitrile-bearing species is possible, at an early time, via the reactions

$$HC^{14}NH^+ + {}^{15}N \rightleftharpoons HC^{15}NH^+ + {}^{14}N. \tag{1.37}$$
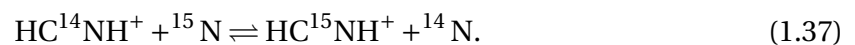
All of the discussion until now takes into account only the role of isotopic-exchange reactions between ion and neutral molecules. Thus, Rodgers and Charnley (2008b) studied
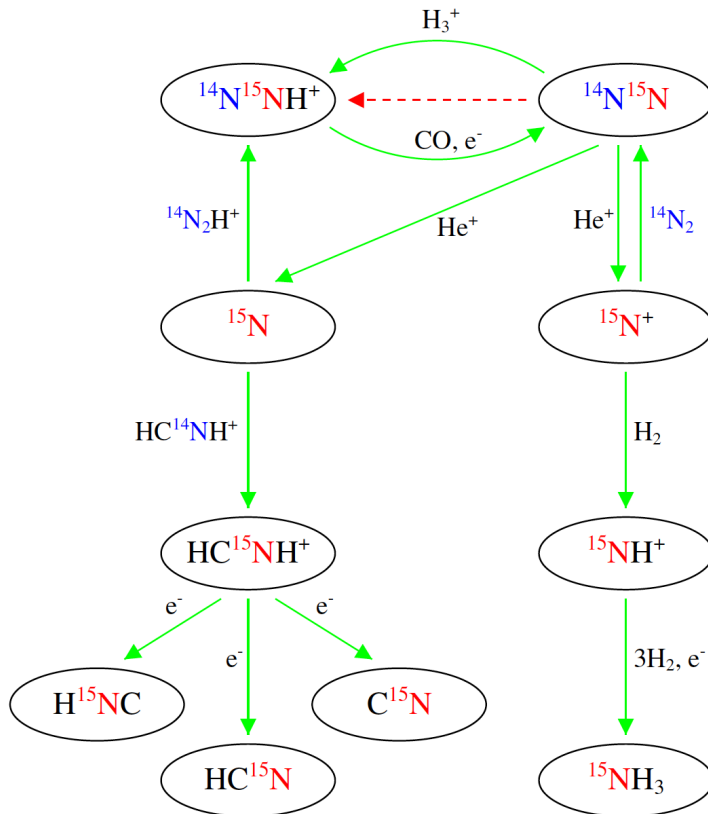
Fig. 1.13: Chemical network showing the main isotopic-exchange reactions responsibile for ^{15}N-enhancements in molecules. Taken from Wirström et al. (2012).

for the first time the possible role of neutral-neutral reactions involving ^{15}N and CN. In particular, they extimated that the reaction

$$C^{14}N + ^{15}N \rightleftharpoons C^{15}N + ^{14}N \tag{1.38}$$

has an exothermicity of 35 K and found that this could be important for ^{15}N-fractionation of nitrile-bearing species at early times.

RECENT OBSERVATIONS AND RELATED CHEMICAL MODELS

PRE-STELLAR CORES: Even if some models for pre-stellar cores were already available before 2000, observations started to constrain them only later, during the last decade.

Gerin et al. (2006) already demonstrated that multiply deuterated ammonia can be very abundant in low-mass pre-stellar cores, and Gerin et al. (2009) derived a $NH_2D/^{15}NH_2D$ abundance ratio from 360 to 810 in a small sample of pre-stellar cores. These ratios are comparable with that of the PSN (441). Subsequently, Lis et al. (2010) derived the $^{14}N/^{15}N$ in ammonia towards two cold, dense molecular clouds, Barnard 1 and NGC 1333. They found a $^{14}N/^{15}N$ of 334±50 and 344±173, respectively. These values are in between the TA value (270) and the PSN one, and can be reproduced only by a gas-phase model that approximates the adsorption on grain surfaces by reducing the elemental abundances in the gas (Gerin et al. 2009), and not by Rodgers and Charnley (2008b) that take into account the

mantle formation and gas-grain interactions. This suggested that many observations, also of other molecules, were needed to constrain chemical models at that time.

Following the results of Rodgers and Charnley (2008b), Bizzocchi et al. (2010) detected for the first time the ^{15}N-containing diazenylium ion (N_2H^+) in the pre-stellar core L1544. To prove if the nitrogen fractionation process is at work in the way described by the models (e.g. Rodgers and Charnley 2008b), L1544 was a perfect target since it was found to have N_2D^+/N_2H^+ ratio of 0.25, and since its central region could reach a temperature of 5.5 K (Crapsi et al. 2007), which is expected to enhance the ^{15}N in molecules. They found a $N_2H^+/N^{15}NH^+$ abundance ratio of 446±71, very similar to the PSN value, and different from what predicted by chemical models. However, Bizzocchi et al. (2013) revised these results by performing a non-LTE analysis, using the physical model proposed for this source by Keto and Caselli (2010). From this new analysis they found $^{14}N/^{15}N= 1000±200$, even more difficult to explain with cold gas-phase isotopic-exchange reaction models.

Wirström et al. (2012) proposed a new chemical network, taking into account both D- and ^{15}N-enrichments in molecules, with the novelty of including the spin-state of H_2, H_2^+ and H_3^+. The major interstellar collision partner, molecular hydrogen, has a 170.5 K difference in zero-point energy between the *para* (*p*, anti-parallel spins) and the *ortho* (*o*, parallel spins) form, with the *o*-H_2 being the higher energy one. Thus, the *ortho*-to-*para* ratio (OPR) can influence the energy balance in exothermic reactions in which H_2 is involved, and hence could affect N-fractionation as well. For example, the reaction

$$N^+ + H_2 \rightarrow NH^+ + H, \tag{1.39}$$

followed by three other reactions with H_2, is important for ammonia formation (see Fig. 1.12), but it presents an activation energy of 200 K that at low temperature could be overcome only by the internal energy of *o*-H_2 (Le Bourlot 1991). Moreover, Dislaire et al. (2012) evaluated from experimental data a different rate coefficient for reaction (1.39) depending on the spin of H_2. So, ammonia fractionation becomes much less efficient as the OPR decreases, and then, as illustrated in Fig. 1.13, an increasing quantity of $^{15}N^+$ goes back into molecular nitrogen by

$$^{15}N^+ + ^{14}N_2 \rightleftharpoons ^{14}N^+ + ^{15}N^{14}N. \tag{1.40}$$
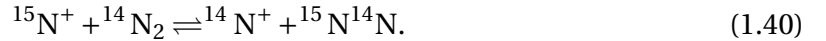
Thus, while the time evolution of the system shows an *o*-H_2 drop, a substantial rise in the ammonia $^{14}N/^{15}N$ is also present, up to almost doubling the PSN value ($\lesssim 800$, see Fig. 1.14). This suggests an age for the fractionated ammonia in L1544 (Gerin et al. 2009) of $\sim 3\times10^5$ yr. Moreover, Wirström et al. (2012) found that while HCN and HNC are enriched in ^{15}N for shorter time scales (t$\sim 2\times10^5$), this is not true for deuterium. However, the results obtained by Bizzocchi et al. (2013) remain puzzling even with this new model since it is expected that N_2H^+ derives from the molecular nitrogen via the protonation reaction

$$N_2 + H_3^+ \rightarrow N_2H^+ + H_2, \tag{1.41}$$

and then it is expected that the $^{14}N/^{15}N$ of N_2H^+ follows that of N_2, i.e. that it diminishes (see Fig. 1.14).

In Fig. 1.15 the main reaction routes for nitrogen molecules in a cold (10 K) cloud are summarised. It can be noted that N-bearing molecules can be divided into two families: nitriles (-CN) and amines (-NH). The former form directly from atomic nitrogen, while the
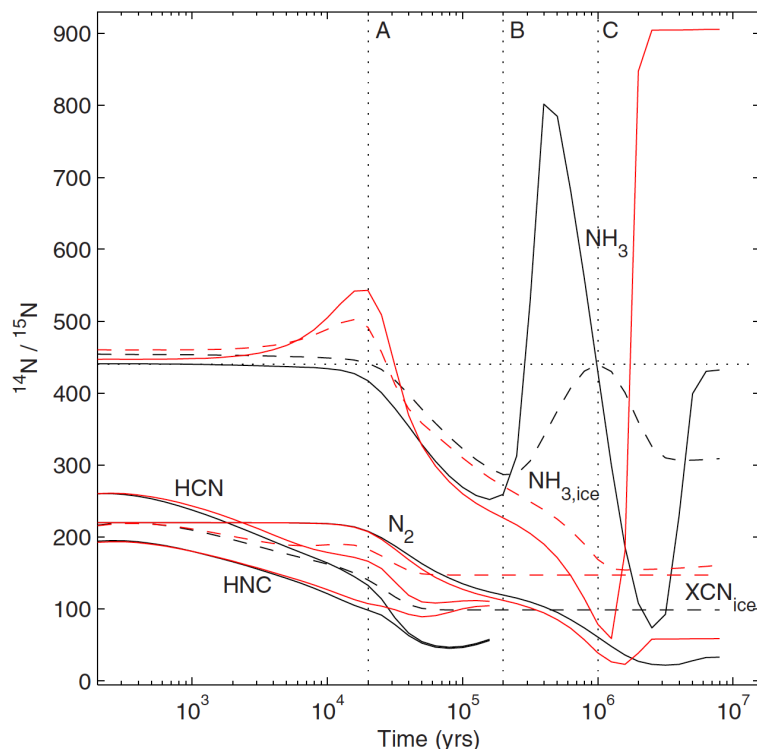
Fig. 1.14: Time evolution of the $^{14}N/^{15}N$ in molecules in gas-phase, and some species in the ice. The black curves represent the results by Wirström et al. (2012), and the red ones the results by Rodgers and Charnley (2008a). The dotted horizontal line represents the PSN value of 441. Taken from Wirström et al. (2012).

latter form from N^+ that is a product of molecular nitrogen. In this sense it is not expected that these two families could exchange ^{15}N, and therefore different $^{14}N/^{15}N$ are predicted. In fact, Hily-Blant et al. (2013a) observed $^{14}N/^{15}N$ of nitrile-bearing species towards pre-stellar cores, to compare models and observations for these molecules. They performed a non-LTE analysis of the fundamental rotational transition of $H^{13}CN$ and $HC^{15}N$ towards the two starless cores L1544 and L183. Adopting a $^{12}C/^{13}C$ of 68 (Milam et al. 2005) they obtained $HCN/HC^{15}N$ ratios from 140 to 360 towards L1544, and from 140 to 250 towards L183. In both sources the high values were measured near the center of the core. These values are significantly lower than that derived from ammonia and N_2H^+, suggesting a differential behaviour in the N-fractionation of nitriles and amines, as already predicted by Rodgers and Charnley (2008b).

From Fig. 1.15 it is clear that evaluating the ^{15}N-fractionation of CN towards pre-stellar cores could be useful to understand the chemical processes that are mainly responsible for the observed isotopic ratios because it is a mediator of the atomic-to-molecular nitrogen conversion. In this context, Hily-Blant et al. (2013b) obtained towards L1544 and L1498 obtaing an average $^{14}N/^{15}N$ of 500±75 from CN. This ratio is larger than those obtained from HCN and is similar to some values observed from hydrides towards dark clouds (e.g. Gerin et al. 2009; Lis et al. 2010). These new results gave new constraints to chemical models. Hily-Blant et al. (2013b) implemented N-fractionation reaction in a gas-phase dark cloud chemical model (n_H=10^4 cm^{-3} and T=10 K), modifying the rate of reactions to the more updated one, as the *ortho–para* conversion of H_2 through proton exchange reactions (Rist et al. 2013). Their model predicted that HCN, HNC and NH were positively fractionated,
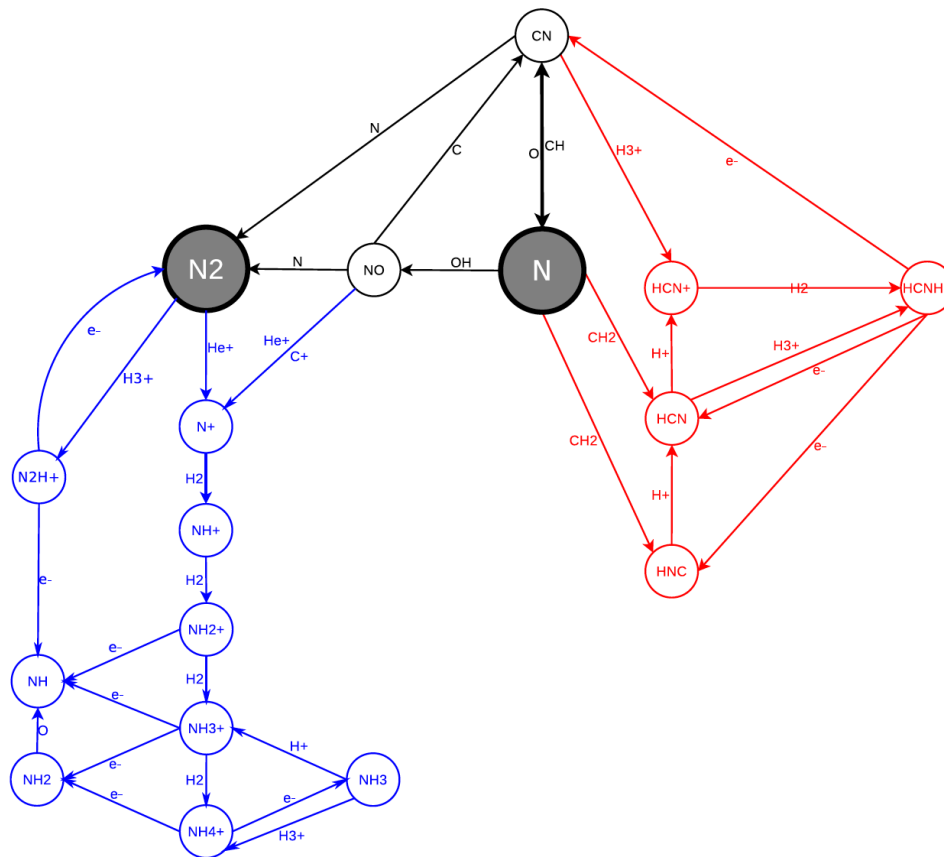
Fig. 1.15: Main chemical routes involving nitrogen-bearing molecules. The routes are clearly separate in two groups, the one containing amine group (blue), and those containing nitrile-bearing species (red). Taken from Hily-Blant et al. (2013a).

while N, NO, and CN were not.

Until 2013, most of the observational studies focused on a single species. Daniel et al. (2013) studied for the first time N-fractionation in the same object in several species, such as N_2H^+, NH_3, CN, HCN and HNC, towards the low-mass pre-stellar core B1b. The main result of this work is that they did not find any substantial differential fractionation between the nitrogen hydride and nitrile-bearing species, with an average value of ~296. A possible explanation of this is the gas temperature in the core center of B1b, estimated to be 17 K, and then higher than the temperature reached during the low-mass pre-stellar phase. Regarding N_2H^+, they found a value lower than that obtained towards L1544 by Bizzocchi et al. (2013). Subsequently, Daniel et al. (2016) targeted the pre-stellar core 16293E and derived a $N_2H^+/N^{15}NH^+$=330±150, which is still lower than that of L1544, and again a possible explanation could be a difference in the central temperature of the core. However, chemical models are not able to reproduce this dependence of fractionation with the temperature.

PROTOSTELLAR OBJECTS: To better understand the link between the pristine Solar system materials and the PSN, evolutionary stages more evolved than pre-stellar cores should be investigated. Wampfler et al. (2014) studied the $^{14}N/^{15}N$ ratio around three nearby low- to intermediate-mass protostars, to investigate whether the signature of nitrogen isotope fractionation also occurs in the embedded protostellar stages, and if they show

differences from both the early pre-stellar phase and the Solar system objects. In fact, apart from low-temperature isotopic-exchange reactions, Liang et al. (2007) demonstrated that also isotopic-selective photodissociation of N_2 could play an important role in the explanation of ^{15}N anomalies in the upper atmosphere of Titan. Wampfler et al. (2014) derived $^{14}N/^{15}N$ ratio for HCN and HNC and they found values for two sources similar to those measured in pre-stellar cores (160–280). However, for the third source, OMC-3 MMS6, they found higher values similar to the PSN one. They proposed as explanation for this difference, the amount of external irradiation the sources are exposed to. In fact, OMC-3 MMS6 is exposed to an enhanced radiation field, resulting in a warmer outer envelope with respect to the other sources. This would argue in favour of chemical fractionation scenario, and against isotope-selective photochemistry. However, to what extent this latter mechanism could have affected the nitrogen isotope composition of the PSN is not clear yet.

PROTOPLANETARY DISCS: Another important evolutionary stage is that of protoplanetary discs since they are the cradle in which protoplanets form. Thus, distinguishing between the different origins of nitrogen isotopic ratios in discs is a key point. In particular, the radial and vertical trends of the $^{14}N/^{15}N$ ratio in each disc would indicate the processes that influence and regulate this fraction. In theory, a constant $^{14}N/^{15}N$ ratio across each disc would favour a scenario where discs inherit their molecular complexity from the natal cloud, while a radial gradient would point to disc chemistry induced by irradiation from the nascent star.

Guzmán et al. (2015) presented the first measurement of the $HCN/HC^{15}N$ in a disc, in particular the protoplanetary disc around the Herbig Ae star MWC 480. They found from Atacama Large Millimeter Array (ALMA) observations an average $^{14}N/^{15}N$ of 200±100, which is consistent with what is observed in comets. Later, Guzmán et al. (2017) presented $0.5''$ angular resolution observations of the J=3–2 transition of $H^{13}CN$ and $HC^{15}N$ towards a sample of six protoplanetary discs. To derive the nitrogen fractionation in HCN, they adopted an isotopic $^{12}C/^{13}C$ ratio of 70. The measured nitrogen isotope ratios range from 83±37 up to 156±78, which is consistent with a constant disc-averaged fractionation level, within the errors. This sample of discs consisted of 4 T Tauri discs and 2 Herbig Ae discs, and they found no differences in the ^{15}N-enhancement level between the two groups of discs that have an order of magnitude difference in the stellar radiation field. Finally, towards the disc V4046 Sgr they found an indication of increasing $^{14}N/^{15}N$ ratio from the inner to the outer part of the disc. This points to an active nitrogen fractionation, suggesting that selective photodissociation induced by the protostellar radiation field is important to fractionate HCN in the inner disc. However, high-angular resolution observations are needed towards more discs to determine if this is a general trend for protoplanetary discs or if V4046 Sgr is a special case. Another evidence that isotopic-exchange reactions do not contribute alone to N-fractionation in discs is the fact that Guzmán et al. (2017) did not find a correlation between D/H (measured by Huang et al. 2017) and $^{14}N/^{15}N$ ratio in the sample. Finally, Hily-Blant et al. (2017) directly measured a $CN/C^{15}N$ ratio of 323±30 in the disc orbiting TW Hya. The comparison with the $HCN/HC^{15}N$ ratios measured towards other discs, demonstrates that CN and HCN in discs are not tracing the same reservoirs, as already shown in pre-stellar cores (Hily-Blant et al. 2013b).

Visser et al. (2018) present the first 2D disc model that includes both low-temperature isotope-exchange reactions and isotope-selective photodissociation of N_2, finding that for

nitrile-bearing species nitrogen isotope fractionation is fully dominated by the second process, and that low-temperature exchange reactions do not contribute at all.

Fig. 1.16 summarises all of the literature values described in this chapter. This figure will be updated in next chapters with more recent results, including those of this thesis.
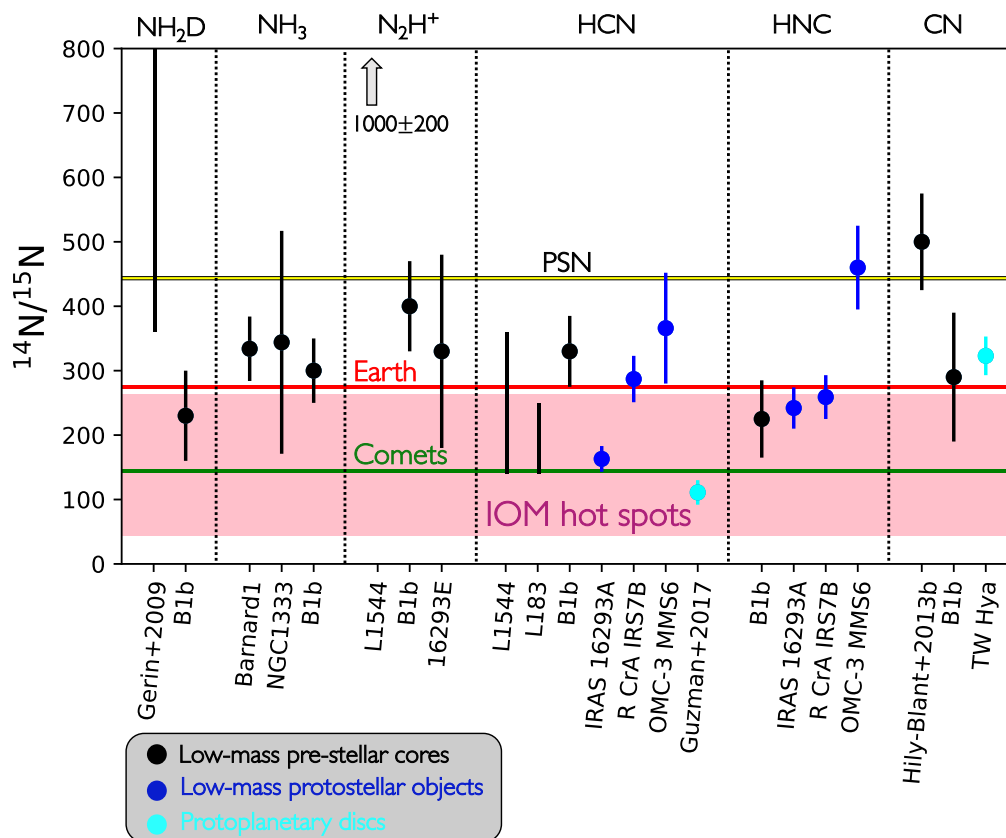
Fig. 1.16: $^{14}N/^{15}N$ ratios obtained for different molecules, as described in Sect. 1.4.4. Black points represent low-mass pre-stellar cores, the blue points are low-mass protostellar objects, and the cyan points indicate protoplanetary discs. The horizontal yellow and red solid lines represent the PSN value of 441 and the TA value of 272, respectively. The green horizontal line denotes the average value measured in comets. Moreover, the pink area represents measurements in carbonaceous chondrites, where the lower ones are the so-called "hot-spots".

UPDATED CHEMICAL NETWORKS: NEW PREDICTIONS FROM CHEMICAL MODELS

Roueff et al. (2015): They studied the fractionation processes in the ISM, re-investigating the study of Terzieva and Herbst (2000). They used a time-dependent gas-phase chemical model, including also the effects of $^{12}C/^{13}C$ on nitrogen fractionation of nitrile-bearing species. If experimental information was available they constrained the rate constants of reactions using it. Conversely, if no experimental data were available, they checked for the possible presence of barriers in the entrance channels of isotopic-exchange reactions through theoretical calculations, and updated the ZPE values involved, deriving the corre-

sponding exothermicity values. In Table 1.1 all the isotopic-exchange reactions taken into account in this work, for N and C, are listed. In particular, for reaction (11) they were able to evaluate an upper limit for the rate coefficient, but they did not take it into account in their model. The type of reactions, given in the first column of the table, are summarised as follows:

A - *direct reactions*: the equilibrium coefficient K is defined as in eq. 1.15;

B - *reactions involving adduct formation, without isomerization*: the statistical theory for the system at thermal equilibrium is applied. Thus, $k_f + k_r = k_{capture}$. From the equilibrium coefficient K, it can be derived that $k_f = k_{capture} \times \frac{f(B,M)}{[f(B,M) + \exp(-\Delta E/k_B T)]}$;

C - *reactions involving adduct formation, with isomerization*: isomerization reaction rate estimated with statistical calculation, and the rate constant depends on the location of the transition state. It is required to study in detail case by case;

D - *other type of reactions*: generally these reactions are discarded.

Moreover, they have also included chemical reactions involving nitrogen atoms and CH, CN, and OH that have been studied experimentally. Thus, they have updated their chemical network with the corresponding reaction rate constants that have been implemented in the KIDA chemical database (Wakelam et al. 2013).

They considered two different models, where the model (a) is a template of TMC-1, with a density n_H of 2×10^4 cm^{-3}. Model (b) is more representative of a pre-stellar core with a density n_H of 2×10^5 cm^{-3}, similar to L134N or Barnard 1. Both models presented a cosmic ray-ionisation rate ζ for H$_2$ of 1.3×10^{-17} s^{-1} and a temperature of 10 K.

As in Wirström et al. (2012) they also took into account the possible role of the *ortho/para* molecular hydrogen into N-fractionation, in particular for the ^{15}N-enhancement of ammonia. They considered the different rate coefficient for reaction (1.39) depending on the spin of H$_2$, as discussed by Dislaire et al. (2012). They also extended the analysis of reaction (1.39) to deuterated forms and those including ^{15}N. In the case of ^{15}N substituted compounds they took into account the small additional term due to the change in ZPE. They found that, since the N$^+$ + HD $\rightarrow$ ND$^+$ + H reaction is less exothermic than N$^+$ + H$_2$ $\rightarrow$ NH$^+$ + H reaction, this creates a NH$_3$/^{15}NH$_3$ ratio that is higher than NH$_2$D/^{15}NH$_2$D at steady state (see Fig. 1.17).

One of the important results that they obtained is that the fractionation reaction of ^{15}N with N$_2$H$^+$ is unlikely due to the presence of a barrier. This is in contrast with the previous chemical models by Terzieva and Herbst (2000) and Rodgers and Charnley (2008a). The main consequence is that the modeled N-isotopic ratio for N$_2$H$^+$ is found to be very close to the PSN value of 441. However, this value is still in contradiction with observations towards L1544 (Bizzocchi et al. 2013). Moreover, the different endothermicity in the reactions of ^{15}NNH$^+$ and N^{15}NH$^+$ with N$_2$ leads to the prediction that ^{15}NNH$^+$ should be less abundant than N^{15}NH$^+$ (see Fig. 1.18).

With the same argument of the presence of a barrier, they also discarded the ^{15}N + HCNH$^+$ and ^{15}N + NO exchange reactions. In particular, discarding the first one results in a predicted ^{14}N/^{15}N for nitrile-bearing species not different from the elemental value (Fig. 1.19). Moreover, since they also included a treatment for C-fractionation, they

Table 1.1: ^{15}N and ^{13}C isotopic-exchange reactions used by Roueff et al. (2015).

Label/comment	Reaction	k_f (cm^3 s^{-1})	$f(B, m)$	ΔE (K)
(1) A	$N^{15}N + N_2H^+ \rightleftharpoons N^{15}NH^+ + N_2$	2.3×10^{-10}	0.5	10.3
(2) A	$N^{15}N + N_2H^+ \rightleftharpoons \,^{15}NNH^+ + N_2$	2.3×10^{-10}	0.5	2.1
(3) A	$N^{15}N + \,^{15}NNH^+ \rightleftharpoons N^{15}NH^+ + N^{15}N$	4.6×10^{-10}	1	8.1
(4) B	$^{15}N^+ + N_2 \rightleftharpoons \,^{14}N^+ + N^{15}N$	$4.8 \times 10^{-10} \times \frac{2}{2 + \exp(-28.3/T)}$	2	28.3
(5) C	$^{15}N + CNC^+ \rightleftharpoons C^{15}NC^+ + \,^{14}N$	$3.8 \times 10^{-12} \times (\frac{T}{200})^{-1}$	1	38.1
(6) barrier	$^{15}N^+ + \,^{14}NO \rightleftharpoons \,^{14}N^+ + \,^{15}NO$	no react	–	24.3
(7) barrier	$^{15}N + N_2H^+ \rightleftharpoons \,^{14}N + N^{15}NH^+$	no react	–	38.5
(8) barrier	$^{15}N + N_2H^+ \rightleftharpoons \,^{14}N + \,^{15}NNH^+$	no react	–	30.4
(9) barrier	$^{15}NNH^+ + H \rightleftharpoons H + N^{15}NH^+$	no react	–	8.1
(10) barrier	$^{15}N + HCNH^+ \rightleftharpoons \,^{14}N + HC^{15}NH^+$	no react	–	37.1
(11) D	$^{15}N + CN \rightleftharpoons \,^{14}N + C^{15}N$	upper limit: $2.0 \times 10^{-10} \times$ $(\frac{T}{300})^{1/6} \times \frac{1}{1 + \exp(-22.9/T)}$	1	22.9
(12) B	$^{15}N + C_2N \rightleftharpoons \,^{14}N + C_2^{15}N$	$1.6 \times 10^{-10} \times$ $(\frac{T}{300})^{1/6} \times \frac{1}{1 + \exp(-26.7/T)}$	1	26.7
(13) D	$^{15}N + \,^{14}NO \rightleftharpoons \,^{14}N + \,^{15}NO$	– (too low: neglected reation)	–	24.3
(14) B	$^{13}C^+ + CO \rightleftharpoons \,^{12}C^+ + \,^{13}CO$	$6.6 \times 10^{-10} \times (\frac{T}{300})^{-0.45} \times$ $\exp(-6.5/T) \times \frac{1}{1 + \exp(-34.7/T)}$	1	34.7
(15) A	$^{13}CO + HCO^+ \rightleftharpoons CO + H^{13}CO^+$	$2.6 \times 10^{-12} \times (\frac{T}{300})^{-0.4}$	1	17.4
(16) B	$^{13}C^+ + CN \rightleftharpoons \,^{12}C^+ + \,^{13}CN$	$3.82 \times 10^{-9} \times$ $(\frac{T}{300})^{-0.4} \times \frac{1}{1 + \exp(-31.1/T)}$	1	31.1
(17) B	$^{13}C + CN \rightleftharpoons \,^{12}C + \,^{13}CN$	$3.0 \times 10^{-10} \times \frac{1}{1 + \exp(-31.1/T)}$	1	31.1
(18) C	$^{13}C + HCN \rightleftharpoons \,^{12}C + H^{13}CN$	– (neglected reaction)	–	48.4
(19) B	$^{13}C + C_2 \rightleftharpoons \,^{12}C + \,^{13}CC$	$3.0 \times 10^{-10} \times \frac{2}{2 + \exp(-26.4/T)}$	2	26.4
(20) barrier	$^{13}CH + CO \rightleftharpoons \,^{13}CO + CH$	no react	–	28.6
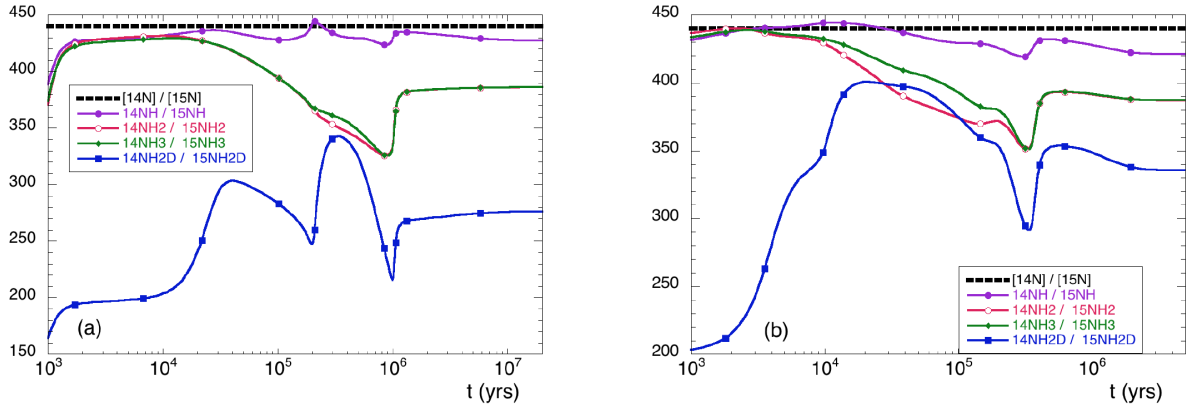
Fig. 1.17: Time dependence of ^{14}N/^{15}N isotopic ratios of NH, NH$_2$, NH$_3$ and NH$_2$D found by Roueff et al. (2015). The panels a) and b) correspond to the models defined in the text; the black dotted line represents the elemental ^{14}N/^{15}N. Taken from Roueff et al. (2015)

were able to compare their results directly with observations of N-fractionation in nitrile-
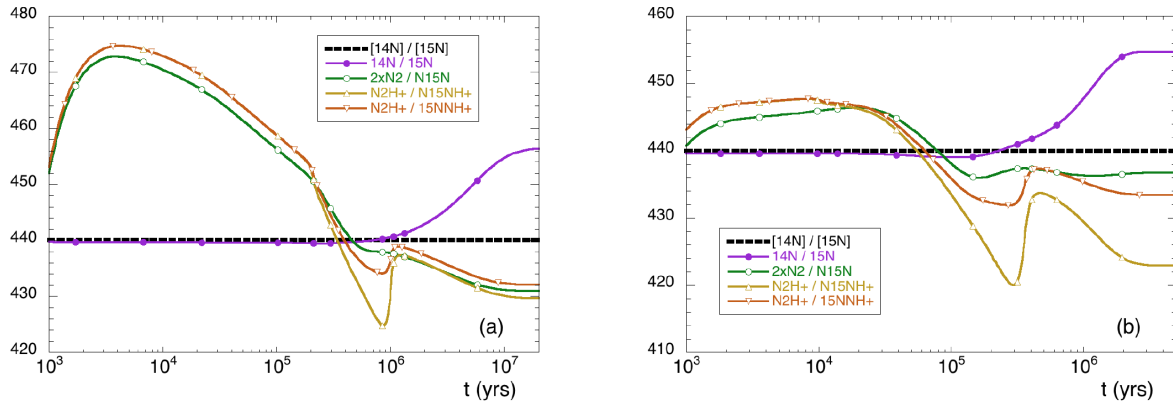
Fig. 1.18: Time dependence of ^{14}N/^{15}N isotopic ratios of atomic and molecular nitrogen and N$_2$H$^+$ ions found by Roueff et al. (2015). The panels a) and b) correspond to the models defined in the text; the black dotted line represents the elemental ^{14}N/^{15}N. Taken from Roueff et al. (2015)

bearing species. In fact, one of the methods to evaluate ^{14}N/^{15}N ratios for nitriles is with the double-isotopes method, that includes observations of the species containing the ^{13}C-isotopologue to avoid optical depth problems. Then, an elemental ^{12}C/^{13}C ratio have to be assumed to evaluate the ^{14}N/^{15}N ratio. They found that the deviation from the elemental value ^{15}N/^{13}C=6.5[10] is significant for HNC, HCN, and CN: 4 for HNC and HCN and almost 7 for CN (Fig. 1.20). The ^{12}C/^{13}C ratio time dependence will be discussed in detail in chapter 5.
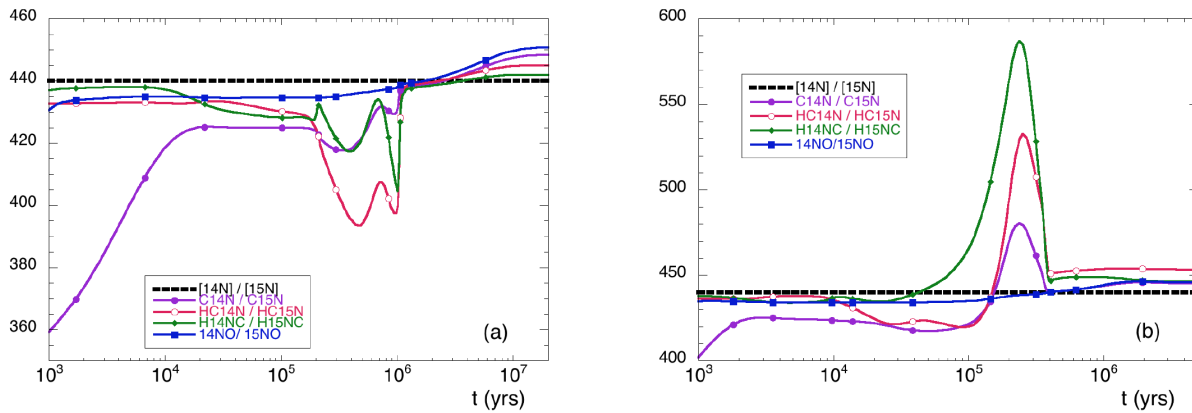
Fig. 1.19: Time dependence of ^{14}N/^{15}N isotopic ratios of CN, HNC, HCN and NO found by Roueff et al. (2015). The panels a) and b) correspond to the models defined in the text; the black dotted line represents the elemental ^{14}N/^{15}N. Taken from Roueff et al. (2015)

Wirström and Charnley (2018): Wirström and Charnley (2018) re-evaluated the calculation by Wirström et al. (2012) in light of the revised Roueff et al. (2015) fractionation chemistry, since there are significant physical and chemical differences in these two models. In particular, Wirström et al. (2012) considered densities similar to pre-stellar core conditions (n_{H_2} of 10^6 cm^{-3}, a temperature of 10 K, a cosmic-ray ionisation rate ζ for H$_2$ of 3×10^{-17}

---

[10] (^{15}N/^{14}N)$\times$(^{12}C/^{13}C)=400/68=6.5.
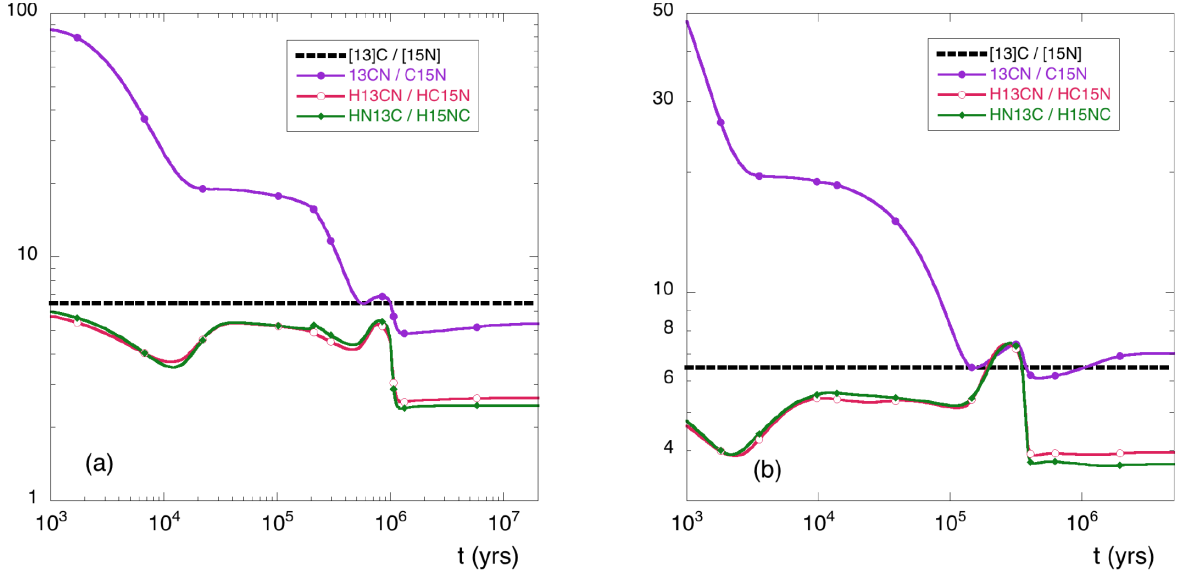
Fig. 1.20: Time evolution of $^{13}C/^{15}N$ ratios of CN, HCN, and HNC for models (a) and (b), found by Roueff et al. (2015). The $^{13}C/^{15}N$ elemental ratio is displayed as a dotted line. Taken from Roueff et al. (2015).

s^{-1}). Moreover, Roueff et al. (2015) did not include the depletion of gas-phase species by freeze-out on dust grains, nor the time dependence in the H_2 OPR. In their work Wirström and Charnley (2018) investigated the possible role of the reaction (11) of Table 1.1, since it was demonstrated that the reaction

$$N + CN \rightarrow N_2 + C \tag{1.42}$$
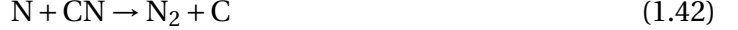
does not present a barrier, and Roueff et al. (2015) found that the isotopic exchange reaction between ^{15}N and CN is plausible. Wirström and Charnley (2018) updated also the model with respect to the specific reaction in the nitrogen chemistry from KIDA database, as already done by Roueff et al. (2015). As initial condition they assumed an elemental $^{14}N/^{15}N$ ratio of 440 with the same initial abundance of ^{15}N and $^{14}N^{15}N$ ($^{15}N/^{14}N^{15}N=1$). This implies a nominal $N_2/^{14}N^{15}N$ ratio of 220.

They followed two different approaches:

- First of all, they compared the results obtained by Wirström et al. (2012) with those obtained updating the old network with only the new reaction rates of isotopic-exchange reactions in Table 1.1. The most important fractionation reactions are shown in Fig. 1.21, and following this network they found an enhancement of a factor ~10 in nitrile-bearing species with respect to the results given by Roueff et al. (2015) (see Fig. 1.22). This behaviour is due to the atomic ^{15}N that rapidly fractionates CN through the reactions (5) and (11) of Table 1.1. Moreover, this ^{15}N-enhancement is successively spread to HCN, e.g. through the reaction

$$CN + NH_3 \rightarrow HCN + NH_2, \tag{1.43}$$

and later to HNC through dissociative electron recombination of $HCNH^+$, formed by reactions of HCN with HCO^+ and H_3O^+.
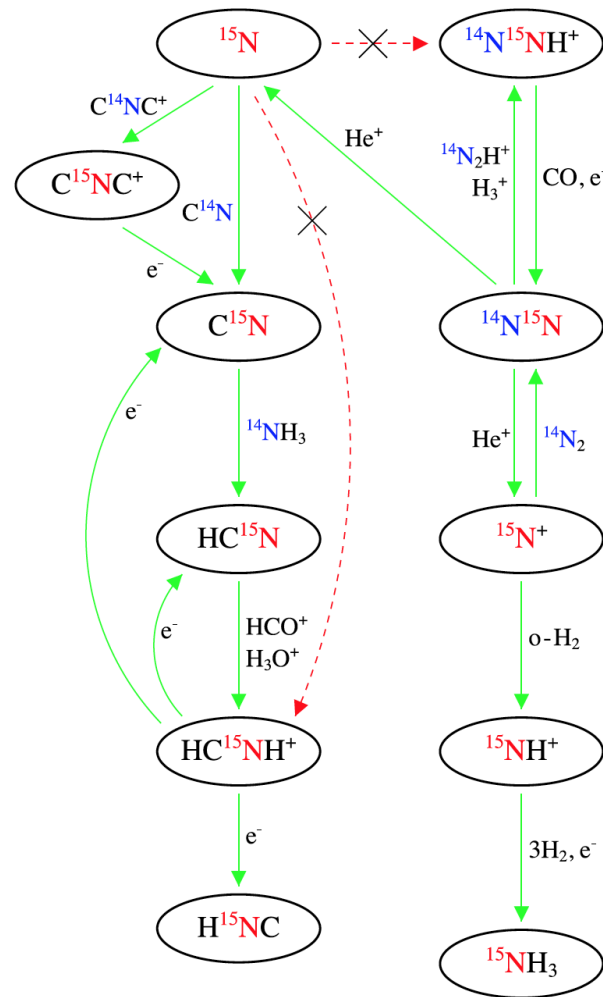
Fig. 1.21: Revised chemical network illustrating the main reactions that causes ^{15}N fractionation in nitrile-bearing species and amines. Red dashed arrows indicate reactions that are ineffective according to Roueff et al. (2015). The lines stop when the molecule freeze-out on grains. Taken from Wirström and Charnley (2018).

They also found that NH$_3$ is not enhanced in ^{15}N because reaction (4) of Table 1.1 allows a faster creation of N^{15}N starting from ^{15}N$^+$, than the creation of ^{15}NH$^+$, when CO is depleted from gas-phase. For diazenylium (N$_2$H$^+$) they found that its ^{15}N fractionation follows that of molecular nitrogen since N$_2$H$^+$ is mainly produced by H$_3^+$ + N$_2$ and destroyed by CO back to N$_2$. When CO depleted from gas-phase (after about 10^4 yr), N$_2$ is more important in the destruction of ^{15}NNH$^+$, converting it into N$_2$H$^+$ and increasing the N$_2$H$^+$/^{15}NNH$^+$ ratio. N^{15}NH$^+$ follows a similar trend but, due to reactions (1) and (2), it has a larger enhancement in ^{15}N with respect to ^{15}NNH$^+$. However, the higher ^{14}N/^{15}N ratios of ^{15}NNH$^+$ with respect to the nominal value of 220 are far from the very depleted ratio observed in L1544 by Bizzocchi et al. (2013).

- Then, they updated the chemistry used by Wirström et al. (2012) with the new nitrogen chemistry given by KIDA database. With this new complete model they found
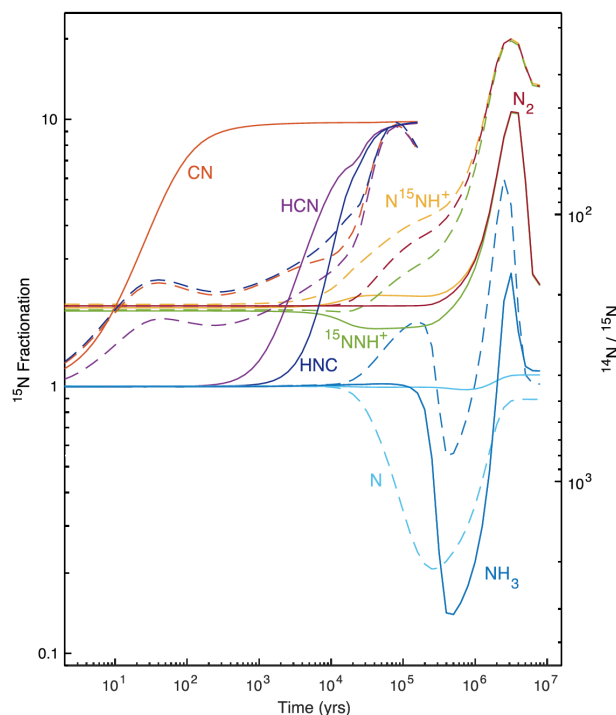
Fig. 1.22: Time dependence of ^{14}N/^{15}N isotopic ratios of the major nitrogen-bearing gas-phase species, as predicted by Wirström et al. (2012) (dashed lines) and the updated model by Wirström and Charnley (2018) with the new rate for isotopic exchange reactions given by Roueff et al. (2015) (solid lines). The lines stop when the molecule freeze-out on grains. Taken from Wirström and Charnley (2018).

the results shown in Fig. 1.23, that two orders of magnitude less CN is maintained in the gas phase of a dense core. Thus, since nitriles are mainly enhanced in ^{15}N from reactions with CN, as discussed above, this low CN abundance suppresses the ^{15}N fractionation in HCN and HNC. The reason why CN is so under abundant with respect to the old model (Wirström et al. 2012) is the reaction 1.42, that previously had a zero reaction rate. Moreover, in this updated network the effects on the ^{15}N fractionation of N$_2$H$^+$ and ammonia are unchanged.

As a conclusion, Wirström and Charnley (2018) also pointed out that the barriers of reactions (7), (8) and (10) were evaluated based on a linear geometry, and other approach angles on the potential energy surface might allow the reaction to proceed. So, laboratory studies are needed to confirm or not the presence of these barriers.

Loison et al. (2019): Up to 2018, no astrochemical model based on gas-phase chemistry alone has been able to produce nitrogen fractionation levels greater than a few per cents. Moreover, since Wirström and Charnley (2018) included only simplified grain processes such as the depletion of gas-phase species onto grains, Loison et al. (2019) developed a new chemical model with also grain surface chemistry and grain desorption. They considered also cosmic-ray induced photodissociations, and introduced new ^{15}N exchange reactions (see Table 1.2). In this work they assumed that all the isotopic-exchange reactions involve adduct formation, which corresponds to the reactions of type B described above.

They assumed a n_{H_2}=2×10^4 cm^{-3}, a gas and dust temperature of 10 K, a cosmic-ray ionisation rate of 1.3 ×10^{-17} s^{-1} and a total visual extinction (A_V) equal to 10. They inves-
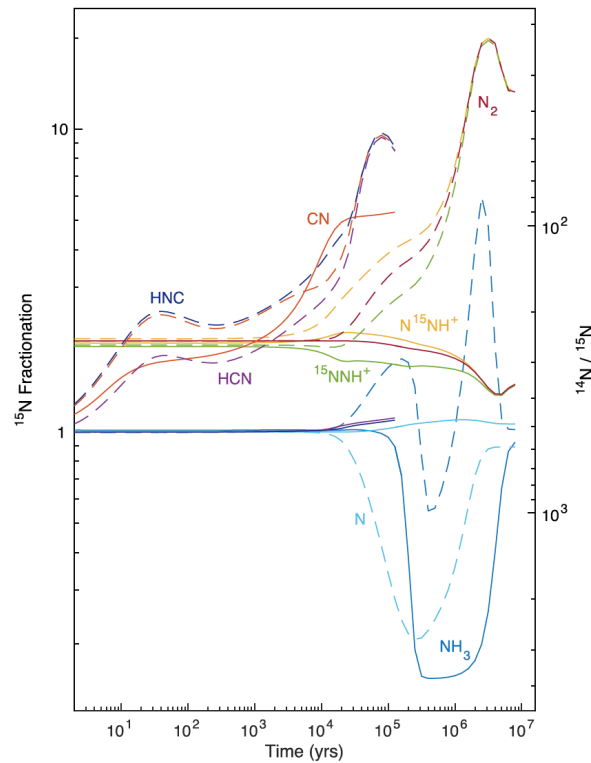
Fig. 1.23: Time dependence of ^{14}N/^{15}N isotopic ratios in the major nitrogen-bearing species in gas-phase, as predicted by Wirström et al. (2012) (dashed) and the updated model by Wirström and Charnley (2018) with the new rate for isotopic exchange reactions given by Roueff et al. (2015) and the nitrogen reaction rates based on Wakelam et al. (2013) (solid lines). Taken from Wirström and Charnley (2018).

tigated reaction (23) of Table 1.2, but since the two exothermic channels form HCN and HC^{15}N with the same rate, then, this reaction is not efficient to fractionate. Moreover, they did not take into account the isotopic-exchange reaction between ^{15}N and CN since the exit channel that gives rise to C + ^{15}NN is the most important one (reaction (21) of Table 1.2; Daranlot et al. 2012).

Their model leads to low fractionation level but with some interesting results:

- As can be noted from Fig. 1.24, it was found a lower ^{14}N/^{15}N for HNC because of reaction (24) that is more efficient in creating H^{15}NC than HC^{15}N.

- Another important result is given by the mass dependence on the accretion time on grain surfaces for different isotopologues. In fact, ^{14}N will be removed from the gas phase more quickly than ^{15}N. As a consequence, for most of the species the ^{14}N/^{15}N is around 400 (slightly lower than the initial condition of 440). However, this process is not efficient for evolved clouds because desorption mechanisms will release ^{14}N-bearing molecules back into the gas phase. Loison et al. (2019) found values, at time scales around $(3–6)\times10^5$ yr, that are still above the typically observed values for different molecular species (e.g. Daniel et al. 2013) or still lower than the observed values for N$_2$H$^+$ in pre-stellar cores (e.g. Bizzocchi et al. 2013). Using an initial ^{14}N/^{15}N of 300 (e.g. Romano et al. 2017) they found results in agreement with most of the observations of CN, HCN, HNC and ammonia (red dotted lines of Fig. 1.24).

Table 1.2: New reactions introduced in the model of Loison et al. (2019).

Label	Reaction	k_f (cm^3 s^{-1})	$f(B, m)$	ΔE (K)
(21)	$^{15}N + CN \rightleftharpoons C + ^{15}NN$	$8.8 \times 10^{-11} \times (\frac{T}{300})^{0.42}$	–	–
	$^{15}N + CN \rightleftharpoons N + C^{15}N$	0	–	–
(22)	$NH_4^+ + ^{15}NH_3 \rightleftharpoons ^{15}NH_4^+ + NH_3$	$1.3 \times 10^{-09} \times (\frac{T}{300})^{-0.5} \times \frac{1}{1+\exp(-14.5/T)}$	1	14.5
(23)	$HCNH^+ + H^{15}NC \rightleftharpoons HC^{15}NH^+ + HCN$	$1.0 \times 10^{-09} \times (\frac{T}{300})^{-0.5}$	–	0
	$HCNH^+ + H^{15}NC \rightleftharpoons HCNH^+ + HC^{15}N$	$1.0 \times 10^{-09} \times (\frac{T}{300})^{-0.5}$	–	0
(24)	$HC^{15}NH^+ + e^- \rightleftharpoons HC^{15}N + H$	$9.34 \times 10^{-08} \times (\frac{T}{300})^{-0.64}$	–	0
	$HC^{15}NH^+ + e^- \rightleftharpoons H^{15}NC + H$	$9.90 \times 10^{-08} \times (\frac{T}{300})^{-0.64}$	–	0

- Finally, they discussed what mechanism could enhance the ^{15}N in N_2H^+. Reactions (1) and (2) of Table 1.1 are inefficient due to their low exothermicity. Taking into account the chemistry of N_2H^+, it is mainly driven by three reactions:

$$N_2 + H_3^+ \rightarrow H_2 + N_2H^+, \tag{1.44}$$

$$N_2H^+ + e^- \rightarrow N_2 + H, \tag{1.45}$$

$$N_2H^+ + CO \rightarrow N_2 + HCO^+. \tag{1.46}$$

Reactions (1.44) and (1.46) are barrierless and then their rate coefficient is not affected by the ZPE difference of any of the N_2H^+ isotopologues. Moreover, they assumed in their model that the rate coefficient for (1.45) for all the isotopologue is the same. However, Lawson et al. (2011) showed experimentally that this could have differences of about 20% between 300 and 500 K, being the reaction for N_2H^+ more efficient than that of $^{15}N_2H^+$ and N_2D^+. So they assumed that, due to the difference in ZPE of the ^{15}N-isotopologues, there is an increase at low temperature for the rate coefficient of $^{15}NNH^+$ and $N^{15}NH^+$. As a consequence, the $N_2H^+/^{15}NNH^+$ and the $N_2H^+/N^{15}NH^+$ ratios will increase above the initial nitrogen isotope ratio value given in the model. In particular, as shown in Fig. 1.25, they found $^{14}N/^{15}N$ around 900 at the age of the typically observed clouds, and when CO depletion is more inefficient, the $^{14}N/^{15}N$ ratio becomes about 600.

In summary, all this demonstrates that current chemical models cannot reproduce observed variation in nitrogen fractionation, and then a lot of work remains to be done to clarify, from a theoretical point of view, the nitrogen fractionation issue from diffuse clouds to the Solar system.

THE FIRST RESULTS TOWARDS HIGH-MASS STAR-FORMING REGIONS

The results shown so far indicate that it is important to gather more data to put stringent constraints on current chemical models. Moreover, as already done for D-fractionation, it is important to investigate the possible link between cometary and ISM material in
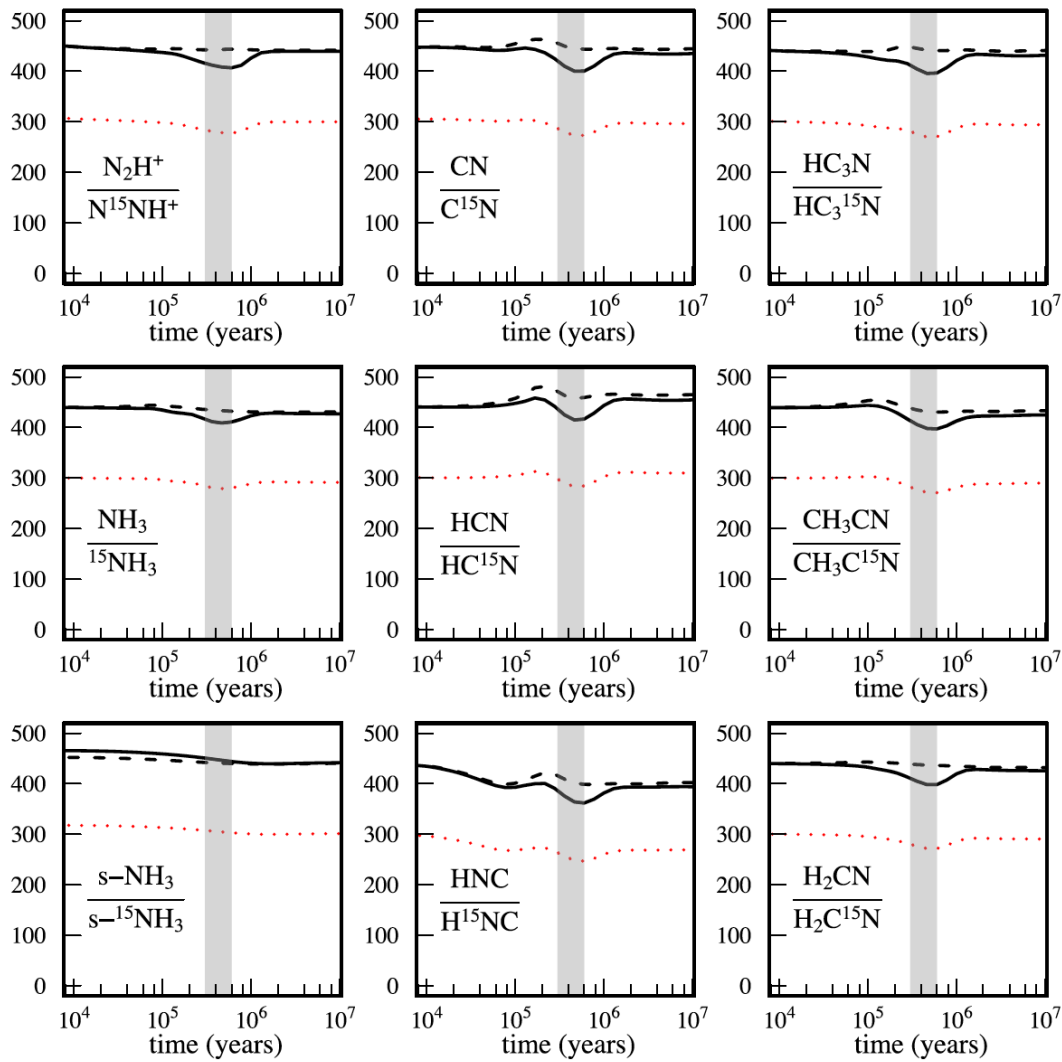
Fig. 1.24: Time dependence of the ^{14}N/^{15}N for the main nitrogen species in the gas phase, for an elemental ^{14}N/^{15}N of 441 (continuous black lines), and equal to 300 (red dotted lines), obtained by Loison et al. (2019). The black dashed lines represent the model with the same sticking rate coefficient for all isotopologues of a given species. The vertical grey rectangle represents the TMC-1 cloud age.

intermediate- and high-mass star-forming regions, since there is growing evidence that our Sun was born in a rich stellar cluster (see Sect. 1.2). Thus, measurements of the ^{14}N/^{15}N ratio in high-mass star-forming regions could provide insight into the initial bulk composition of the PSN.

One of the first samples of high-mass star-forming regions was observed by Adande and Ziurys (2012). They measured the ^{14}N/^{15}N ratios from CN, and HNC, and found values between ~194 and ~391. For CN they found a range of values from ~122 up to ~361 and for HNC from ~134 up to ~406. The main goal of their work was to derive the ^{14}N/^{15}N ratio as a function of the Galactocentric distance (D_{GC}). The importance of this behaviour and its link with the prediction of Galactic chemical evolution models will be discussed in chapter 3.

Fontani et al. (2015b) continued this observational investigation deriving the ^{14}N/^{15}N ratio for N$_2$H$^+$ in the same sample of sources studied in Fontani et al. (2011). The
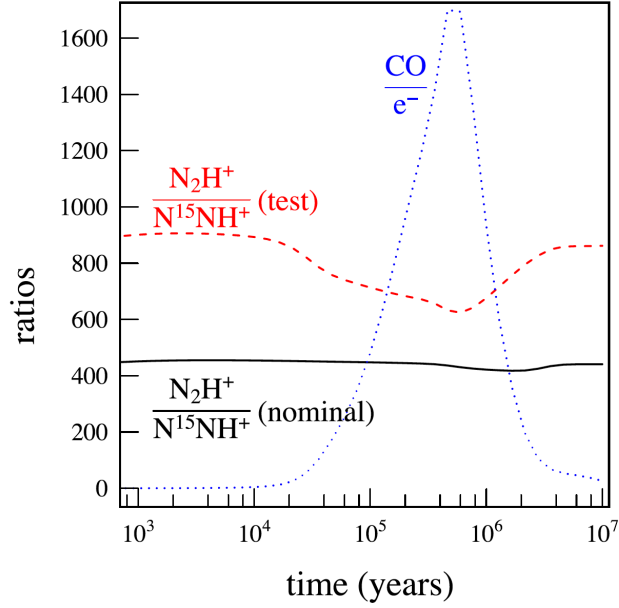
Fig. 1.25: Time dependence of the $N_2H^+/N^{15}NH^+$ ratio for the nominal model (black solid line) and for a N_2H^+ dissociative recombination rate divided by 2 (dashed red line). The dotted blue line corresponds to the CO/e^- ratio. Taken from Loison et al. (2019).

$^{14}N/^{15}N$ ratios that they found show a large spread of values, from ~180 up to ~1300. They were also able to derive the N-fractionation from CN in 13 of the sources of the total sample, finding $^{14}N/^{15}N$ in between ~190 and ~450. These values are consistent, within the errors, with both the TA value (270) and the PSN value (441). An important conclusion of their work is the non-correlation of the $^{14}N/^{15}N$ ratios with the evolutionary stage of the sources, which, differently for the D/H ratio, indicates that time is irrelevant for the fractionation of nitrogen. Moreover, they found the first hints of a possible anticorrelation between H/D and $^{14}N/^{15}N$ ratios, in agreement with the prediction of Wirström et al. (2012). The possible link between the two isotopic ratios will be discussed in more detail in chapter 2.

Later, Zeng et al. (2017) observed a sample of 22 cold and dense cores at the initial stages of their evolution (IRDCs), which are believed to be the precursors of high-mass stars and star clusters. These regions present physical conditions that resemble those of the early stages of the Solar system formation. Towards this sample Zeng et al. (2017) found $^{14}N/^{15}N$ ratios between ~70 and ~458 for HCN (excluding the lower limits), and between ~161 and ~541 for HNC. The IRDCs that they observed towards G034.77-00.55 (cloud G) show lower nitrogen isotopic ratios than the other clouds. One possible explanation is the lower mass surface densities that they present (~0.4 g cm^{-2}) and also the fact that they are in an earlier stage of evolution. The authors proposed that, instead of temperature, the gas density may be the predominant parameter influencing the $^{14}N/^{15}N$ in the young PSN.

Updating the Fig. 1.16 with the results towards high-mass star-forming regions, Fig. 1.26 is obtained. Even towards these sources there are hints of differences between protonated molecules (N_2H^+) and nitrile-bearing species. However, the number of sources is still low, and a direct comparison between different molecules in the same sample of sources is still missing. Indeed, this is exactly the starting point of this thesis that will be presented in detail in next chapters.
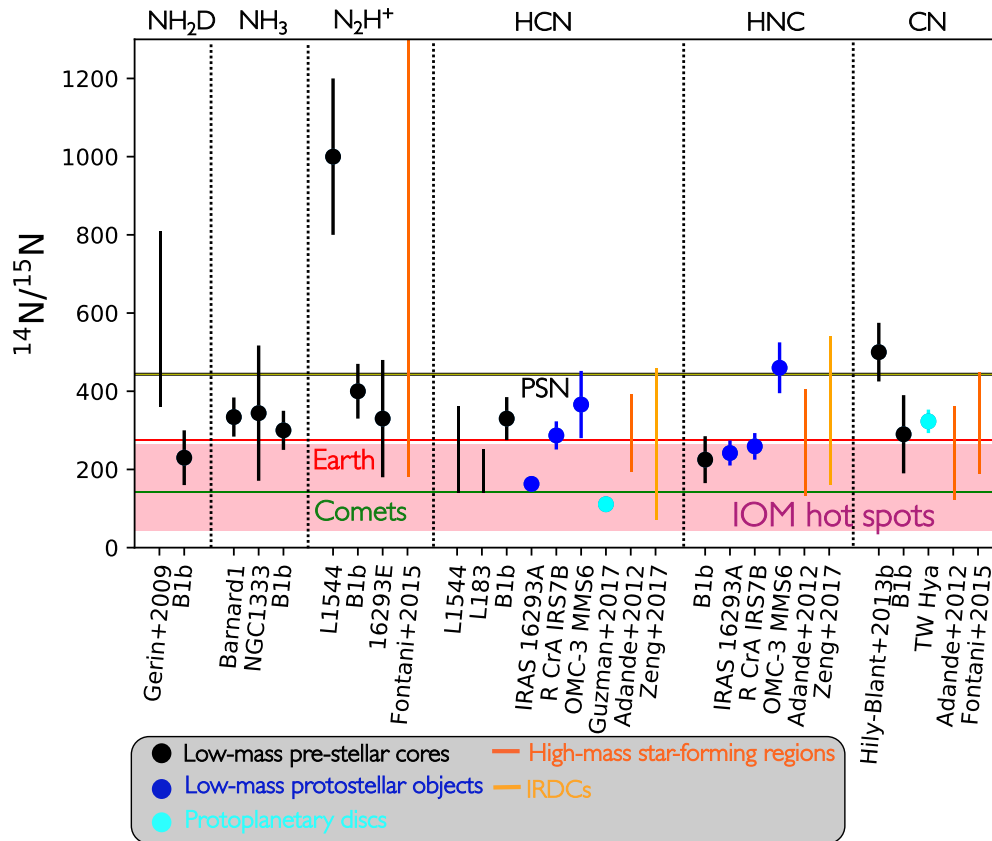
Fig. 1.26: The same as Fig. 1.16. Moreover, light orange ranges represent the IRDCs, and the dark orange indicate high-mass star-forming regions.

1.5. THESIS PROJECT

The mechanisms leading to enrichments of the less abundant isotopes of elements in molecules in different phases of star-formation are still not well known. In this introduction we have presented the state-of-the-art of the observational results in low- and high-mass star-forming regions, and the comparison between H- and N-fractionation, which shows the largest anomalies in pristine Solar system material. Moreover, we have presented the history of chemical models that tried (and still try) to interpret these results, and give an answer to these anomalous isotopic enrichments. We have also shown the relevance of studying the environment where massive stars are born, since nowadays there is a growing evidence that our Sun was born in a rich cluster, containing also massive stars.

The main goals of this thesis are summarised as follows:

(i) To study the N-fractionation of HCN and HNC in the same sample of high-mass star-forming regions in which Fontani et al. (2011) analysed N_2H^+ and compare H- and N-fractionation in this sample.

(ii) To study the behaviour of the $^{14}N/^{15}N$ ratio as a function of the Galactocentric distance in a large sample of high-mass star forming regions (87 sources); and compare with the Galactic Chemical Evolution models of Romano et al. (2017) and Romano et al. (2019).

(iii) To zoom into one of the sources of the sample (IRAS 05358+3543) with interfero-
metric observations, studying the morphology of ^{15}N-enrichments in N_2H^+ at linear
scales capable to resolve different sub-structures of the source.

(iv) To develop a gas-grain chemical model to study in detail the behaviour of ^{12}C/^{13}C of
nitrile-bearing species in different types of star-forming regions and how this can
influence the calculation of the N-fractionation that starts from ^{13}C-bearing species.

This thesis is organised as follows:

- In chapter 2 and 3 I present the study of a sample of high-mass star-forming regions
with single-dish observations in order to give statistically significant results both on
the comparison between H- and N-fractionation and on the Galactic chemical evo-
lution of the ^{14}N/^{15}N.

- In chapter 4 I present an interferometric study of the source IRAS 05358+3543 to
investigate how the ^{14}N/^{15}N of N_2H^+ changes towards an entire high-mass star-
forming region on scales of a few arcseconds.

- Finally, in chapter 5 I present a chemical model to study the ^{12}C/^{13}C ratio for nitrile-
bearing species and to estimate the error made in evaluating the ^{14}N/^{15}N ratio as-
suming a fixed ^{12}C/^{13}C that only depends on the Galactocentric distance.

- In Chapter 6 I summarise the main conclusions of this thesis.

2

NITROGEN AND HYDROGEN FRACTIONATION IN HIGH-MASS STAR-FORMING REGIONS

ABSTRACT

The ratio between the two stable isotopes of nitrogen, ^{14}N and ^{15}N, is well measured in the terrestrial atmosphere (~ 272), and for the PSN (~ 441, deduced from the Solar wind). Interestingly, some pristine Solar system materials show enrichments in ^{15}N with respect to the PSN value. However, it is not yet clear if and how these enrichments are linked to the past chemical history because we have only a limited number of measurements in dense star-forming regions that are believed to be progenitors of stellar systems like our own. In this respect, dense cores, which are believed to be the precursors of clusters and also contain intermediate- and high-mass stars, are important targets because the Solar system was probably born within a rich stellar cluster, and such clusters are formed in high-mass star-forming regions. The number of observations in such high-mass dense cores has remained limited so far. In this chapter we show the results of IRAM 30m observations of the J=1–0 rotational transition of the molecules HCN and HNC and their ^{15}N-bearing counterparts towards 27 intermediate- and high-mass dense cores that are divided almost equally into three evolutionary categories: high-mass starless cores, high-mass protostellar objects, and ultra-compact HII regions. We have also observed the DNC(2–1) rotational transition to search for a relation between the isotopic ratios D/H and ^{14}N/^{15}N. We have derived average ^{14}N/^{15}N ratios of 359 ± 16 in HCN and of 438 ± 21 in HNC, with a dispersion of about 150-200. We have found no trend of the ^{14}N/^{15}N ratio with the evolutionary stage. This result agrees with what has been found for N_2H^+ and its isotopologues in the same sources, although the ^{14}N/^{15}N ratios from N_2H^+ show a higher dispersion than in HCN/HNC, and on average, their uncertainties are larger as well. Moreover, we have found no correlation between D/H and ^{14}N/^{15}N in HNC. These findings indicate that (1) the chemical evolution does not seem to play a role in the fractionation of nitrogen, and that (2) the fractionation of hydrogen and nitrogen in these objects is not related.

2.1. INTRODUCTION

Since comets and organic material in chondrites and IDPs are enriched in both D and ^{15}N, the question of whether these enrichments have a common origin is a natural one. As discussed in chapter 1, the low-temperature environment seems to be responsible in producing some enrichment in ^{15}N and enormous molecular D/H ratios. Thus, one would expect ^{15}N and D hotspots to always be spatially correlated. An argument against this behaviour is that D-enriched spots in chondrites and IDPs do not coincide spatially with ^{15}N-enriched ones. In fact, while ^{15}N and D meteoritic hotspots seem to correlate in some samples (Aléon et al. 2003), they do not in others (e.g. Busemann et al. 2006; Gourier et al. 2008). Similarly, while the D-enrichment differs by a factor three in 103P, 67P, and other Oort cloud comets, the ^{15}N-enrichment is practically the same in all comets (see Fig. 1.8). Therefore, very likely D- and ^{15}N-enrichments do not have a common origin in the PSN.

Wirström et al. (2012) showed in their model the evolution of the deuterium fractionation in H_3^+ together with the ^{15}N-enhancement in HCN and NH$_3$. They considered the *ortho-para* dependence on the ion-molecule reactions involving H$_2$ and found that in general the highest ^{15}N enhancement and lowest deuterium enrichments should be carried by nitriles (see Sect. 1.4.4). However, these results were criticized by Roueff et al. (2015), who revised the chemical fractionation reactions and found high barrier for reactions that enrich ^{15}N in nitrile-bearing molecules, like HCN and HNC.

It is therefore important to gather more observational data, also in sources that are good candidates to represent the environment in which our Sun was born to place stringent constraints on current chemical models. In this respect, intermediate- and high-mass star-forming cores are interesting targets because growing evidence shows that the Sun was born in a rich cluster that also contained massive stars (see Sect. 1.2). In any case, because the statistics are still poor, more observations in star-forming cloud cores in different evolutionary stages are useful for a better understanding of whether and how the ^{15}N-fractionation process might be influenced by evolution. An example of existing work about ^{15}N-fractionation in high-mass dense cores is Adande and Ziurys (2012). These authors worked with a larger beam than was used in our observations, and they did not have an evolutionary classification of the sources, which does not allow to investigate the relation between ^{14}N/^{15}N ratio and core evolution.

We here report the first measurements of the ^{14}N/^{15}N ratio derived from HCN and HNC, with IRAM 30m observations, in a sample of 27 dense cores associated with different stages of the high-mass star formation process that have previously been studied for their deuterated molecules and the ^{15}N-bearing species of N$_2$H$^+$ (Fontani et al. 2011; Fontani et al. 2015a; Fontani et al. 2015b). In particular, Fontani et al. (2015b) for the first time measured the ^{14}N/^{15}N isotopic ratio for N$_2$H$^+$ towards the same sources. Therefore, these new data allow us to investigate the possible difference between nitrogen protonated molecules and nitrile-bearing species that have been proposed by both theoretical studies (Wirström et al. 2012) and observational findings (Hily-Blant et al. 2013a). We also report measurements of the D/H ratios for HNC to search for relations between the two isotopic ratios.

2.2. Observations and data reduction

We performed observations of the J=1–0 rotational transition of $H^{15}NC$, $HN^{13}C$, $HC^{15}N$, and $H^{13}CN$ towards the 27 sources observed by Fontani et al. (2015b) from 6 to 9 June 2015 (see Table 2.1), using the 3 mm receiver of the single-dish IRAM 30m radiotelescope. We simultaneously observed the J=2–1 transition of DNC with the 2 mm receiver. Table 2.2 presents the observed spectral windows and some main technical observational parameters. Tables 2.3 and 2.4 present the hyperfine frequencies of the $H^{13}CN$(1–0) and $HN^{13}C$(1–0) lines, respectively. The atmospheric conditions were very stable during the whole observing period, with precipitable water vapour usually in the range 3 – 8 mm. The observations were made in wobbler-switching mode with a wobbler throw of 240″. Pointing was checked almost every hour on nearby quasars, planets, or bright HII regions. The data were calibrated with the chopper wheel technique (see Kutner and Ulich 1981), with a calibration uncertainty of about 10% . The spectra were obtained in antenna temperature units, T_A^*, and then converted into main beam brightness temperature, T_{MB}, via the relation $T_A^* = T_{MB}(B_{eff}/F_{eff}) = T_{MB}\eta_{MB}$, where $\eta_{MB} = B_{eff}/F_{eff}$ is the ratio between the main beam efficiency (B_{eff}) of the telescope and the forward efficiency of the telescope (F_{eff}). The spectra were obtained with the fast Fourier transform spectrometers with the finest spectral resolution (FTS50), providing a channel width of 50 kHz. All calibrated spectra were analysed using the GILDAS[1] software developed at the IRAM and the Observatoire de Grenoble. In particular, the analysis of all the spectra was done with the GILDAS tool CLASS. Baselines in the spectra were all fitted by constant functions or polynomials of order 1. The rest frequencies used for the line identification were taken from different laboratory works: $HC^{15}N$ from Cazzoli et al. (2005a), $H^{13}CN$ from Cazzoli and Puzzarini (2005b), $HN^{13}C$ from van der Tak et al. (2009), $H^{15}NC$ from Pearson et al. (1976), and DNC from Bechtel et al. (2006). The other spectroscopic parameters used to derive the column densities were taken from the Cologne Molecular Database for Spectroscopy[2] (CDMS; Endres et al. 2016; Müller et al. 2005), except for $H^{15}NC$, for which we have used the Jet Propulsion Laboratory database[3].

Description of the source sample

The source list is in Table 2.1, where the source coordinates, the distances from the Sun and the Galactocentric distances are given. The 27 molecular cores were divided by Fontani et al. (2011) into: 11 HMSCs, 9 HMPOs, and 7 UC HII regions. These evolutionary stages were already described in Sect. 1.1.1. The source coordinates were centered towards infrared, millimeter or centimeter interferometric continuum peaks, or high-density gas tracer peaks, as NH_3. The objects with a continuum peak distance less than 8″ were rejected to avoid the presence of multiple cores within the IRAM 30m beam. The evolutionary stage of each source was established based on a collection of evidence: HMSCs are massive cores embedded in IRDCs or other massive star-forming regions without clear evidence of ongoing star formation; HMPOs are associated with powerful outflows, infrared sources, and/or faint radio-continuum emission (with a flux at 3.6 cm < 1 mJy); UC HII regions are associated with a strong radio-continuum flux (> 1 mJy at 3.6 mm). Among the HMSCs sources,

---

[1] The GILDAS software is available at http://www.iram.fr/IRAMFR/GILDAS
[2] https://cdms.astro.uni-koeln.de/classic/entries/
[3] https://spec.jpl.nasa.gov/

Table 2.1: List of the observed sources. Cols. 2, 3, 4 and 5 give the coordinates (equatorial and Galactic) of the sources and Col. 6 give the source distance to the Sun of the associated star-forming region. In Col. 7 the Galactocentric distances of the sources obtained from the distance to the Sun and the corresponding Galactic longitude (Col. 4) are listed. For the references on distances from the Sun see Fontani et al. (2011). In Col. 8 the $^{12}C/^{13}C$ ratios, derived from eq. (2.5), are given. H_2 column densities for each sources are listed in Col. 9, and are taken from Fontani et al. (2018b).

Source	α(J2000) (h m s)	δ(J2000) ($^{\circ\,\prime\,\prime\prime}$)	l ($^{\circ}$)	b ($^{\circ}$)	d (kpc)	D_{GC} (kpc)	$^{12}C/^{13}C$	v_{LSR} (km s^{-1})	N(H$_2$) ($\times 10^{22}$ cm^{-2})
			HMSC						
I00117-MM2	00:14:26.3	+64:28:28.0	118.9580	+1.8886	1.8	9.5	69	-36.3	–
AFGL5142-EC	05:30:48.7	+33:47:53.0	174.2024	-0.0688	1.8	10.3	74	-3.9	11.3±3.4^s
05358-mm3	05:39:12.5	+35:45:55.0	173.4798	+2.4451	1.8	10.3	74	-17.6	10.6±2.4^s
G034-G2(MM2)	18:56:50.0	+01:23:08.0	34.7802	-0.568	2.9	6.3	50	+43.6	4.1±1.0^a
G034-F1(MM8)	18:53:19.1	+01:26:53.0	34.4350	+0.2420	3.7	5.8	47	+57.7	1.2±0.3^s
G034-F2(MM7)	18:53:16.5	+01:26:10.0	34.4194	+0.2462	3.7	5.8	47	+57.7	1.6±0.4^s
G028-C1(MM9)	18:42:46.9	-04:04:08.0	28.3247	+0.0669	5.0	4.7	40	+78.3	3.6±0.8^s
G028-C3(MM11)	18:42:44.0	-04:01:54.0	28.3523	+0.0946	5.0	4.7	40	+78.3	2.4±0.6^a
I20293-WC	20:31:10.7	+40:03:28.0	78.9793	+0.3591	2.0	8.3	62	+6.3	7.4±1.9^s
I22134-G	22:15:10.5	+58:48:59.0	103.8765	+1.8514	2.6	9.5	69	-18.3	3.6±0.9^s
I22134-B	22:15:05.8	+58:48:59.0	103.8681	+1.8571	2.6	9.5	69	-18.3	2.0±0.6^s
			HMPO						
I00117-MM1	00:14:26.1	+64:28:44.0	118.9582	+1.8930	1.8	9.5	69	-36.3	–
AFGL5142-MM	05:30:48.0	+33:47:54.0	174.2009	-0.0707	1.8	10.3	74	-3.9	10.1±2.4^s
05358-mm1	05:39:13.1	+35:45:51.0	173.4818	+2.4462	1.8	10.3	74	-17.6	8.4±2.1^s
18089-1732	18:11:51.4	-17:31:28.0	12.8891	+0.4894	3.6	5	43	+32.7	9.6±2.4^s
18517+0437	18:54:14.2	+04:41:41.0	37.4297	+1.5179	2.9	6.4	51	+43.7	7.9±1.3^a
G75-core	20:21:44.0	+37:26:38.0	75.7821	+0.3428	3.8	8.4	63	+0.2	4.4±1.1^s
I20293-MM1	20:31:12.8	+40:03:23.0	78.9821	+0.3529	2.0	8.3	62	+6.3	4.9±1.2^s
I21307	21:32:30.6	+51:02:16.0	94.2589	-0.4108	3.2	9.3	68	-46.7	2.9±0.7^s
I23385	23:40:54.5	+61:10:28.0	114.5337	-0.5420	4.9	11.4	81	-50.5	2.4±0.6^s
			UC HII						
G5.89-0.39	18:00:30.5	-24:04:01.0	5.8855	-0.3926	1.3	7.2	55	+9.0	55±14^s
I19035-VLA1	19:06:01.5	+06:46:35.0	40.6220	-0.1380	2.2	7	54	+32.4	3.6±0.9^s
19410+2336	19:43:11.4	+23:44:06.0	59.7837	+0.0645	2.1	7.7	58	+22.4	13.6±3.0^a
ON1	20:10:09.1	+31:31:36.0	69.5402	-0.9757	2.5	8	60	+12.0	–
I22134-VLA1	22:15:09.2	+58:49:08.0	103.8756	+1.8551	2.6	9.5	69	-18.3	2.1±0.5^s
23033+5951	23:05:24.6	+60:08:09.0	110.0915	-0.0657	3.5	10.2	74	-53.0	7.8±1.8^s
NGC 7538-IRS9	23:14:01.8	+61:27:20.0	111.5674	+0.7519	2.8	9.9	72	-57.0	11.9±2.7^s

^{s} measured from the maps of the SCUBA survey (for more information see Fontani et al. 2018b);
^{a} measured from the maps of the APEX ATLASGAL survey (for more information see Fontani et al. 2018b).

three sources (AFGL5142-EC, 05358-mm3, and I22134-G) have been defined as "warm" because they have a kinetic temperature (T_k) higher than 20 K. In fact, high angular resolution observations indicate that they could be externally heated and then, perturbed by nearby star formation (e.g. Zhang et al. 2002).

Table 2.2: Line rest frequencies and observational parameters.

Line	Frequency (GHz)	HPBW ($''$)	Δv^a (km s^{-1})	T_{sys}^b (K)	η_{MB}	F_{eff}
HC^{15}N(1–0)	86.0549	28	~ 0.16	100–150	0.84	0.94
H^{13}CN(1–0)	86.3399	28	~ 0.16	100–150	0.84	0.94
HN^{13}C(1–0)	87.0908	28	~ 0.16	100–150	0.84	0.94
H^{15}NC(1–0)	88.8657	27	~ 0.16	100–150	0.84	0.94
DNC(2–1)	152.60977	15	~ 0.096	200–250	0.72	0.94

[a] velocity resolution of the spectrum,
[b] system temperature.

Table 2.3: Frequencies of the hyperfine components of the transition H^{13}CN(1–0). F is the quantum number associated with the sum between the orbital angular momentum |J| and the ^{14}N nuclear angular momentum. The hyperfine spitting due to ^{13}C is negligible. Taken from Cazzoli and Puzzarini (2005b). The separation in velocity between the hyperfine lines are shown in the last column.

J'-J"	F'-F"	Frequency (GHz)	Velocity separation (km s^{-1})
1–0	1–1	86.33873	-5.0
	2–1	86.34016	0
	0–1	86.34225	7.2

Table 2.4: Frequencies of the hyperfine components of the transition HN^{13}C(1–0). F1 is the quantum number associated with the sum between the orbital angular momentum |J| and the ^{14}N nuclear angular momentum. F2 is the sum between |J| and the ^{13}C nuclear angular momentum, and F is the sum between |J| and the H angular momentum. Taken from van der Tak et al. (2009). The separation in velocity between the hyperfine lines are shown in the last column.

J'–J"	F1', F2', F'–F1", F2", F"	Frequency (GHz)	Velocity separation^a (km s^{-1})
1–0	0,1,1–1,2,2	87.09067	0
	2,2,2–1,1,1 / 2,2,2–1,2,2 / 2,2,1–1,1,0 / 2,2,1–1,2,1	87.09079	0.4
	2,3,3–1,2,2 / 2,3,2–1,1,1 / 2,3,2–1,2,1	87.09083	0.5
	1,1,1–1,1,1 / 1,2,2–1,2,1 / 1,2,2–1,2,2	87.09089	0.7

[a] Note that in this case, since the typical line width of the observed sources is of ~2 km s^{-1}, it is not possible to disentangle the different hyperfine components in the spectra.

2.3. Results: column densities and isotopic ratios

2.3.1. $H^{15}NC$, $HN^{13}C$, $HC^{15}N$, and $H^{13}CN$

The $H^{15}NC(1-0)$ line was detected in 26 cores (96.3%): 11 HMSCs, 8 HMPOs. and 7 UC HIIs; the $HC^{15}N(1-0)$ line was detected in 24 cores (88.8%): 8 HMSCs, 9 HMPOs and 7 UC HIIs; the $HN^{13}C(1-0)$ line was detected in all sources (100%), and the $H^{13}CN(1-0)$ line was also clearly detected in all sources (100%).

Neither $H^{15}NC(1-0)$ nor $HC^{15}N(1-0)$ have hyperfine structure, therefore almost of the lines were fitted with a single Gaussian. For some sources these two lines were fitted with two Gaussian profiles since a secondary velocity peak was present. Conversely, $HN^{13}C(1-0)$ and $H^{13}CN(1.-0)$ do have hyperfine structure. This cannot be resolved for the $HN^{13}C(1-0)$ because the line widths are always comparable to (or larger than) the separation in velocity between the hyperfine components (see Table 2.4). Then almost all of these lines were also fitted with single Gaussians, and since the column densities are derived from the total integrated area of the rotational line (see explanation below), this simplified approach does not affect our measurements as long as the lines are optically thin. This assumption is justified by the optical depth derived by fitting the lines hyperfine structure with the method *hfs* in CLASS: as it can be seen in fourth column of Table 2.7, the lines are indeed optically thin. On the other hand, the fit with a single Gaussian can overestimate the intrinsic line width. To estimate how much the line widths are overestimated using single Gaussian fits, we fitted the line for all the sources both with the Gaussian and the hyperfine method. We found that, on average, with a single Gaussian the line width is about 30% broader than the one obtained taking into account the hyperfine structure. Even in this case for some sources we have disentangled the presence of a secondary velocity peak fitting them with two Gaussians. Finally, for $H^{13}CN(1-0)$ we were able to resolve the hyperfine structure (see Table 2.3) and then we fitted the lines with the *hfs* method. This method assumes that all the hyperfine components have the same excitation temperature, T_{ex}, and width, and that their separation in velocity is fixed to the laboratory value. The opacity of the main component is then derived assuming the theoretical relative intensity of the hyperfine components. The main component opacity is then converted in the total one of the rotational transition as described in the CLASS manual[4]. Moreover, to obtain the integrated intensity of the lines we used the PRINT AREA command in CLASS. This fitting procedure gave good results in all spectra. The Gaussian fitting results are listed in Tables 2.5 and 2.6, and the hyperfine fitting results are listed in Table 2.7. In Figs. 2.1, 2.2, 2.3, and 2.4 the spectra of the $H^{15}NC$, $HC^{15}N$, $HN^{13}C$, and $H^{13}CN(1-0)$ lines, for all the 27 sources, are shown. The hyperfine components of $H^{13}CN(1-0)$ were always detected. The spectra of AFGL5142-EC may be partially contaminated from the nearby core AFGL5142-mm, but this emission is not expected to be dominant because the angular separation between the two cores is 30″ (Busquet et al. 2011), the same as the beam of the telescope.

---

[4] https://www.iram.fr/IRAMFR/GILDAS/doc/html/class-html/node11.html

Table 2.5: Values obtained with a Gaussian fit to the HN^{13}C and H^{15}NC(1–0) lines. The errors come from the fitting procedure and do not take the calibration error on T_{MB} into account. In the second and third columns we list the centroid velocities and the line Full Width at Half Maximum (FWHM). The fourth column lists the integrated intensities, and the fifth column the r.m.s of the spectra. The cases in which the line is not detected, and therefore only upper limits on column density could be obtained as explained in Sect. 2.3.1, are indicated with a minus. The source names are taken from Fontani et al. (2015b).

| Source | HN^{13}C(1–0) | | | | H^{15}NC(1–0) | | | |
	v_{LSR} (km s^{-1})	$\Delta v_{1/2}$ (km s^{-1})	$\int T_{MB}\,dv$ (K km s^{-1})	σ (mK)	v_{LSR} (km s^{-1})	$\Delta v_{1/2}$ (km s^{-1})	$\int T_{MB}\,dv$ (K km s^{-1})	σ (mK)
			HMSC					
I00117-MM2	-35.27 ± 0.06	2.30 ± 0.02	0.30 ± 0.02	10	-35.1 ± 0.1	1.3 ± 0.4	0.05 ± 0.01	9
AFGL5142-EC	-1.92 ± 0.03	2.47 ± 0.08	1.43 ± 0.04	30	-1.60 ± 0.08	1.9 ± 0.2	0.28 ± 0.03	20
05358-mm3	-15.39 ± 0.02	2.32 ± 0.06	1.65 ± 0.03	20	-14.92 ± 0.08	2.2 ± 0.2	0.32 ± 0.02	20
G034-G2(MM2)	42.24 ± 0.03	1.84 ± 0.08	0.67 ± 0.02	20	42.9 ± 0.2	2.4 ± 0.6	0.1 ± 0.02	10
G034-F1(MM8)	58.74 ± 0.06	1.40 ± 0.09	0.72 ± 0.07	10	59.20 ± 0.09	1.4 ± 0.2	0.07 ± 0.01	10
G034-F2(MM7)	56.93 ± 0.03	1.35 ± 0.06	0.36 ± 0.01	10	57.3 ± 0.1	0.7 ± 0.2	0.02 ± 0.008	7
G028-C1(MM9)	81.19 ± 0.09	1.9 ± 0.1	0.95 ± 0.1	10	80.9 ± 0.1	2.7 ± 0.3	0.15 ± 0.01	9
G028-C3(MM11)	81.56 ± 0.03	1.55 ± 0.08	0.36 ± 0.01	10	82.1 ± 0.2	1.6 ± 0.3	0.05 ± 0.009	8
I20293-WC	7.76 ± 0.09	1.6 ± 0.1	0.58 ± 0.08	10	8.4 ± 0.1	1.2 ± 0.2	0.09 ± 0.01	10
I22134-G	-17.85 ± 0.01	1.47 ± 0.04	0.60 ± 0.01	10	-17.55 ± 0.06	1.5 ± 0.2	0.11 ± 0.01	10
I22134-B	-17.98 ± 0.04	1.5 ± 0.1	0.20 ± 0.01	10	-17.43 ± 0.09	1.0 ± 0.2	0.03 ± 0.006	7
			HMPO					
I00117-MM1	-35.44 ± 0.04	1.56 ± 0.09	0.29 ± 0.01	10	-35.1 ± 0.1	1.2 ± 0.2	0.05 ± 0.008	9
AFGL5142-MM	-2.01 ± 0.02	2.68 ± 0.05	1.72 ± 0.03	20	-1.70 ± 0.07	2.2 ± 0.1	0.30 ± 0.02	10
05358-mm1	-15.53 ± 0.02	2.41 ± 0.05	1.73 ± 0.03	20	-15.23 ± 0.06	2.0 ± 0.1	0.28 ± 0.02	10
18089-1732	32.30 ± 0.03	1.6 ± 0.1	0.9 ± 0.2	20	32.7 ± 0.2	1.4 ± 0.3	0.11 ± 0.05	10
18517+0437	44.52 ± 0.02	2.66 ± 0.04	1.54 ± 0.02	10	44.84 ± 0.08	2.5 ± 0.2	0.23 ± 0.01	10
G75-core	0.57 ± 0.07	4.6 ± 0.3	0.86 ± 0.04	10	1.1 ± 0.1	1.9 ± 0.4	0.10 ± 0.01	10
I20293-MM1	6.67 ± 0.01	1.95 ± 0.03	1.49 ± 0.02	10	7.02 ± 0.06	1.8 ± 0.1	0.20 ± 0.01	10
I21307	-45.8 ± 0.01	2.6 ± 0.3	0.20 ± 0.02	10	$-$	$-$	$-$	8
I23385	-49.5 ± 0.1	2.0 ± 0.2	0.27 ± 0.03	10	-49.1 ± 0.2	1.4 ± 0.5	0.04 ± 0.009	9
			UC HII					
G5.89-0.39	9.05 ± 0.01	2.87 ± 0.02	9.54 ± 0.07	30	9.35 ± 0.03	2.93 ± 0.08	1.26 ± 0.03	10
I19035-VLA1	33.33 ± 0.05	4.0 ± 0.1	1.01 ± 0.03	20	33.1 ± 0.2	2.6 ± 0.8	0.1 ± 0.02	10
19410+2336	23.16 ± 0.01	1.81 ± 0.03	1.60 ± 0.02	20	23.50 ± 0.03	1.45 ± 0.09	0.22 ± 0.01	10
ON1	12.25 ± 0.01	3.73 ± 0.03	2.89 ± 0.02	10	12.70 ± 0.06	3.3 ± 0.2	0.38 ± 0.02	10
I22134-VLA1	-17.83 ± 0.02	1.45 ± 0.06	0.45 ± 0.01	10	-17.48 ± 0.08	1.5 ± 0.2	0.08 ± 0.009	8
23033+5951	-52.54 ± 0.02	2.15 ± 0.05	0.14 ± 0.02	20	-52.27 ± 0.09	2.2 ± 0.2	0.22 ± 0.02	10
NGC 7538-IRS9	-56.37 ± 0.03	2.21 ± 0.08	0.97 ± 0.03	20	-56.1 ± 0.1	3.0 ± 0.5	0.22 ± 0.02	10

Table 2.6: Values obtained with Gaussian fits to the HC^{15}N and DNC(2–1) lines. The errors come from the fitting procedure and do not take the calibration error on T_{MB} into account. In the second and in the third colums we list the centroid velocities and the line FWHM, respectively. The fourth column lists the integrated intensities, and the fifth column the r.m.s of the spectra. The cases in which the line is not detected, and therefore only upper limits on column density could be obtained as explained in Sect. 2.3.1, are indicated with a minus.

Source	HC^{15}N(1–0)				DNC(2–1)			
	v_{LSR} (km s^{-1})	$\Delta v_{1/2}$ (km s^{-1})	$\int T_{MB}\,dv$ (K km s^{-1})	σ (mK)	v_{LSR} (km s^{-1})	$\Delta v_{1/2}$ (km s^{-1})	$\int T_{MB}\,dv$ (K km s^{-1})	σ (mK)
HMSC								
I00117-MM2	-35.8 ± 0.2	2.2 ± 0.4	0.11 ± 0.02	10	-34.83 ± 0.03	1.73 ± 0.09	0.41 ± 0.02	20
AFGL5142-EC	-2.64 ± 0.07	3.0 ± 0.2	1.07 ± 0.05	30	-1.67 ± 0.03	1.55 ± 0.07	1.50 ± 0.05	60
05358-mm3	-16.01 ± 0.06	2.7 ± 0.1	0.76 ± 0.03	20	-15.38 ± 0.03	2.22 ± 0.08	1.88 ± 0.05	50
G034-G2(MM2)	–	–	–	10	42.18 ± 0.02	1.18 ± 0.06	0.46 ± 0.02	20
G034-F1(MM8)	58.0 ± 0.2	1.4 ± 0.3	0.06 ± 0.01	10	58.5 ± 0.2	1.2 ± 0.2	0.27 ± 0.01	20
G034-F2(MM7)	–	–	–	10	56.74 ± 0.03	0.81 ± 0.07	0.15 ± 0.01	20
G028-C1(MM9)	80.3 ± 0.4	4 ± 1	0.14 ± 0.03^a	10	81.4 ± 0.1	1.6 ± 0.2	0.29 ± 0.04	20
G028-C3(MM11)	–	–	–	10	81.32 ± 0.09	1.2 ± 0.2	0.1 ± 0.01	20
I20293-WC	7.5 ± 0.1	1.3 ± 0.2	0.13 ± 0.04	10	7.80 ± 0.01	1.26 ± 0.02	0.91 ± 0.03	20
I22134-G	-18.46 ± 0.03	1.56 ± 0.07	0.39 ± 0.01	10	-18.13 ± 0.02	1.17 ± 0.06	0.34 ± 0.02	20
I22134-B	-18.25 ± 0.08	1.3 ± 0.2	0.07 ± 0.008	9	-18.37 ± 0.04	1.03 ± 0.07	0.12 ± 0.08	10
HMPO								
I00117-MM1	-36.0 ± 0.1	2.1 ± 0.2	0.15 ± 0.06	10	-35.48 ± 0.05	1.8 ± 0.1	0.26 ± 0.02	20
AFGL5142-MM	-2.67 ± 0.04	3.3 ± 0.1	1.42 ± 0.04	20	-1.62 ± 0.04	3.2 ± 0.1	2.55 ± 0.08	60
05358-mm1	-16.12 ± 0.05	2.8 ± 0.1	0.80 ± 0.03	20	-15.62 ± 0.03	2.11 ± 0.07	1.50 ± 0.04	40
18089-1732	32.15 ± 0.07	2.8 ± 0.2	0.820 ± 0.002	20	32.19 ± 0.05	1.9 ± 0.1	0.74 ± 0.04	30
18517+0437	44.00 ± 0.04	2.9 ± 0.1	0.89 ± 0.03	20	44.37 ± 0.04	2.77 ± 0.09	1.48 ± 0.04	40
G75-core	0.07 ± 0.01	3.1 ± 0.2	0.79 ± 0.09	10	0.3 ± 0.2	2.5 ± 0.2	0.28 ± 0.01	20
I20293-MM1	6.42 ± 0.05	2.2 ± 0.1	0.44 ± 0.02	20	6.53 ± 0.06	2.6 ± 0.2	0.76 ± 0.04	30
I21307	-46.2 ± 0.1	2.2 ± 0.2	0.13 ± 0.01	10	-46.29 ± 0.08	1.7 ± 0.2	0.18 ± 0.02	20
I23385	-50.1 ± 0.01	2.4 ± 0.3	0.32 ± 0.03	10	-49.43 ± 0.07	1.2 ± 0.2	0.15 ± 0.02	20
UC HII								
G5.89-0.39	8.94 ± 0.03	3.9 ± 0.1	4.4 ± 0.2	20	8.06 ± 0.01	1.98 ± 0.04	2.28 ± 0.06	30
I19035-VLA1	32.9 ± 0.2	4.7 ± 0.4	0.35 ± 0.03	10	32.9 ± 0.1	2.6 ± 0.3	0.34 ± 0.05	20
19410+2336	22.60 ± 0.03	1.94 ± 0.08	0.66 ± 0.02	20	22.87 ± 0.01	1.85 ± 0.04	1.31 ± 0.02	20
ON1	11.83 ± 0.05	4.1 ± 0.1	1.01 ± 0.03	10	12.59 ± 0.04	5.11 ± 0.09	1.69 ± 0.03	20
I22134-VLA1	-18.34 ± 0.03	1.47 ± 0.08	0.09 ± 0.001	10	-18.19 ± 0.04	1.72 ± 0.08	0.33 ± 0.01	20
23033+5951	-52.93 ± 0.06	2.6 ± 0.1	0.51 ± 0.02	20	-52.48 ± 0.02	1.11 ± 0.06	0.64 ± 0.004	30
NGC 7538-IRS9	-56.82 ± 0.08	4.1 ± 0.3	0.77 ± 0.04	20	-56.54 ± 0.05	1.9 ± 0.1	0.61 ± 0.03	30

^{a} tentative detection, as explained in Sect. 2.3.1.

Table 2.7: Best fit parameters obtained fitting the $H^{13}CN(1–0)$ lines with method *hfs* in CLASS (except for the integrated line intensities in col. 7, derived with command PRINT AREA). The errors come from the fitting procedure and do not take the calibration error on T_{MB} into account. The second and third columns list the centroid velocities and the FWHM, respectively. The fourth and fifth columns list the total optical depths of the rotational transition (obtained as described in Sect. 2.3.1) and the antenna temperatures times the optical depths. The sixth column lists the r.m.s of the spectra, and the last column shows the integrated intensities.

Source	v_{LSR} (km s^{-1})	$\Delta v_{1/2}$ (km s^{-1})	τ	$T_A \times \tau$ (K)	σ (mK)	$\int T_{MB}\,dv$ (K km s^{-1})
			HMSC			
I00117-MM2	-36.37 ± 0.05	1.8 ± 0.1	0.1 ± 0.1	0.142 ± 0.008	10	0.42 ± 0.02
AFGL5142-EC	-3.35 ± 0.02	3.30 ± 0.04	0.10 ± 0.06	0.94 ± 0.01	30	5.81 ± 0.08
05358-mm3	-16.65 ± 0.03	3.00 ± 0.05	0.10 ± 0.04	0.80 ± 0.01	30	4.51 ± 0.07
G034-G2(MM2)	41.1 ± 0.1	1.7 ± 0.2	0.1 ± 0.4	0.087 ± 0.007	10	0.23 ± 0.02
G034-F1(MM8)	57.62 ± 0.08	1.7 ± 0.1	0.1 ± 0.4	0.16 ± 0.01	10	0.50 ± 0.02
G034-F2(MM7)	55.69 ± 0.04	0.8 ± 0.1	0.25 ± 0.02	0.11 ± 0.01	10	0.23 ± 0.01
G028-C1(MM9)	79.43 ± 0.05	3.09 ± 0.09	0.1 ± 0.2	0.180 ± 0.006	10	1.02 ± 0.03
G028-C3(MM11)	80.31 ± 0.08	2.2 ± 0.3	0.5 ± 0.7	0.12 ± 0.03	10	0.45 ± 0.03
I20293-WC	6.83 ± 0.06	1.0 ± 0.1	0.60 ± 0.03	0.15 ± 0.02	10	1.33 ± 0.03
I22134-G	-19.04 ± 0.01	1.65 ± 0.03	0.10 ± 0.03	0.63 ± 0.01	10	1.85 ± 0.03
I22134-B	-18.95 ± 0.02	1.43 ± 0.06	0.1 ± 0.4	0.164 ± 0.006	10	0.45 ± 0.02
			HMPO			
I00117-MM1	-36.54 ± 0.03	1.96 ± 0.09	0.3 ± 0.3	0.21 ± 0.02	10	0.74 ± 0.02
AFGL5142-MM	-3.43 ± 0.01	3.27 ± 0.03	0.26 ± 0.06	1.27 ± 0.03	20	7.52 ± 0.05
05358-mm1	-16.8 ± 0.02	2.99 ± 0.04	0.50 ± 0.02	0.91 ± 0.01	20	4.68 ± 0.06
18089-1732	31.8 ± 0.4	2 ± 1	0.1 ± 0.1	01.48 ± 0.02	30	6.51 ± 0.05
18517+0437	43.29 ± 0.01	2.97 ± 0.02	0.1 ± 0.03	1.024 ± 0.007	20	5.76 ± 0.05
G75-core	-0.596 ± 0.004	2.5 ± 0.1	0.1 ± 0.02	0.48 ± 0.02	10	3.27 ± 0.02
I20293-MM1	5.79 ± 0.02	2.38 ± 0.03	0.100 ± 0.002	0.80 ± 0.01	20	3.64 ± 0.04
I21307	-47.00 ± 0.04	2.3 ± 0.1	0.2 ± 0.3	0.18 ± 0.02	10	0.75 ± 0.03
I23385	-50.9 ± 0.3	1 ± 1	0.6 ± 0.1	0.26 ± 0.01	10	1.16 ± 0.02
			UC HII			
G5.89-0.39	8.24 ± 0.01	3.83 ± 0.01	0.12 ± 0.01	3.75 ± 0.2	30	20.97 ± 0.05
I19035-VLA1	32.17 ± 0.05	4.4 ± 0.1	0.4 ± 0.2	0.30 ± 0.02	10	2.26 ± 0.04
19410+2336	22.01 ± 0.002	2.186 ± 0.002	0.10 ± 0.02	1.090 ± 0.005	20	4.64 ± 0.04
ON1	11.12 ± 0.02	3.71 ± 0.04	0.73 ± 0.08	0.93 ± 0.03	10	5.55 ± 0.04
I22134-VLA1	-18.98 ± 0.01	1.76 ± 0.03	0.10 ± 0.03	0.513 ± 0.007	10	1.67 ± 0.03
23033+5951	-53.63 ± 0.02	2.73 ± 0.02	0.10 ± 0.02	0.621 ± 0.003	20	3.17 ± 0.04
NGC 7538-IRS9	-57.64 ± 0.02	3.60 ± 0.04	0.10 ± 0.03	0.65 ± 0.01	20	4.43 ± 0.04
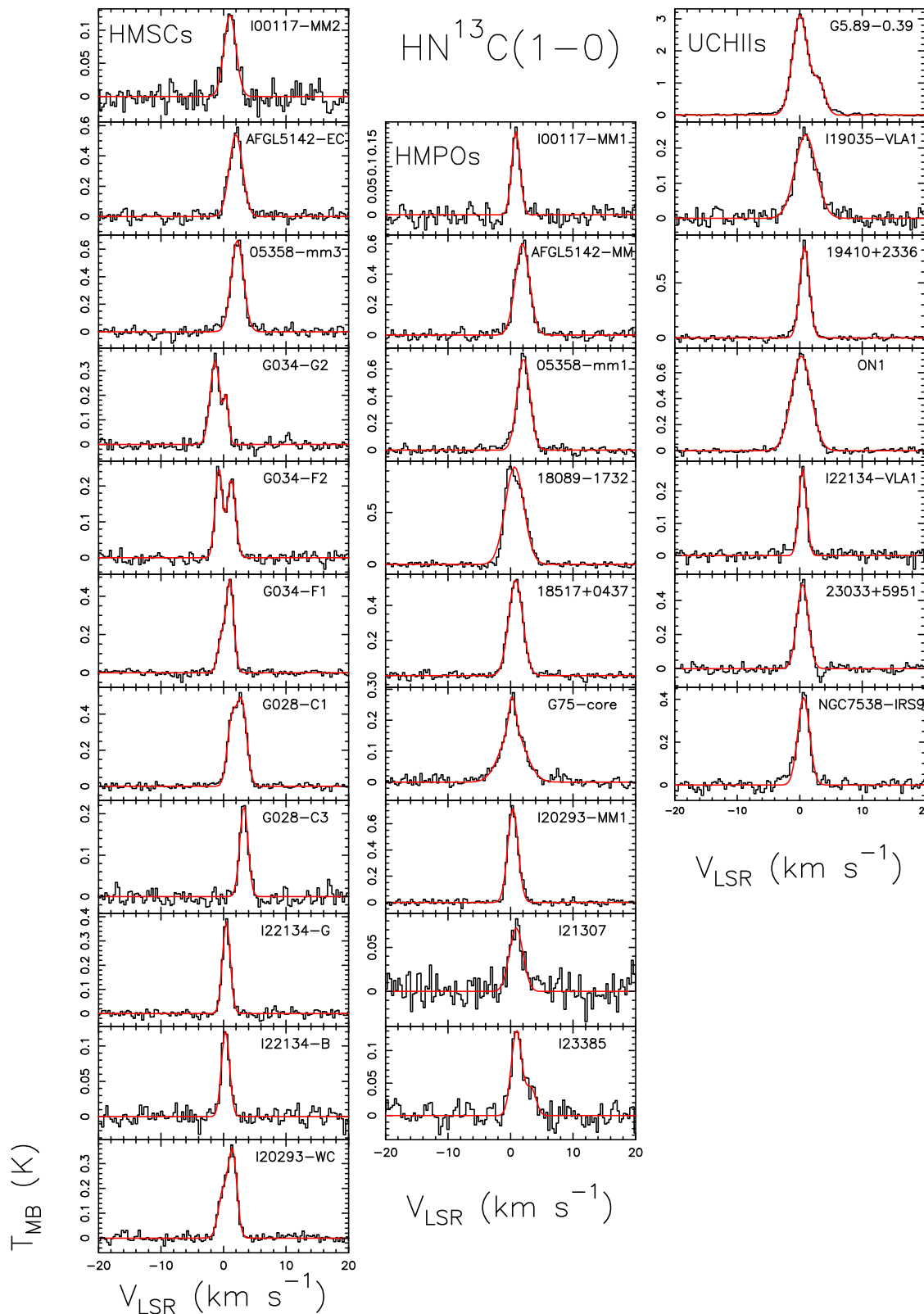
Fig. 2.1: Spectra of HN^{13}C(1–0) obtained for the sources classified as HMSCs (first column), HMPOs (second column), and UC HII regions (third column) . For each spectrum the x-axis represents a velocity interval of ±20 km s^{-1} around the systemic velocity listed in Table 2.1. The y-axis shows the intensity in main-beam temperature. The red curves are the best Gaussian fits obtained with CLASS. For some sources (I20293-WC, G034-G2, G034-F2, G5.89-0.39, G034-F1, G028-C1, and I23385), we have observed two components: we have fitted both lines and used only the line centered on the systemic velocity of the source to compute the column densities.
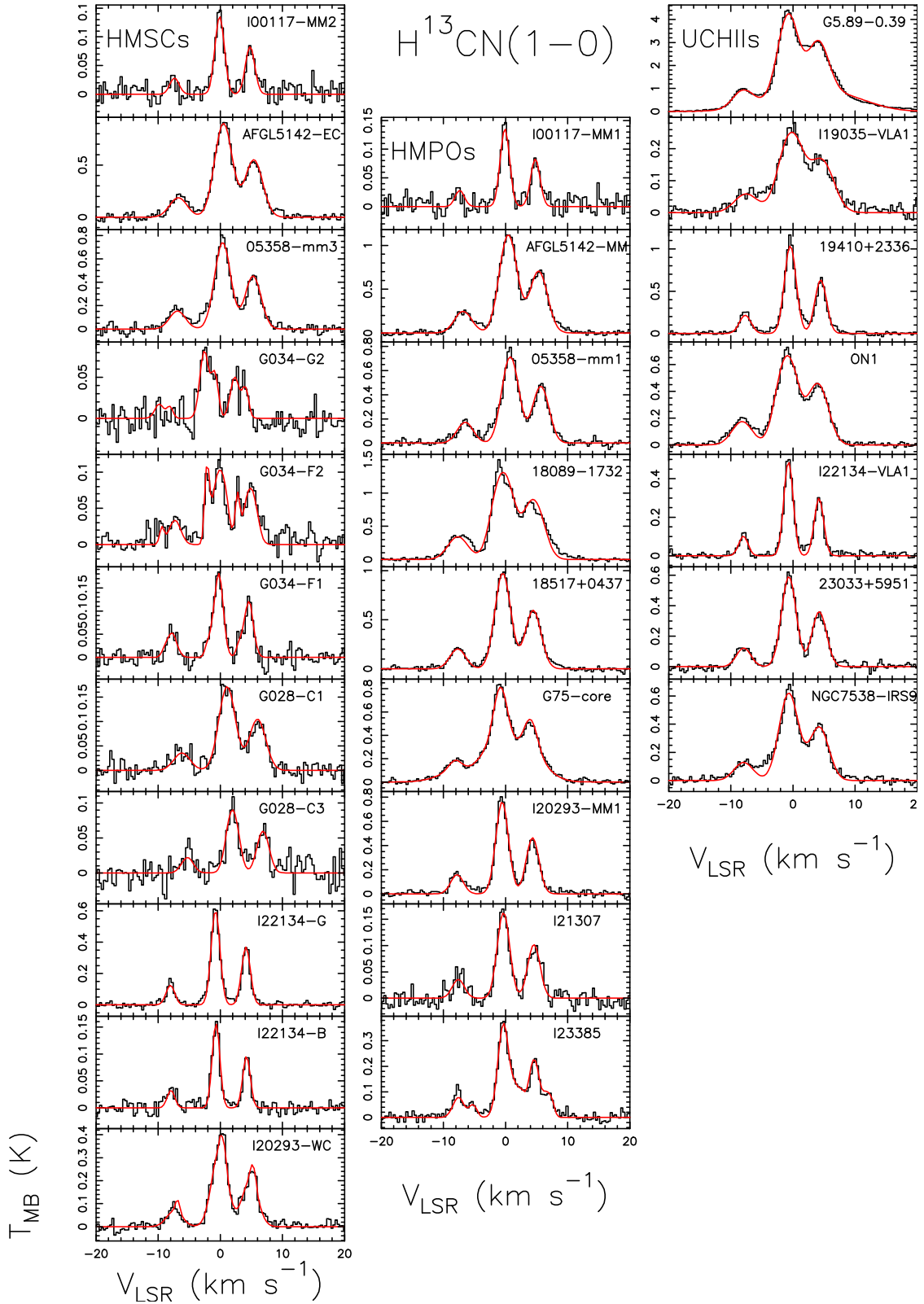
Fig. 2.2: Same as Fig.2.1 for $H^{13}CN(1-0)$. Here the red curves are the best hyperfine fits obtained with CLASS. We note the presence of the second velocity component in the same sources that were indicated in the caption of Fig. 2.1.
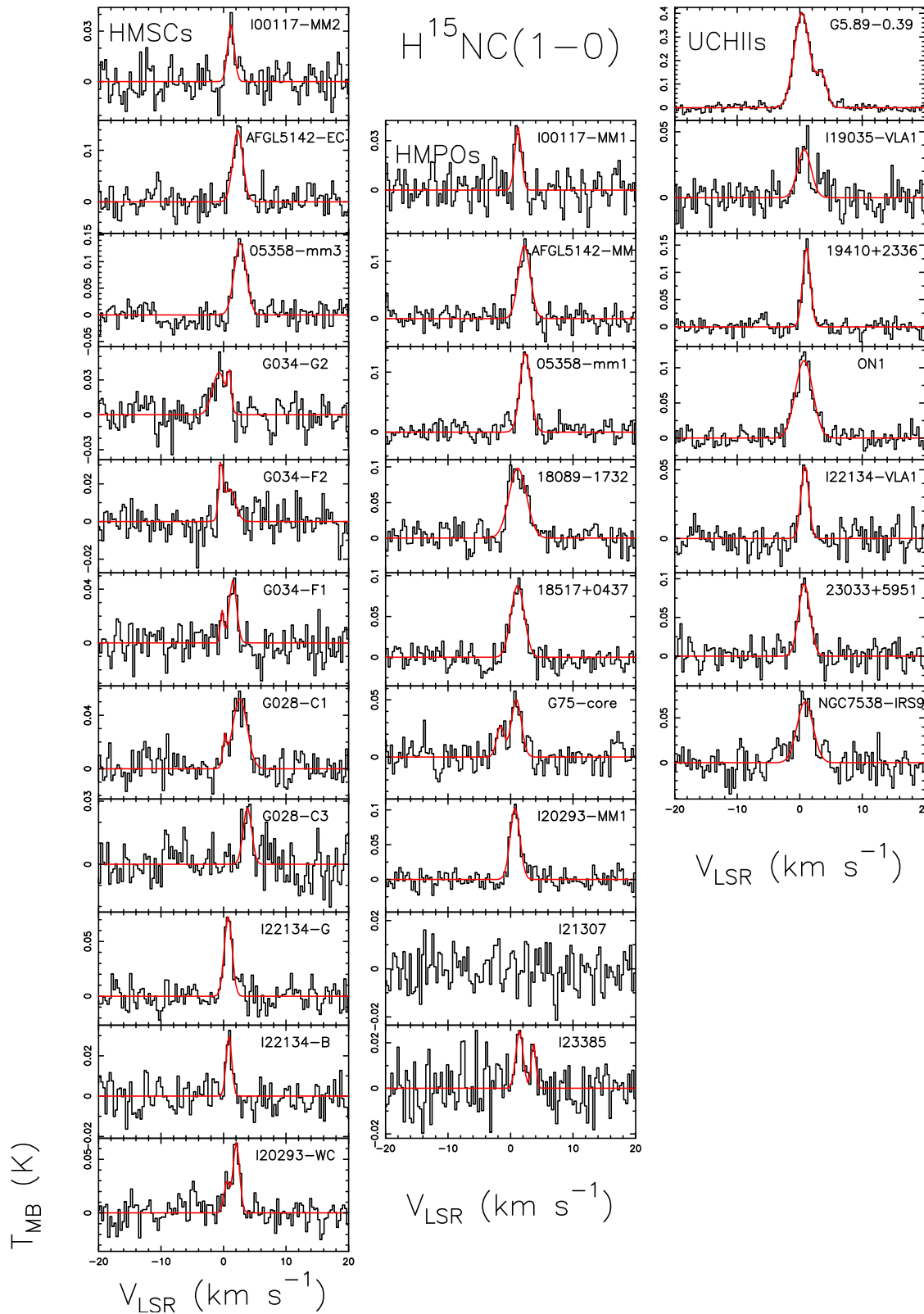
Fig. 2.3: Same as Fig.2.1 for $H^{15}NC(1-0)$. For I21307, this line was not detected, and we have obtained an upper limit on the column density, as explained in Sect. 2.3.1.
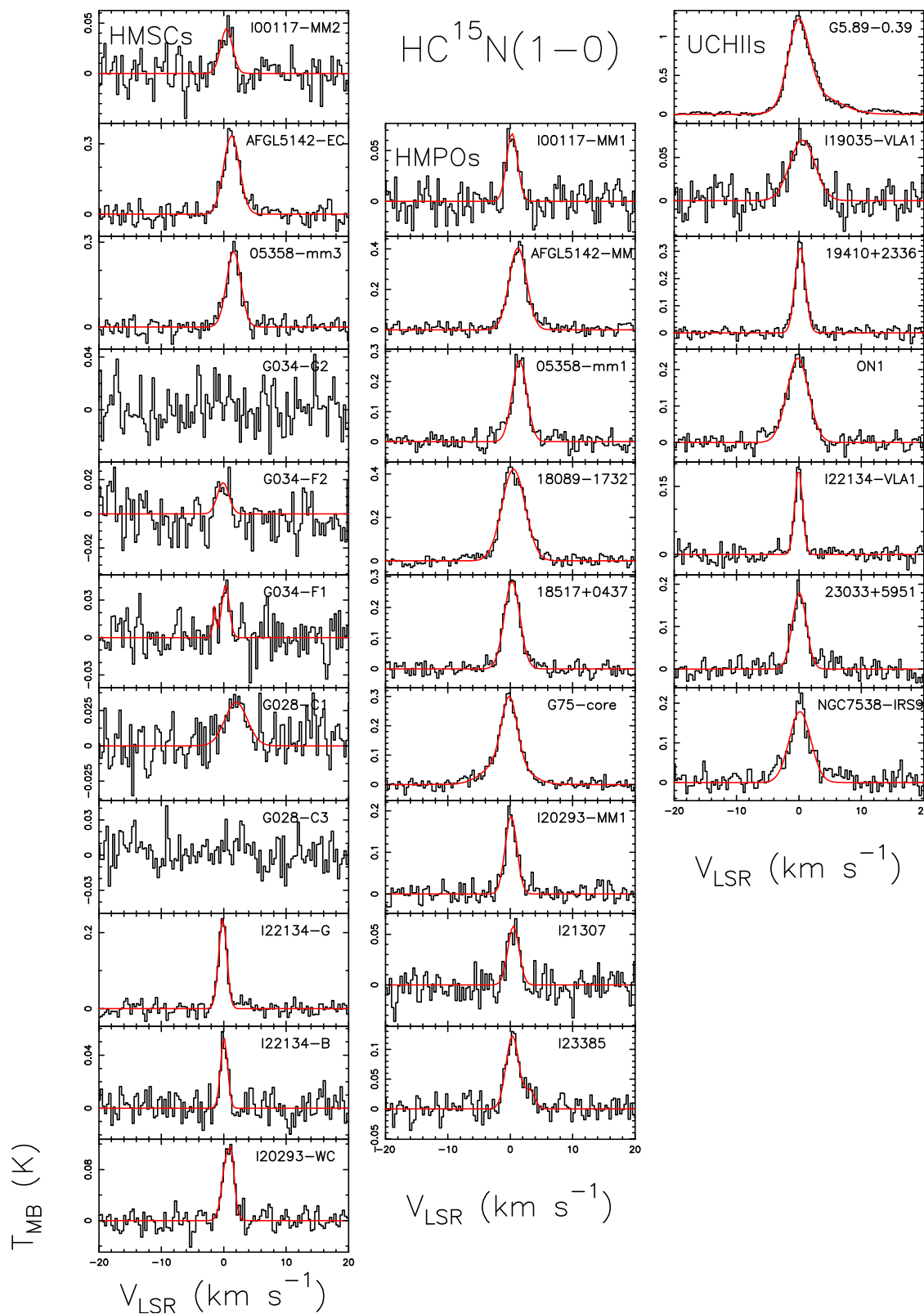
Fig. 2.4: Same as Fig.2.1 for HC^{15}N(1–0). For G034-G2, G028-C3, and G034-F2, the line was not detected, and we obtained upper limits on the column density, as explained in Sect. 2.3.1. For G034-F1 we did not have a clear detection, but we have obtained from the Gaussian fit that $T_{\mathrm{MB}}^{peak} \gtrsim 2.5\sigma$, we have computed as usual the column density, and we refer to this latter as "tentative detection" (see also Table 2.6).

Total column densities

The beam-averaged total column densities of the four species were evaluated from the to-tal line-integrated intensity using eq. (A4) of Caselli et al. (2002), which assumes that T_{ex} is the same for all transitions within the same molecule, and optically thin conditions. In particular, the formula used is:

$$N_{TOT} = \frac{8\pi\nu_{ij}^3}{c^3 A_{ij}} \frac{1}{g_i} \frac{W}{(J_{\nu_{ij}}(T_{ex}) - J_{\nu_{ij}}(T_{BG}))} \frac{1}{\left(1 - \exp\left(-\frac{h\nu_{ij}}{kT_{ex}}\right)\right)} \frac{Q(T_{ex})}{\exp\left(-\frac{E_j}{kT_{ex}}\right)}, \qquad (2.1)$$

where ν_{ij} is the transition frequency, A_{ij} is the Einstein coefficient of spontaneous emission, g_i is the statistical weight of the upper level, E_j is the energy of the lower level, c is the speed of light, k is the Boltzmann constant, T_{ex} is the excitation temperature of the transition, $Q(T_{ex})$ is the partition function at temperature T_{ex}, and T_{BG} is the background temperature (2.7 K), $J_{\nu_{ij}}(T)$ is

$$J_{\nu_{ij}}(T) = \frac{h\nu_{ij}}{k} \frac{1}{\exp\left(\frac{h\nu_{ij}}{kT}\right) - 1}, \qquad (2.2)$$

W is the integrated intensity of the line, $W = \int T_B \, dv = (\int T_{MB} \, dv)\theta_{FF}$, where T_B is the brightness temperature and θ_{FF} is the beam-filling factor, defined as:

$$\theta_{FF} = \frac{\theta_S^2}{\theta_S^2 + \theta_{MB}^2}. \qquad (2.3)$$

In the latter formula θ_S is the molecular emission size and θ_{MB} is the beam size. Since we do not know θ_S for each source, we cannot correct for this factor, and we can only give beam-average total column densities. These column densities correspond also to a special case of formula 2.3. In fact, if the molecular emission is larger than the beam size then $\theta_{FF}=1$.

The assumption of optically thin lines is justified because from all the hyperfine fits of $H^{13}CN(1–0)$ we found opacities $\tau \ll 1$, and well-constrained values ($\Delta\tau/\tau \leq 1/3$) for most of the sources. Those with $\tau=0.1$ are never well-constrained because this is the minimum mathematical value that the software CLASS is able to provide with the *hfs* method. However, we do not use the value of the opacity in the derivation of the column density, but only the assumption (consistent with the fit results) that the lines are optically thin. We assume that the lines of the other isotopologues are also optically thin. We assume local thermal equilibrium (LTE) conditions, as all the observed sources have average H_2 volume densities of the order of $\sim 10^5$ cm^{-3} (see H_2 column densities listed in Table 2.1, derived with SCUBA observations with a beam of $\sim12''$), that is comparable to or marginally lower than the critical densities of the observed lines, thus this assumption is also reasonable. Because T_{ex} cannot be deduced from our optically thin spectra (and also because we have only one transition), we adopted as T_{ex} the kinetic temperatures given by Fontani et al. (2011), who derived them following the method described in Tafalla et al. (2004) based on Monte Carlo models, from which they obtained a relation among the kinetic temperature, T_k, and the NH_3 rotation temperature between metastable levels. The T_k values are given in the last column of Tables 2.8 and 2.9. This last assumption is critical for the single column densities, but the $HN^{13}C/H^{15}NC$ and $H^{13}CN/HC^{15}N$ column density ratios do not change significantly by varying T_k between 20 and 100 K: changes are of one per cent or ten per cent, depending on the source.

The derived beam-averaged column densities are given in Tables 2.8 and 2.9. We have considered lines with $T_{\mathrm{MB}}^{peak} \geq 3\sigma$ as detections. Moreover, for the lines that were not clearly detected, we distinguished those with $2.5\sigma \leq T_{\mathrm{MB}}^{peak} < 3\sigma$ (tentative detection), and those with $T_{\mathrm{MB}}^{peak} < 2.5\sigma$ (non-detection). For the former, considered as tentative detections, we have derived the total column densities as explained above, and for the non-detection we have given an upper limit to the integrated areas, and hence to the total column densities, using

$$\int T_{\mathrm{MB}} \, dv = \frac{\Delta v_{1/2} T_{\mathrm{MB}}^{peak}}{2\sqrt{\frac{ln2}{\pi}}}, \tag{2.4}$$

where σ is the r.m.s. of the spectra, T_{MB}^{peak} is taken equal to 3σ, and $\Delta v_{1/2}$ is the average value of the Full Width at Half Maximum (FWHM) of the lines that are detected for the corresponding transition and evolutionary stage of the source. The average value $\Delta v_{1/2}$ for the high-mass starless cores in our data is $\Delta v_{\mathrm{HMSC}} = 2.2 \pm 0.3$ km s^{-1}, while for the high-mass protostellar objects, it is $\Delta v_{\mathrm{HMPO}} = 1.8 \pm 0.2$ km s^{-1}. Finally, we have derived the column density uncertainties from the errors on the line areas for optically thin lines, given by $\sigma \times \Delta v \times \sqrt{N}$ (σ = r.m.s. noise in the spectrum, Δv = spectral velocity resolution, and N = number of channels with signal) and taking into account the calibration error (10%) for the T_{MB}.

^{14}N/^{15}N ratios

To evaluate the isotopic ratios, we, first of all, used the ^{13}C-bearing species of HCN and HNC because the main isotopologues are usually optically thick. Then, the ^{14}N/^{15}N ratios were derived from the column density ratio of the two isotopologues and correcting them by the ^{12}C/^{13}C Galactic trend given by Milam et al. (2005):

$$^{12}\mathrm{C}/^{13}\mathrm{C} = (6.01 \pm 1.19) \, \mathrm{kpc}^{-1} \times \mathrm{D_{GC}} + (12.28 \pm 9.33). \tag{2.5}$$

This trend is measured with observations of CN in a sample of 18 molecular clouds that lie in the range of Galactocentric distances 0.09–16.41 kpc. Galactocentric distances were taken from Fontani et al. (2014) and Fontani et al. (2015a), and are summarised in Table 2.1. It has to be noted that Milam et al. (2005) derived the Galactocentric distances of their sample using a Sun Galactocentric distance of 7.9 kpc, different from the one used by Fontani et al. (2014) and Fontani et al. (2015a) of 8.4 kpc (Reid et al. 2014). We have evaluated again the ^{12}C/^{13}C ratio behaviour they found updating the Sun distance and we have found a Galactocentric trend that is equal to eq. (2.5), within the error. Uncertainties in the ^{14}N/^{15}N ratios were computed from the propagation of errors on the column densities, as explained above, without taking the calibration uncertainties into account because the lines were observed in the same spectrum (see Sect. 2.2), so that the calibration error cancels out in their ratio.

We point out that the derivation of beam-average total column densities would imply that the ^{14}N/^{15}N ratios are also beam-averaged values. However, they are not affected by this issue since the beam is the same for all the rotational transitions that we have observed. Then, assuming that the emission regions of the four molecules is the same, the θ_{FF} is the same both in the numerator and in the denominator when deriving the ^{14}N/^{15}N ratios, and thus the molecular ratios are independent of the emission size.

In Table 2.8 and 2.9 the ^{14}N/^{15}N ratios derived are listed.

Table 2.8: Total column densities (beam averaged), computed as explained in Sect. 2.3.1, of $H^{15}NC$, $HN^{13}C$, and DNC. In the third and fifth columns we list the error on column densities without considering the calibration error (ΔN). In the seventh, eighth, and ninth columns we list the corresponding $^{14}N/^{15}N$ and D/H isotopic ratios. Uncertainties in the column densities and in the isotope ratios have been computed as explained in Sect. 2.3.1 and 2.3.2. In the last column we list the kinetic temperatures of the clumps derived from Fontani et al. (2015a): for the sources without a derivation of T_k, the mean value for that evolutionary stage was taken (for the HMSCs the average was computed without the "warm" ones, i.e. those with $T_k < 20$ K).

Source	N(H^{15}NC) ($\times 10^{10}$cm^{-2})	ΔN	N(HN^{13}C) ($\times 10^{11}$cm^{-2})	ΔN	N(DNC) (10^{11}cm^{-2})	$\frac{HNC}{H^{15}NC}$ [a]	$\frac{HNC}{DNC}$ [b]	$\frac{DNC}{HNC}$	T_k (K)
HMSC									
I00117-MM2	12 ± 4	2	8 ± 1	0.4	4.2 ± 0.6	460 ± 80	406 ± 77	$(2.5 \pm 0.5) \times 10^{-3}$	14
AFGL5142-EC^w	104 ± 20	10	56 ± 7	1	19 ± 3	398 ± 39	674 ± 136	$(1.5 \pm 0.3) \times 10^{-3}$	25
05358-mm3^w	141 ± 24	10	74 ± 9	1	27 ± 3	388 ± 28	627 ± 103	$(1.6 \pm 0.3) \times 10^{-3}$	30
G034-G2(MM2)	26 ± 8	5	19 ± 3	0.6	4.8 ± 0.7	365 ± 71	612 ± 131	$(1.6 \pm 0.3) \times 10^{-3}$	16^c
G034-F1(MM8)	19 ± 4	2	20 ± 4	2	2.9 ± 0.4	495 ± 72	1002 ± 243	$(1.0 \pm 0.2) \times 10^{-3}$	16^c
G034-F2(MM7)	6 ± 3	2	10 ± 1	0.4	1.6 ± 0.3	783 ± 263	908 ± 193	$(1.1 \pm 0.2) \times 10^{-3}$	16^c
G028-C1(MM9)	43 ± 8	4	28 ± 6	2	3.2 ± 0.8	260 ± 30	1081 ± 356	$(0.9 \pm 0.3) \times 10^{-3}$	17
G028-C3(MM11)	13 ± 4	2	11 ± 1	0.4	1.0 ± 0.3	338 ± 53	1360 ± 426	$(0.7 \pm 0.2) \times 10^{-3}$	17
I20293-WC	24 ± 7	4	17 ± 4	2	10 ± 1	439 ± 90	326 ± 83	$(3.1 \pm 0.8) \times 10^{-3}$	17
I22134-G^w	43 ± 8	4	23 ± 3	0.5	4.4 ± 0.6	369 ± 35	1114 ± 210	$(0.9 \pm 0.2) \times 10^{-3}$	25
I22134-B	10 ± 3	2	6.0 ± 0.9	0.3	1.3 ± 0.2	414 ± 85	984 ± 211	$(1.0 \pm 0.2) \times 10^{-3}$	17
HMPO									
I00117-MM1	16 ± 4	3	9 ± 1	0.4	3.0 ± 0.5	388 ± 75	640 ± 128	$(1.6 \pm 0.3) \times 10^{-3}$	20
AFGL5142-MM	147 ± 24	9	86 ± 10	1	39 ± 5	433 ± 27	504 ± 87	$(2.0 \pm 0.3) \times 10^{-3}$	34
05358-mm1	154 ± 25	9	97 ± 11	2	25 ± 3	466 ± 29	887 ± 146	$(1.1 \pm 0.2) \times 10^{-3}$	39
18089-1732	58 ± 34	29	52 ± 14	9	12 ± 2	385 ± 204	576 ± 182	$(1.7 \pm 0.5) \times 10^{-3}$	38
18517+0437	130 ± 21	8	89 ± 10	1	25 ± 3	349 ± 21	561 ± 92	$(1.8 \pm 0.3) \times 10^{-3}$	40^c
G75-core	124 ± 31	18	109 ± 16	5	10 ± 1	554 ± 84	2122 ± 377	$(5.0 \pm 0.9) \times 10^{-4}$	96
I20293-MM1	103 ± 17	7	80 ± 9	1	12 ± 2	481 ± 33	1277 ± 257	$(0.8 \pm 0.1) \times 10^{-3}$	36
I21307	$\leq 15^u$	–	7 ± 1	0.6	2.1 ± 0.4	≥ 317	700 ± 167	$(1.4 \pm 0.4) \times 10^{-3}$	21
I23385	19 ± 7	5	15 ± 3	2	2.4 ± 0.6	639 ± 189	1564 ± 501	$(0.6 \pm 0.2) \times 10^{-3}$	37
UC HII									
G5.89-0.39	576 ± 70	13	453 ± 49	3	33 ± 4	432 ± 10	2333 ± 379	$(4.3 \pm 0.7) \times 10^{-4}$	32^c
I19035-VLA1	54 ± 16	10	57 ± 7	2	6 ± 1	570 ± 107	1585 ± 328	$(0.6 \pm 0.1) \times 10^{-3}$	39
19410+2336	74 ± 11	4	55 ± 6	0.6	15 ± 2	431 ± 24	657 ± 113	$(1.5 \pm 0.3) \times 10^{-3}$	21
ON1	149 ± 21	6	116 ± 12	0.9	22 ± 2	467 ± 19	978 ± 135	$(1.0 \pm 0.1) \times 10^{-3}$	26
I22134-VLA1	53 ± 11	6	28 ± 4	0.9	6.3 ± 0.9	364 ± 43	948 ± 191	$(1.1 \pm 0.2) \times 10^{-3}$	47
23033+5951	82 ± 15	7	44 ± 5	0.9	8.1 ± 0.9	397 ± 35	1242 ± 197	$(0.8 \pm 0.1) \times 10^{-3}$	25
NGC 7538-IRS9	100 ± 21	11	46 ± 6	1	9 ± 1	331 ± 37	1137 ± 195	$(0.9 \pm 0.1) \times 10^{-3}$	32^c

^{a} multiplied by $\frac{^{12}C}{^{13}C}$ as described in Sect. 2.3.1 and given in Col. 8 of Table 2.1; ^{b} multiplied by $\frac{^{12}C}{^{13}C}$ and by the correction for the different beams 3.09; ^{t} tentative detection; ^{u} upper limits; ^{w}:"warm" HMSC; ^{c} average value for the specific evolutionary stage.

Table 2.9: Total column densities (beam averaged), computed as explained in Sect. 2.3.1, of HC^{15}N and H^{13}CN(1–0) transitions. In the third and fifth columns we list the error on column densities without considering the calibration error (ΔN). In the sixth column we list the corresponding ^{14}N/^{15}N isotopic ratios. Uncertainties have been derived as explained in Sect. 2.3.1. In the last column we list the kinetic temperatures of the clumps derived from Fontani et al. (2015a).

Source	N(HC^{15}N) ($\times 10^{10}$cm^{-2})	ΔN	N(H^{13}CN) ($\times 10^{11}$cm^{-2})	ΔN	$\frac{HCN}{HC^{15}N}$ [a]	T_k (K)
			HMSC			
I00117-MM2	22 ± 6	4	9 ± 1	0.5	282 ± 54	14
AFGL5142-EC^w	327 ± 47	14	176 ± 20	2	398 ± 18	25
05358-mm3^w	270 ± 39	12	158 ± 18	2	433 ± 20	30
G034-G2(MM2)	$\leq 17^u$	–	5 ± 1	0.3	≥ 147	16^b
G034-F1(MM8)	14 ± 4	3	11 ± 2	0.4	369 ± 80	16^b
G034-F2(MM7)	$\leq 14^u$	–	5 ± 1	0.3	≥ 168	16^b
G028-C1(MM9)	32 ± 9^t	6	23 ± 3	0.7	287 ± 55	17
G028-C3(MM11)	$\leq 16^u$	–	10 ± 2	0.8	≥ 250	17
I20293-WC	31 ± 12	9	31 ± 4	0.6	620 ± 180	17
I22134-G^w	120 ± 17	5	56 ± 6	0.8	322 ± 14	25
I22134-B	17 ± 4	2	10 ± 1	0.4	406 ± 50	17
			HMPO			
I00117-MM1	38 ± 8	4	19 ± 2	0.6	345 ± 38	20
AFGL5142-MM	558 ± 70	14	292 ± 31	2	387 ± 10	34
05358-mm1	351 ± 50	14	205 ± 23	2	432 ± 18	39
18089-1732	354 ± 36	9	278 ± 30	2	338 ± 9	38
18517+0437	405 ± 52	11	259 ± 28	2	326 ± 9	40^b
G75-core	790 ± 88	9	324 ± 35	2	258 ± 3	96
I20293-MM1	187 ± 28	9	152 ± 17	2	504 ± 25	36
I21307	35 ± 7	4	20 ± 3	0.7	389 ± 46	21
I23385	134 ± 26	12	48 ± 6	0.9	290 ± 26	37
			UC HII			
G5.89-0.39	1674 ± 246	81	775 ± 79	2	255 ± 12	32^b
I19035-VLA1	157 ± 28	12	99 ± 11	2	340 ± 27	39
19410+2336	176 ± 23	5	123 ± 13	1	405 ± 12	21
ON1	319 ± 40	8	174 ± 18	1	327 ± 8	26
I22134-VLA1	152 ± 22	7	86 ± 10	1	390 ± 18	47
23033+5951	155 ± 23	7	96 ± 11	1	458 ± 21	25
NGC 7538-IRS9	288 ± 43	14	164 ± 18	1	410 ± 20	32^b

^{a} multiplied by $\frac{^{12}C}{^{13}C}$ as described in Sect. 2.3.1 and given in Col. 8 of Table 2.1; ^{t} tentative detection; ^{u} upper limits; ^{w}: "warm" HMSC; ^{b} average value for the specific evolutionary stage.

2.3.2. DNC

We also detected the rotational transition DNC(2–1) for all the 27 sources. These lines are used to measure the D/H ratio, which is compared with the ^{14}N/^{15}N ratio. Such a high detection rate indicates that deuterated gas is present at every stage of the massive star and star cluster formation process, as has been noted by Fontani et al. (2011). The transition possesses a hyperfine structure that is not resolved because of the broad line widths (see Table 2.6), as for the HN^{13}CN(1–0) transition. Therefore, we have fitted the lines with a single Gaussian. To estimate how much the line widths are overestimated using single Gaussian fits, we fitted all lines both with the Gaussian and the hyperfine method. We found, on average, that with a single Gaussian, the line width is about 10% broader than that obtained taking into account the hyperfine structure. We point out that for evolved sources (HMPOs and UC HIIs) another line in the spectra partly overlaps DNC(2–1). This is identified as acetaldehyde, CH$_3$CHO, at 152.608 GHz (the $J_{Ka,Kc} = 8_{0,8}$-$7_{0,7}$ transition). The fact that the line is only detected in the evolved objects is consistent with the idea that acetaldehyde is probably released from grain mantles in warmer and more turbulent objects (see e.g. Codella et al. 2015). When we fitted the DNC lines with Gaussians, we excluded the contribution of this line by fitting the two lines simultaneously, and when possible, we excluded this line from the fit. The fitting results are listed in Table 2.6.

We have derived the total column densities, also in this case, under the assumption of optically thin conditions and same T_{ex} using Eq. (A4) of Caselli et al. (2002), as described above. However, in this case, the HNC/DNC ratio depends on the temperature because of the different excitation conditions of the two rotational transitions observed (J=(2–1) for DNC and J=(1–0) for HN^{13}C), so that the ratio depends on the temperature by the factor $\exp(E_j/k_B T)$. We also corrected the HNC/DNC ratios for the different beams of the antenna at the frequencies of the two lines multiplying both the numerator and the denominator by the corresponding beam filling factor (eq. 2.3), assuming that the emission size of DNC(2–1) and HNC(1–0) are the same and less extended than the beam size of DNC(2–1). This last correction results in a factor 3.09 that is to be multiplied with the HNC/DNC ratio:

$$\left(\frac{1.22\frac{\lambda_1}{D}}{1.22\frac{\lambda_2}{D}}\right)^2 = \left(\frac{\lambda_1}{\lambda_2}\right)^2 = \left(\frac{\nu_2}{\nu_1}\right)^2 = 3.09,$$

where λ_1 and λ_2 are the wavelengths of the HNC(1–0) and DNC(2–1) transitions, respectively, and ν_1 and ν_2 are the corresponding frequencies. In Fig. 2.5 we show the spectra of DNC(2–1) for all the 27 sources. The total column densities and the D/H (and H/D) ratios are listed in Table 2.8. Finally, we derived the errors as explained in Sect. 2.3.1, but here for the D/H ratios we also considered the calibration uncertainties because the two lines were observed in separate spectral setups.
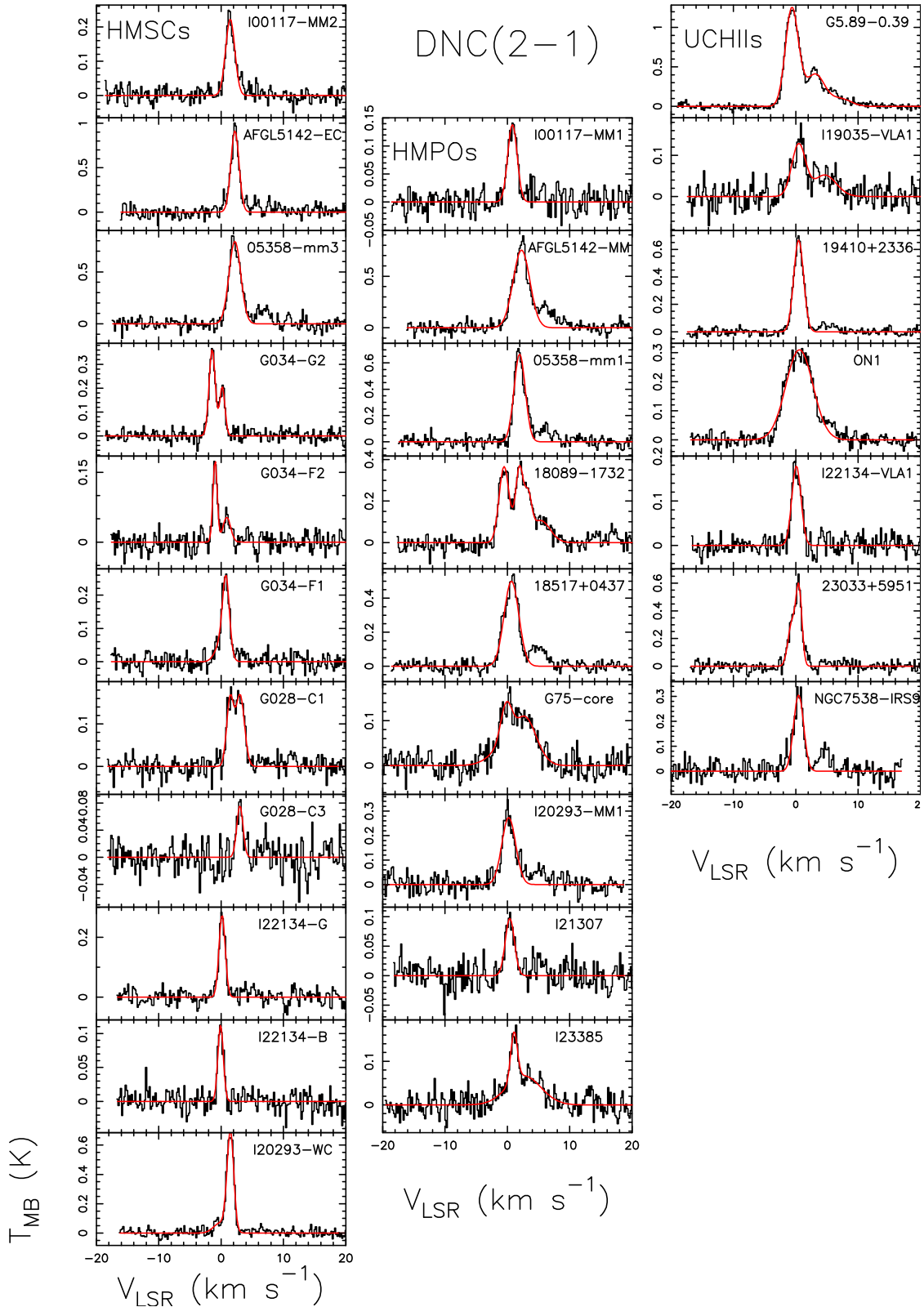
Fig. 2.5: Same as Fig.2.1 for DNC(2–1). For evolved sources (HMPOs and UC HII) the acetaldehyde (CH$_3$CHO) line is also present, as explained in Sect. 2.3.2: when possible, we have excluded the line from the Gaussian fit, otherwise we have fitted the two lines together and used only the DNC(2–1) transition to compute the column densities.

2.4. Isotopic fractionation

2.4.1. ^{15}N-fractionation as a function of evolutionary stages

The comparison between the column densities of the ^{15}N-containing species and those of their main isotopologues, derived as explained in Sect. 2.3.1, is shown in the top panels of Fig. 2.6. The corresponding ^{14}N/^{15}N ratios are given in Tables 2.8 and 2.9, and the bottom panel of Fig. 2.6.

We first discuss the ^{15}N-fractionation found for HCN. The top left panel of Fig. 2.6 shows no large spread of measured ^{14}N/^{15}N values, which are very similar to the value found for the PSN (441, from the Solar wind). The mean values for the three evolutionary stages are 346±37 for HMSCs, 363±25 for HMPOs, and 369±25 for UC HIIs. Although the HMSCs have the highest ^{15}N-enrichment (lowest ^{14}N/^{15}N ratio), the mean values for the three evolutionary categories are consistent within the errors, which indicates that time does not seem to play a role in the fractionation of nitrogen (at least until the formation of a HII region). In the top panels of Fig. 2.7 we show the ^{14}N/^{15}N ratios calculated for HCN in the 27 sources as a function of the Galactocentric distance, of the line width, and of the kinetic temperature, respectively: again, there is no evidence of a trend of these ratios with any of the adopted parameters. In particular, the lack of correlation with either temperature or line width, which are both thought to increase with the evolution of the source, confirms the independence of the ^{14}N/^{15}N ratio from the core age.

We now examine the ^{15}N- fractionation found for HNC: we did not find a large spread of values for this molecule either (top right panel of Fig. 2.6). The mean values found for the three evolutionary stages are 428±40 for HMSCs, 462±31 for HMPOs, and 428±29 for UC HIIs, which is consistent, within the errors, with the ^{14}N/^{15}N ratio measured for the PSN of about 441. For this molecule, no trend between the isotopic ratio and either the line width or the kinetic temperature was found either (bottom panels of Fig. 2.7).

In conclusion, time does not seem to play a role for either ratio. The lack of correlation with evolutionary parameters was also found by Fontani et al. (2015b) for N_2H^+, but the dispersion of the ratios is much smaller in our study (from 180 up to 1300 in Fontani et al. 2015b and from 250 up to 650 in this work). The reason may also be that they have, on average, larger uncertainties. Note also that the ^{14}N/^{15}N ratios for HCN and HNC are obtained under the assumption that the emission of all isotopologues comes from the same molecular regions. If this is not true we should correct source by source the column densities of the molecules by the θ_{FF}. However, until today there are no high resolution observations towards these sources that can give us this information. The lack of correlation between the ^{14}N/^{15}N isotopic ratios and evolutionary parameters or physical parameters (FWHM, T_k) is somewhat consistent with the prediction of the chemical model of Roueff et al. (2015). In fact, as already discussed in Sect. 1.4.4, they predicted no fractionation for HCN and HNC in cold and dense conditions. However, their models are more appropriate for low-mass dense cores, with a T_k of 10 K, than for the warmer high-mass objects studied in this work (see e.g. temperatures in Table 2.8). We stress that ^{13}C may, in theory, have reduced abundances because nitriles and isonitriles are predicted to be significantly depleted in ^{13}C (Roueff et al. 2015). Furthermore, the ^{13}C-fractionation is dependent on the time and temperature evolution (e.g. Szűcs et al. 2014; Röllig and Ossenkopf 2013), and observational
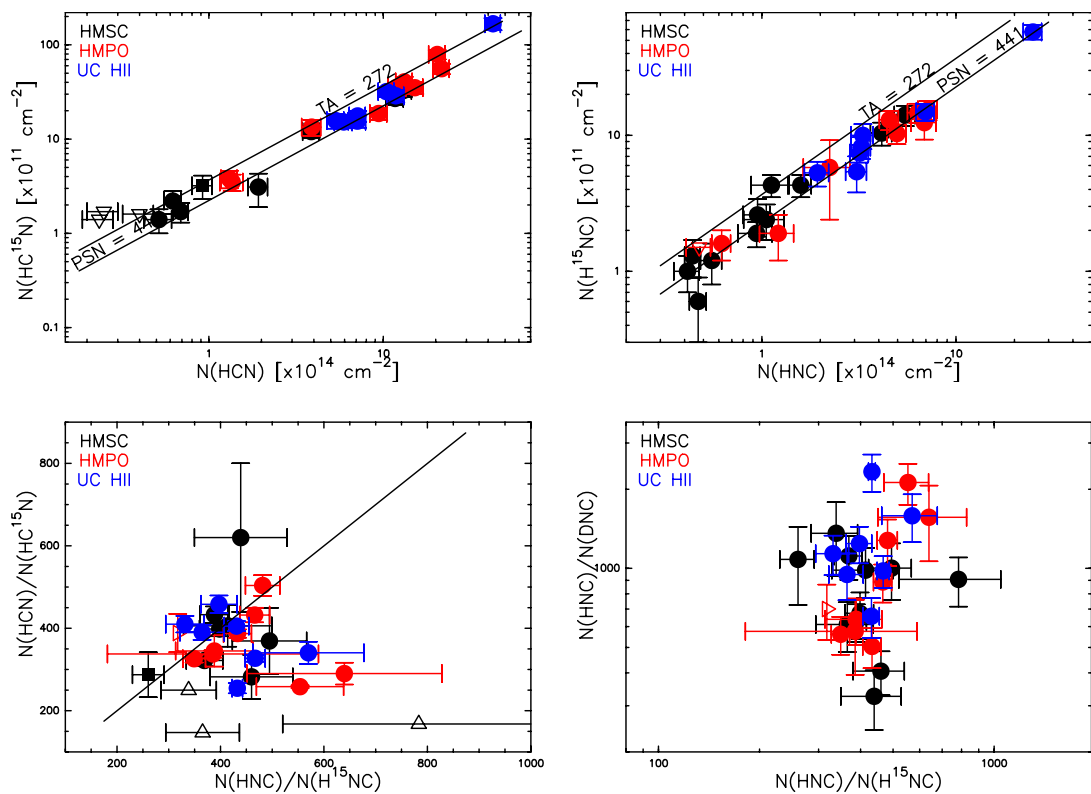
Fig. 2.6: Top panels: column density of HCN compared with that of HC^{15}N (left) and of HNC compared with that of H^{15}NC (right). Bottom panels: comparison between the ^{14}N/^{15}N isotopic ratios derived from the column density ratios N(HCN)/N(HC^{15}N) and N(HNC)/N(H^{15}NC) (right) and comparison between the H/D and ^{14}N/^{15}N isotopic ratios in HNC (left). In all panels, the filled circles represent the detected sources (black=HMSCs; red=HMPOs; blue=UC HIIs). The open triangles in the top panels are the upper limits on N(H^{15}NC) (left) and N(HC^{15}N) (right), while in the bottom panels the open triangles indicate lower limits on either N(HCN)/N(HC^{15}N) or N(HNC)/N(H^{15}NC). The filled squares represent tentative detections. The solid lines in the top panels indicate the mean atomic composition as measured in the terrestrial atmosphere (TA) and in the protosolar nebula (PSN), while in the bottom left panel, the solid line indicates the locus of points where N(HCN)/N(HC^{15}N) is equal to N(HNC)/N(H^{15}NC).

tests to verify whether this theoretical effect is real have yet to be performed. This point will be discussed more in detail in chapter 5.

Interestingly, the ^{14}N/^{15}N ratio measured for HNC towards the source HMSC G034-F2 is an outlier (too high) in the distribution of the ratios for HNC (~780), but with larger errors than in other objects. A similarly high value was found by Bizzocchi et al. (2013) in L1544, which is a typical low-mass pre-stellar core. In particular, Bizzocchi et al. found a value of ^{14}N/^{15}N=1000±200 from the N$_2$H$^+$. Moreover, recently, Redaelli et al. (2018) derived the N$_2$H$^+$/^{15}NNH$^+$ and N$_2$H$^+$/N^{15}NH$^+$ ratios towards the low-mass pre-stellar cores L183, L429 and L694-2 with the IRAM 30m radiotelescope. They modeled the emission with a non-LTE analysis and they found values in the range 630–770. As already discussed in Sect. 1.4.4, these results are not consistent with the predictions of current models on nitrogen fractionation for N$_2$H$^+$ (~440, e.g. Roueff et al. 2015; Wirström and Charnley 2018; Loison et al. 2019).
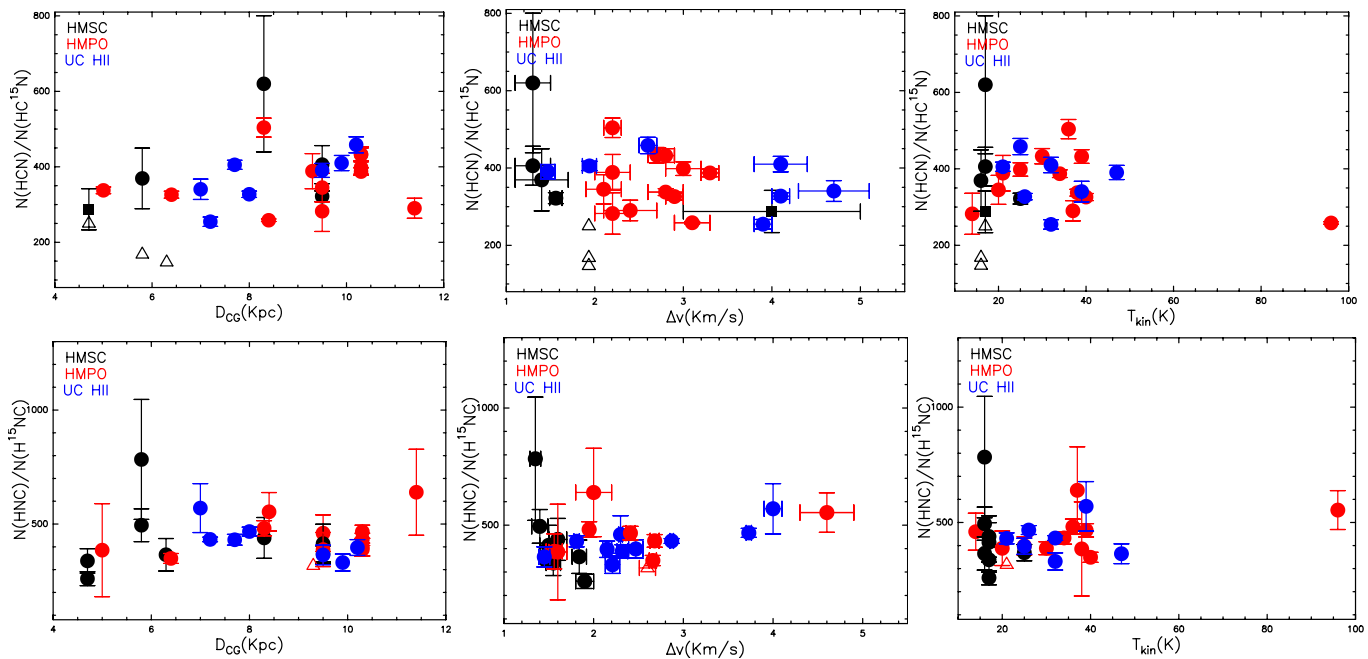
Fig. 2.7: Top panels: N(HCN)/N(HC^{15}N) as a function of Galactocentric distances, line widths, and kinetic temperatures. Bottom panels: N(HNC)/N(H^{15}NC) as a function of Galactocentric distances, line widths, and kinetic temperatures. The symbols are the same as in the bottom panels of Fig. 2.6.

Finally, the ^{14}N/^{15}N ratios for HCN and HNC towards the cores G028-C1, G034-C3, G028-F2, G034-F1, and G034-G2 have also been studied independently by Zeng et al. (2017). The results that they obtained are different by a factor of two with respect to those described in this chapter. Taking into account HC^{15}N in G028-C1 and comparing our spectrum with that of Zeng et al. (2017) at the same velocity resolution of 0.68 km s^{-1}, we obtained a r.m.s of 0.01 K, while they obtained a r.m.s of 0.02 K. Our T$_{MB}^{peak}$ is 0.03 K, that is, more than 2.5 σ, so we can refer to this line as a tentative detection, while Zeng et al. (2017) reported an r.m.s that is comparable with the peak of our line. They also derived the upper limit of the column density using a $\Delta v_{1/2}$ of the line of 2 km s^{-1}, while with our fit we obtained a $\Delta v_{1/2}$ of 4 km s^{-1}: this is the reason for the factor 2 of difference in the integrated area of this line in the two works. This effect is the same in the other spectra (compare Figs. A1, A2, and A3 of their work with our Figs. 2.1, 2.2, 2.3, 2.4), and the different integrated areas are also due to the different resolution and sensitivity.

DEPENDENCE ON ^{14}N/^{15}N RATIO BETWEEN HNC AND HCN

To analyse more in detail the results, we have also performed a Kolmogorov-Smirnov test, which is a non-parametric statistical test that verifies the compatibility between two data samples taken independently. Thus, it tests if the probability distribution of the two separate data sets differs or not. The test evaluates the D value of maximum discrepancy between the two data sets, and the $P-value$ that is the probability that the null hypothesis,
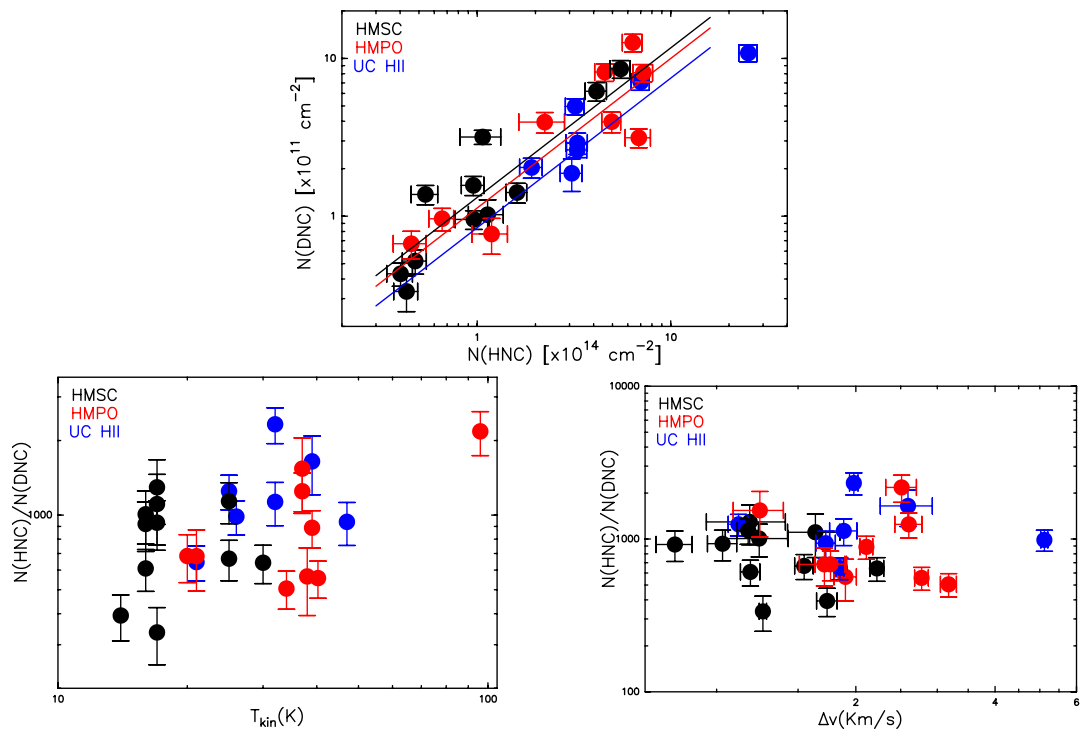
Fig. 2.8: Top panel: column density of HNC compared with that of DNC. The three lines represent the mean values of D/H (see text) for different evolutionary stages: black for HMSCs, red for HMPOs and blue for UC HIIs. Bottom panels: N(HNC)/N(DNC) as a function of line widths and kinetic temperatures. The filled circles have the same meaning as in Fig.2.6.

H_0 verified. In this case H_0 is the fact that the two probability distributions are the same, and then $D=0$. If $P - value$ ≤0.05 we would discard the previous hypothesis and the the two distributions would be independent.

With this test we wanted to determine whether the two data sets (the first set is the $HC^{14}N/HC^{15}N$ ratios and the second is the $H^{14}NC/H^{15}NC$ ratios) belong to the same distributions, and we found $D=0.33$ and a $P - value=0.078$. As described above, the test indicates independence only if $P - value$ ≤0.05, and this could mean that we cannot conclude anything about the dependence or the independence of the two samples with our results. From the literature it is known that $H^{15}NC$ and $HC^{15}N$ can form through the same reactions (see Sect. 1.4.4). Thus, it is not expected a different $^{14}N/^{15}N$ ratio for the two molecules.

2.4.2. D-FRACTIONATION

The top panel of Fig. 2.8 shows the comparison between the column densities of DNC and HNC, derived as explained in Sect. 2.3.2. The N(HNC)/N(DNC) mean values obtained for the three evolutionary stages are 823±94 for HMSCs, 983±189 for HMPOs, and 1275±210 for UC HIIs, indicated by three different lines in Fig. 2.8. Accordingly, the D/H mean ratios are $(1.4±0.2)×10^{-3}$ for HMSCs, $(1.3±0.2)×10^{-3}$ for HMPOs, and $(0.9±0.1)×10^{-3}$ for UC HIIs. The D/H mean values were obtained from computing the average for all the D/H values shown in Table 2.8. We note that the D/H values are slightly higher in the early stages, but because of the large dispersions, the differences between the three evolutionary categories are not statistically significant. This result confirms the marginally decreasing trend

found by Fontani et al. (2014), derived from the DNC (1–0) transition in a subsample of the sources observed in this work. Fontani et al. (2014) found an average D/H of 0.012, 0.009, and 0.008 in HMSCs, HMPOs, and UC HIIs, respectively, with no statistically significant differences among the three evolutionary groups. As already discussed in Sect. 1.4.3, these results together reinforce the theory for which D_{frac}(HNC) does not change significantly going from the colder phase to the active star formation phases. This indicates a clear different behaviour between D_{frac}(HNC) and D_{frac}(N_2H^+) in high-mass star-forming cores (e.g. Fontani et al. 2011).

2.4.3. COMPARISON BETWEEN D/H AND ^{14}N/^{15}N

As discussed in the Introduction of this chapter (Sect. 2.1), it is interesting to search for an indication as to whether the N and H fractionation are linked towards the same source. The bottom right panel in Fig. 2.6 shows HNC/DNC as a function of HNC/H^{15}NC. The data show independence between the two data sets, and this can be shown by computing the Kendall τ test. This is a non-parametric test used to measure the ordinal association between two data sets; its definition is

$$\tau = \frac{(\# \text{ concordant pairs}) - (\# \text{ discordant pairs})}{\frac{n(n-1)}{2}}, \qquad (2.6)$$

with n the number of the total pairs. If $\tau = 1$, there is a full correlation, if $\tau = -1$, there is full anti-correlation, and if $\tau = 0$, the two data sets are independent. We chose this statistical test because compared to other non-parametric tests (e.g. the Spearman ρ correlation coefficient), this test is more robust. Moreover, it allows to compare our analysis with that performed by Fontani et al. (2015b), where the same test was used. In particular, they suggested a possible anti-correlation between the two isotopic ratios for N_2H^+. Following this approach, the τ for the two data sets HNC/DNC and HNC/H^{15}NC was computed, and it was found $\tau \sim 0.13$, which means that the D- and ^{15}N- fractionation in these sources for HNC are independent. This finding arises mostly from the fact that the ^{14}N/^{15}N ratio does not vary with the core evolution, while the D-fractionation shows a faint decreasing trend. This result indicates that the parameters that cause D-enrichment in HCN and HNC on these spatial scales may not influence the fractionation of nitrogen. The independence we found reflects what has been found in some pristine Solar system material, in which the spots of high D-enrichments are not always spatially coincident with those with high ^{15}N enrichment. From the point of view of the models, as discussed in Wirström et al. (2012), the D- and ^{15}N- enrichments do not need to be spatially correlated (although they could be produced by the same mechanism, i.e. exothermic reactions due to the different zero-point energy of the heavier isotope), because relevant reactions for D- and ^{15}N- enrichments have different energy barriers. Finally, Guzmán et al. (2017) did not find a correlation between the low ^{14}N/^{15}N ratios (~80–160) and the D/H ratios (~2×10^{-5}) in the same sample of six protoplanetary discs, concluding that probably at discs spatial scales the cold ion-molecule fractionation pathways do not regulate alone the nitrogen and hydrogen fractionation.

It should be noted that we derived the D_{frac}(HNC) assuming that the molecular emission size is lower than the beam of DNC(2–1), as described in Sect. 2.3.2. Even making different assumptions, like that the emission size is more extended than the beam of HNC(1–0), or assuming a source size, the results obtained in this section and in the previous one

(Sect. 2.4.2) will not change since the D/H would only be multiplied by the same factor, and hence all the trends found would be only shifted. Moreover, the D/H ratios can be influenced by non-dense gas of the envelope at larger spatial scales, that we have observed at the edge of the single-dish beam. This gas can lead to lower D/H ratios. However, all of this information is unknown until high-angular resolution observations will be done.

2.5. THE HCN/HNC RATIO

For completeness, we have also derived the ratio between N(HCN) and N(HNC). Figure 2.9 shows the column density of HCN versus HNC, and it can immediately be noted that HM-SCs show values of HCN/HNC$\lesssim$1 unlike HMPOs and UC HIIs, for which the ratio is >1. The mean values are 0.8 ±0.2 for HMSCs, 2.5 ±0.2 for HMPOs, and 2.0±0.2 for UC HIIs. More-
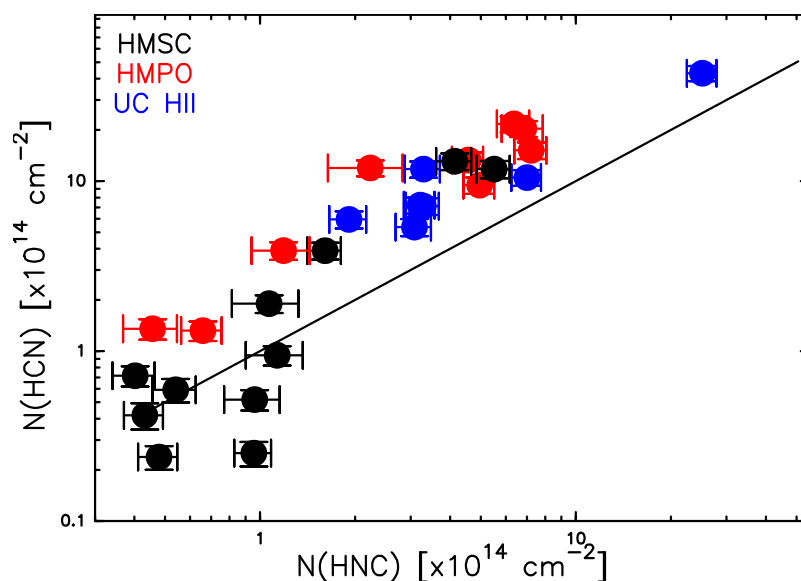
Fig. 2.9: Column density of HCN compared with that of HNC. The solid line is the locus where N(HCN)/N(HNC) is equal to 1, as statistically expected. The filled circles have the same meaning as in Fig. 2.6.

over, we have derived the HCN/HNC ratio in the two data sets: (HMSCs) and (HMPOs+UC HIIs). Using the non-parametric statistical Kolmogorov-Smirnov test, we have obtained a P-value=0.025, which indicates that the two distributions are independent. Schilke et al. (1992) reported predictions and observations for the Orion hot core OMC-1, which is the prototype of a high-mass hot core. They found that the HCN/HNC abundance ratio is very high (∼80) in the vicinity of Orion-KL, but it rapidly declines in adjacent positions to values of ∼5. They compared the observations with the predictions of molecular cloud chemistry and found an agreement with steady-state models. More recently, Jin et al. (2015) found that the abundance HCN/HNC ratio increases if the sources evolved from IRDCs to UC HIIs, and they suggested that this might occur for neutral-neutral reactions where HNC is selectively consumed for T$\gtrsim$24 K (Hirota et al. 1998):

$$HNC + H \rightarrow HCN + H; \tag{2.7}$$

$$HNC + O \rightarrow NH + CO. \tag{2.8}$$
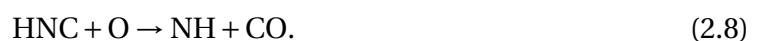
For the first reaction, a 2000 K barrier was found, and the second barrier has not yet been theoretically and experimentally studied, but if the reaction is possible, N(HCN)/N(HNC) would increase rapidly in warm gas. Therefore, future laboratory measurements of these reactions are really important, especially at low temperatures.

We have also checked the $HC^{15}N/H^{15}NC$ column density ratio, and we have found that it is roughly 1 for HMSCs (with an average value of 1±0.5) and more than 1 for HMPOs and UC HIIs (with an average value of ~ 3 ± 1). Loison et al. (2014) showed that in cold regions, where C and CO are depleted, the dissociative recombination of $HCNH^+$ acts to isomerize HCN into HNC, producing HCN/HNC ratios close to or slightly above one. Moreover, Loison et al. (2019) discussed that if the HCN/HNC of the main isotopologues is equal to 1, the statistical theory leads to a branching ratio equal to 0.91 for $HC^{15}N/H^{15}NC$, considering the variation in the ro-vibrational densities of states. In hot gas, the $CN + H_2$ reaction with its high activation energy (2370 K, Jacobs et al. 1988) and the isomeration process C + HNC → C + HCN (Loison et al. 2014) may be responsible for the high HCN/HNC ratios measured in hot cores (Schilke et al. 1992). That the $HC^{15}N/H^{15}NC$ ratios measured in this work towards HMSCs are always close to one imply that both species are probing similar low-temperature gas.

Recently, Nakamura et al. (2019) evaluated the HCN/HNC ratio towards the outflow-shocked region, OMC-2 FIR4 (hereafter FIR4) using the Nobeyama 45m telescope. They found an average ratio towards the N_2H^+ clump (~2) that is consistent, within the error, with the values found in our works towards the high-mass protostellar objects. Aguado et al. (2017) proposed that FUV radiation can photodissociate HNC more than HCN (photodissociation cross sections larger for HNC), leading to higher HCN/HNC ratios for stronger FUV. However, Nakamura et al. (2019) found a HCN/HNC ratio lower towards the region VLA 13 (a protostar nearby FIR4) than in the N_2H^+ clump. Thus, since VLA 13 shows a FUV radiation strength 140 times larger than the N_2H^+ clump of FIR4 (Ishii et al. 2019), they concluded that the effect of a temperature higher than 24 K is the main responsible for the observed HCN/HNC ratios.

Note that also in this case the HCN/HNC (and $HC^{15}N/H^{15}NC$) ratios are obtained under the assumption that the angular size of the emission of all isotopologues is the same. Only high-resolution observations could add the missing information about the molecular source size.

2.6. Conclusions

We have observed the J=1–0 rotational transitions of $H^{15}NC$, $HN^{13}C$, $H^{13}CN$, and $HC^{15}N$ together with the J=2–1 transition of DNC towards 27 massive star-forming cores in different evolutionary stages to derive the ^{15}N- and D-fractionation, and to compare the ratios with each other. We find $^{14}N/^{15}N$ for HCN between ~200 and ~700, and for HNC between ~250 and ~620, with a small spread around the PSN value of 441. Comparing the $^{14}N/^{15}N$ ratios for different evolutionary stages, we did not find any trend, indicating that time does not seem to play a role in the N-fractionation; furthermore, we cannot conclude about the correlation between the ^{15}N-fractionation for the two molecules HNC and HCN. Our findings are in agreement with the recent chemical models of Roueff et al. (2015) and Loison et al. (2019).

Considering both D- and ^{15}N-fractionation for HNC towards the same sources, we found no correlation. This is consistent with the possible anti-correlation found by Fontani et al. (2015b) in N_2H^+: the causes of D-enrichment in HCN and HNC do not affect the ^{15}N-fractionation. This result is in agreement with the prediction made by Wirström et al. (2012). The independence between D/H and ^{14}N/^{15}N ratios confirms also the recent findings of Guzmán et al. (2017) in protoplanetary discs. At a typical distance of the massive star-forming regions studied in this work of ~3 kpc, the angular size on which we can evaluate the ^{14}N/^{15}N is of ~0.4 pc. The order of magnitude of these scales is that of the massive dense cores, MDC, described in Sect. 1.1.1 (see also Fig. 1.2). Conversely, the PSN linear scale corresponds to that of a low-mass pre-stellar core, i.e. ~0.01 pc (see Fig. 1.2). The fact that we found at larger spatial scales a value similar to the PSN one suggests a direct chemical heritage at smaller scales. Moreover, the low ^{14}N/^{15}N ratios (~100) that Guzmán et al. (2017) found towards protoplanetary discs for HCN, do not contradict our findings. In fact, this is an evolutionary stage after that of the PSN, and these values can hence be due to a subsequent chemical reprocessing. For example, the isotope-selective photodissociation could explain the lowering of the ^{14}N/^{15}N ratios, as suggested by Heays et al. (2014). In fact, HCN traces the upper warm layer of the disc (Visser et al. 2018), which are photon dominated regions. We will discuss in more detail the possible effect of isotope-selective photodissociation for N-fractionation in massive star-forming regions in chapter 4.

<div style="text-align: right; font-size: 3em; font-weight: bold;">3</div>

NITROGEN FRACTIONATION ACROSS THE GALAXY

ABSTRACT

To put more stringent observational constraints on N-fractionation in star-forming regions located in different chemical environments, in this chapter we describe observations taken with the IRAM-30m telescope of a large sample of 66 cores in massive star-forming regions placed at different Galactocentric distances. We targeted the (1–0) rotational transition of $HN^{13}C$, $HC^{15}N$, $H^{13}CN$, and $HC^{15}N$, and derived the $^{14}N/^{15}N$ ratio for both HCN and HNC. We also have performed a global analysis of the $^{14}N/^{15}N$ ratio including the 27 sources already presented in chapter 2, so that the final sample analysed in this chapter consists of 87 objects, and represents the largest statistical sample ever analysed in $^{14}N/^{15}N$. The $^{14}N/^{15}N$ ratios are distributed around the PSN value with a lower limit near the terrestrial atmosphere value (~272). We have also derived the $^{14}N/^{15}N$ ratio as a function of the Galactocentric distance and deduced a linear trend based on unprecedented statistics. The Galactocentric dependences that we have found are consistent, in the slope, with past works but we have found a new local $^{14}N/^{15}N$ value of ~400, i.e. closer to the PSN. A second analysis was done, and a parabolic Galactocentric trend was found. Comparison with Galactic chemical evolution models shows that the slope until 8 kpc is consistent with the linear analysis, while the flattening trend above 8 kpc is well reproduced by the parabolic analysis.

This chapter is based on the work published in the peer-reviewed scientific journal *Monthly Notices of the Royal Astronomical Society* in the paper: Colzi et al. (2018b).

3.1. INTRODUCTION

In addition to giving information on the chemical history of our Solar system, the abundance ratio $^{14}N/^{15}N$ is also considered a good indicator of stellar nucleosynthesis. In fact, the two elemental isotopes are not originated in the same way. Both isotopes have indeed an important secondary production in the CNO cycles. There are two types of CNO cycles: a cold cycle and a hot cycle. The cold CNO cycle takes place in main-sequence stars and in the H-burning shells of red giants: ^{14}N is created from ^{13}C or ^{17}O and brought to stellar
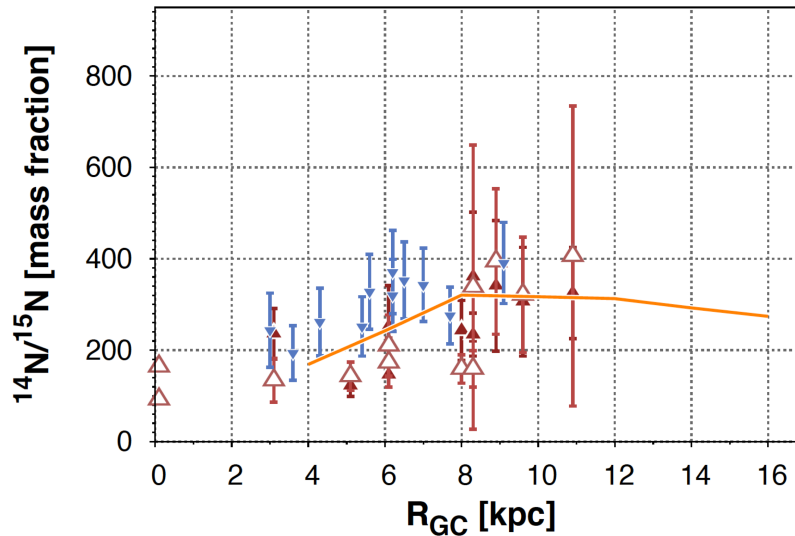
Fig. 3.1: Nitrogen isotopic ratios as a function of the Galactocentric distance. The orange solid line is the present-day model. The different symbols represents the ^{14}N/^{15}N ratios described by Adande and Ziurys (2012): red filled triangles represent CN observations, red open triangles represent HNC observations and blue filled triangles represent HCN observations. Taken from Romano et al. (2017).

surfaces through dredge-up on the red giant branch. The hot CNO cycle occurs instead in novae outbursts (Clayton 2003) and is the main way to produce ^{15}N. However, there is also a strong primary component of ^{14}N created in the so-called Hot Bottom Burning (HBB) of asymptotic giant branch (AGB) stars (e.g. Schmitt and Ness 2002, Izzard et al. 2004). Moreover, there is an (over-)production of ^{15}N with respect to ^{14}N in the relative role played by massive stars and novae (Romano and Matteucci 2003, Romano et al. 2017). Therefore, ^{15}N is principally a secondary element, while fast-rotating intermediate- and high-mass stars produce large amounts of primary ^{14}N at low metallicities (Meynet and Maeder 2002).

A different origin of the two nitrogen isotopes leads to an increase of ^{14}N/^{15}N ratio with the Galactocentric distance, up to a distance of ~8 kpc, as predicted by models of Galactic chemical evolution (GCE, Romano and Matteucci 2003, Romano et al. 2017). In fact, until this distance the novae outbursts create more ^{15}N in the inner part of the Galaxy, given the highest star formation with respect to the outer Galaxy. However, the relative importance of the different processes that create the isotopes, or the eventual existence of additional processes, is still unclear. The only way to test the predictions of GCE models is to provide more observational constraints. The GCE model made by Romano et al. (2017) was compared with measurements of the ^{14}N/^{15}N ratios in a sample of warm molecular clouds observed by Adande and Ziurys (2012). The model seems able to reproduce the trend found by Adande and Ziurys (2012), but this latter was obtained from a small sample (22 sources), and mixing up data from different molecules and different instruments (i.e. different observational parameters). Romano et al. (2017) adopted for massive stars the grid of yields suggested by Nomoto et al. (2013). Fig. 3.1 shows the results of the GCE model of Romano et al. (2017) for the Galactocentric trend of ^{14}N/^{15}N ratio, and the comparison with the observations.

However, the importance of stellar rotation is not accounted for the stellar yields used by Romano et al. (2017). So, Romano et al. (2019) updated and implemented a new GCE

model with the stellar yields given by Limongi and Chieffi (2018), and they compare this model with the results described in this chapter. We will discuss their results in Sect. 3.5.

In this work we report the measurements of the ^{14}N/^{15}N ratio derived in a sample of 66 dense cores that span Galactocentric distances in the range ~ 2–12 kpc. Moreover, together with the sources studied by Colzi et al. (2018a) and described in chapter 2, we present a new Galactocentric behavior of ^{14}N/^{15}N, based now on 87 sources, which makes this new Galactocentric dependence statistically more robust than that of past works. We compare also this trend to GCE models. The new sample of sources is presented in Sect. 3.2. The results are presented in Sect. 3.3 and a discussion of the results is presented in Sect. 3.4 and 3.5.

3.2. SAMPLE AND OBSERVATIONS

3.2.1. DESCRIPTION OF THE SAMPLE

The source list of the 66 sources is reported in Table 3.1, where the source coordinates and the distances from the Sun are shown. 35 sources of the sample were compiled from a list of high-mass young stellar objects from northern millimeter continuum surveys (Sridharan et al. 2002, Beuther et al. 2002a). These sources were selected with (i) distances < 5 kpc, to sample comparable spatial scales, (ii) strong (peak intensity > 0.5 Jy/beam) and compact 1.2 mm continuum emission, suggestive of high-mass young objects embedded in the dust, and (iii) observable with the IRAM 30m telescope. Note that we do not consider any criteria related to the line intensity or molecular richness of the source, nor do we consider the centimeter continuum emission and luminosity, to avoid possible biases. The sources cover a broad range of luminosities and evolutionary stages (traced with different star formation signposts, e.g. presence of masers, infrared sources, HII regions) which will permit to study the dependence of chemical properties with luminosity and evolutionary stage. The other 31 sources, indicated with ** in Table 3.1, were selected from the literature (Fontani et al. 2011; Wouterloot et al. 1993; Beltrán and de Wit 2016; Cesaroni et al. 2017; Tan et al. 2014). This sample is not classified in evolutionary stages, like that of chapter 2, yet. This classification has been investigated in the Ph.D. thesis of Chiara Mininni. The whole sample and their properties will be presented in a forthcoming paper (Mininni et al.; in prep.), while in this paper we focus on the lines of the isotopologues of HCN and HNC.

The distances are kinematic distances based on the rotation curve of the Galaxy, and are taken from Sridharan et al. (2002), Beuther et al. (2002a) and from the other works cited above. For the sources with the ambiguity of distance we have chosen the near one.

The sample of 66 sources was implemented with the 27 described in chapter 2, to obtain a statistically significant sample. Because 6 sources of the two samples were in common: 00117+6412M1, 18089-1732M1, 18517+0437M1, G75, 20081+3122M2 and NGC7538IRS9, we have decided to keep the results found in the first work, described in the previous chapter, as the S/N of those observations was better than that of the observations presented in this chapter by a factor of ~2 (compare spectra of Figs. 3.2, 3.3, 3.4, 3.5, 3.6, 3.7, 3.8 and 3.9 with Figs. 2.1, 2.2, 2.3, and 2.4). Despite the ratios found by Colzi et al. (2018a) were derived using the kinetic temperatures calculated from ammonia (as described in Sect. 2.3.1), that are different from the excitation temperature (T_{ex}) adopted in this work, the ^{14}N/^{15}N ratios

are almost independent (differences of 1–10%) of the chosen temperature, and then the results obtained, for these 6 sources, in the previous work could be used to increment our sample.

We finally have a sample of 87 sources: the 27 of Colzi et al. (2018a) and the 60 of this work, not in common with the previous one.

Table 3.1: List of the observed sources. Cols. 2, 3, 4 and 5 give the coordinates (equatorial and Galactic) of the sources and Col. 6 gives the source distance to the Sun of the associated star-forming region. In Col. 7 the Galactocentric distances of the sources obtained from the distance to the Sun (Col. 6) and the corresponding Galactic longitude (Col. 4) are listed. In Col. 8 we give the T_{ex} used to fit the lines for all the sources, derived fitting the K-ladder of $CH_3CN(5-4)$ (Mininni et al., in prep.). The sources for which the T_{ex} is not showed are those without detection of the observed transitions in this work.

Source	α(J2000)	δ(J2000)	l	b	d	D_{GC}	T_{ex}
	(h m s)	(°′″)	(°)	(°)	(kpc)	(kpc)	(K)
I00117-MM1**	00:14:26.1	+64:28:44.0	118.96	+1.89	1.8	9.4	35***
I04579-VLA1**	05:01:39.9	+47:07:21.0	160.14	+3.16	2.5	10.7	35***
18089-1732M1	18:11:51.5	-17:31:29.0	12.89	+0.49	3.6*	4.9	87
18089-1732M4	18:11:54.0	-17:29:59.0	12.92	+0.49	3.6*	4.9	36
18151-1208M1	18:17:58.0	-12:07:27.0	18.34	+1.77	3.0	5.6	37
18151-1208M2	18:17:50.4	-12:07:55.0	18.32	+1.79	3.0	5.6	42
18182-1433M1	18:21:09.2	-14:31:49.0	16.59	-0.05	4.5*	4.2	52
18264-1152M1	18:29:14.6	-11:50:22.0	19.88	-0.53	3.5*	5.2	50
18272-1217M1	18:30:02.9	-12:15:17.0	19.61	-0.90	2.9	5.7	52
18290-0924M2	18:31:46.3	-09:22:23.0	22.36	+0.06	5.3*	4.0	–
18306-0835M1	18:33:24.0	-08:33:31.0	23.27	+0.08	4.9*	4.3	39
18306-0835M2	18:33:17.2	-08:33:26.0	23.25	+0.10	4.9*	4.3	36
18308-0841M1	18:33:33.1	-08:39:10.0	23.20	-0.00	4.9*	4.3	36
18310-0825M2	18:33:44.0	-08:21:20.0	23.48	+0.10	5.2*	4.1	38
18310-0825M3	18:33:42.2	-08:21:36.0	23.48	+0.10	5.2*	4.1	34
18372-0541M1	18:39:56.0	-05:38:47.0	26.60	-0.02	1.8*	6.8	71
18385-0512M1	18:41:13.3	-05:09:01.0	27.19	-0.08	2.0*	6.6	49
18445-0222M3	18:47:07.7	-02:21:26.0	30.34	-0.12	5.3*	4.6	15
18454-0136M1	18:48:02.5	-01:33:26.0	31.16	+0.05	2.7*	6.2	33
18472-0022M1	18:49:52.4	-00:18:56.0	32.47	+0.20	3.2*	5.9	32
18488+0000M1	18:51:25.6	+00:04:06.0	32.99	+0.03	5.4*	4.8	36
18517+0437M1	18:54:14.3	+04:41:40.0	37.43	+1.5	2.9	6.3	41
18521+0134M1	18:54:40.8	+01:38:05.0	34.76	+0.02	5.0*	5.1	37
19012+0536M1	19:03:45.4	+05:40:43.0	39.39	-0.14	4.6*	5.6	37
19035+0641M1	19:06:01.6	+06:46:43.0	40.62	-0.14	2.2	6.8	49
19095+0930	19:11:54.0	+09:35:52.0	43.80	-0.13	3.3	6.4	57
19282+1814M1	19:30:23.1	+18:20:25.0	53.62	+0.03	1.9*	7.4	44
19410+2336M1	19:43:10.9	+23:44:10.0	59.78	+0.07	2.1*	7.5	32
19411+2306M1	19:43:18.0	+23:13:59.0	59.36	-0.21	2.9*	7.3	27
19413+2332M1	19:43:29.3	+23:40:18.0	59.76	-0.03	1.8*	7.6	36
ON1**	20:10:09.1	+31:31:36.0	69.54	-0.98	2.5	7.8	85
20126+4104M1	20:14:25.9	+41:13:34.0	78.12	+3.63	1.7	8.2	71
20216+4107M1	20:23:23.5	+41:17:38.0	79.13	+2.28	1.7	8.2	54

Table 3.1: Continued.

Source	α(J2000) (h m s)	δ(J2000) (°′″)	l (°)	b (°)	d (kpc)	D_{GC} (kpc)	T_{ex} (K)
20319+3958M1	20:33:49.1	+40:08:35.0	79.35	+0.00	1.6	8.2	58
20332+4124M1	20:34:59.7	+41:34:49.0	80.63	+0.68	3.9	8.6	35***
20343+4129M1	20:36:07.9	+41:39:57.0	80.83	+0.57	1.4	8.2	52
22187+5559V3**	22:20:33.7	+56:14:29.1	103.06	-0.69	2.9	9.4	–
22187+5559V5**	22:20:35.6	+56:14:46.4	103.06	-0.69	2.9	9.4	–
22198+6336**	22:21:26.8	+63:51:37.2	107.30	+5.64	0.7	8.6	64
22570+5912M2	22:58:59.2	+59:27:36.0	109.08	-0.35	5.1	11.1	35***
23033+5951M1	23:05:25.3	+60:08:06.0	110.09	-0.07	3.5	10.1	26
23139+5939M1	23:16:10.5	+59:55:28.0	111.26	-0.77	4.8	11.0	39
G75-core**	20:21:44.0	+37:26:38.0	75.78	+0.34	3.8	8.3	56
G08.14+0.22**	18:03:01.3	-21:48:05.0	8.14	+0.22	3.4	5.0	52
G14.33-0.65**	18:18:54.8	-16:47:53.0	14.33	-0.65	2.6	5.9	49
G14.99-0.67**	18:20:17.6	-16:13:55.0	14.99	-0.67	2.4	6.0	22
G14.99-2**	18:20:17.6	-16:13:55.0	14.99	-0.67	2.4	6.0	35***
G15.02-0.62**	18:20:10.3	-16:10:35.0	15.02	-0.62	2.4	6.1	14
G24.78+0.08**	18:36:12.6	-07:12:10.9	24.79	+0.08	7.7	2.1	93
G31.41+0.31**	18:47:34.2	-01:12:45.0	31.41	+0.31	7.9	3.5	–
G34.82+0.35**	18:53:37.4	+01:50:32.0	34.82	+0.35	3.6	5.6	35
G35.03+0.35**	18:54:00.6	+02:01:19.3	35.02	+0.35	3.2	6.0	40
G35.20-0.74**	18:58:13.0	+01:40:36.0	35.20	-0.74	2.2	6.7	50
G36.70+0.09**	18:57:59.3	+03:24:05.0	36.71	+0.10	9.7	5.6	–
G37.55+0.19**	18:59:11.4	+04:12:14.0	37.56	+0.20	5.6	5.1	44
G40.28-0.22**	19:05:42.1	+06:26:08.0	40.28	-0.22	4.9	5.4	43
G42.03+0.19**	19:07:29.0	+08:10:39.0	42.03	+0.19	11.1	7.2	–
G42.30-0.30**	19:09:44.2	+08:11:33.0	42.30	-0.30	10.5	7.0	35***
G42.70-0.15**	19:09:55.8	+08:36:56.0	42.70	-0.15	15.9	11.2	–
G48.99-0.30**	19:22:26.3	+14:06:37.0	48.99	-0.30	5.1	5.8	37
G49.41+0.33**	19:20:58.9	+14:46:46.0	49.41	+0.33	12.2	9.2	–
G50.78+0.15**	19:24:17.2	+15:53:54.0	50.78	+0.15	7.0	6.5	–
G52.92+0.41**	19:27:35.2	+17:54:26.0	52.92	+0.41	5.1	6.5	–
G53.04+0.11**	19:28:55.7	+17:52:01.0	53.04	+0.11	9.4	8.0	32
G53.14+0.07**	19:29:17.5	+17:56:24.0	53.14	+0.07	1.9	7.4	42
NGC7538-IRS1**	23:13:43.3	+61:28:10.6	111.54	+0.78	2.8	7.0	43
NGC7538-IRS9**	23:14:01.8	+61:27:20.0	111.57	+0.75	2.8	9.7	39

* sources with distance ambiguity, due to their position within the Solar circle, for which we have chosen the near distance. For details see Sridharan et al. (2002).

** sources selected from the literature (Fontani et al. 2011, Wouterloot et al. 1993; Beltrán and de Wit 2016; Cesaroni et al. 2017; Tan et al. 2014).

*** sources for which it was not possible to obtain T_{ex} from CH_3CN and then we have used a T_{ex} of 35 K, which is the mean value of the excitation temperatures of the sources.

3.2.2. Observations

The 66 sources analyzed in this work were observed with the IRAM 30m telescope on August 2014. We have used the FTS spectrometer (Fast Fourier Transform Spectrometer; Klein et al. 2012) to cover the frequency range 85.7–93.5 GHz with a frequency resolution of 200 kHz, corresponding to 0.6 km s^{-1} at the observed frequencies. The half-power beam width (HPBW) is about 29″. The observations were made in position-switching mode. The pointing was checked every 1.5 hours, and the focus was corrected at the beginning of the observations and every 4-6 hours. The integration time ranged from 10 to 30 minutes, except for some sources, as 04579+4703, for which it was less (about 5 minutes). The r.m.s. noise levels of the spectra are shown in Tables 3.3, 3.4, 3.5 and 3.6. The system temperature was in the range of 100–150 K during the observations. The observed spectra were first calibrated and reduced using the CLASS/GILDAS package (Pety 2005), the data were corrected for platforming and spike channels were removed. The beam efficiency (B_{eff}) for the IRAM 30m telescope at these frequencies is 0.84, while the forward efficiency (F_{eff}) is 0.94. The antenna temperatures were converted to main beam temperatures by using the expression: $T_{\mathrm{A}}^* = T_{\mathrm{MB}}\eta_{\mathrm{MB}}$, where $\eta_{\mathrm{MB}} = B_{\mathrm{eff}}/F_{\mathrm{eff}}$. The spectra obtained were exported from the software package CLASS of GILDAS[1] to MADCUBA[2] (see e.g. Rivilla et al. 2016; Rivilla et al. 2017). With MADCUBA we have selected the part of the spectra around the four targeted lines, and we have fitted the baselines with a maximum order of 1. MADCUBA was then used to identify the lines we wanted to study, and analyze them. In particular, we have observed the rotational transition (1–0) of H^{13}CN, HN^{13}C, HC^{15}N, and H^{15}NC, as already done in the previous work. For the analysis we have used the spectroscopic parameters from the Jet Propulsion Laboratory (JPL) molecular catalog[3]. Rest frequencies are taken from the laboratory works and quantum-chemical calculations referred in Table 3.2 and Sect. 2.2.

3.3. Results

In this section the line detection and fitting procedure are described. Moreover, the total column densities and the ^{14}N/^{15}N related to the observed transitions are presented.

3.3.1. Line detection

We have considered detections of HN^{13}C(1–0), H^{15}NC(1–0), H^{13}CN(1–0), and HC^{15}N(1–0) if the spectral lines show a peak main beam temperature ($T_{\mathrm{MB}}^{\mathrm{peak}}$)≥3$\sigma$, where σ is the r.m.s noise of the spectrum; for the detections close to the 3σ limit, we have distinguished between tentative detections ($2.5\sigma \leq T_{\mathrm{MB}}^{\mathrm{peak}} < 3\sigma$) and non-detections ($T_{\mathrm{MB}}^{\mathrm{peak}} < 2.5\sigma$). The percentage of detected lines (together with tentative detections) is the following: the HN^{13}C line is clearly detected in 58 cores (88%), the H^{13}CN line is detected in 58 cores (88%) which, however, are not the same (see Tables 3.3 and 3.5), the H^{15}NC line is detected in 45 cores (68%) and the HC^{15}N line is detected in 49 cores (74%).

Both HN^{13}C(1–0) and H^{13}CN(1–0) present hyperfine structure, but we were able to re-

---

[1] The GILDAS software is available at http://www.iram.fr/IRAMFR/GILDAS
[2] Madrid Data Cube Analysis on ImageJ is a software developed in the Center of Astrobiology (Madrid, INTA-CSIC) to visualize and analyze single spectra and datacubes (Martín et al. 2019).
[3] http://spec.jpl.nasa.gov/
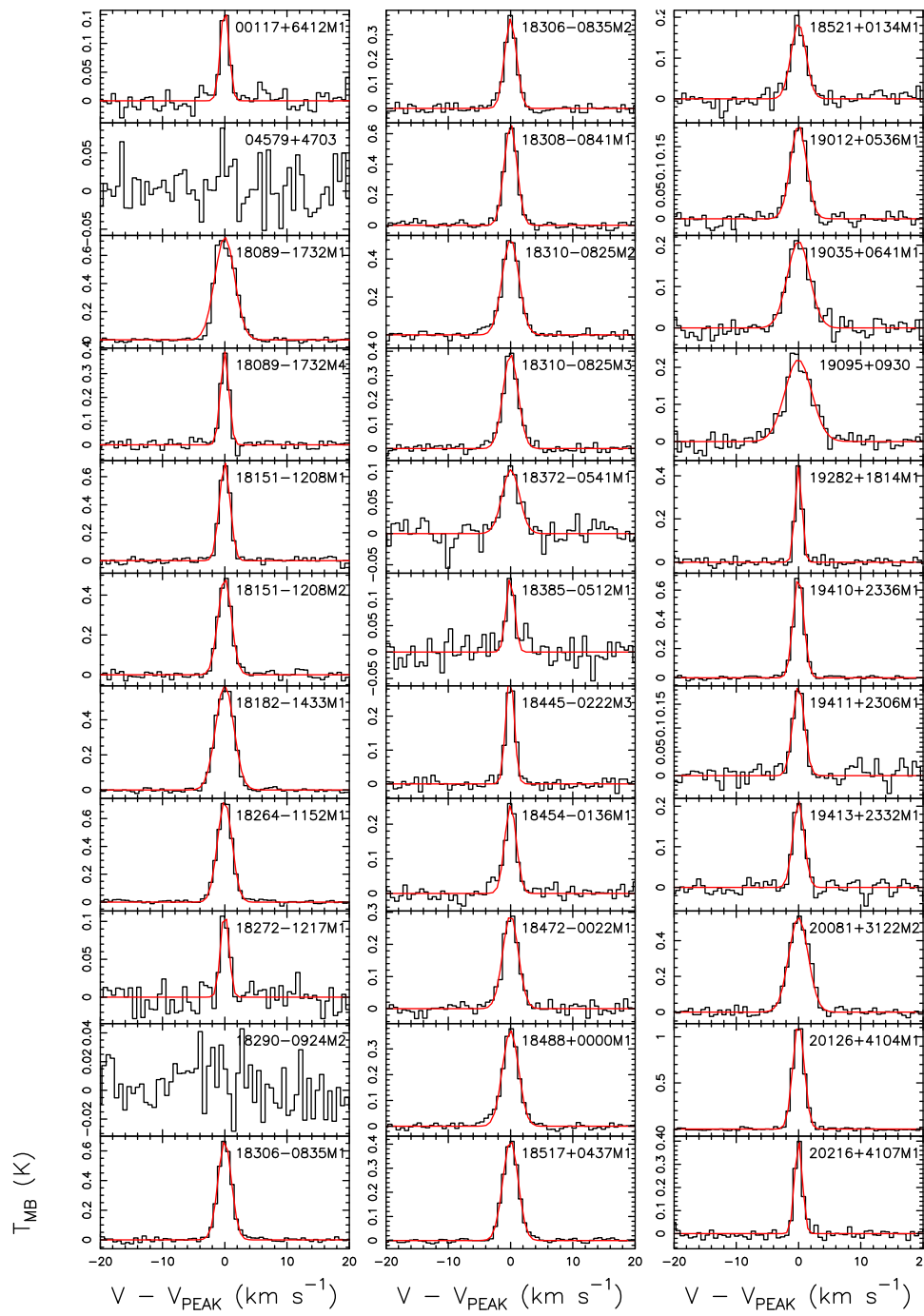
Fig. 3.2: Spectra of HN^{13}C(1–0) obtained for the sources. For each spectrum the x-axis represents a velocity interval of ± 20 km s^{-1} around the velocity listed in the second column of Table 3.3. The y-axis shows the intensity in main beam temperature. The red curves are the best Gaussian fits obtained with MADCUBA.
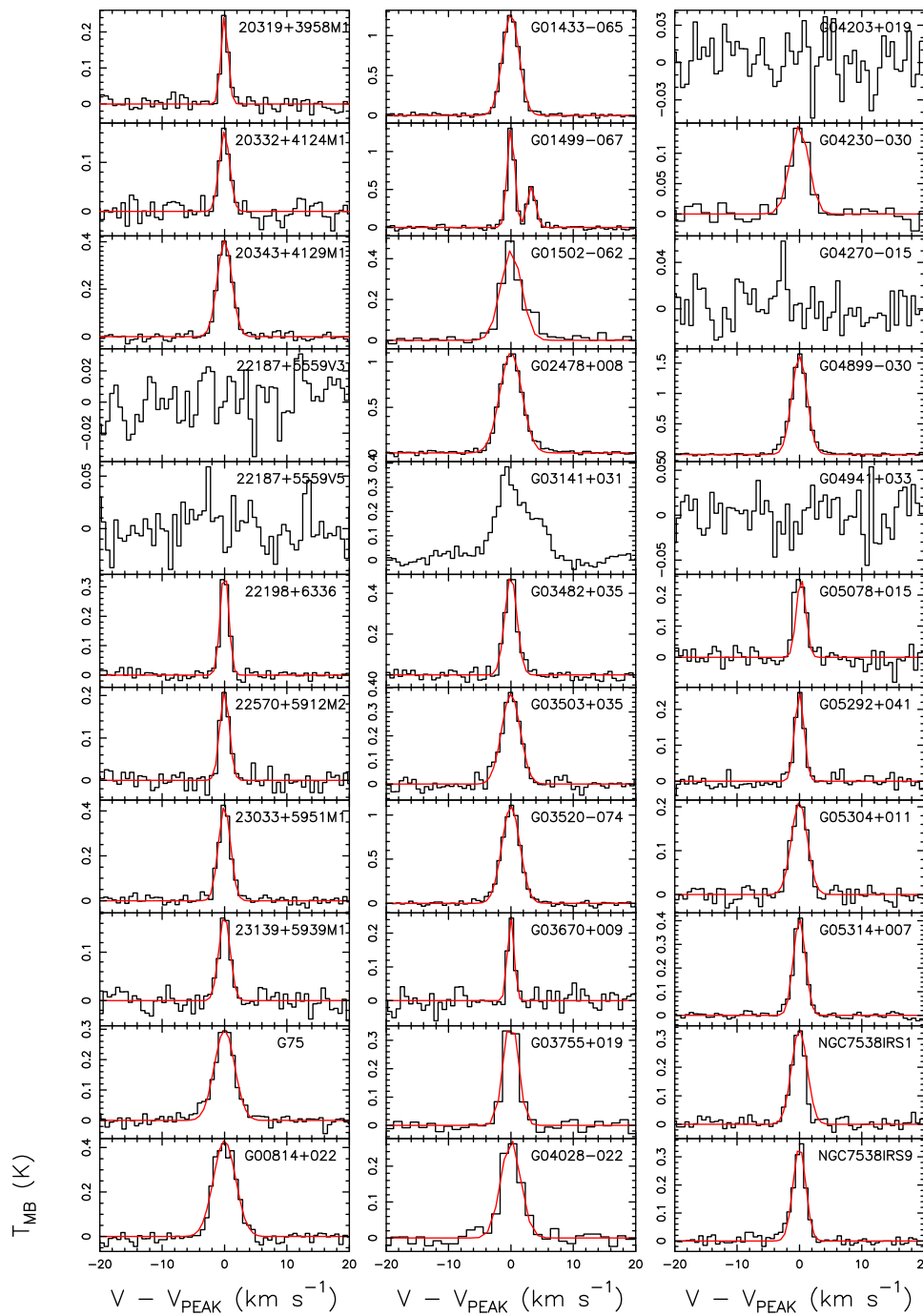
Fig. 3.3: Fig. 3.2 continued. Note that for the source G01499-067 we have observed two velocity components: we have fitted both lines and we have used both separately to compute the column densities.
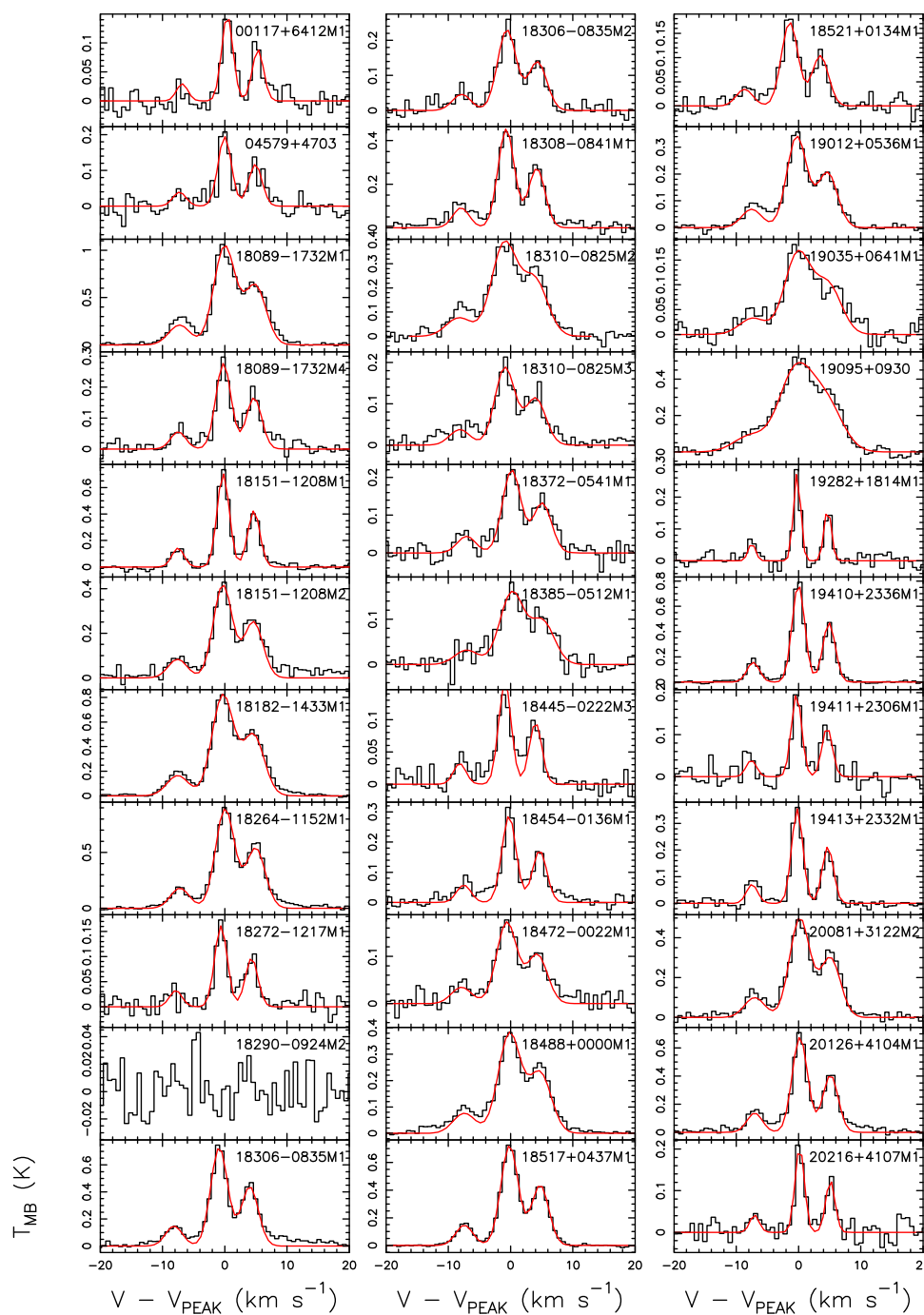
Fig. 3.4: Spectra of H^{13}CN(1–0) obtained for the sources. For each spectrum the x-axis represents a velocity interval of ± 20 km s^{-1} around the velocity listed in the second column of Table 3.5. The y-axis shows the intensity in main beam temperature. The red curves are the best Gaussian fits obtained with MADCUBA.
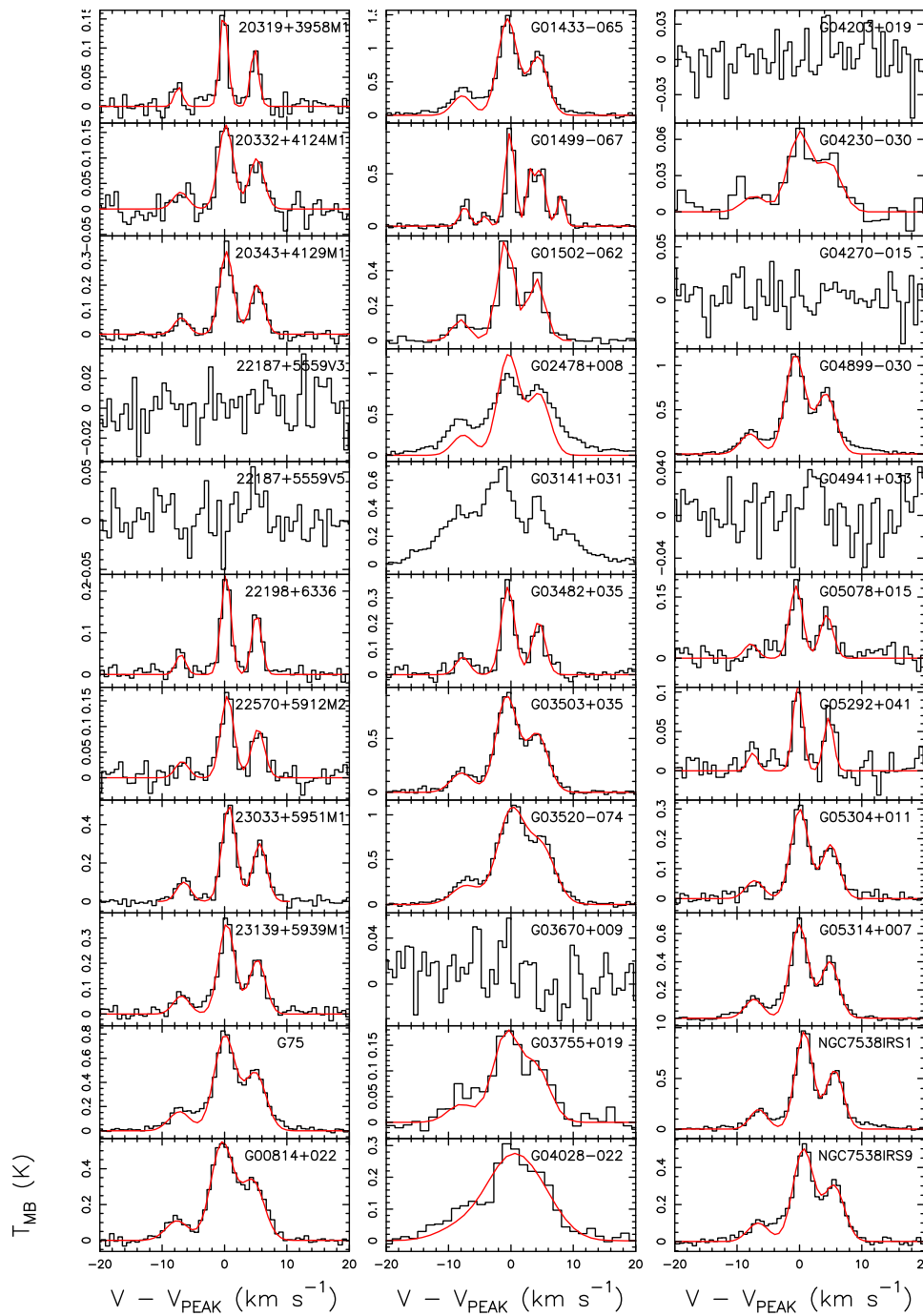
Fig. 3.5: Fig. 3.4 continued. Note that for the source G01499-067 we have observed two velocity components: we have fitted both lines and we have used both separately to compute the column densities.
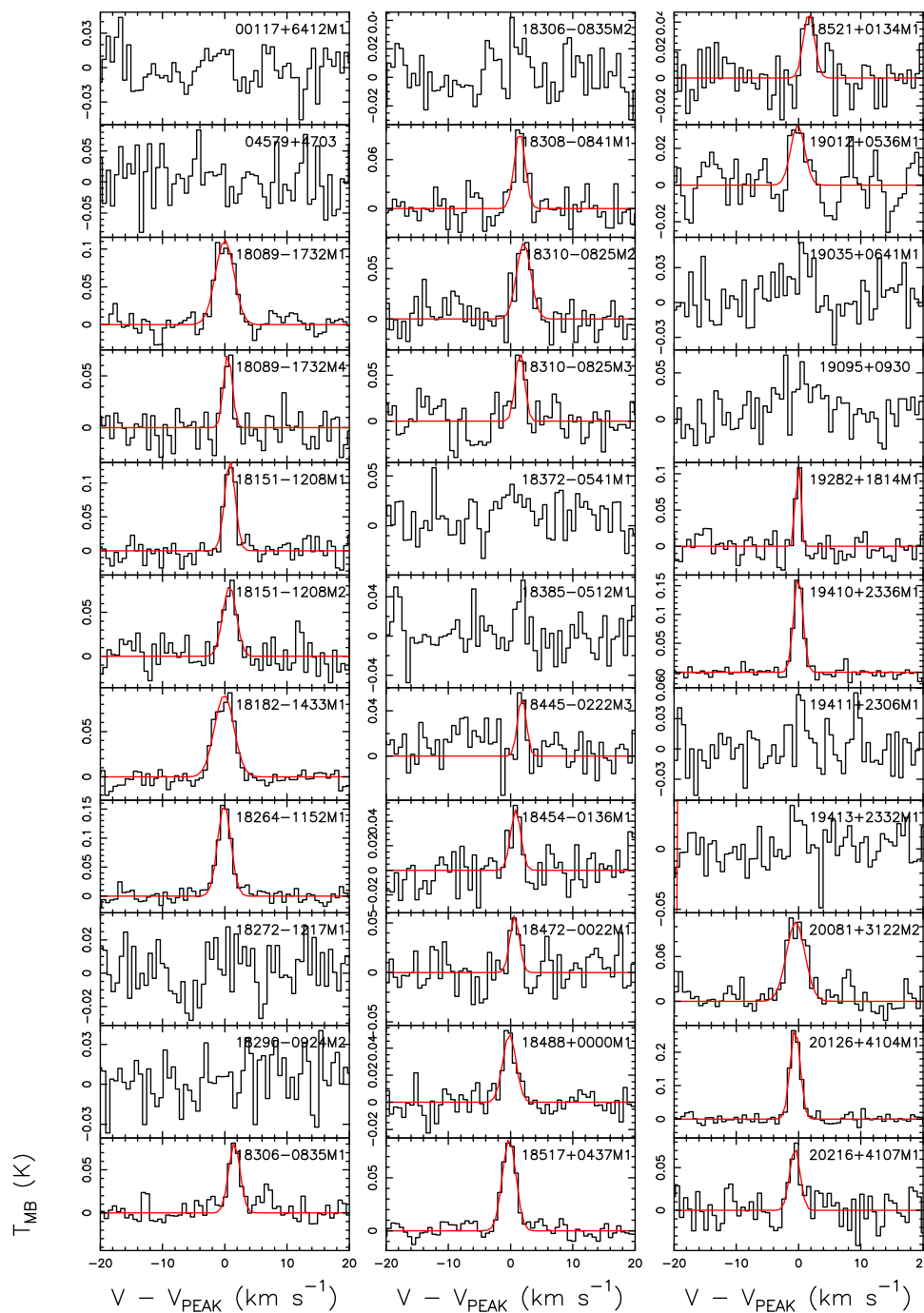
Fig. 3.6: Spectra of $H^{15}NC(1-0)$ obtained for the sources. For each spectrum the x-axis represents a velocity interval of ± 20 km s^{-1} around the velocity listed in the second column of Table 3.4. The y-axis shows the intensity in main beam temperature. The red curves are the best Gaussian fits obtained with MADCUBA.
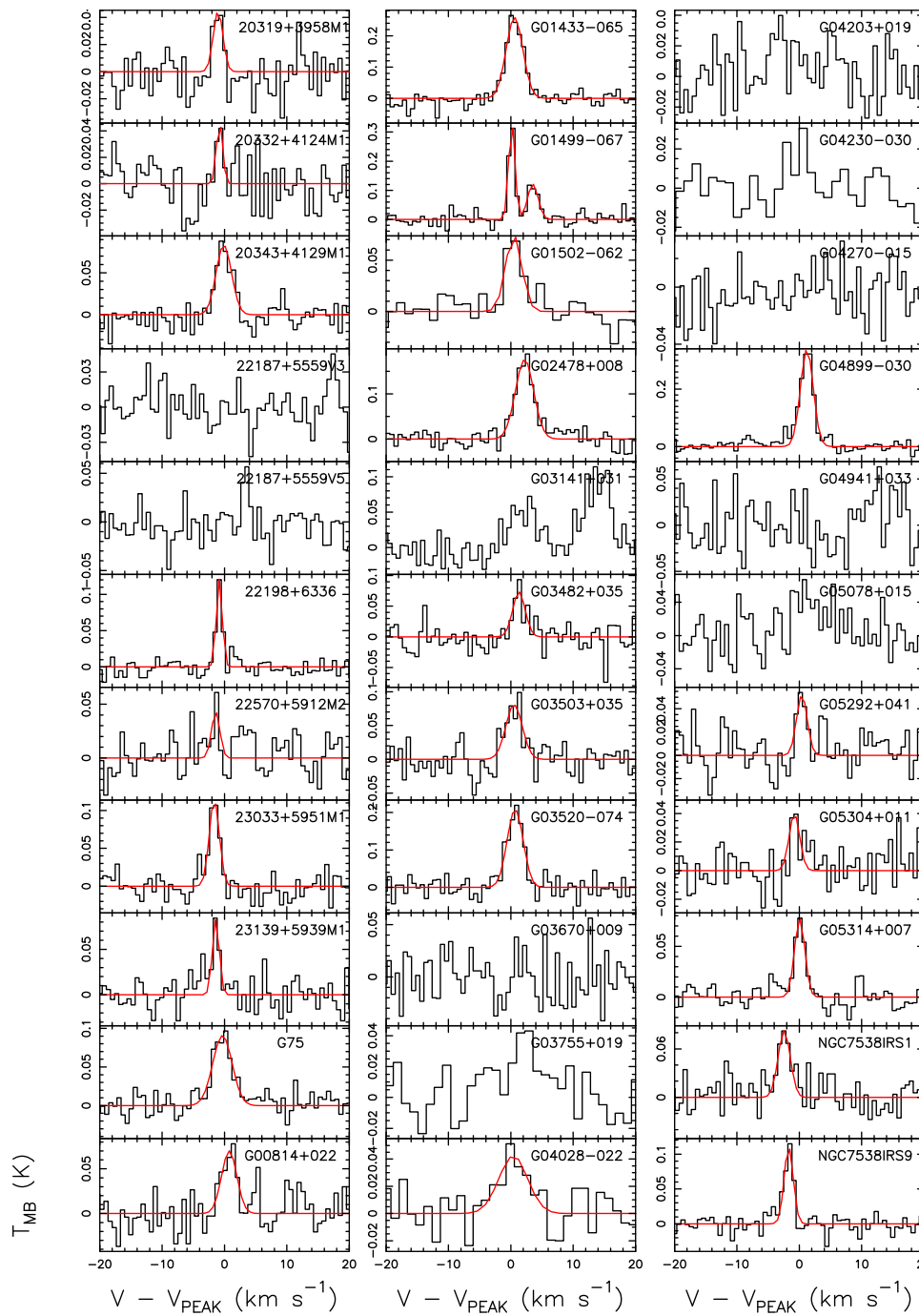
Fig. 3.7: Fig. 3.6 continued. Note that for the source G01499-067 we have observed two velocity components: we have fitted both lines and we have used both separately to compute the column densities.
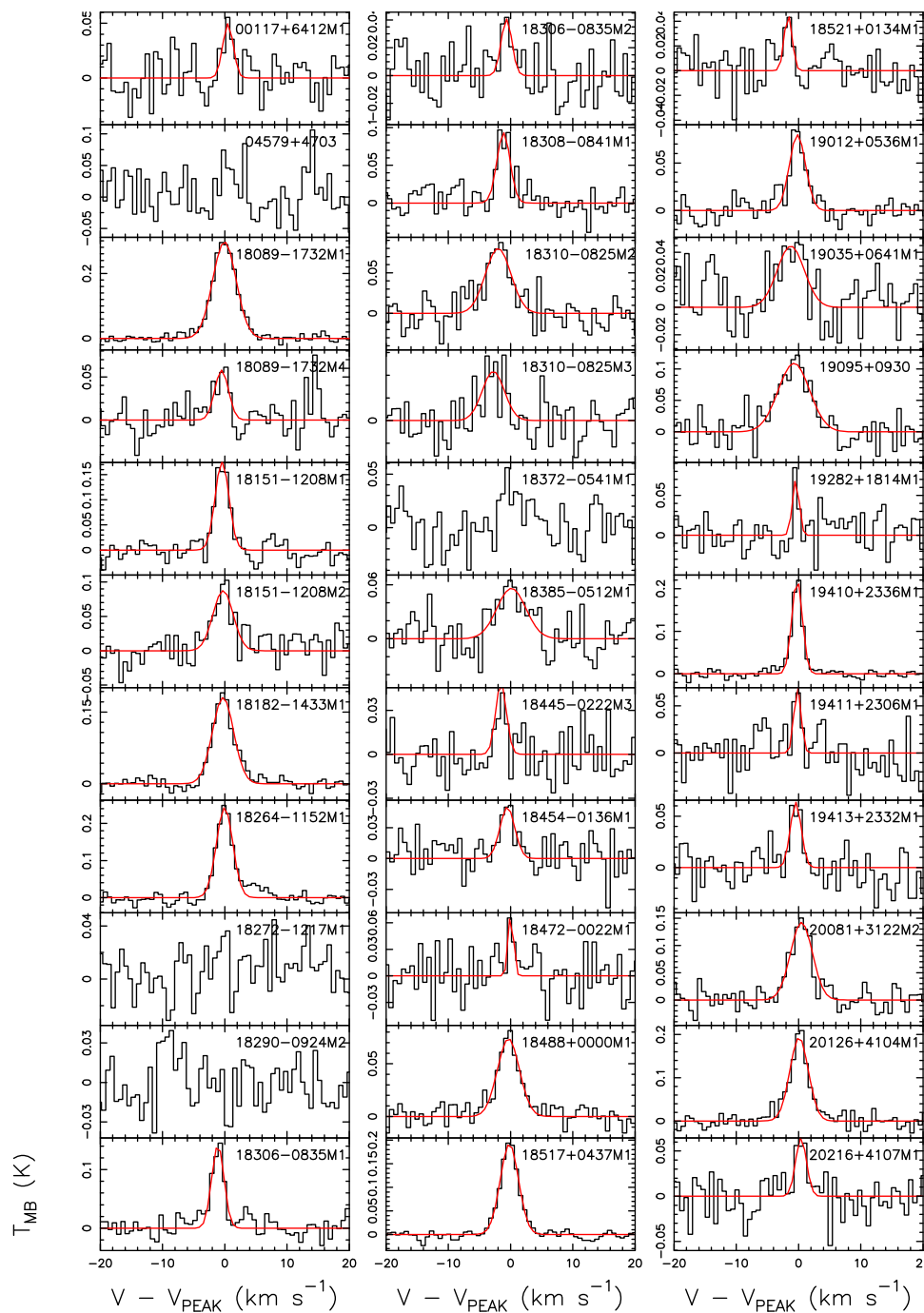
Fig. 3.8: Spectra of HC^{15}N(1–0) obtained for the sources. For each spectrum the x-axis represents a velocity interval of ±20 km s^{-1} around the velocity listed in the second column of Table 3.6. The y-axis shows the intensity in main beam temperature. The red curves are the best Gaussian fits obtained with MADCUBA.
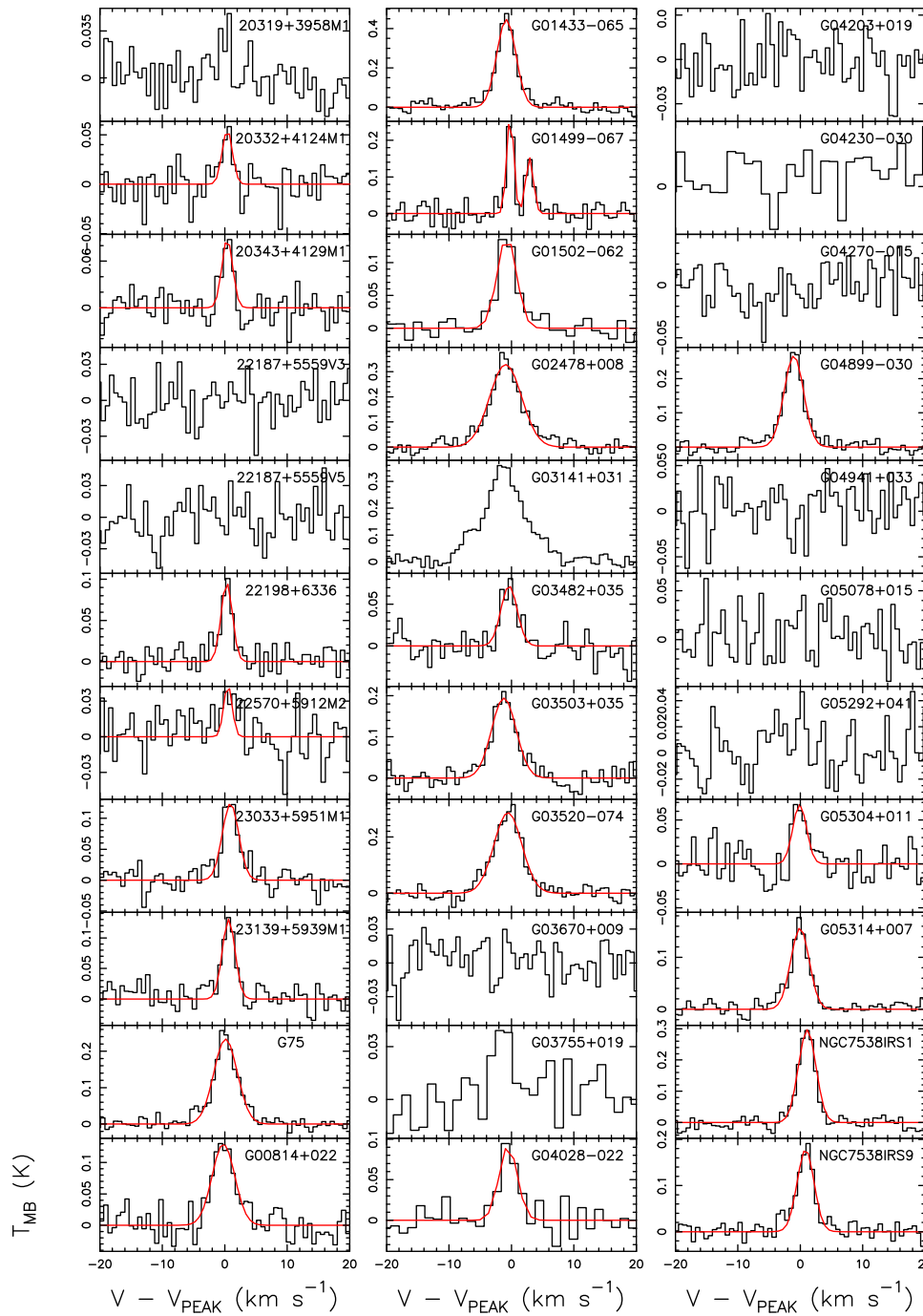
Fig. 3.9: Fig. 3.8 continued. Note that for the source G01499-067 we have observed two components: we have fitted both lines and we have used both to compute the column densities.

Table 3.2: Line rest frequencies and observational parameters. F is the quantum number associated with the sum between the total angular momentum $|J|$ and the ^{14}N nuclear angular momentum.

Line	Hyperfine Component	Frequency (GHz)	$\log_{10}(A_{ij}*)$	E_U** (K)
H^{13}CN(1–0)	F= 1–1	86.3387[1]	-4.62444***	4.1
	F= 2–1	86.3402[1]		
	F=0–1	86.3423[1]		
HN^{13}C(1–0)		87.0908[2]	-4.72878	4.2
HC^{15}N(1–0)		86.0549[3]	-4.62943	4.1
H^{15}NC(1–0)		88.8657[4]	-4.70235	4.3

*Einstein coefficient of the transition;
**Energy of the upper level;
***It refers to the whole transition;
[1] Cazzoli and Puzzarini (2005b);
[2] van der Tak et al. (2009);
[3] Cazzoli et al. (2005a);
[4] Pearson et al. (1976).

solve it only for H^{13}CN(1–0) because the line widths found (~3 km s^{-1}) are smaller than the separations in velocity of the hyperfine components (see Figs. 3.2, 3.3, 3.4, and 3.5, and Tables 2.3 and 2.4). Conversely, H^{15}NC(1–0) and HC^{15}N(1–0) do not have hyperfine structure. All the lines were fitted with single Gaussians, except in the case of H^{13}CN(1–0) for which we take into account the hyperfine structure, using the same T_{ex} and $\Delta v_{1/2}$ for each transition. Fitting the HN^{13}C(1–0) with a single Gaussian can overestimate the line width. To estimates how much the line widths are overestimated by this simplified approach, when possible, we fitted a line both with one Gaussian and considering the hyperfine structure. We found that with a single Gaussian, the line width is about 10% broader than with the hyperfine structure method.

One of the sources, G31.41+0.31, requires some comments: it is a prototypical hot molecular core (HMC) which harbours deeply embedded young stellar objects (YSOs), and the HMC is separated by ~5″ from an ultra-compact HII region (UC HII). Observations with the IRAM Plateau de Bure demonstrated the existence of a velocity gradient across the core (Beltrán et al. 2004 and Beltrán et al. 2005). Subsequently, observations with the Submillimeter Array confirmed the velocity gradient (Cesaroni et al. 2011), supporting the claim of the presence of a rotating toroid. Moreover, observations of ^{12}CO and ^{13}CO revealed self-absorption caused by infalling gas close to the HMC (Cesaroni et al. 2011). Therefore, G31.41+0.31 is a very complicated source and, as can be noted for example from the spectra in Fig. 3.2, there is an evidence of possible self-absorption at the center of the lines (for H^{13}CN and HN^{13}C in particular) and a distorted line profile due to the possible presence of the rotating toroid at larger scales, together with the possibility of outflows from the center of the HMC (Cesaroni et al. 2017, Beltrán et al. 2018). For these reasons we were not able to fit the lines neither with a single Gaussian nor with the three hyperfine components, because of the complex line shape. All of this makes it very difficult to fit the lines with the approximation used for the other sources; therefore, we decided to exclude this

source from the analysis.

For G14.99-0.67, instead, we have identified two velocity components and fitted them simultaneously (G14.99-0.67 and G14.99-2).

All the spectra are shown in Figs. 3.2, 3.3, 3.4, 3.5, 3.6, 3.7, 3.8 and 3.9.

3.3.2. Fitting procedure and column density calculation

To fit the lines and to compute the total column densities from the extracted spectra we have used MADCUBA assuming LTE conditions. The MADCUBA-AUTOFIT tool takes into account four parameters to create a synthetic LTE line profile: total column density (N), excitation temperature (T_{ex}), peak velocity (v), and full width half maximum ($\Delta v_{1/2}$).

As in the work presented in chapter 2, the total column densities of all species have been evaluated without correcting for the beam-filling factor θ_{FF}, since we do not have any measurement of the emitting size of the molecular emission. Therefore, the derived column densities are beam-averaged values. Observations towards low-mass protostars at high-angular resolution with the NOEMA interferometer indicate that the $H^{13}CN$ and $HC^{15}N$(1–0) line emission is indeed very similar (Zapata et al. 2013; Wampfler et al., personal comunication). Therefore, the assumed filling factor should not influence the $^{14}N/^{15}N$ ratio.

Moreover, we have fitted all the lines fixing also the T_{ex}. We have used the excitation temperature derived from the K-ladder of the J=5-4 transition of the CH_3CN molecule, which is a good thermometer of massive dense cores (e.g. Araya et al. 2005; Purcell et al. 2006). The detailed analysis of this species will be presented in a forthcoming paper (Mininni et al., in prep.). The critical densities of the analysed transitions are relatively high ($\sim 3 \times 10^5$ cm^{-3}), thus the observed transitions could be in non-LTE conditions. As shown by Daniel et al. (2016), if the excitation temperatures are lower than the kinetic temperatures, the excitation temperature of the less abundant isotopologue (with ^{15}N) could be different from that of the more abundant one and the isotopic ratio could also be affected. Therefore, we have checked with RADEX[4] how T_{ex} would change in non-LTE conditions and we have found that the T_{ex} are lower compared with those obtained with CH_3CN. However, the T_{ex} of both isotopologues are similar (within $\sim$16%), being that of the more abundant isotopologue always higher. Therefore, the hypothesis that the rotational levels of the two molecules are populated with the same T_{ex} is valid.

Leaving free the other parameters (N, v, and $\Delta v_{1/2}$) the AUTOFIT tool compares the LTE synthetic spectra with the observed spectra and provides the best non-linear least squared fit using the Levenberg-Marquardt algorithm. When the algorithm converges, it provides also the associated errors to the parameters. Note that the total column density N is related to the other parameter from eq. (2.1), in the optically thin case. However, MADCUBA takes into account also the opacity and then that formula has to be multiplied by $\tau/(1-\exp(-\tau))$. From the parameters found by AUTOFIT, the tool calculates also the opacity as an output of the fit. In fact, the line opacity between levels i and j, τ_{ij}, is related to the parameters of the fit with the formula:

$$\tau_{ij} = \frac{h}{\Delta v_{1/2}} N_i B_{ij} (e^{h v_{ij}/K T_{ex}} - 1), \tag{3.1}$$

where B_{ij} is the Einstein B-coefficient, h is the Planck constant, and N_i is the column den-

---

4   http://var.sron.nl/radex/radex.php

sity in the upper level i, which is calculated with the expression:

$$N_i = \frac{N}{Q(T_{ex})} g_i e^{-E_i/KT_{ex}},$$ (3.2)

where Q is the partition function and g_i and E_i are the degeneracy and the energy of the upper level i, respectively.

Column densities, line widths, peak velocities and opacity (τ) derived from the fit are given in Tables 3.3, 3.4, 3.5 and 3.6. It can be seen that all the transitions are optically thin as expected. It should also be noted that the opacities are lower limits of the real opacity of the lines since we assume that the emission of the lines comes from the entire beam. Despite this, we do not expect much higher opacities. To test this, we have assumed a source size of $10''$ and found that the τ values increase at most by a factor 10, so that the values would be ~ 0.01–0.1.

For the non-detections upper limits to the column densities are derived with the SLIM tool. Fitting the baseline of the spectrum, without considering line emission, this tool can estimate the rms of a channel. They have been derived from the formula $3\sigma \times \Delta v/\sqrt{N_{chan}}$, where N_{chan} is the number of channels covered by the line width Δv. The average value of the $\Delta v_{1/2}$ of the observed transitions are: $\Delta v_{HN^{13}C} = 2.6 \pm 0.1$ km s^{-1}, $\Delta v_{H^{13}CN} = 3.3 \pm 0.2$ km s^{-1}, $\Delta v_{H^{15}NC} = 2.3 \pm 0.1$ km s^{-1} and $\Delta v_{HC^{15}N} = 3.1 \pm 0.2$ km s^{-1}.

Table 3.3: Values obtained with the procedure described in Sect. 3.3.2 to the HN^{13}C lines. In the second and in the third columns the centroid velocities and the FWHM are listed. In the fourth column the total column densities derived for the sources are listed, and in the fifth column there are the opacity of the lines. In the sixth column the r.m.s. of observed lines are listed. The cases in which the line is not detected, and therefore only column density upper limits could be obtained as explained in Sect. 3.3.2, are indicated with – .

Source	HN^{13}C(1–0)				
	v_{LSR} (km s^{-1})	$\Delta v_{1/2}$ (km s^{-1})	N_{tot} ($\times 10^{12}$cm^{-2})	τ	σ (mK)
I00117-MM1	-36.03±4	1.6±0.1	1.5± 0.3	0.0051±0.0006	16
I04579-VLA1	–	–	≤1.1	–	27
18089-1732M1	33.02±0.08	3.8±0.01	35 ± 4	0.0087±0.0004	11
18089-1732M4	33.20±0.06	1.58±0.08	3.5 ± 0.5	0.0120±0.0008	14
18151-1208M1	33.31±0.04	2.01±0.05	8 ± 1	0.0211±0.0007	15
18151-1208M2	29.78±0.07	2.51±0.07	8 ± 1	0.0126±0.0005	15
18182-1433M1	59.86±0.06	3.42±0.07	16 ± 2	0.0123±0.0004	9
18264-1152M1	43.68±0.05	2.76±0.05	15 ± 2	0.0156±0.0004	10
18272-1217M1	34.0±0.1	1.6±0.2	1.4± 0.3	0.0023±0.0002	14
18290-0924M2	–	–	≤0.6	–	15
18306-0835M1	78.15±0.05	2.53±0.04	10 ± 1	0.0188±0.0004	11
18306-0835M2	76.7±0.1	2.23±0.08	4.7± 0.6	0.0112±0.0005	15
18308-0841M1	76.78±0.04	2.40±0.05	9 ± 1	0.0204±0.0006	16
18310-0825M2	84.92±0.08	3.15±0.09	9 ± 1	0.0146±0.0006	15
18310-0825M3	85.71±0.09	2.9±0.1	6.0 ± 0.8	0.0127±0.0006	15
18372-0541M1	22.3±0.2	3.3±0.3	3.5± 0.7	0.0015±0.0002	18
18385-0512M1	25.5±0.1	1.6±0.3	1.7± 0.4	0.0031±0.0007	19
18445-0222M3	112.13±0.9	1.75±0.06	1.6 ± 0.2	0.0270±0.0006	13
18454-0136M1	38.7±0.2	2.2±0.2	2.9 ± 0.5	0.0086±0.0008	13

Table 3.3: Continued.

Source	HN^{13}C(1–0)				
	v_{LSR} (km s^{-1})	$\Delta v_{1/2}$ (km s^{-1})	N_{tot} ($\times 10^{12}$cm^{-2})	τ	σ (mK)
18472-0022M1	49.7±0.1	3.0±0.1	4.5 ± 0.6	0.0101±0.0006	15
18488+0000M1	83.39±0.05	3.04±0.08	6.5 ± 0.8	0.0114±0.0004	8
18517+0437M1	44.02±0.03	2.89±0.04	7.8 ± 0.9	0.0110±0.0002	7
18521+0134M1	76.8±0.1	2.8±0.2	3.1 ± 0.5	0.0055±0.0005	13
19012+0536M1	66.3±0.1	3.0±0.1	3.5 ± 0.5	0.0058±0.0003	10
19035+0641M1	32.7±0.1	4.2±0.2	6.6± 0.9	0.0046±0.0003	15
19095+0930	44.5±0.2	5.1±0.2	9± 1	0.0041±0.0003	17
19282+1814M1	23.0±0.1	1.30±0.06	4.0 ± 0.6	0.0111±0.0007	15
19410+2336M1	22.62±0.08	1.98±0.04	7.2 ± 0.9	0.0244±0.0007	8
19411+2306M1	29.5±0.2	2.2±0.1	1.9± 0.3	0.0080±0.0005	18
19413+2332M1	20.7±0.1	2.1±0.1	2.6± 0.4	0.0065±0.0005	13
ON1	11.83±0.06	3.6±0.1	24 ± 3	0.0065±0.0004	15
20126+4104M1	-3.69±0.04	2.15±0.03	26 ± 3	0.0172±0.0004	13
20216+4107M1	-1.68±0.09	1.47±0.08	4.8 ± 0.7	0.0080±0.0006	17
20319+3958M1	8.5±0.1	1.32±0.08	2.8 ± 0.4	0.0045±0.0004	12
20332+4124M1	-2.8±0.2	1.9±0.2	1.6 ± 0.3	0.0061±0.0008	15
20343+4129M1	11.40±0.08	2.76±0.07	9 ± 1	0.0083±0.0003	13
22187+5559V3	–	–	≤0.6	–	15
22187+5559V5	–	–	≤0.7	–	17
22198+6336	-11.1±0.1	1.57±0.07	5.4 ± 0.7	0.0059±0.0004	11
22570+5912M2	-47.74±0.08	1.8±0.1	2.1 ± 0.3	0.0066±0.0007	15
23033+5951M1	-53.12±0.09	2.28±0.09	4.3 ± 0.6	0.019±0.001	14
23139+5939M1	-44.1±0.2	2.1±0.1	2.3 ± 0.4	0.0049±0.0005	15
G75-core	0.3±0.1	3.8±0.1	9 ± 1	0.0056±0.0003	13
G08.14+0.22	19.2±0.1	4.2±0.1	14 ± 2	0.0089±0.0005	18
G14.33-0.65	22.53±0.03	3.12±0.05	30 ± 3	0.0281±0.0006	19
G14.99-0.67	18.71±0.09	1.4±0.3	8 ± 2	0.073±0.019	21
G14.99-2	22.10±0.08	1.60±0.09	3.4 ± 0.5	0.029±0.005	21
G15.02-0.62	19.3±0.2	3.9±0.3	5 ± 0.9	0.042±0.005	20
G24.78+0.08	110.4±0.1	4.14±0.07	62 ± 7	0.0123±0.0003	17
G31.41+0.31	–	–	–	–	21
G34.82+0.35	56.9±0.1	2.3±0.1	6.2 ± 0.9	0.015±0.001	18
G35.03+0.35	53.7±0.1	3.5±0.1	8 ± 1	0.0102±0.0005	18
G35.20-0.74	34.10±0.06	3.42±0.06	29 ± 3	0.0237±0.0006	19
G36.70+0.09	51.9±0.4	1.25±0.07	1.8± 0.3	0.0079±0.0006	20
G37.55+0.19	84.987±0.05	2.7±0.1	7± 1	0.0096±0.0006	20
G40.28-0.22	73.0±0.1	3.7±0.2	7 ± 1	0.0069±0.0006	19
G42.03+0.19	–	–	≤0.7	–	16
G42.30-0.30	27.9±0.2	3.4±0.2	2.8± 0.4	0.0046±0.0004	15
G42.70-0.15	–	–	≤0.7	–	17
G48.99-0.30	67.93±0.04	2.84±0.05	27 ± 3	0.049±0.001	15
G49.41+0.33	–	–	≤1	–	24

Table 3.3: Continued.

Source	HN^{13}C(1–0)				
	v_{LSR} (km s^{-1})	$\Delta v_{1/2}$ (km s^{-1})	N_{tot} ($\times 10^{12}$cm^{-2})	τ	σ (mK)
G50.78+0.15	42.36±0.09	2.2±0.1	3.4± 0.5	0.0080±0.0005	23
G52.92+0.41	45.5±0.1	1.7±0.1	2.4 ± 0.3	0.0078±0.0006	15
G53.04+0.11	4.7±0.2	3.0±0.1	3.3 ± 0.5	0.0073±0.0005	15
G53.14+0.07	21.71±0.08	2.26±0.07	6.0 ± 0.8	0.0106±0.0005	9
NGC7538-IRS1	-57.57±0.05	3.0±0.3	7 ± 1	0.008±0.001	15
NGC7538-IRS9	-57.03±0.08	2.4±0.1	5.0 ± 0.7	0.0094±0.0007	12

[t] tentative detection, as explained in Sect. 3.3.1.

Table 3.4: Same as Table 3.3 for the H^{15}NC(1–0) lines.

Source	H^{15}NC(1–0)				
	v$_{LSR}$ (km s^{-1})	Δv$_{1/2}$ (km s^{-1})	N_{tot} ($\times 10^{12}$cm^{-2})	τ	σ (mK)
I00117-MM1	–	–	≤5.9	–	16
I04579-VLA1	–	–	≤ 10.1	–	28
18089-1732M1	32.3±0.2	3.5±0.3	47 ± 8	0.0010±0.0001	10
18089-1732M4	33.7±0.4	1.6±0.3	6 ± 2	0.0022±0.0006	14
18151-1208M1	33.0±0.3	2.0±0.2	15 ± 3	0.0040±0.0005	15
18151-1208M2	29.4±0.1	2.5±0.4	13 ± 3	0.0021±0.0005	16
18182-1433M1	59.6±0.3	3.7±0.2	25 ± 4	0.0018±0.0002	9
18264-1152M1	43.9±0.1	2.5±0.1	29 ± 4	0.0034±0.0002	10
18272-1217M1	–	–	≤7.1	–	14
18290-0924M2	–	–	≤6.2	–	17
18306-0835M1	78.1±0.3	2.2±0.3	10 ± 2	0.0023±0.0005	12
18306-0835M2		–	≤4.4	–	16
18308-0841M1	76.6±0.2	2.0±0.3	10 ± 2	0.0029±0.0006	16
18310-0825M2	86.3±0.2	2.7±0.4	10 ± 1	0.0022±0.0005	16
18310-0825M3	85.5±0.1	1.7±0.3	7 ± 2	0.0025±0.0007	15
18372-0541M1	–	–	≤1.2	–	18
18385-0512M1	–	–	≤9.1	–	19
18445-0222M3	112.5±0.1	0.98±0.66	2.0 ± 0.9	0.0045±0.0003	14
18454-0136M1	39.4±0.2	1.9±0.5	5 ± 1	0.0017±0.0005	15
18472-0022M1	49.1±0.3	1.8±0.5	5 ± 2	0.0020±0.0008	16
18488+0000M1	84.7±0.6	2.5±0.3	7 ± 1	0.0015±0.0003	8
18517+0437M1	43.9±0.4	2.6±0.1	13 ± 2	0.0023±0.0002	7
18521+0134M1	75.9±0.5	2.1±0.7	5 ± 2	0.0014±0.0006	13
19012+0536M1	66.0±0.5	2.6±0.6	5 ± 1^t	0.0010±0.0003	10
19035+0641M1	–	–	≤7.4	–	15
19095+0930	–	–	≤9.4	–	17
19282+1814M1	22.4±0.3	0.9±0.2	7 ± 2	0.0032±0.0009	16
19410+2336M1	22.8±0.2	1.71±0.07	14 ± 2	0.0059±0.0003	8
19411+2306M1	–	–	≤5.3	–	18
19413+2332M1	–	–	≤5.1	–	14
ON1	11.2±0.1	3.2±0.5	40 ± 9	0.0013±0.0001	15
20126+4104M1	-3.6±0.1	1.89±0.08	51 ± 7	0.0040±0.0002	13
20216+4107M1	-1,4±0.4	2.0±0.4	10 ± 3	0.0014±0.0004	17
20319+3958M1	8.9±0.3	1.8±0.4	7 ± 2	0.0008±0.0003	12
20332+4124M1	-3.2±0.2	1.2±0.5	3 ± 1^t	0.0017±0.0009	16
20343+4129M1	11.0±0.4	2.9±0.04	18 ± 4	0.0017±0.0003	13
22187+5559V3	–	–	≤ 5.6	–	15
22187+5559V5	–	–	≤ 6.7	–	18
22198+6336	-11.4±0.4	1.1±0.1	12 ± 3	0.0020±0.0004	11
22570+5912M2	-48.0±0.3	0.8±0.3	3 ± 1^t	0.0014±0.0005	15
23033+5951M1	-53.2±0.2	1.9±0.2	9 ± 2	0.0050±0.0009	16
23139+5939M1	-45.0±0.4	1.3±0.3	6 ± 2	0.0023±0.0009	15

Table 3.4: Continued.

Source	H^{15}NC(1–0)				
	v_{LSR} (km s^{-1})	$\Delta v_{1/2}$ (km s^{-1})	N_{tot} ($\times 10^{12}$cm^{-2})	τ	σ (mK)
G75-core	0.1±0.4	3.7±0.3	27 ± 5	0.0017±0.0002	13
G08.14+0.22	19.4±0.2	2.8±0.6	15 ± 4	0.0014±0.0004	19
G14.33-0.65	22.72±0.09	3.2±0.1	59 ± 8	0.0057±0.0004	20
G14.99-0.67	18.7±0.1	1.2±0.3	15 ± 4	0.018±0.005	21
G14.99-2	22.4±0.1	2.0±0.2	9 ± 2	0.006±0.001	21
G15.02-0.62	19.7±0.1	3.0±0.4	6 ± 1	0.007±0.001	21
G24.78+0.08	110.1±0.3	3.5±0.2	80 ± 10	0.0020±0.0002	22
G31.41+0.31	–	–	–	–	23
G34.82+0.35	57.1±0.3	2.4±0.6	9 ± 3	0.0023±0.0008	19
G35.03+0.35	52.9±0.3	3.1±0.7	15 ± 4	0.0022±0.0007	19
G35.20-0.74	34.44±0.08	3.0±0.3	46 ± 8	0.0045±0.0006	19
G36.70+0.09	–	–	≤7	–	19
G37.55+0.19	–	–	≤8.6	–	20
G40.28-0.22	74.0±0.3	5±1	10 ± 3	0.0019±0.0006	20
G42.03+0.19	–	–	≤5.7	–	16
G42.30-0.30	–	–	≤5.6	–	16
G42.70-0.15	–	–	≤6	–	17
G48.99-0.30	67.85±0.08	2.4±0.1	46 ± 6	0.0101±0.0007	14
G49.41+0.33	–	–	≤8.4	–	23
G50.78+0.15	–	–	≤8.7	–	24
G52.92+0.41	46.0±0.1	1.7±0.6	5 ± 2	0.0016±0.0003	16
G53.04+0.11	6.0±0.3	2.5	4 ± 1	0.0010±0.0003	15
G53.14+0.07	21.9±0.2	1.9±0.2	9 ± 2	0.0020±0.0003	10
NGC7538-IRS1	-58.4±0.3	2.3±0.8	12 ± 4	0.0021±0.0009	17
NGC7538-IRS9	-56.5±0.2	1.7±0.2	11 ± 2	0.0031±0.0005	12

^{t} tentative detection, as explained in Sect. 3.3.1.

Table 3.5: Same as Table 3.3 for the $H^{13}CN$ lines. Note that in some cases (e.g. 18310-0825M3) for the two isotopologues the fitted line width can be different and this can be explained by a higher r.m.s. in a spectrum than in the other cases. The higher r.m.s. noise worsen the S/N ratio for the ^{15}N-isotopologues which have weaker emission lines with respect to the ^{13}C-isotopologues.

Source	$H^{13}CN(1-0)$				
	v_{LSR} (km s^{-1})	$\Delta v_{1/2}$ (km s^{-1})	N_{tot} ($\times 10^{12}$cm^{-2})	τ^1	σ (mK)
I00117-MM1	-36.2±0.2	2.1± 0.2	2.7 ± 0.4	0.0046±0.0005	15
I04579-VLA1	-16.7±0.2	2.5± 0.2	4.2±0.8	0.0061±0.0008	27
18089-1732M1	32.95±0.07	4.0± 0.1	78 ± 9	0.0125±0.0004	11
18089-1732M4	33.4±0.1	2.9± 0.1	7.0 ± 1.0	0.0085±0.0005	15
18151-1208M1	33.41±0.04	2.30± 0.05	14 ± 2	0.0211±0.0006	15
18151-1208M2	29.79±0.08	3.6± 0.1	14 ± 2	0.0108±0.0006	16
18182-1433M1	59.53±0.07	4.07± 0.07	40 ± 4	0.0169±0.0004	9
18264-1152M1	43.75±0.06	3.58± 0.07	36 ± 4	0.0193±0.0005	9
18272-1217M1	34.2±0.4	2.4± 0.2	4.5±0.7	0.0033±0.0003	15
18290-0924M2	–	–	≤1	–	16
18306-0835M1	78.11±0.06	3.20± 0.09	21 ± 3	0.0206±0.0008	13
18306-0835M2	76.7±0.2	3.5± 0.1	6.9 ± 0.9	0.0070±0.0004	15
18308-0841M1	77.0±0.1	3.1± 0.1	12 ± 2	0.0139±0.0006	16
18310-0825M2	84.5±0.2	4.8± 0.2	17 ± 2	0.0110±0.0005	15
18310-0825M3	85.4±0.3	3.8± 0.1	5.9 ± 0.8	0.0061±0.0004	15
18372-0541M1	23.6±0.2	3.5± 0.2	12±1	0.0032±0.0002	18
18385-0512M1	26.1±0.4	4.5± 0.3	8 ± 1	0.0035±0.0003	19
18445-0222M3	112.0±0.2	3.0± 0.2	1.9 ± 0.3	0.0118±0.0008	14
18454-0136M1	38.7±0.2	2.7± 0.1	2.0 ± 0.5	0.0097±0.0007	13
18472-0022M1	49.8±0.2	3.8± 0.2	5.1 ± 0.7	0.0060±0.0004	16
18488+0000M1	83.0±0.1	4.2± 0.1	14 ± 2	0.0116±0.0004	8
18517+0437M1	43.93±0.05	3.25± 0.02	23 ± 2	0.0194±0.0002	7
18521+0134M1	76.1±0.3	3.1± 0.1	4.8±0.7	0.0051±0.0003	13
19012+0536M1	65.8±0.2	3.76± 0.09	11 ± 1	0.0101±0.0003	9
19035+0641M1	33.1±0.4	5.0± 0.3	9 ± 1	0.0036±0.0003	15
19095+0930	43.9±0.2	6.2± 0.2	35 ± 4	0.0083±0.0003	17
19282+1814M1	23.0±0.1	1.36± 0.07	3.8 ± 0.6	0.0068±0.0005	16
19410+2336M1	22.57±0.04	2.35± 0.05	14 ± 2	0.0274±0.0007	8
19411+2306M1	29.3±0.1	2.0± 0.2	2.6 ± 0.5	0.0083±0.0009	18
19413+2332M1	20.2±0.1	2.12± 0.07	6.5 ± 0.8	0.0109±0.0005	13
ON1	11.9±0.1	3.82± 0.09	35 ± 4	0.0061±0.0002	15
20126+4104M1	-3.63±0.08	2.90± 0.09	31 ± 4	0.0101±0.0004	12
20216+4107M1	-1.7±0.1	1.8± 0.1	4.5 ± 0.7	0.0041±0.0004	17
20319+3958M1	8.20±0.07	1.5± 0.1	3.2±0.5	0.0030±0.0003	12
20332+4124M1	-2.7±0.1	2.8± 0.2	3.4 ± 0.5	0.0062±0.0006	16
20343+4129M1	11.52±0.07	2.59± 0.08	10 ± 1	0.0069±0.0003	13
22187+5559V3	–	–	≤0.6	–	15
22187+5559V5	–	–	≤0.8	–	18
22198+6336	-11.3±0.2	1.84± 0.08	6.3 ± 0.9	0.0040±0.0002	11

Table 3.5: Continued.

Source	$H^{13}CN(1-0)$				
	v_{LSR}	$\Delta v_{1/2}$	N_{tot}	τ^1	σ
	(km s^{-1})	(km s^{-1})	($\times 10^{12}$cm^{-2})		(mK)
22570+5912M2	-48.0±0.3	2.5± 0.2	3.3 ± 0.5	0.0050±0.0005	15
23033+5951M1	-53.16±0.05	2.65± 0.06	9 ± 1	0.0222±0.0007	15
23139+5939M1	-44.51±0.08	3.0± 0.1	10 ± 1	0.0100±0.0005	15
G75-core	0.1±0.08	3.99± 0.09	40 ± 5	0.0150±0.0005	13
G08.14+0.22	19.07±0.06	4.26± 0.07	27 ± 3	0.0112±0.0003	19
G14.33-0.65	22.41±0.07	3.6± 0.1	59 ± 7	0.0318±0.0012	19
G14.99-0.67	18.71±0.04	1.8± 0.2	10 ± 2	0.049±0.008	21
G14.99-2	21.86±0.09	1.4± 0.2	4.0 ± 0.8	0.026±0.004	21
G15.02-0.62	18.91±0.08	3.1± 0.1	8 ± 1	0.055±0.003	19
G24.78+0.08	111.2±0.2	4	100 ± 10	0.0148±0.0008	17
G31.41+0.31	–	–	–	–	19
G34.82+0.35	56.9±0.1	2.5± 0.1	7 ± 1	0.0109±0.0007	18
G35.03+0.35	53.31±0.06	4.04± 0.06	34 ± 4	0.0245±0.0005	17
G35.20-0.74	34.57±0.07	5.1± 0.1	60 ± 7	0.0223±0.0007	18
G36.70+0.09	–	–	≤0.8	–	19
G37.55+0.19	84.2±0.5	5.0± 0.4	8±1	0.0042±0.0004	18
G40.28-0.22	73.5±0.3	8.7± 0.7	18 ± 2	0.0052±0.0005	19
G42.03+0.19	–	–	≤0.7	–	16
G42.30-0.30	27.3±0.3	4.3± 0.4	2.4±0.4	0.0021±0.0003	16
G42.70-0.15	–	–	≤0.7	–	16
G48.99-0.30	67.89±0.07	3.66± 0.08	36 ± 4	0.034±0.001	14
G49.41+0.33	–	–	≤0.9	–	22
G50.78+0.15	42.3±0.2	2.4± 0.2	3.6±0.6	0.0056±0.0007	21
G52.92+0.41	45.9±0.3	1.8± 0.2	1.7±0.3	0.0035±0.0005	15
G53.04+0.11	5.0±0.2	3.30± 0.09	7.8 ± 1	0.0104±0.0004	15
G53.14+0.07	21.59±0.09	3.37± 0.08	22 ± 3	0.0173±0.0006	9
NGC7538-IRS1	-57.47±0.05	3.28± 0.06	32 ± 4	0.0244±0.0006	15
NGC7538-IRS9	-57.4±0.1	3.9± 0.1	18 ± 2	0.0140±0.0005	12

[1] opacity of the main hyperfine component;
[t] tentative detection, as explained in Sect. 3.3.1.

Table 3.6: Same as Table 3.3 for the HC^{15}N(1–0) lines.

Source	HC^{15}N(1–0)				
	v$_{LSR}$ (km s^{-1})	Δv$_{1/2}$ (km s^{-1})	N_{tot} ($\times 10^{12}$cm^{-2})	τ	σ (mK)
I00117-MM1	-36.1±0.4	2.0± 0.7	5 ± 2 ^{t}	0.0015±0.0008	17
I04579-VLA1	–	–	≤11	–	29
18089-1732M1	33.1±0.1	4.4± 0.1	140 ± 20	0.0035±0.0001	12
18089-1732M4	33.7±0.5	2.6± 0.5	7 ± 2	0.0018±0.0005	17
18151-1208M1	33.5±0.1	2.6± 0.2	23 ± 4	0.0052±0.0007	17
18151-1208M2	30.1±0.3	3.8± 0.6	18 ± 4	0.0023±0.0005	17
18182-1433M1	59.8±0.2	4.0± 0.2	48 ± 6	0.0037±0.0002	10
18264-1152M1	43.8±0.1	3.1± 0.2	48 ± 7	0.0052±0.0004	12
18272-1217M1	–	–	≤9.3	–	16
18290-0924M2	–	–	≤7.1	–	18
18306-0835M1	78.1±0.2	2.3± 0.2	17 ± 3	0.0040±0.0006	13
18306-0835M2	77.0±0.1	2.0± 0.8	4 ± 2	0.0012±0.0007	15
18308-0841M1	76.7±0.3	2.5± 0.4	11 ± 3	0.0028±0.0006	17
18310-0825M2	84.2±0.4	4.8± 0.6	19 ± 4	0.0023±0.0004	15
18310-0825M3	85.2±0.1	4± 1	8 ± 3 ^{t}	0.0014±0.0005	16
18372-0541M1	–	–	≤13	–	18
18385-0512M1	23.4±0.2	5± 1	19 ± 5	0.0012±0.0003	19
18445-0222M3	113.6±0.6	1.5± 0.5	1.6 ± 0.6	0.0040±0.0006	16
18454-0136M1	37.9±0.2	2.8± 0.5	6 ± 2	0.0017±0.0005	16
18472-0022M1	48.9±0.9	1.0± 0.5	3 ± 1	0.0030±0.0009	19
18488+0000M1	83.1±0.3	4.1± 0.3	15 ± 2	0.0022±0.0003	9
18517+0437M1	43.1±0.3	3.47± 0.08	35 ± 4	0.0051±0.0002	9
18521+0134M1	–	–	≤6.3	–	15
19012+0536M1	65.6±0.6	3.0± 0.3	12 ± 2	0.0024±0.0004	11
19035+0641M1	31.4±0.3	5± 1	14 ± 4 ^{t}	0.0010±0.0003	15
19095+0930	44.0±0.4	5.9± 0.6	46 ± 8	0.0020±0.003	17
19282+1814M1	24.8±0.2	0.86	4 ± 2	0.0017±0.0005	19
19410+2336M1	22.3±0.2	1.98± 0.08	19 ± 3	0.0077±0.0004	8
19411+2306M1	29.0±0.3	1.3± 0.4	3 ± 1	0.003±0.001	21
19413+2332M1	20.4±0.2	2.0± 0.4	6 ± 2	0.0019±0.0006	15
ON1	11.3±0.3	3.8± 0.3	55 ± 9	0.0017±0.0004	18
20126+4104M1	-3.8±0.4	3.5± 0.2	59 ± 9	0.0028±0.0003	13
20216+4107M1	-2.0±0.2	2.0± 0.6	9 ± 3	0.0013±0.0005	20
20319+3958M1	–	–	≤8.2	–	13
20332+4124M1	-2.±1	1.9± 0.6	4 ± 1	0.0020±0.0008	15
20343+4129M1	11.8±0.2	2.0± 0.3	12 ± 3	0.0018±0.0004	13
22187+5559V3	–	–	≤6.3	–	16
22187+5559V5	–	–	≤7.2	–	18
22198+6336	-11.6±0.2	2.1± 0.3	16 ± 3	0.0016±0.0003	12
22570+5912M2	-48.1±0.3	0.85	2.0 ± 0.9 ^{t}	0.0014±0.0004	15
23033+5951M1	-53.4±0.5	3.1± 0.3	14 ± 3	0.0055±0.0008	16
23139+5939M1	-44.1±0.3	2.4± 0.2	116 ± 3	0.0037±0.0005	15

Table 3.6: Continued.

Source	HC^{15}N(1–0)				
	v$_{LSR}$ (km s^{-1})	Δv$_{1/2}$ (km s^{-1})	N_{tot} ($\times 10^{12}$cm^{-2})	τ	σ (mK)
G75-core	-0.05±0.3	4.4± 0.2	72 ± 10	0.0044±0.0003	14
G08.14+0.22	19.4±0.4	4.3± 0.4	36 ± 7	0.0027±0.0004	20
G14.33-0.65	22.17±0.09	3.6± 0.1	100 ± 10	0.0098±0.0005	19
G14.99-0.67	18.9±0.3	1.3± 0.4	11 ± 4	0.014±0.006	21
G14.99-2	22.10±0.07	1.5± 0.2	7 ± 2	0 0.008±0.002	21
G15.02-0.62	18.9±0.3	3.6± 0.3	12 ± 2	0.013±0.001	20
G24.78+0.08	110.9±0.2	6.0± 0.2	220 ± 30	0.0037±0.0002	20
G31.41+0.31	–	–	–	–	19
G34.82+0.35	56.3±0.3	3.1± 0.5	10 ± 2	0.0023±0.0005	19
G35.03+0.35	52.8±0.2	4.6± 0.3	47 ± 7	0.0053±0.0004	19
G35.20-0.74	34.2±0.2	5.2± 0.2	90 ± 10	0.0061±0.0004	20
G36.70+0.09	–	–	≤7.8	–	20
G37.55+0.19	–	–	≤9.5	–	19
G40.28-0.22	73.6±0.4	3.4± 0.7	18 ± 5	0.0023±0.0006	20
G42.03+0.19	–	–	≤6.5	–	16
G42.30-0.30	–	–	≤6.8	–	17
G42.70-0.15	–	–	≤7	–	18
G48.99-0.30	67.67±0.09	3.7± 0.1	48 ± 6	0.0079±0.0005	14
G49.41+0.33	–	–	≤9.4	–	24
G50.78+0.15	–	–	≤9.3	–	23
G52.92+0.41	–	–	≤7	–	18
G53.04+0.11	4.9±0.2	2.6± 0.5	8 ± 2	0.0023±0.0006	19
G53.14+0.07	22.0±0.1	3.5± 0.2	29 ± 4	0.0040±0.0003	11
NGC7538-IRS1	-57.54±0.07	3.3± 0.2	55 ± 9	0.0075±0.0008	16
NGC7538-IRS9	-57.4±0.3	3.2± 0.2	29 ± 5	0.0050±0.0005	12

^{t} tentative detection, as explained in Sect. 3.3.1.

Table 3.7: Total column densities of observed transitions, and ^{14}N/^{15}N ratios. In Cols. 2, 3, 4 and 5 are listed the total column densities (beam-averaged), computed as explained in Sect. 3.3.3, of HN^{13}C, H^{15}NC, H^{13}CN and HC^{15}N. In Col. 6 and 7 the ^{14}N/^{15}N ratios for HNC and HCN are listed. In Col. 8 the ^{12}C/^{13}C ratios, used to compute the ratio, are listed.

Source	N(HN^{13}C) ($\times10^{12}$cm^{-2})	N(H^{15}NC) ($\times10^{11}$cm^{-2})	N(H^{13}CN) ($\times10^{12}$cm^{-2})	N(HC^{15}N) ($\times10^{11}$cm^{-2})	$\frac{HNC}{H^{15}NC}$	$\frac{HCN}{HC^{15}N}$	^{12}C/^{13}C
I00117-MM1	1.5± 0.3	≤5.9	2.7 ± 0.4	5 ± 2 ^{t}	≥174	370 ± 139	68
I04579-VLA1	≤1.1	≤ 10.1	4.2±0.8	≤11	–	≥293	77
18089-1732M1	35 ± 4	47 ± 8	78 ± 9	140 ± 20	311 ± 97	233 ± 68	42
18089-1732M4	3.5 ± 0.5	6 ± 2	7.0 ± 1.0	7 ± 2	244 ± 92	418 ± 151	42
18151-1208M1	8 ± 1	15 ± 3	14 ± 2	23 ± 4	244 ± 74	279 ± 88	46
18151-1208M2	8 ± 1	13 ± 3	14 ± 2	18 ± 4	282 ± 101	356 ± 118	46
18182-1433M1	16 ± 2	25 ± 4	40 ± 4	48 ± 6	241 ± 76	314 ± 99	38
18264-1152M1	15 ± 2	29 ± 4	36 ± 4	48 ± 7	225 ± 66	326 ± 96	43
18272-1217M1	1.4± 0.3	≤7.1	4.5±0.7	≤9.3	≥92	≥225	46
18290-0924M2	≤0.6	≤6.2	≤1	≤7.1	–	–	36
18306-0835M1	10 ± 1	10 ± 2	21 ± 3	17 ± 3	382 ± 131	471 ± 152	38
18306-0835M2	4.7± 0.6	≤4.4	6.9 ± 0.9	4 ± 2	≥408	658 ± 296	38
18308-0841M1	9 ± 1	10 ± 2	12 ± 2	11 ± 3	343 ± 118	416 ± 166	38
18310-0825M2	9 ± 1	10 ± 1	17 ± 2	19 ± 4	334 ± 101	332 ± 117	37
18310-0825M3	6.0 ± 0.8	7 ± 2	5.9 ± 0.8	8 ± 3 ^{t}	318 ± 120	274 ± 155	37
18372-0541M1	3.5± 0.7	≤1.2	12±1	≤13	≥155	≥490	53
18385-0512M1	1.7± 0.4	≤9.1	8 ± 1	19 ± 5	≥97	217 ± 76	52
18445-0222M3	1.6 ± 0.2	2.0 ± 0.9	1.9 ± 0.3	1.6 ± 0.6	321 ± 169	476 ± 236	40
18454-0136M1	2.9 ± 0.5	5 ± 1	2.0 ± 0.5	6 ± 2	287 ± 112	165 ± 65	49
18472-0022M1	4.5 ± 0.6	5 ± 2	5.1 ± 0.7	3 ± 1	430 ± 167	812 ± 406	48
18488+0000M1	6.5 ± 0.8	7 ± 1	14 ± 2	15 ± 2	383 ± 128	385 ± 120	41
18517+0437M1	7.8 ± 0.9	13 ± 2	23 ± 2	35 ± 4	301 ± 85	329 ± 89	50
18521+0134M1	3.1 ± 0.5	5 ± 2	4.8±0.7	≤6.3	267 ± 107	≥328	43
19012+0536M1	3.5 ± 0.5	5 ± 1 ^{t}	11 ± 1	12 ± 2	322 ± 126	422 ± 131	46
19035+0641M1	6.6± 0.9	≤7.4	9 ± 1	14 ± 4 ^{t}	≥476	343 ± 134	53
19095+0930	9± 1	≤9.4	35 ± 4	46 ± 8	≥485	385 ± 117	51
19282+1814M1	4.0 ± 0.6	7 ± 2	3.8 ± 0.6	4 ± 2	324 ± 106	538 ± 226	57
19410+2336M1	7.2 ± 0.9	14 ± 2	14 ± 2	19 ± 3	295 ± 78	423 ± 112	57
19411+2306M1	1.9± 0.3	≤5.3	2.6 ± 0.5	3 ± 1	≥202	487 ± 241	56
19413+2332M1	2.6± 0.4	≤5.1	6.5 ± 0.8	6 ± 2	≥296	628 ± 220	58
ON1	24 ± 3	40 ± 9	35 ± 4	55 ± 9	356 ± 113	378 ± 103	59
20126+4104M1	26 ± 3	51 ± 7	31 ± 4	59 ± 9	313 ± 82	323 ± 87	61
20216+4107M1	4.8 ± 0.7	10 ± 3	4.5 ± 0.7	9 ± 3	296 ± 111	306 ± 122	62
20319+3958M1	2.8 ± 0.4	7 ± 2	3.2±0.5	≤8.2	246 ± 81	≥240	62
20332+4124M1	1.6 ± 0.3	3 ± 1 ^{t}	3.4 ± 0.5	4 ± 1	342 ± 157	545 ± 227	64
20343+4129M1	9 ± 1	18 ± 4	10 ± 1	12 ± 3	309 ± 95	515 ± 179	62
22187+5559V3	≤0.6	≤ 5.6	≤0.6	≤6.3	–	–	69
22187+5559V5	≤0.7	≤ 6.7	≤0.8	≤7.2	–	–	69
22198+6336	5.4 ± 0.7	12 ± 3	6.3 ± 0.9	16 ± 3	287 ± 83	251 ± 79	64
22570+5912M2	2.1 ± 0.3	3 ± 1 ^{t}	3.3 ± 0.5	2.0 ± 0.9 ^{t}	554 ± 250	1305 ± 650	79
23033+5951M1	4.3 ± 0.6	9 ± 2	9 ± 1	14 ± 3	349 ± 104	469 ± 127	73
23139+5939M1	2.3 ± 0.4	6 ± 2	10 ± 1	116 ± 3	301 ± 145	491 ± 130	79
G75-core	9 ± 1	27 ± 5	40 ± 5	72 ± 10	207 ± 59	345 ± 90	62

Table 3.7: Continued.

Source	N(HN^{13}C) ($\times 10^{12}$cm^{-2})	N(H^{15}NC) ($\times 10^{11}$cm^{-2})	N(H^{13}CN) ($\times 10^{12}$cm^{-2})	N(HC^{15}N) ($\times 10^{11}$cm^{-2})	$\frac{HNC}{H^{15}NC}$	$\frac{HCN}{HC^{15}N}$	^{12}C/^{13}C
G08.14+0.22	14 ± 2	15 ± 4	27 ± 3	36 ± 7	395 ± 158	318 ± 102	42
G14.33-0.65	30 ± 3	59 ± 8	59 ± 7	100 ± 10	242 ± 68	280 ± 78	47
G14.99-0.67	8 ± 2	15 ± 4	10 ± 2	11 ± 4	257 ± 105	439 ± 200	48
G14.99-2	3.4 ± 0.5	9 ± 2	4.0 ± 0.8	7 ± 2	184 ± 58	278 ± 94	49
G15.02-0.62	5 ± 0.9	6 ± 1	8 ± 1	12 ± 2	406 ± 141	325 ± 98	49
G24.78+0.08	62 ± 7	80 ± 10	100 ± 10	220 ± 30	197 ± 81	116 ± 47	25
G31.41+0.31	–	–	–	–	–	–	33
G34.82+0.35	6.2 ± 0.9	9 ± 3	7 ± 1	10 ± 2	316 ± 130	322 ± 104	46
G35.03+0.35	8 ± 1	15 ± 4	34 ± 4	47 ± 7	258 ± 100	350 ± 99	48
G35.20-0.74	29 ± 3	46 ± 8	60 ± 7	90 ± 10	330 ± 95	349 ± 94	52
G36.70+0.09	1.8 ± 0.3	≤7	≤0.8	≤7.8	≥118	–	46
G37.55+0.19	7 ± 1	≤8.6	8 ± 1	≤9.5	≥350	≥362	43
G40.28-0.22	7 ± 1	10 ± 3	18 ± 2	18 ± 5	312 ± 124	446 ± 165	45
G42.03+0.19	≤0.7	≤5.7	≤0.7	≤6.5	–	–	55
G42.30-0.30	2.8 ± 0.4	≤5.6	2.4 ± 0.4	≤6.8	≥273	≥193	55
G42.70-0.15	≤0.7	≤6	≤0.7	≤7	–	–	80
G48.99-0.30	27 ± 3	46 ± 6	36 ± 4	48 ± 6	275 ± 79	352 ± 101	47
G49.41+0.33	≤1	≤8.4	≤0.9	≤9.4	–	–	68
G50.78+0.15	3.4 ± 0.5	≤8.7	3.6 ± 0.6	≤9.3	≥201	≥199	51
G52.92+0.41	2.4 ± 0.3	5 ± 2	1.7 ± 0.3	≤7	246 ± 95	≥124	51
G53.04+0.11	3.3 ± 0.5	4 ± 1	7.8 ± 1	8 ± 2	496 ± 196	586 ± 186	60
G53.14+0.07	6.0 ± 0.8	9 ± 2	22 ± 3	29 ± 4	377 ± 115	429 ± 114	56
NGC7538-IRS1	7 ± 1	12 ± 4	32 ± 4	55 ± 9	318 ± 137	317 ± 88	55
NGC7538-IRS9	5.0 ± 0.7	11 ± 2	18 ± 2	29 ± 5	322 ± 93	439 ± 119	71

^{t} tentative detection, as explained in Sect. 3.3.1.

3.3.3. ^{14}N/^{15}N RATIOS

The reason why we have observed H^{13}CN and HN^{13}C (as in Colzi et al. 2018a) is that HNC and HCN are usually optically thick in their lower energy rotational transitions. Hence, we decided to use the ^{13}C-bearing species that have been found to be optically thin in high-mass star-forming cores with similar densities (Colzi et al. 2018a). Then, the ^{14}N/^{15}N ratio was computed from the column density ratio of the two isotopologues and corrected by the ^{12}C/^{13}C Galactic trend given by eq. (2.5). As already discussed in Sect. 2.3.1, Milam et al. (2005) derived the Galactocentric distances of their sources using a Sun Galactocentric distance of 7.9 kpc, different from the one we used of 8.4 kpc (Reid et al. 2014). However, the trend of the ^{12}C/^{13}C ratio remains the same, within the errors, after updating it for the new Sun Galactocentric distance. We have derived the ^{14}N/^{15}N ratios for HNC and HCN, along with uncertainties derived propagating the error on total column densities (Table 3.7). The uncertainties do not include the calibration errors, which cancels out in the ratio because the two lines were obtained in the same spectral setup. In Table 3.7 the ^{14}N/^{15}N ratios are given. Assuming that the emission regions of the four molecules is the same, the θ_{FF} is also the same both in the numerator and in the denominator when deriving the ^{14}N/^{15}N ratios. Thus, the ^{14}N/^{15}N ratios are not affected by the issue of the beam-size.
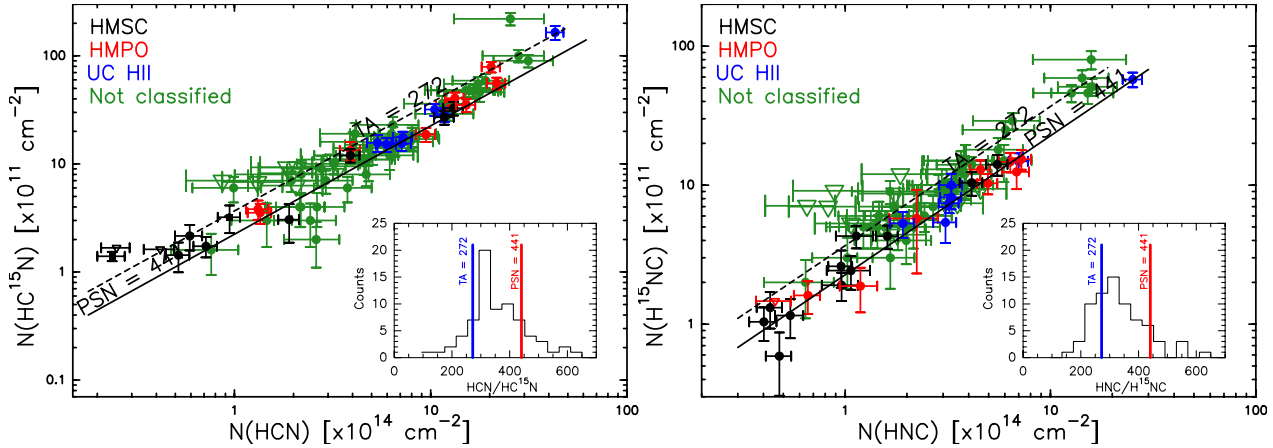
Fig. 3.10: Column densities of HCN against those of HC^{15}N (left panel) and of HNC against those of H^{15}NC (right panel). HCN and HNC column densities are derived from those of H^{13}CN and HN^{13}C, respectively (see Sect. 3.3.3). In both panels the filled circles represent the detected sources and the open triangles are the upper limits for the corresponding column densities. In green the 60 sources of this chapter, in black, red and blue the 27 sources of previous chapter (Colzi et al. 2018a) divided in the three evolutionary stages: high-mass starless cores (HMSCs), high-mass protostellar objects (HMPOs), and ultra-compact HII regions (UC HIIs), respectively. The dashed and solid line indicate the mean atomic composition as measured in the TA and the solid line that measured in the PSN, respectively. In the lower right corner of each panel we show the distribution of ^{14}N/^{15}N values for HCN (left) and HNC (right). The blue and the red vertical lines represent the TA value and the PSN value, respectively.

Furthermore, we have tested how the ratios can change if we use a non-LTE analysis (RADEX), and we have found that the ratios would be, on average, lower by a factor from 1.1 up to 1.6. It is interesting to note that a factor 1.6 lower means ^{14}N/^{15}N ratios of ~250 that are similar to the TA value of 270 and start to approach the pristine Solar system material values (~50–250). However, we stress that a precise non-LTE analysis can not be made because we don't know H$_2$ column densities and kinetic temperatures of all the sources.

As discussed in Sect. 3.2.1, we have implemented these observations with those analysed and described in chapter 2. The observations of this sample were made with the same receiver and spectrometer of this work, giving us the possibility to combine the two samples with consistency. The isotopic ratios ^{14}N/^{15}N of the whole sample are in the range ~115–1305 from HCN, and in the range ~185–780 from HNC, as can be noted in Table 3.7. All of the ratios found in this work are on average consistent with those derived in the previous work (Fig. 3.10). The most direct result of this work, based on an unprecedented statistics, is a firm confirmation of the finding suggested by Colzi et al. (2018a): the lowest values found in pristine Solar System material (e.g. ~50, see Fig. 1.16) are not typical at the scales resolved with these observations (massive dense cores of ~0.4 pc, see also discussion in Sect. 2.6).

In Fig. 3.10, where the column densities of the two samples are shown, at the bottom right of each panel we have made a histogram, with a bin width of 40, that shows the distribution on the ratios. We can note that for both molecules the distribution is asymmetric and centered in the bin $310 \leq ^{14}$N/^{15}N≤ 350, namely below the PSN value (~441) and just above the TA value (~272).

3.4. THE GALACTOCENTRIC BEHAVIOUR

3.4.1. LINEAR ANALYSIS

The merged sample of 87 objects, given by the sources studied in this work and those analysed in chapter 2, are located at different distances from the Galactic Centre (D_{GC}). This allowed us to study the Galactocentric trend of the $^{14}N/^{15}N$ ratio.

Besides our study, one of the most recent works on the $^{14}N/^{15}N$ Galactocentric gradient is that of Adande and Ziurys (2012). These authors evaluated the ratio from rotational lines of CN, HCN, and HNC towards a sample of mixed low- and high-mass star-forming regions observed with different telescopes. In total, their statistics is poorer, as the sample only contains 22 objects. They found an increasing trend of the $^{14}N/^{15}N$ with D_{GC} and with an unweighted linear regression fit to the data set they obtained:

$$^{14}N/^{15}N = (21.1 \pm 5.2) \text{ kpc}^{-1} \times D_{GC} + (123.8 \pm 37.1). \tag{3.3}$$

Even in this case the authors assume a Sun Galactocentric distance of 7.9, but updating the source distances taking into account the updated value (8.4 kpc) the $^{14}N/^{15}N$ Galactocentric trend is the same, within the errors. Our total sample increases the statistics by a factor 4, and we can properly constrain for the first time the $^{14}N/^{15}N$ Galactocentric trend with this robust statistics. We have chosen to separate the results of the two molecules because the distributions presented in Fig. 3.10 suggest a possible difference between the two isomers. We have first computed an unweighted linear regression fit to the data (excluding the lower limits), to compare it to the results of Adande and Ziurys (2012), and found:

$$HCN/HC^{15}N = (21 \pm 9) \text{ kpc}^{-1} \times D_{GC} + (250 \pm 67), \tag{3.4}$$

$$HNC/H^{15}NC = (20 \pm 6) \text{ kpc}^{-1} \times D_{GC} + (221 \pm 42). \tag{3.5}$$

These trends are shown in Fig. 3.11. Both slopes are consistent with that found by Adande and Ziurys (2012) and are also consistent with each other. However, we found a general trend that shows an offset of about 100 toward larger values for the $^{14}N/^{15}N$, as can be noted also in both panels of Fig. 3.11. We have also tried to fit the data with a single power-law relation using the maximum-likelihood Bayesian tool *linmix* by Kelly (2007). This is a Bayesian Linear regression method that derives the linear dependence considering measurement uncertainties, intrinsic scatter in the data, and eventually the lower limits. In our analysis we have excluded the lower limits (Fig. 3.12). The best fits we found are:

$$HCN/HC^{15}N = (17 \pm 6) \text{ kpc}^{-1} \times D_{GC} + (223 \pm 12), \tag{3.6}$$

$$HNC/H^{15}NC = (22 \pm 6) \text{ kpc}^{-1} \times D_{GC} + (198 \pm 12). \tag{3.7}$$

The linear regression fit is consistent with the best Bayesian fit within the uncertainties, as can be seen in Fig. 3.12, mostly for HNC. Note that in the case of the Bayesian analysis the errors are lower than in the linear regression fit because in the standard analysis the errors on the parameters are computed separately, as they are considered independent. On the contrary in the Bayesian analysis an optimised procedure, that takes into account the dependence between the two parameters, is performed and converges to the best parameters with lower errors than in the other analysis.
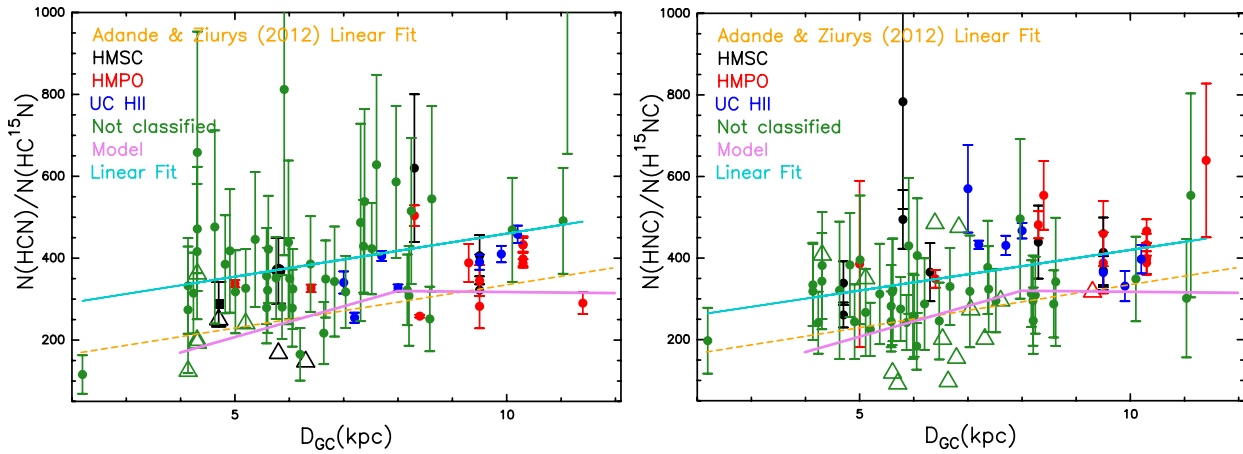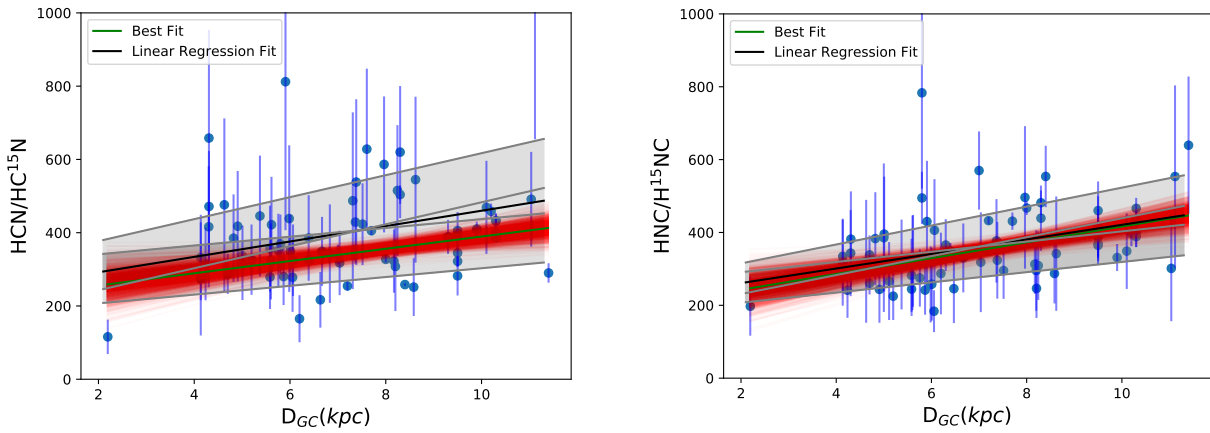
Fig. 3.11: ^{14}N/^{15}N ratios for HCN (left panel) and HNC (right panel) as a function of Galactocentric distances of the sources listed in Table 3.1. Symbols are the same of Fig. 3.10 but the open triangles are lower limits for the corresponding ^{14}N/^{15}N ratio. The cyan solid line is the linear regression fit computed for the two data sets of this work and the pink solid line is the model of Romano et al. (2017). The dashed orange line is the regression linear fit obtained by Adande and Ziurys (2012). Note that we used the scale from 50 to 1000 of y-axes for visualization purposes, and that one source for HCN, with value 1305±650, falls outside.

Fig. 3.12: ^{14}N/^{15}N ratios for HCN (left panel) and HNC (right panel) as a function of Galactocentric distances of the sources. In both panels only the detections (not the upper limits), are represented with blue filled circles. The red solid lines, which form the red area, are all the linear fits found with the Bayesian method, as described in text, and the green solid line is the best fit performed with *linmix*. For comparison we have added with black solid lines the linear regression fits (in grey are represented the errors of this fit), computed as explained in Sect. 3.4.1. Note that we used the scale from 0 to 1000 of y-axes for visualization purposes, and that one source for HCN, with value 1305±650, falls outside.

DEPENDENCE WITH SPATIAL DISTRIBUTION IN THE GALAXY

To investigate a dependence with the Galactic longitude (l, listed in Table 3.1), we have plotted our results in the Galactic plane view of the Milky Way made by Reid et al. (2014). The solid curved lines trace the center of spiral arms as measured with masers associated with young, high-mass stars. We have plotted in the Galactic plane the position of our sources and we have divided the ratio into three intervals: $^{14}N/^{15}N \leq 300$, $300 \leq$ $^{14}N/^{15}N \leq 390$ and $^{14}N/^{15}N \geq 390$ (Fig. 3.13). We have decided to use these ranges because each of them contains a similar number of objects. For both molecules no clear trend along spiral arms was found. We have also checked if there was any residual trend after subtracting from all the $^{14}N/^{15}N$ ratios the values obtained at the corresponding D_{GC} with the Bayesian fit, but we have not found trends either. Thus, we conclude that the Galactocentric gradient, probably, is related only to the source distances and not to other local processes.
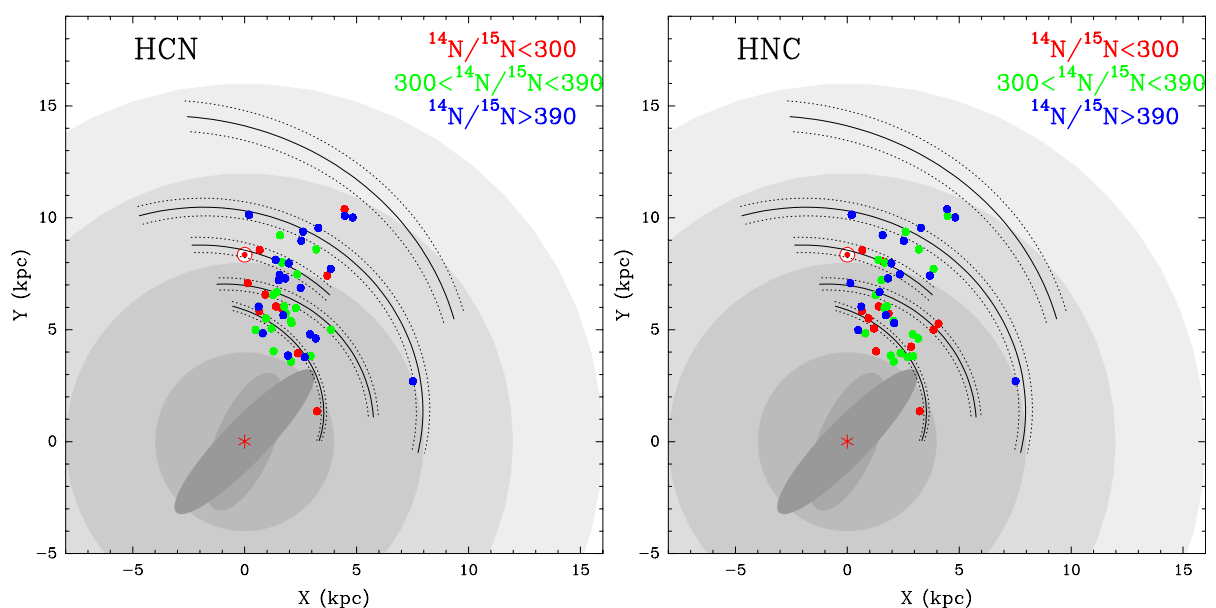
Fig. 3.13: Plan view of the Milky Way. The Galactic center (red asterisk) is at (0,0) and the Sun (red Sun symbol) is at (0,8.34) (Reid et al. 2014). The background grey discs correspond to the Galactic bar region (~4 kpc), the solar circle (~8 kpc), co-rotation of spiral pattern (~12 kpc) and the edge of major star-formation regions (~16 kpc). The solid black lines are the center of spiral arms traced by masers, and the dotted lines the 1σ widths. For more details see Reid et al. (2014). The filled circles represent sources of the new sample described in this chapter implemented with those analysed in chapter 2, and the three colors are the $^{14}N/^{15}N$ ratios measured for HCN (left panel) and HNC (right panel): in red $^{14}N/^{15}N \leq 300$, in green $300 \leq ^{14}N/^{15}N \leq 390$ and in blue $^{14}N/^{15}N \geq 390$.

3.4.2. PARABOLIC ANALYSIS

The linear analysis relies on the $^{12}C/^{13}C$ relation by Milam et al. (2005) (eq. (2.5)), that we have assumed to compute $^{14}N/^{15}N$ ratios. Note that what can be measured directly from our observations are the $H^{13}CN/HC^{15}N$ and $HN^{13}C/H^{15}NC$ ratios. In the upper panels of Fig. 3.14 these ratios have been plotted as a function of the Galactocentric distances, and, since the points suggest a negative linear trend, we have computed unweighted linear re-
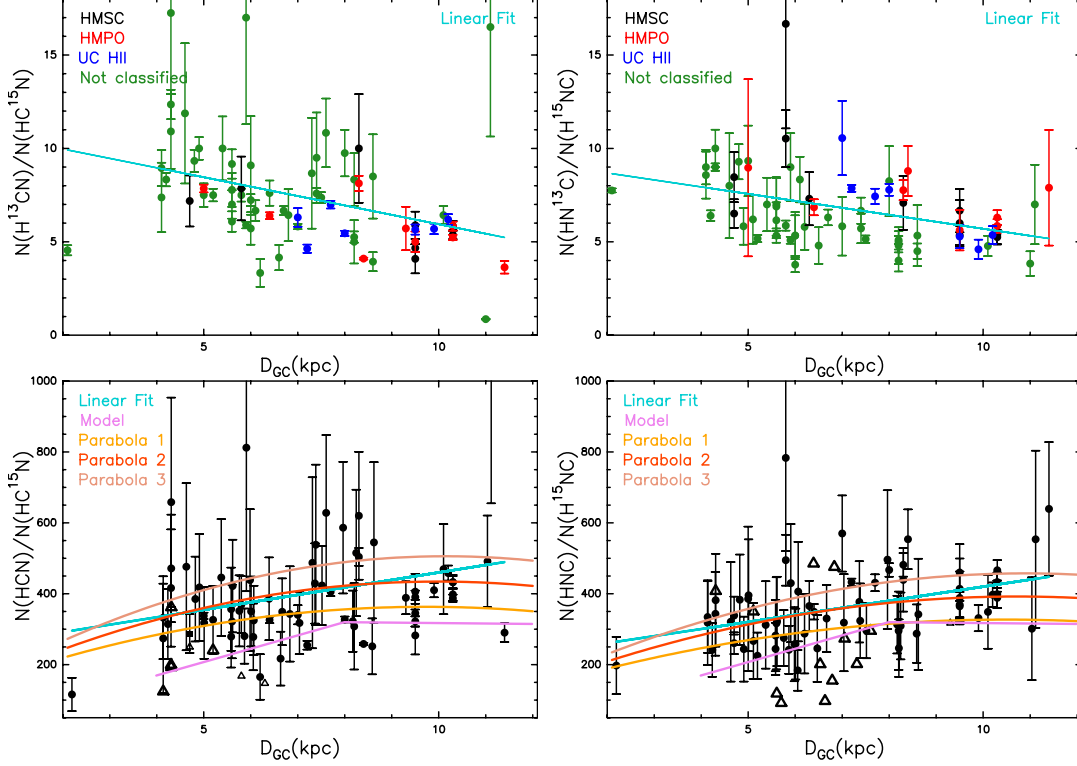
Fig. 3.14: Upper panels: $^{13}C^{14}N/^{12}C^{15}N$ ratios for HCN (left panel) and HNC (right panel) as a function of Galactocentric distances of the sources. Symbols are the same of Fig. 3.11 and the cyan solid line is the linear regression fit computed from the two data sets. Note that the negative slope is the consequence of the two combined ratios, $^{13}C/^{12}C$ and $^{14}N/^{15}N$. Bottom panels: same of Fig. 3.11 with all the sources in black, while the three parabolas are described in Sect. 3.4.2. The yellow one is found using the minimum value in slope of eq. (2.5) (Parabola 1), the red one is found using the central value of the slope (Parabola 2) and the pink one is found using the maximum value of the slope (Parabola 3). Note that we used the scale from 50 to 1000 of y-axes for visualization purposes, and that one source for HCN, with value 1305±650, falls outside.

gression fits to these data, obtaining:

$$H^{13}CN/HC^{15}N = (-0.5 \pm 0.2) \, \text{kpc}^{-1} \times D_{GC} + (11.0 \pm 1.2), \tag{3.8}$$

$$HN^{13}C/H^{15}NC = (-0.4 \pm 0.1) \, \text{kpc}^{-1} \times D_{GC} + (9.4 \pm 0.8). \tag{3.9}$$

We have tested the linearity of these two datasets also using a non-parametric statistics that allows to explore the data sets without assuming an underlying model that describes the data. In particular, we have used the python fit tool *NonParamRegression*. As a result, we have found a linear trend for both the ratios with the Galactocentric distances (Fig. 3.15). In fact, the possible non-linear trend found for HCN from 2 up to 4 kpc is mainly due to the absence of points in between these distances. So this part of the results is biased by the absence of a robust statistics.

   The $^{14}N/^{15}N$ ratios, that have been derived in this work, are the product between $^{14}N^{13}C/^{15}N^{12}C$ and $^{12}C/^{13}C$. Considering that $^{14}N^{13}C/^{15}N^{12}C$ ratios are well fitted by a linear trend, and the assumption that $^{12}C/^{13}C$ is also linear with D_{GC} (Milam et al. 2005), then the derived $^{14}N/^{15}N$ must have a parabolic trend. The parabolas have equations, for HCN

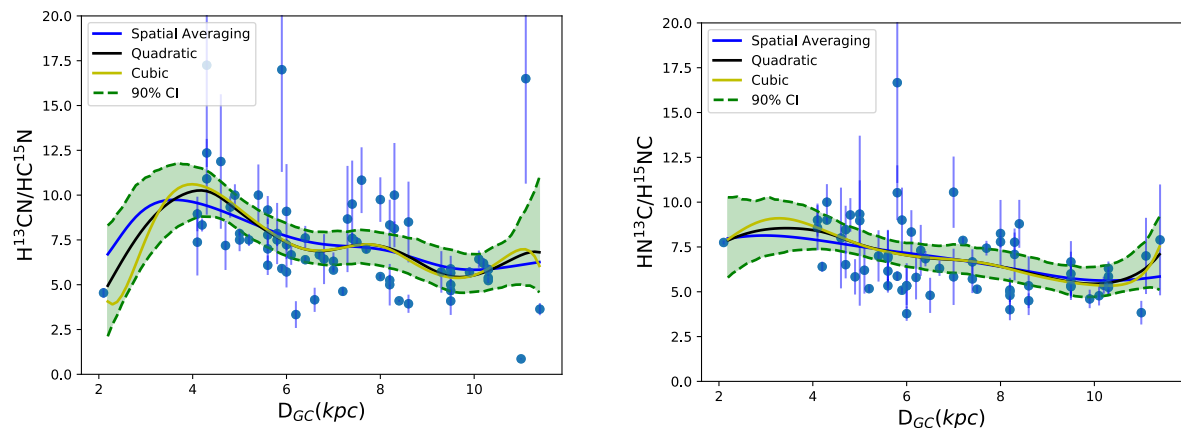Fig. 3.15: $^{13}C^{14}N/^{12}C^{15}N$ ratios for HCN (left panel) and HNC (right panel) as a function of Galactocentric distances of the sources. In both panels the detection are represented with blue filled circles. The blue solid lines represent the spatial averaging of the points. The black solid lines represent the quadratic dependence of the points, and the green area is the 90% confidence interval. The yellow solid lines are the cubic dependence of the data points.

and HNC, respectively:

$$HCN/HC^{15}N = [(-0.5 \pm 0.2) \, kpc^{-1} \times D_{GC} + (11.0 \pm 1.2)] \times [^{12}C/^{13}C], \qquad (3.10)$$

$$HNC/H^{15}NC = [(-0.4 \pm 0.1) \, kpc^{-1} \times D_{GC} + (9.4 \pm 0.8)] \times [^{12}C/^{13}C]. \qquad (3.11)$$

In the bottom panels of Fig. 3.14 the three parabolas obtained choosing the slope of $^{12}C/^{13}C$ as the minimum, the centered and the maximum in the error, are plotted. Interestingly, with this analysis we can reproduce the flattening trend above ~8 kpc predicted by the GCE models of Romano et al. (2017) and Romano et al. (2019). This is the distance where the parabolic trend starts to disagree with the linear trend of the linear analysis. This result remains the same whatever the assumption of the $^{12}C/^{13}C$.

Note that also in this work, as discussed in chapter 2, the $^{14}N/^{15}N$ ratios for HCN and HNC are obtained under the assumption that the angular size of the emission of all isotopologues is the same.

Moreover, also Adande and Ziurys (2012) observed their sample of sources with a single-dish radiotelescope, the 12m Arizona Radio Observatory. In particular, with a beam size of 70″ at 90 GHz they were able to resolve a spatial scale of ~1 pc at a typical distance of the sources of ~3 kpc, i.e. a factor of ~3 larger than that resolved in our work with the IRAM 30m radiotelescope. Thus, with the beam of their observations they encompass the more diffuse gas in the envelope that could contain several MDCs in different evolutionary stages. Since they observe, on average, $^{14}N/^{15}N$ lower than those observed in this work (e.g. Fig. 3.11), this points to an increase of ^{15}N in HCN and HNC at larger spatial scales, where less dense gas is present. We will discuss a possible explanation of this behaviour in the next chapter.

3.5. Discussion and Conclusions

We have observed the rotational transitions J=1–0 of HN^{13}C, H^{15}NC, H^{13}CN and HC^{15}N towards 66 massive star-forming cores to derive the ^{14}N/^{15}N ratios. We have complemented this sample with that observed by Colzi et al. (2018a), obtaining a total sample of 87 sources. The isotopic ratios measured range from 115 up to 1305 for HCN and from 185 up to 780 for HNC, which are higher than the low values in the pristine Solar System material. Updating Fig. 1.26 with the values found by Colzi et al. (2018a) and Colzi et al. (2018b), Fig. 3.16 is found.
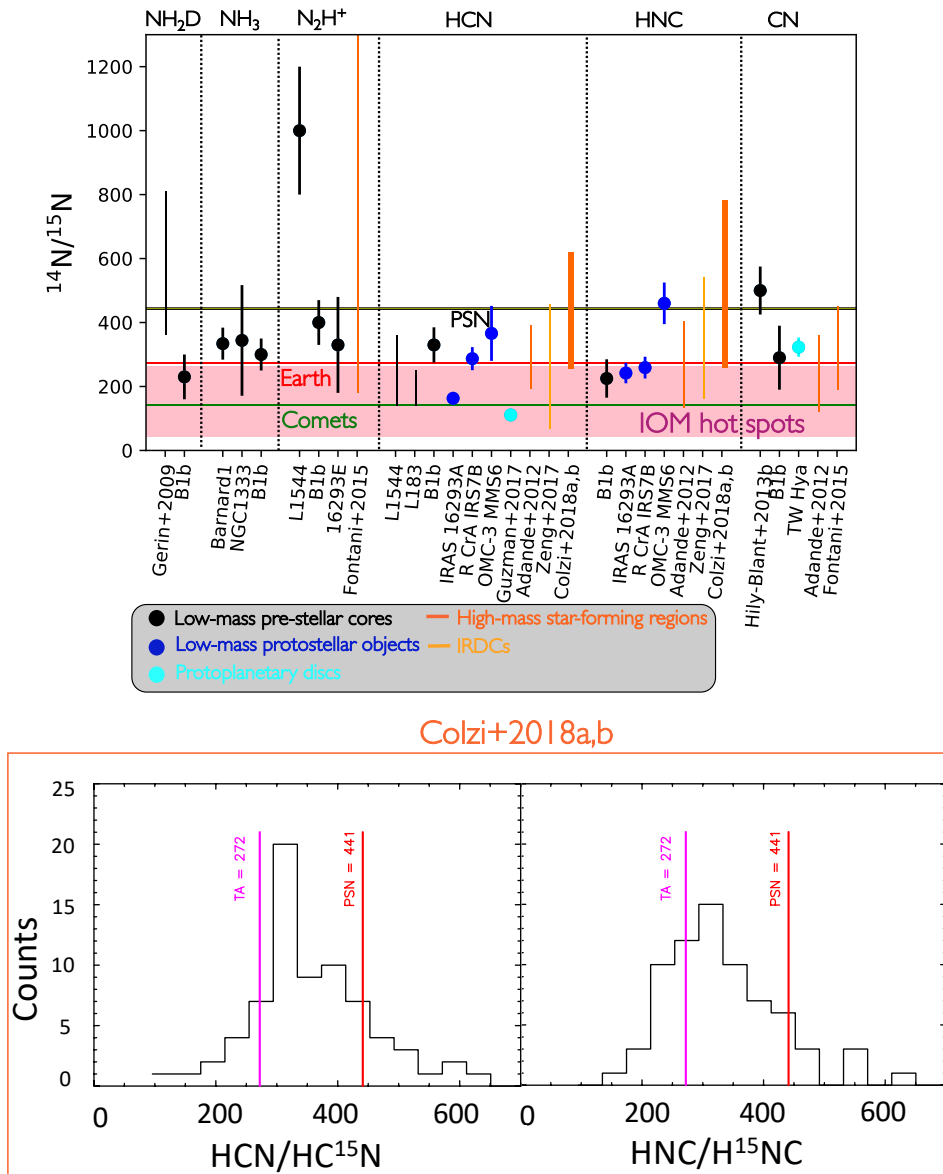

Fig. 3.16: *Upper panel*: Same as Fig. 1.26 updated with values found by Colzi et al. (2018a) and Colzi et al. (2018b). *Lower panels*: the same as in the insets of Fig. 3.10, showing the histogram of the ^{14}N/^{15}N ratios found in the full sample.

With the strong statistics of 87 sources a new Galactocentric trend has been derived.

From the linear fits given in Eq. (3.6) and (3.7), we derive that the $^{14}N/^{15}N$ ratios in the local interstellar medium (ISM), i.e. the values calculated at the Galactocentric distance of the Sun (~8.4 kpc, Reid et al. 2014[5]), are 366±51 for HCN and 383±51 for HNC. More recently, Hunt et al. (2016) evaluated a Sun Galactocentric distance of 7.9±0.3 kpc with combined *Gaia*-DR1/RAVE data of disk stars in the solar neighborhood, and Boehle et al. (2016) derived a distance of 7.86±0.18 analysing stars orbiting Sgr A*. Moreover, Gravity Collaboration et al. (2019) derived a very accurate value of 8.173±0.035. Thus, taking a range of 7.6–8.4 kpc, the local ISM $^{14}N/^{15}N$ is of ~352–366 for HCN and ~365–383 for HNC. These values are all higher than 301±44 which was obtained from the gradient of Adande and Ziurys (2012) at 8.4 kpc. Despite the large uncertainties, our new local interstellar values are more similar to the PSN value of ~441, measured from the Solar wind adopting a different approach (see chapter 1). It has to be noted that a new Sun Galactocentric distance influences also the source Galactocentric distances, since they are evaluated from the formula:

$$D_{GC} = \sqrt{R_\odot^2 + d^2 + 2R_\odot d \cos(l)}, \tag{3.12}$$

where $R_\odot$ is the Sun Galactocetric distance. Thus, a simple scaling factor to the Galactocentric trend could not be sufficient. We tried to evaluate again the distances of the sample from the Galactic center, using the more recent Sun Galactocentric distance of 8.173 kpc. We found that the source distances are very similar and the $^{14}N/^{15}N$ behaviour as a function of D_{GC} (intercepta with the y-axis and slope) is exactly the same for both HCN and HNC.

Let us now discuss briefly our findings in the general context of the origin of ^{14}N and ^{15}N in the Galaxy. As discussed in Sect. 3.1, primary contributors to ^{14}N are massive stars in He-shell burning, while the main contributor of ^{15}N, which is a secondary element, is the hot CNO cycle in novae outbursts. In our Galaxy the abundance of heavy elements is found to decrease with the distance, as observed by Maciel and Costa (2009). Therefore the $^{14}N/^{15}N$ ratio should increase with Galactocentric distance as the main contributors of ^{15}N are novae and some supernovae events (for example, Romano et al. 2017 and Romano et al. 2019). The positive trend found with the Galactocentric distance suggests that there is not a primary component production of ^{15}N, which is instead important for ^{14}N in the environment with a high rate of star formation, like at D_{GC}<8 kpc. The slope of the GCE model of Romano et al. (2017), which takes novae as the main contributors of ^{15}N into account, is in agreement with our observational results (Fig. 3.11), up to 8 kpc. Then, up to 12 kpc the curve in the model flattens. With our linear fit we can not say what is happening after 8 kpc as the linear trend can be biased by points at smaller distances.

A second analysis points out a parabolic trend of $^{14}N/^{15}N$ ratios with the Galactocentric distance. This is based on taking into account the linear assumption made for the $^{12}C/^{13}C$ ratios (eq. (2.5), Milam et al. 2005). With this analysis we were able to reproduce the flattening trend above 8 kpc, as predicted by the GCE models of Romano et al. (2017) and Romano et al. (2019). The flattening of the $^{14}N/^{15}N$ gradient for $D_{GC} > 8$ kpc in the model of Romano et al. (2017) is due to the absence of substantial ^{14}N-enrichment from low-metallicity massive stars (Nomoto et al. 2013). This is also reproduced with the updated low-metallicity massive stellar yields taken into account by Romano et al. (2019).

---

[5] They found a value of 8.34±0.16 kpc from measuremente of trigonometric parallaxes from masers associated with young high-mass stars.
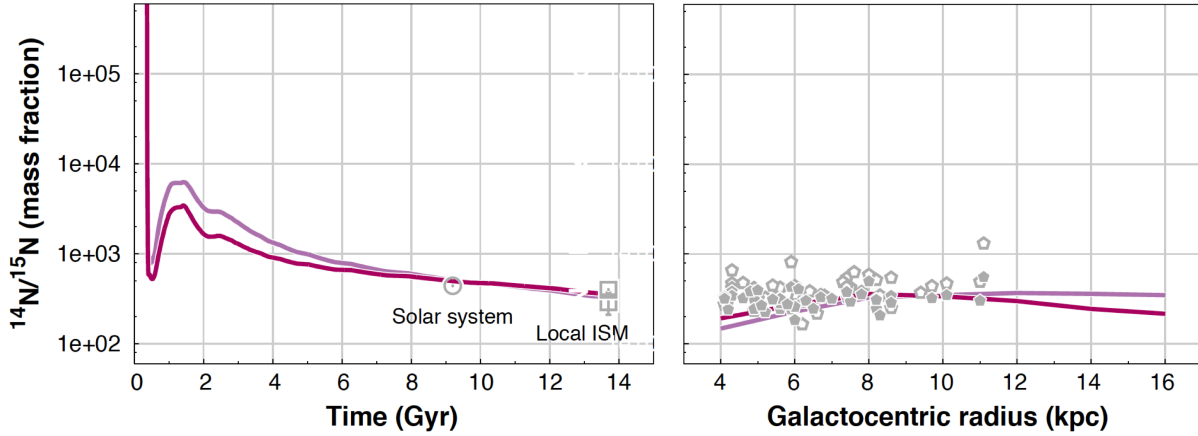
Fig. 3.17: *Left panel*: evolution of the N isotopic ratio in the solar vicinity as a function of cosmic time. The values at the time of the formation of the Solar System, and present local ISM value are labelled. *Right panel*: present-time Galactocentric behaviour of the N isotopic ratio. The bordeaux and lilac solid lines represents the theoretical predictions by Romano et al. (2019) and the grey points represent the results obtained in this work (Colzi et al. 2018b). The two theoretical models differ in the stellar yields of low- and intermediate-mass stars and super-AGB stars. Taken from Romano et al. (2019).

Note that the GCE model result of Romano et al. (2017) is a lower limit of the ^{14}N/^{15}N ratios found (Fig. 3.11 and bottom panels of Fig. 3.14). An interpretation of this result could be that the first N-fractionation is regulated by the nucleosynthesis processes, and afterwards, there could be local (at core level) enrichments of ^{14}N/^{15}N. Another possibility is given by the fact that in Romano et al. (2017) GCE model they assumed an ejected mass (M_{ej}) in the form of ^{15}N for a single novae outburst, to reproduce the observations of Adande and Ziurys (2012). In particular, they assumed $M_{ej}=10^{-7}$ M$_\odot$. Thus, in the new GCE model of Romano et al. (2019) they assumed a lower $M_{ej}=(5\pm6.5)\times10^{-7}$ M$_\odot$ to reproduce the absolute values derived in the work described in this chapter. The results of these new models are shown in Fig. 3.17. As can be noted from the right panel of Fig. 3.17, the absolute values of the GCE model and our observations coincide. This means that the trend with the Galactocentric distance could be explained only by the chemical evolution of the Galaxy and that the spread of values at each distance is due by chemical fractionation effects.

Moreover, as a function of the time, the GCE models of Romano et al. (2017) and Romano et al. (2019) predict a lower trend in the solar vicinity (Fig. 3.18 and left panel of Fig. 3.17) and nowadays predicts a local value lower than the PSN value of 441, in agreement with the new local ISM ^{14}N/^{15}N ratio found in this work of 375±50. As a consequence, chemical models should use as initial ^{14}N/^{15}N a lower value than the 441, as already done by Loison et al. (2019) (red dotted lines of Fig. 1.24).

Of course, to confirm our results, more observations of sources in the outer Galaxy are needed. New observations could place important constraints on the amount of ^{14}N produced by massive stars in low-metallicity environments. The trend we have found in our Milky Way can be relevant also as a "template" for extra-galactic sources, in which the ^{14}N/^{15}N ratio has been measured in a few objects. For example, toward the massive star-forming region N113 in the Large Magellanic Cloud a ^{14}N/^{15}N ratio, for HCN, of 111±17 was found (Chin et al. 1999). Toward the nuclear region of nearby Seyfert 2 galaxy NGC 1068 a ^{14}N/^{15}N ratio greater than 419 was found from HCN and HNC observations (Wang
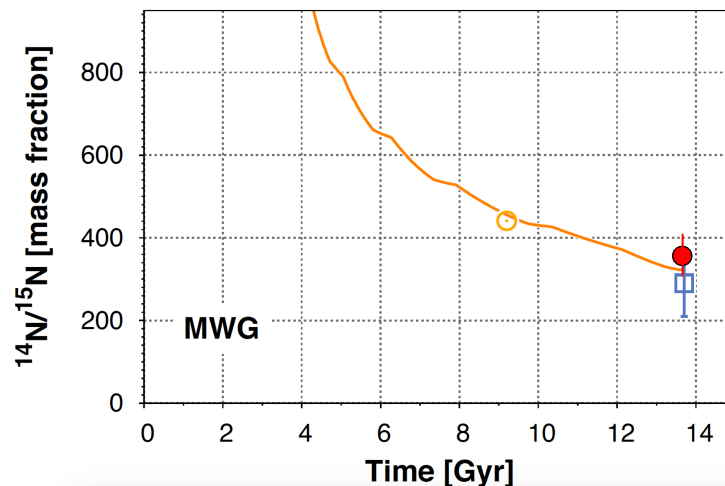
Fig. 3.18: Evolution of the nitrogen isotopic ratio in the solar vicinity predicted by the GCE model of Romano et al. (2017), which includes also novae (orange line). The orange Sun symbol is the PSN ^{14}N/^{15}N ratio, and the blue open square is the old local ISM value derived by Adande and Ziurys (2012). The red circle represents the new local ISM value of 375±50 found in this work. Adapted from Romano et al. (2017).

et al. 2014). Towards the z=0.89 spiral galaxy, located on the line of sight to the quasar PKS1830-211, an average ratio of 152±27 was measured from observation of absorption lines of HCO^{+}, HCN, HNC and SiO(Muller et al. 2011). Moreover, through millimeter molecular absorption lines of HCO^{+}, HCN, CS and H$_2$S, arising in the z=0.68 absorber towards B0218+357, a ratio of ~120 was measured (Wallström et al. 2016). These measurements indicate that even in external galaxies the ^{14}N/^{15}N is far from being homogeneous. However, the estimates of N-fractionation ratio in the dusty interstellar medium of high-redshift starbust galaxies could offer a unique glimpse into the shape of the stellar initial mass function (IMF) in extreme environments that can not be accessed with direct observations (for example from the star counts). We stress, however, that the comparison between local clouds in the Milky Way and external galaxies should be taken with caution. In this kind of sources the relative contribution of the processes responsible for changes in the ^{14}N/^{15}N (nucleosynthesis and/or chemical fractionation), has not been explored. Moreover, it is difficult to determine local trends because the single clouds cannot be resolved easily. From a theoretical point of view, recently, Viti et al. (2019) found with an astrochemical model that the ^{14}N/^{15}N ratio for CN can be different from that of HCN and HNC for $n < 10^5$ cm^{-3} and cosmic-ray ionization rates higher than 1000 times the standard one (5×10^{-17} s^{-1}). So, there is the possibility that chemical fractionation could account for observed differences between different molecular species, also in external galaxies.

As already discussed, most of the observations analysed in this chapter and in chapter 2 are obtained with a single-dish radiotelescope. Given the distance of the sources (~3 kpc on average), the angular size of these observations encompasses a region that could harbour, in principle, gas with different physical properties, such as compact dense cores with higher temperatures than more diffuse regions. The measured D/H and ^{14}N/^{15}N ratios are averaged values under the assumption that the emission size of the molecules is the same. For example, the D/H ratios can be influenced by less dense gas of the envelope in the beam

of single-dish observations, which tends to make them lower. Hence, only high angular resolution observations can disentangle the different contributions and allow to associate the measured D/H and ^{14}N/^{15}N to precise physical parameters. For this reason, in the next chapter we will analyse nitrogen fractionation at high-angular resolution towards one of the sources of the sample described in this work.

<div align="right">

4

</div>

Enhanced nitrogen fractionation at core scales

Abstract

As explained in chapter 1, nitrogen fractionation is used as a tool to search for a link between the chemical history of the Solar system and star-forming regions. A large variation of ^{14}N/^{15}N is observed towards different astrophysical sources, and current chemical models cannot reproduce it. However, all results obtained so far are based on single-dish telescopes which, at the typical distances of massive star-forming regions, can only provide spectra averaged over angular regions that can contain cores or sub-structures with very different physical (and hence chemical) conditions. With the advent of high angular resolution radiotelescopes it is now possible to search for N-fractionation at core scales. In this chapter we present IRAM NOEMA observations of the J=1–0 transition of N_2H^+, ^{15}NNH$^+$ and N^{15}NH$^+$ towards the high-mass protocluster IRAS 05358+3543. We find ^{14}N/^{15}N ratios that span from ~100 up to ~220 and these values are lower or equal than those observed with single-dish observations towards the same source. Since N-fractionation changes across the studied region, this means that it is likely regulated by local environmental effects. We find also the possibility, for one of the four cores defined in the protocluster, to have a more abundant ^{15}NNH$^+$ with respect to N^{15}NH$^+$. This is another indication that current chemical models may be missing chemical reactions or may not take into account other mechanisms, like photodissociation or grain surface chemistry, that could be important.

This work has been published by the peer-reviewed scientific journal *Monthly Notices of the Royal Astronomical Society* in the paper: Colzi et al. (2019).

4.1. Introduction

As already discussed in Sect. 1.4.4, from a theoretical point of view, two possible mechanisms were proposed to explain ^{15}N-fractionation: isotope-exchange reactions, favoured at low temperatures (T<20K, e.g. Roueff et al. 2015, Wirström and Charnley 2018, Loison et al. 2019), or selective photo-dissociation of ^{14}N^{15}N over ^{14}N$_2$ (Heays et al. 2014), that for example is favoured in the external layers of the discs exposed directly to the illumination of

the central (proto-)star. Visser et al. (2018) confirmed that isotope-selective photodissociation could be crucial to understand the N-fractionation in protoplanetary discs, especially those exposed to strong irradiation fields. In particular, for N_2H^+, this is true if the dominant fractionation mechanism are reactions with atomic N.

In the work described in this chapter we will focus on N_2H^+. Summarising what already discussed in chapter 1, Terzieva and Herbst (2000) proposed that the reactions that cause most of ^{15}N-enrichment in N_2H^+ are:

$$N_2H^+ + {}^{15}N \leftrightarrow N^{15}NH^+ + N, \tag{4.1a}$$

$$N_2H^+ + {}^{15}N \leftrightarrow {}^{15}NNH^+ + N. \tag{4.1b}$$

However, the most recent chemical models have challenged this scenario, due to the recent discovery that reactions (4.1a) and (4.1b) do not occur in cold environments due to the presence of an entrance barrier (Roueff et al. 2015; Wirström and Charnley 2018). These chemical models fail to reproduce both the anti-fractionation (i.e. $^{14}N/^{15}N > 500$) measured in cold pre-stellar cores (Redaelli et al. 2018) and the large spread of values measured from different high-mass star-forming regions (Fontani et al. 2015b). This also suggests that chemical reactions may still be missing in existing models, or that the ^{15}N-enrichment (or the contrary, i.e. ^{15}N-depletion, which causes anti-fractionation) is a local phenomenon occurring in spatial regions smaller than the beam size of single-dish observations described above. In fact, for example with the single-dish observations made by Fontani et al. (2015b), the isotopic ratios obtained were average values over angular sizes of $\sim 30''$, which hence include both the large-scale envelope and the dense core(s) embedded within it.

A more recent chemical model of Furuya and Aikawa (2018) proposed that anti-fractionation could be explained by introducing other mechanisms in chemical models, like isotope selective photodissociation of N_2 and grain surface chemistry. The former process was first proposed and thoroughly investigated theoretically by Heays et al. (2014). Subsequently, Furuya and Aikawa (2018) suggested that in the more diffuse part of a molecular clump, where the external UV radiation field is not fully shielded, the $^{14}N^{15}N$ molecule is photodissociated, while the $^{14}N_2$ is not because more abundant and self-shielded. This cause an enrichment of the atomic ^{15}N (decrease of $[^{14}N/^{15}N]_{atomic}$) and an increase of the $[^{14}N/^{15}N]_{N_2}$. The subsequent adsorption of atomic N creates an enrichment of ^{15}N in the icy mantles of dust grains. As long as the desorption of grain-surface species is not efficient, the net effect is the loss of ^{15}N from the gas phase. However, these results are based on a specific physical model adapted for clouds with densities of $\sim 10^4 cm^{-3}$, which could not be appropriate for dense sources. To understand the existing ^{15}N-observations more numerical studies of ^{15}N-fractionation are needed. We will discuss this point in Sect. 4.4.4.

In this work we report, for the first time, an interferometric analysis of the isotopic ratio $^{14}N/^{15}N$ towards the high-mass star-forming protocluster IRAS 05358+3543 (hereafter 05358) from N_2H^+. We discuss the possible different N-fractionation between $^{15}NNH^+$ and $N^{15}NH^+$ and the possible ^{15}N-enrichment at core scales ($\sim 5''$, i.e. ~ 0.044 pc at the distance of the source of 1.8 kpc). N-fractionation in N_2H^+ towards this source was already studied by Fontani et al. (2015b), who analysed IRAM 30m observations towards a sample of 26 high-mass star-forming regions, including 05358. In particular, for this source they found that the $^{14}N/^{15}N$ is lower (~ 200) than in the other massive star-forming regions.

The source and the observations are described in Sect. 4.2, the results are presented in Sect. 4.3 and a discussion of the results is presented in Sect. 4.4.

4.2. SOURCE AND OBSERVATIONS

05358 is part of a sample of 69 high-mass protostellar objects studied by Sridharan et al. (2002), Beuther et al. (2002a), Beuther et al. (2002b) and Beuther et al. (2002c) in the millimeter wavelengths. The source lies at a distance of 1.8 kpc in the Auriga molecular cloud complex (Heyer et al. 1996), in the Perseus spiral arm of the Milky Way, and has a bolometric luminosity of 6300 $L_\odot$ (Snell et al. 1990). The source is part of a complex group of HII regions: SH 235 is the brightest of four optical HII regions and it is excited by the O9.5 star BD+351201 (Georgelin 1975). The source 05358 is associated with the HII region SH 231 which is approximately 25′ west and 5′ south of SH 235. Fig. 4.1 shows the large structure of the molecular cloud complex in which 05358 is embedded.
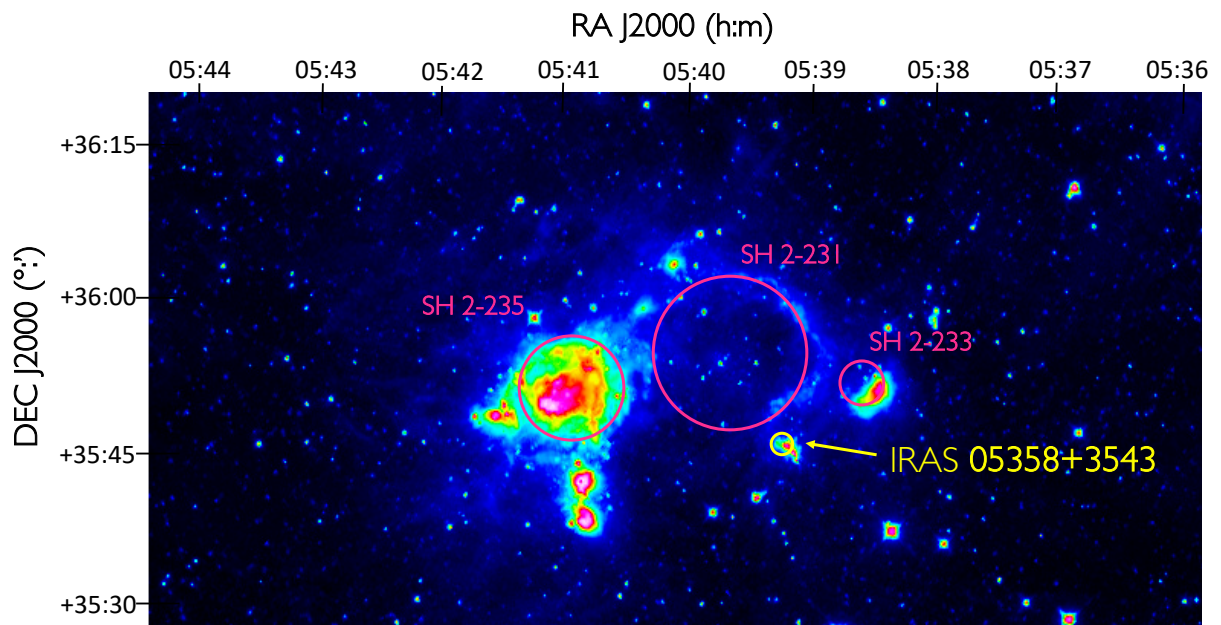

Fig. 4.1: WISE observations of the Auriga molecular cloud complex. This image is the merging of different wavelenghts: 3.4 and 4.6 μm, which is primarily light emitted from hot stars, and 12 and 22 μm, which is mostly light from warm dust. Pink circles represent the HII regions (e.g. Georgelin 1975). The yellow circle represents the position of 05358.

As evidence for massive star-formation, the source is associated with maser emissions (e.g. Minier et al. 2000, Hu et al. 2016) and massive outflows (e.g. Beuther et al. 2002d, Ginsburg et al. 2009). Beuther et al. (2007b) resolved 05358 in at least three continuum subsources (Table 4.1 and Fig. 4.2):

- mm1: it has a typical spectrum of a young massive protostar where the central source has already started hydrogen burning. The source could be a B1 Zero-Age-Main-Sequence star, with a luminosity of ~$10^{3.72}$ $L_\odot$ and a stellar mass of ~13 $M_\odot$ (Lang 1992). From the vicinity of the source, a collimated outflow is ejected with a rate of 6×10^{-4} $M_\odot$/yr (Beuther et al. 2002d), indicating that the protostar is still accreting gas. Moreover, the source is associated with 8.3 GHz emission (VLA data) that is likely

from a hyper-compact HII region. The main (sub)mm continuum source, which is at the center of two molecular outflows (Beuther et al. 2002d), is resolved in two separate (sub)mm continuum peaks, mm1a and mm1b;

- mm2: it consists of at least two sub-sources, mm2a and mm2b, and the position of mm2b shifts from 1.2 mm to 875 μm. There is also the presence of other peaks (mm2c and mm2d). The source mm2a is detected as a compact one and this could indicate that only this source is a star-forming region, while the others could be transient sources caused by the multiple outflow system in the region;

- mm3: for this source there is neither cm nor compact line detection (Leurini et al. 2007) and then it could be a very cold massive core in an early evolutionary stage. The grey-body function used to fit the SED is constrained by the high-frequency (~700 GHz) measurement by Beuther et al. (2007b) to dust temperatures below 20 K.
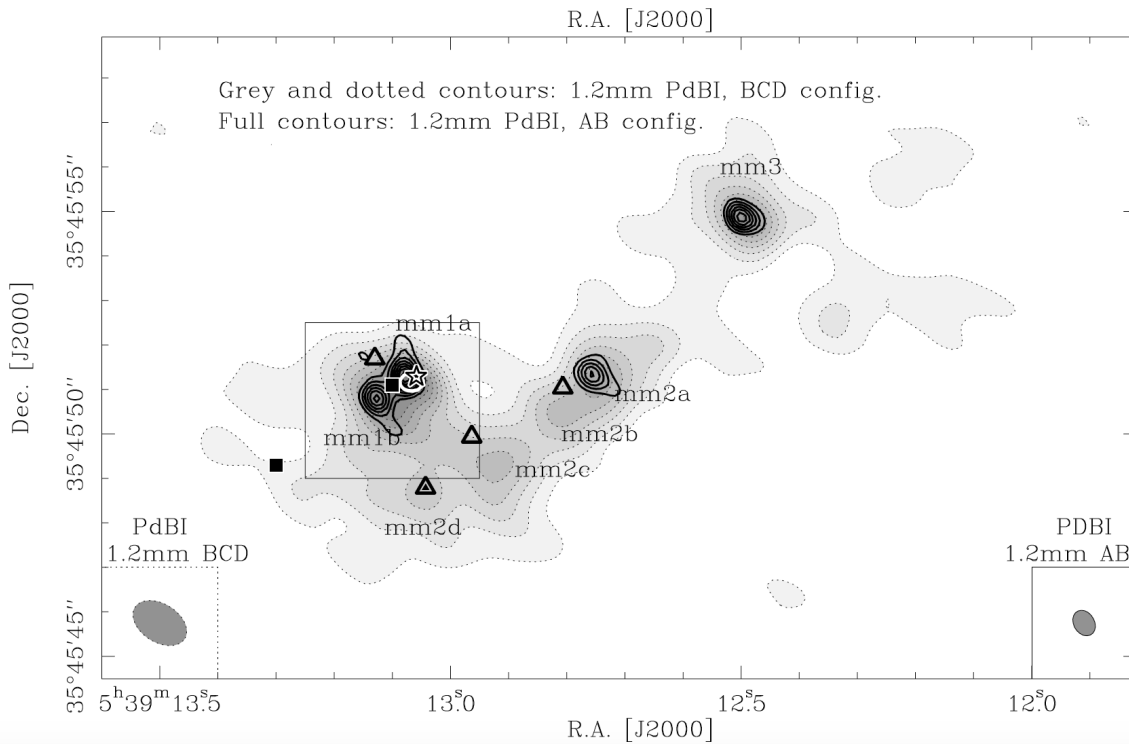

Fig. 4.2: Millimeter continuum image towards 05358 observed by Beuther et al. (2007b) with the Plateau de Bure Interferometer (PdBI). In grey-scale and dotted contours the 1.2 mm data (BCD configuration), and in full contours the 1.2 mm data observed in the AB configuration. The white ellipse is the VLA 50% contour level at 3.6 cm. Moreover, the star, triangles and squares indicate the position of Class II CH$_3$OH maser, H$_2$O masers and mid-infrared sources, respectively. Taken by Beuther et al. (2007b).

We carried on observations with the IRAM NOEMA Interferometer of the J=1–0 transition of N$_2$H$^+$, ^{15}NNH$^+$, and N^{15}NH$^+$ towards 05358. Rest frequencies are 93.1734 GHz (Cazzoli et al. 2012), 90.2638 GHz and 91.2057 GHz (Dore et al. 2009), for the J=1–0 transition of N$_2$H$^+$, ^{15}NNH$^+$ and N^{15}NH$^+$, respectively. In Table 4.2 the energy of the upper

Table 4.1: Coordinates of the dust continuum sources in the 05358 region.

Source	RA[J2000]	DEC[J2000]
	(h m s)	(°$'$$''$)
mm1a	05:39:13.08	35:45:51.3
mm1b	05:39:13.13	35:45:50.8
mm2	05:39:12.76	35:45:51.3
mm3	05:39:12.50	35:45:54.9
mm4[a]	05:39:12.46	35:45:40.9

[a] This continuum source has been discovered for the first time in this work.

Table 4.2: Molecular transitions of the J=1–0 transition of N_2H^+, $^{15}NNH^+$ and $N^{15}NH^+$.

Molecule	Frequency	Transition	E_U	$\log_{10}(A_{ij}^a)$
	(GHz)		(K)	
$N_2H^{+\,b}$	93.1734	J=1–0	4.5	-4.44034
$^{15}NNH^+$	90.2635	J=1–0, F=1–1	4.3	-4.48168
	90.2639	J=1–0, F=2–1		
	90.2645	J=1–0, F=0–1		
$N^{15}NH^+$	91.2043	J=1–0, F=1–1	4.4	-4.46810
	91.2060	J=1–0, F=2–1		
	91.2086	J=1–0, F=0–1		

[a] Einstein coefficient of the transition;
[b] For this molecule only the rotational transition between level i and j is given, since with our spectral setup was not possible to resolve the hyperfine structure.

levels, the Einstein coefficients and rest frequencies of each hyperfine transition are given, except for N_2H^+(1–0) for which only the rotational frequency is given since the hyperfine structure is not resolved in our spectra. In fact, the N_2H^+(1–0) transition was observed with the Widex correlator at a spectral resolution of ~5 km s^{-1}, while $^{15}NNH^+$, and $N^{15}NH^+$(1–0) were observed with the Narrow correlator at a resolution of ~0.5 km s^{-1}. To discuss our results, in Sect. 4.4.1 we will also use the averaged emission map of the J=5–4, K=0,1 transitions of CH_3CN. Rest frequencies are 91.987 GHz and 91.985 GHz, respectively (Cazzoli and Puzzarini 2006). Because these lines were in the same spectral band of the J=1–0 transition of N_2H^+, synthesized beam, spectral resolution and rms are the same.

Observations were carried out in 4 days from September 29 to November 3, 2016, with 8 antennas in C and D configurations, providing baselines between 15 and 240 m, corresponding to an angular resolution of ~3.1× 3.0$''$. The amount of precipitable water vapour was generally between 5 and 10 mm. Visibility amplitudes and phases were calibrated on 0552+398 and 0548+378. The absolute flux density scale was calibrated on MWC349 and LKHA101. The bandpass calibration was performed on 3C84 or 3C454.3. To incorporate short spacings to the interferometric maps, we have reduced and analysed IRAM-30m ob-

Table 4.3: Observational parameters of the NOEMA data..

Spw	Synthesized beam ($'' \times ''$)	PA (°)	Δv (km s^{-1})	rms (mJy/beam)
Continuum	3.0×2.6	-110.2	–	0.2
N_2H^+	3.0×2.6	-109.5	6.5	0.5
$^{15}NNH^+$	3.1×3.1	-41.9	0.5	7
$N^{15}NH^+$	3.1×3.1	-41.9	0.5	7

servations of the J=1–0 transition of N_2H^+, $^{15}NNH^+$ and $N^{15}NH^+$. These observations were carried out on March 5, 6, and 7, 2017. We have obtained large-scale maps on an angular region of ~120$''$, i.e. about twice the NOEMA primary beam at the frequency of the N_2H^+(1–0) transition. The data were obtained with the on-the-fly mapping mode. Pointing was checked every hour on nearby quasars. The focus was checked at the beginning of the observations, and after sunset. The creation of the synthetic visibilities and the merging of the two data sets were performed through standard procedures available in the GILDAS software package MAPPING. The final spectral resolution obtained for the N_2H^+(1–0) transition is of ~6.5 km s^{-1}, and for the $^{15}NNH^+$, and $N^{15}NH^+$(1–0) transitions is of ~0.5 km s^{-1}.

Calibration and imaging were performed using CLIC and MAPPING software of the GILDAS package[1]. The synthesized beam, the final velocity resolution and the rms (root mean square) of the datacubes are given in Table 4.3. The analysis of the data was done with the MADCUBA[2] software package. For the analysis we have used the spectroscopic parameters from the CDMS molecular catalog[3] (Müller et al. 2001; Müller et al. 2005; Endres et al. 2016).

4.3. Results

4.3.1. Continuum map

In Fig. 4.3 the 3 mm continuum map towards the source is shown. With this map we can distinguish the already known continuum millimeter sources mm1, mm2, and mm3 (Beuther et al. 2007b). However, our observations are not able to resolve mm1 as a binary system composed of mm1a and mm1b (Table 4.1) because of the insufficient spatial resolution (Table 4.3). Moreover, we have observed the continuum emission of a new millimeter source (mm4) at right ascension α_{2000}= 05^h:39^m:12.46^s and declination δ_{2000}=35°:45$'$:40.9$''$. Since this source is out of the primary beam at 1 mm, it was not analysed by Beuther et al. (2007b) that focused their work in characterising the properties of 05358 at the center of the field of view.

---

[1]　The GILDAS software is available at http://www.iram.fr/IRAMFR/GILDAS
[2]　Madrid Data Cube Analysis on ImageJ is a software developed in the Center of Astrobiology (Madrid, INTA-CSIC) to visualise and analyse single spectra and datacubes (Martín et al. 2019)
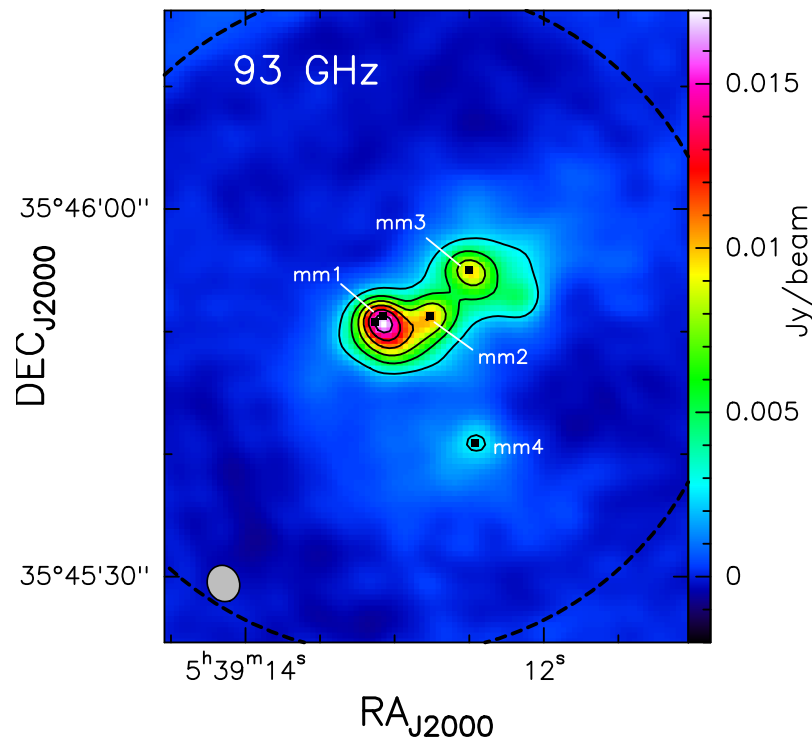[3]　https://www.astro.uni-koeln.de/cdms/

Fig. 4.3: 93 GHz continuum emission obtained with the IRAM NOEMA Interferometer. The first contour level is the 15% of the maximum value of the map, which corresponds to 17 mJy/beam. The other contour levels are the 30%, 45%, 60%, 75% and 90% of the maximum value, respectively. The black squares indicate the position of mm1a, mm1b, mm2, mm3 and mm4 (Table 4.1). The dashed circle represents the NOEMA field of view and the synthesized beam is the ellipse indicated in the lower left corner.

4.3.2. Morphology of N_2H^+ and ^{15}N-isotopologues emission

In Fig. 4.4 we show the averaged emission map of N_2H^+(1–0), which arises mainly from 3 cores: one associated with both mm1 and mm2 not resolved, another associated with mm3, and finally one associated with mm4. We have also highlighted the presence of two other N_2H^+(1–0) emission regions (A and B) and we will discuss them in Sect. 4.4.1. It can also be noted that the N_2H^+(1–0) emission peaks are shifted by ~2–3″ with respect to the mm1, mm2, and mm3 continuum sources. We will discuss this result in Sect. 4.4.1.

In Fig. 4.5 the averaged emission maps of the $^{15}NNH^+$(1–0) and $N^{15}NH^+$ (1–0) transitions are shown. They are obtained by integrating the lines over the channels with the signal above the 3σ level, in the Narrow spectra. In particular, for $N^{15}NH^+$(1–0) we were able to resolve the hyperfine structure in three distinct components (see Table 4.2). However, since the J=1–0, F=1-1 and J=1–0, F=0-1 transitions are near the noise level, we have decided to create the emission map integrating only over the channels that correspond to the strongest component, namely the J=1-0, F=2-1 transition. Moreover, in Fig. 4.5 the blue contours correspond to the polygons from which we have extracted the spectra, to derive the total column densities of the three molecules, and the corresponding $^{14}N/^{15}N$ ratios, in eight different regions towards 05358. The polygons are defined from the 5σ of the corresponding averaged map. In particular, P1a, P2a, P3a, and P4a correspond to a value of 5×0.72 mJy/beam (from $^{15}NNH^+$, left panel of Fig. 4.5), while P1b, P2b, P3b, and P4b correspond to a value of 5×0.5 mJy/beam (from $N^{15}NH^+$, right panel of Fig. 4.5).

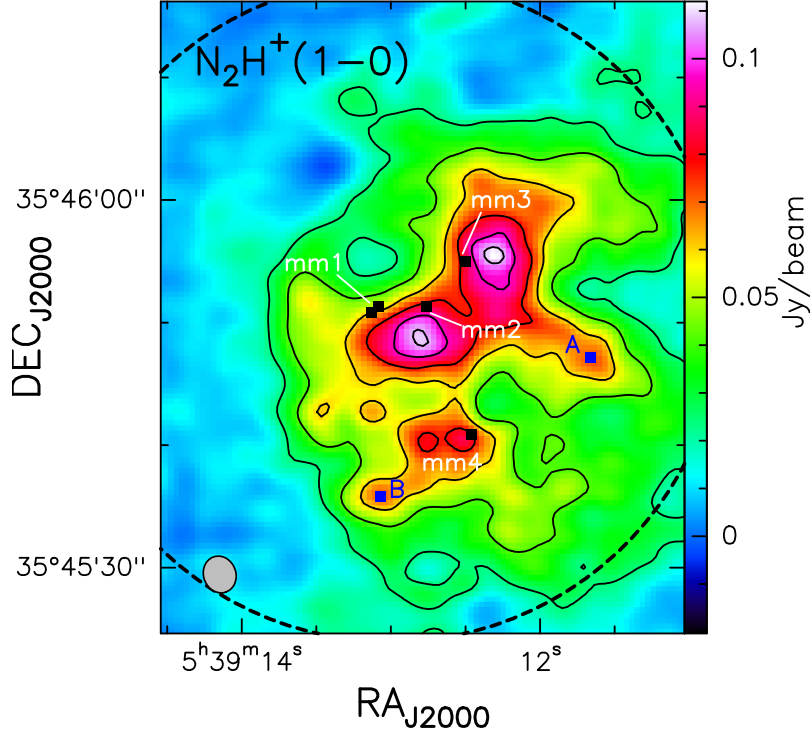Fig. 4.4: Averaged map of N_2H^+(1–0) at 93.1734 GHz (velocity range between -34.6 and -0.1 km s^{-1}) obtained from the NOEMA Widex correlator. The contour levels are 4, 7, 10, 13, 16 and 18 times the 1σ rms of the map, equal to 6 mJy/beam. The black squares indicate the position of mm1a, mm1b, mm2, mm3 and mm4 (Table 4.1). The blue squares correspond to the N_2H^+(1–0) emission peaks A and B, described in Sect. 4.4.1. The dashed circle represents the NOEMA field of view and the synthesized beam is the ellipse indicated in the lower left corner.

We have also extracted spectra from polygons defined as the intersection of the 5σ of the two ^{15}N-isotopologues averaged maps (I1, I2, I3, and I4, left panel of Fig. 4.6). This has been done to compare the $^{14}N/^{15}N$ ratios obtained from $^{15}NNH^+$ and $N^{15}NH^+$ from the same regions of the source. Finally, we have decided to estimate the $^{14}N/^{15}N$ ratios in the regions defined in the right panel of Fig. 4.6, D1, D2, and D3, less bright and corresponding to diffuse N_2H^+ emission.

4.3.3. FITTING PROCEDURE AND COLUMN DENSITY CALCULATION

To fit the lines and to compute the total column densities from the extracted spectra we have used MADCUBA assuming local thermal equilibrium (LTE) conditions. This is a reasonable assumption since the observed cores present volume densities of the order of 10^6 cm^{-3} (see Beuther et al. 2007b), which is higher than the critical densities of the observed lines ($\sim$1.5–2$\times10^5$ cm^{-3}, assuming kinetic temperatures from 20 K up to 50 K).

The procedure used to fit the lines and evaluate the total column density N is the same explained in Sect. 3.3.2. We have fitted all the lines fixing the T_{ex}. We have performed the analysis with different T_{ex} values (20, 30, 40 and 50 K) since we had only one transition for each molecule and we were not able to derive it directly from the data. These temperature values are also consistent with the kinetic temperatures derived for 05358 from NH_3(1,1) by Lu et al. (2014).

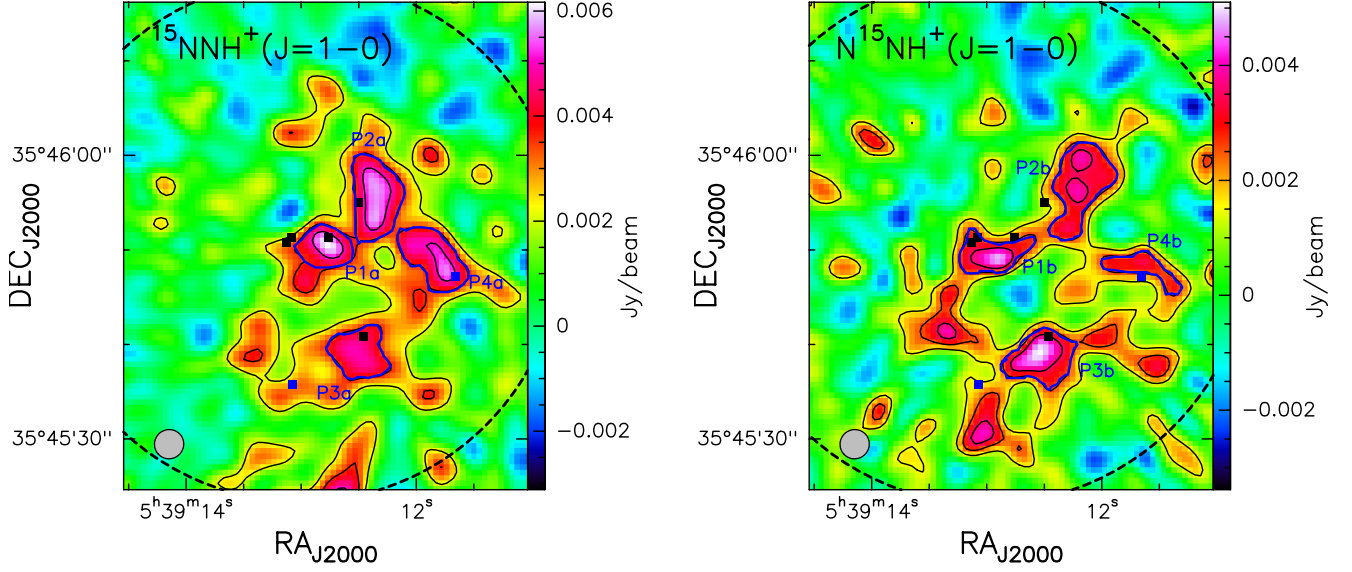The three lines that we have observed, the N_2H^+(1–0), $^{15}NNH^+$(1–0) and $N^{15}NH^+$(1–

Fig. 4.5: *Left panel*: Averaged map of ^{15}NNH$^+$(1–0) at 90.26 GHz (velocity range between -19.3 and -14.2 km s^{-1}) obtained from the NOEMA Narrow correlator. The thin black contour levels are 3, 5 and 7 times the 1σ rms of the map, equal to 0.72 mJy/beam. *Right panel*: Averaged map of the J=1–0, F=2-1 transition of N^{15}NH$^+$ (main hyperfine component) at 91.20 GHz (velocity range between -19.5 and -15 km s^{-1}) obtained from the NOEMA Narrow correlator. The thin black contour levels are 3, 5 and 7 times the 1σ rms of the map, equal to 0.5 mJy/beam. In both panels, the blue contours correspond to the 5σ level of the averaged maps, from which the spectra have been extracted: P1a, P2a, P3a, and P4a for ^{15}NNH$^+$ and P1b, P2b, P3b and P4b for N^{15}NH$^+$. The black and blue squares indicate the positions of the continuum sources (Table 4.1) and the N$_2$H$^+$ peak positions A and B, respectively, as in Fig. 4.4. The dashed circle represents the NOEMA field of view and the synthesized beam is the ellipse indicated in the lower left corner.

0) transitions, have hyperfine structure. We can resolve it only for N^{15}NH$^+$(1–0) since the line width found (~2 km s^{-1}) is smaller than the separation in velocity of the hyperfine components (e.g. Fig. 4.7). However, we have fitted the spectra of both the ^{15}NNH$^+$(1–0) and N^{15}NH$^+$(1–0) transitions taking the hyperfine structure into account, to be consistent with the analysis of the two different ^{15}N-isotopologues of N$_2$H$^+$. Conversely, for N$_2$H$^+$(1–0) we have performed the analysis taking into account only the rotational transition J=1–0, as if it was a single line. We did this because the low spectral resolution (~6.5 km s^{-1}) permits the convergence of the fits only fixing a FWHM>6.5 km s^{-1}, which is not the real one of the source (~2 km s^{-1} from the fits of ^{15}N-isotopologues). The fit to a single transition permits to leave the FWHM as a free parameter and, even if the final FWHM is not reliable, the convergence of the fit is more precise. In Appendix A a detailed analysis demonstrates that the use of this method gives similar results of the analysis of the same N$_2$H$^+$ simulated spectrum where the hyperfine structure could be resolved, within the errors. In the same Appendix we also show that the low resolution of the N$_2$H$^+$ emission is not hiding saturated line profiles, and then our N$_2$H$^+$ column densities estimates are accurate.

All the extracted spectra from the P1a–P4a, P1b–P4b, I1, I2, I3, and I4 regions, and the more diffuse N$_2$H$^+$ emission regions D1, D2, and D3 (see Sect. 4.3.2) are shown in Figs. 4.7, 4.8 and 4.9. Column densities, FWHM, velocities, and opacities derived from the fit of the extracted spectra are given in Tables 4.4, 4.5 and 4.6.

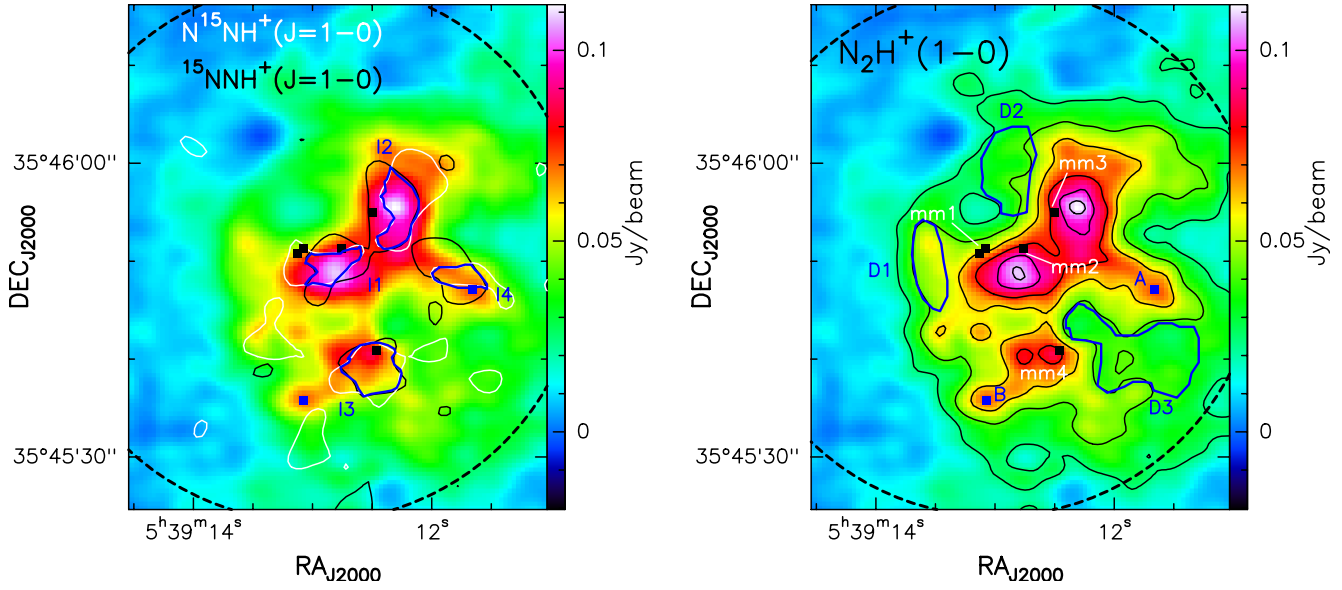For the main isotopologue, N$_2$H$^+$, we have found column densities of the order of 10^{14}

Fig. 4.6: *Left panel*: The color-scale image represents the averaged emission of $N_2H^+(1-0)$. The black contours are the 5σ levels of $^{15}NNH^+(1-0)$ averaged emission and the white contours are the 5σ levels of $N^{15}NH^+(1-0)$ averaged emission. The intersection between the black and the white contours (I1, I2, I3, and I4) is indicated with blue polygons. *Right panel*: Same panel as in Fig. 4.4, where we have over-plotted blue contours that define three different zones (D1, D2, and D3) of the diffuse N_2H^+ envelope. In both panels, the black and blue squares indicate the positions of the continuum sources and the N_2H^+ peak positions A and B, respectively. The dashed circle represents the NOEMA field of view.

cm^{-2} in all regions. In particular, column densities towards P1a and P2a are higher than those towards P3a and P4a, of a factor ~ 1.5. The same trend is followed by P1b and P2b with respect to P3b and P4b, with a decrease of a factor ~ 3. However, for the ^{15}N-isotopologues, column densities are the same in each region, within the errors, and are of the order of $10^{11} cm^{-2} - 10^{12} cm^{-2}$, depending on the assumed T_{ex}. In fact, as a general trend for all the analysed molecules, N_2H^+, $^{15}NNH^+$ and $N^{15}NH^+$, column densities increase with the T_{ex}, but their ratios remain the same, within the uncertainties.

Table 4.4: Values obtained with the fitting procedure described in Sect. 4.3.3 to the J=1–0 transition of N$_2$H$^+$and ^{15}NNH$^+$ towards P1a, P2a, P3a, and P4a (top panel of the table), and of the J=1–0 transition of N$_2$H$^+$and N^{15}NH$^+$ towards P1b, P1b, P3b and P4b (bottom panel of the table).

Source									τ^b	
		N$_2$H$^+$(1–0)					^{15}NNH$^+$(1–0)			
	T_{ex}	$FWHM^a$	v$_{LSR}$	τ	N_{tot}	T_{ex}	$FWHM$	v$_{LSR}$	τ^b	N_{tot}
	(K)	(km s^{-1})	(km s^{-1})		($\times10^{14}$cm^{-2})	(K)	(km s^{-1})	(km s^{-1})		($\times10^{11}$cm^{-2})
P1a	20	11.1±0.6	-15.2±0.3	0.26±0.02	1.0±0.1	20	2.2±0.7	-16.2±0.3	0.002±0.001	5±1
	30	11.3±0.6	-15.2±0.3	0.16±0.02	1.3±0.2	30	2.2±0.7	-16.2±0.3	0.002±0.001	7±2
	40	11.3±0.6	-15.2±0.3	0.112±0.008	1.6±0.2	40	2.3±0.7	-16.2±0.3	0.002±0.001	9±2
	50	11.4±0.6	-15.2±0.3	0.087±0.006	1.9±0.3	50	2.3±0.7	-16.2±0.3	0.0013±0.0005	11±3
P2a	20	10.6±0.7	-14.7±0.3	0.25±0.02	0.9±0.1	20	1.8±0.3	-15.6±0.1	0.0027±0.0005	5±1
	30	10.8±0.7	-14.7±0.3	0.15±0.02	1.2±0.2	30	1.8±0.3	-15.6±0.1	0.0017±0.0003	7±1
	40	10.9±0.7	-14.7±0.3	0.105±0.008	1.4±0.2	40	1.8±0.3	-15.6±0.1	0.0013±0.0003	9±2
	50	10.9±0.7	-14.7±0.3	0.082±0.006	1.7±0.3	50	1.8±0.3	-15.6±0.1	0.0010±0.0002	11±2
P3a	20	11±1	-15.0±0.5	0.17±0.02	0.6±0.1	20	2.3±0.6	-16.6±0.2	0.002±0.001	5±1
	30	11±1	-15.0±0.5	0.10±0.02	0.8±0.1	30	2.3±0.6	-16.6±0.2	0.0013±0.0003	7±1
	40	11±1	-15.0±0.5	0.073±0.009	1.0±0.2	40	2.3±0.6	-16.6±0.2	0.0010±0.0002	9±2
	50	11±1	-15.0±0.5	0.057±0.007	1.2±0.2	50	2.3±0.6	-16.6±0.2	0.0008±0.0002	11±2
P4a	20	10.2±0.6	-14.6±0.3	0.20±0.02	0.7±0.1	20	2.7±0.6	-15.6±0.2	0.0021±0.0005	6±1
	30	10.3±0.6	-14.6±0.3	0.12±0.01	0.9±0.1	30	2.7±0.6	-15.6±0.2	0.0013±0.0003	8±2
	40	10.3±0.6	-14.6±0.3	0.089±0.007	1.2±0.2	40	2.7±0.6	-15.6±0.2	0.0009±0.0002	10±2
	50	10.4±0.6	-14.6±0.3	0.069±0.005	1.4±0.2	50	2.7±0.6	-15.6±0.2	0.0007±0.0002	13±3

Source									τ^b	
		N$_2$H$^+$(1–0)					N^{15}NH$^+$(1–0)			
	T_{ex}	$FWHM^a$	v$_{LSR}$	τ	N_{tot}	T_{ex}	$FWHM$	v$_{LSR}$	τ^b	N_{tot}
	(K)	(km s^{-1})	(km s^{-1})		($\times10^{14}$cm^{-2})	(K)	(km s^{-1})	(km s^{-1})		($\times10^{11}$cm^{-2})
P1b	20	11.2±0.7	-15.2±0.3	0.27±0.02	1.0±0.2	20	1.2±0.2	-16.27±0.07	0.004±0.001	5±1
	30	11.4±0.7	-15.2±0.3	0.16±0.02	1.3±0.2	30	1.2±0.2	-16.27±0.07	0.0022±0.0004	6±1
	40	11.5±0.7	-15.2±0.3	0.114±0.009	1.7±0.3	40	1.2±0.2	-16.27±0.07	0.0016±0.0003	8±2
	50	11.5±0.7	-15.2±0.3	0.089±0.007	2.0±0.3	50	1.2±0.2	-16.27±0.07	0.0013±0.0002	9±2
P2b	20	11.0±0.7	-14.7±0.3	0.23±0.02	0.9±0.1	20	1.9±0.3	-15.5±0.1	0.004±0.001	7±2
	30	11.1±0.6	-14.7±0.3	0.14±0.01	1.2±0.2	30	1.9±0.3	-15.5±0.1	0.0023±0.0004	10±2
	40	11.2±0.6	-14.7±0.3	0.110±0.007	1.4±0.2	40	1.9±0.3	-15.5±0.1	0.0016±0.0003	13±3
	50	11.2±0.6	-14.7±0.3	0.078±0.006	1.7±0.3	50	1.9±0.3	-15.5±0.1	0.0013±0.0002	15±3
P3b	20	11±1	-14.9±0.5	0.20±0.03	0.7±0.1	20	2.0±0.3	-16.5±0.2	0.003±0.001	7±1
	30	11±1	-14.9±0.5	0.12±0.02	0.9±0.2	30	2.0±0.3	-16.5±0.2	0.0019±0.0004	9±2
	40	11±1	-14.9±0.5	0.08±0.01	1.2±0.2	40	2.0±0.3	-16.5±0.2	0.0014±0.0003	11±3
	50	11±1	-14.9±0.5	0.065±0.008	1.4±0.3	50	2.0±0.3	-16.5±0.2	0.0011±0.0002	14±3
P4b	20	10.7±0.6	-14.7±0.3	0.082±0.006	0.30±0.04	20	1.5±0.3	-16.7±0.2	0.0010±0.0003	1.6±0.4
	30	10.7±0.6	-14.7±0.3	0.051±0.004	0.40±0.06	30	1.5±0.3	-16.7±0.2	0.0006±0.0002	2.2±0.6
	40	10.7±0.6	-14.7±0.3	0.037±0.003	0.50±0.07	40	1.5±0.3	-16.7±0.2	0.0005±0.0001	2.7±0.7
	50	10.7±0.6	-14.7±0.3	0.029±0.002	0.61±0.09	50	1.5±0.3	-16.7±0.2	0.00040±0.00009	3.3±0.9

^{a} Note that these FWHM overestimate those obtained with the ^{15}N-isotopologues since N$_2$H$^+$ has a spectral resolution higher than the physical FWHM;
^{b} line opacity of the main hyperfine component.

Table 4.5: Values obtained with the fitting procedure described in Sect. 4.3.3 to the N_2H^+(1–0), $^{15}NNH^+$(1–0) and $N^{15}NH^+$(1–0) transitions towards I1, I2, I3, and I4.

Source	T_{ex}	$FWHM^a$	v_{LSR}	τ	N_{tot}
	(K)	(km s^{-1})	(km s^{-1})		($\times 10^{14}$cm^{-2})
I1	20	11.3±0.7	-15.3±0.3	0.29±0.03	1.1±0.2
	30	11.5±0.7	-15.3±0.3	0.17±0.02	1.5±0.2
	40	11.6±0.7	-15.3±0.3	0.124±0.009	1.8±0.3
	50	11.7±0.7	-15.3±0.3	0.096±0.007	2.2±0.3
I2	20	11.0±0.6	-14.7±0.3	0.25±0.02	1.0±0.2
	30	11.1±0.7	-14.7±0.3	0.15±0.02	1.2±0.2
	40	11.2±0.7	-14.7±0.3	0.109±0.009	1.5±0.3
	50	11.3±0.7	-14.7±0.3	0.084±0.007	1.9±0.3
I3	20	11.0±0.9	-15.0±0.5	0.17±0.02	0.6±0.1
	30	11.1±0.9	-15.0±0.5	0.10±0.01	0.8±0.2
	40	11.2±0.9	-15.0±0.5	0.073±0.008	1.0±0.2
	50	11.2±0.9	-15.0±0.5	0.057±0.006	1.2±0.2
I4	20	10.8±0.6	-14.8±0.3	0.18±0.02	0.7±0.1
	30	10.9±0.6	-14.8±0.3	0.111±0.008	0.9±0.1
	40	11.0±0.6	-14.7±0.3	0.079±0.006	1.1±0.2
	50	11.0±0.6	-14.7±0.3	0.062±0.004	1.3±0.2

Source	$^{15}NNH^+$(1–0)					$N^{15}NH^+$(1–0)				
	T_{ex}	$FWHM$	v_{LSR}	τ^b	N_{tot}	T_{ex}	$FWHM$	v_{LSR}	τ^b	N_{tot}
	(K)	(km s^{-1})	(km s^{-1})		($\times 10^{11}$cm^{-2})	(K)	(km s^{-1})	(km s^{-1})		($\times 10^{11}$cm^{-2})
I1	20	1.7±0.5	-16.4±0.2	0.005±0.001	5±1	20	1.3±0.3	-16.1±0.1	0.005±0.001	4±1
	30	1.7±0.5	-16.4±0.2	0.002±0.001	7±2	30	1.3±0.3	-16.1±0.1	0.003±0.001	6±2
	40	1.7±0.5	-16.4±0.2	0.002±0.001	9±2	40	1.3±0.3	-16.1±0.1	0.002±0.001	7±2
	50	1.7±0.5	-16.4±0.2	0.002±0.001	11±2	50	1.3±0.3	-16.1±0.1	0.0019±0.0005	9±2
I2	20	1.6±0.4	-15.7±0.2	0.006±0.002	6±1	20	1.7±0.3	-15.5±0.1	0.007±0.001	7±2
	30	1.9±0.3	-15.6±0.1	0.0030±0.0005	8±2	30	1.7±0.3	-15.5±0.1	0.004±0.001	10±2
	40	1.9±0.3	-15.6±0.1	0.0022±0.0003	11±2	40	1.7±0.3	-15.5±0.1	0.003±0.001	12±3
	50	1.9±0.3	-15.6±0.1	0.0017±0.0003	13±2	50	1.7±0.3	-15.5±0.1	0.0024±0.0004	15±3
I3	20	2.6±0.6	-16.6±0.2	0.003±0.001	6±1	20	2.2±0.3	-16.5±0.2	0.005±0.001	7±2
	30	2.6±0.6	-16.6±0.2	0.002±0.001	7±2	30	2.2±0.3	-16.5±0.2	0.003±0.001	9±2
	40	2.6±0.6	-16.6±0.2	0.0015±0.0004	9±2	40	2.2±0.3	-16.5±0.2	0.0021±0.0004	11±3
	50	2.6±0.6	-16.6±0.2	0.0012±0.0003	11±2	50	2.2±0.3	-16.5±0.2	0.0017±0.0003	14±3
I4	20	3.2±0.8	-15.3±0.3	0.003±0.001	7±2	20	1.4±0.3	-16.4±0.1	0.006±0.001	5±1
	30	3.2±0.8	-15.3±0.3	0.002±0.001	9±2	30	1.4±0.3	-16.4±0.1	0.003±0.001	6±2
	40	3.2±0.8	-15.3±0.3	0.0014±0.0004	11±3	40	1.4±0.3	-16.4±0.1	0.003±0.001	8±2
	50	3.2±0.8	-15.3±0.3	0.0011±0.0003	14±3	50	1.4±0.3	-16.4±0.1	0.002±0.001	10±3

^{a} Note that these FWHM overestimate those obtained with the ^{15}N-isotopologues since N_2H^+ has a spectral resolution higher than the physical FWHM;
^{b} line opacity of the main hyperfine component.

Table 4.6: Values obtained with the fitting procedure described in Sect. 4.3.3 to the N_2H^+(1–0), $^{15}NNH^+$(1–0) and $N^{15}NH^+$(1–0) transitions towards D1, D2, and D3. The upper limits and tentative detections are obtained as explained in Sect. 4.3.3.

Source		N_2H^+(1–0)			
	T_{ex}	$FWHM^a$	v_{LSR}	τ	N_{tot}
	(K)	(km s^{-1})	(km s^{-1})		($\times 10^{13}$cm^{-2})
D1	20	10.0±0.7	-15.0±0.4	0.14±0.02	4.9±0.8
	30	10.0±0.7	-15.0±0.4	0.087±0.008	6±1
	40	10.1±0.7	-15.0±0.4	0.063±0.006	8±2
	50	10.1±0.7	-15.0±0.4	0.049±0.004	10±2
D2	20	8.9±0.9	-14.4±0.4	0.12±0.02	3.7±0.7
	30	9.0±0.9	-14.4±0.4	0.075±0.009	4.9±0.9
	40	9.0±0.9	-14.4±0.4	0.054±0.007	6±1
	50	9.0±0.9	-14.4±0.4	0.042±0.005	7±2
D3	20	9±1	-14.8±0.5	0.11±0.02	3.4±0.7
	30	9±1	-14.7±0.5	0.069±0.01	4.5±0.9
	40	9±1	-14.7±0.5	0.050±0.007	6±1
	50	9±1	-14.7±0.5	0.039±0.006	7±2

Source		$^{15}NNH^+$(1–0)					$N^{15}NH^+$(1–0)			
	T_{ex}	$FWHM$	v_{LSR}	τ^b	N_{tot}	T_{ex}	$FWHM$	v_{LSR}	τ^b	N_{tot}
	(K)	(km s^{-1})	(km s^{-1})		($\times 10^{11}$cm^{-2})	(K)	(km s^{-1})	(km s^{-1})		($\times 10^{11}$cm^{-2})
D1	20				≤2	20				≤2.4
	30				≤2.6	30				≤3.2
	40				≤3.3	40				≤4
	50				≤4	50				≤4.9
D2	20	0.8±0.2	-15.1±0.1	0.002±0.001	1.1±0.4^c	20				≤2.4
	30	0.8±0.2	-15.1±0.1	0.0014±0.0005	1.5±0.6^c	30				≤3.3
	40	0.8±0.2	-15.1±0.1	0.0010±0.0004	1.9±0.7^c	40				≤4.2
	50	0.8±0.2	-15.1±0.1	0.0008±0.0003	2.4±0.8^c	50				≤5
D3	20				≤1.4	20				≤1
	30				≤1.8	30				≤1.4
	40				≤2.3	40				≤1.7
	50				≤2.8	50				≤2.1

^{a} Note that these FWHM overestimate those obtained with the ^{15}N-isotopologues since N_2H^+ has a spectral resolution higher than the physical FWHM;
^{b} line opacity of the main hyperfine component;
^{c} tentative detection.

Table 4.7: Values obtained with the fitting procedure described in Sect. 4.3.3 to the N_2H^+(1–0), $^{15}NNH^+$(1–0) and $N^{15}NH^+$(1–0) transitions towards mm1 and mm3 in regions equals to the IRAM-30m beam (see Sect 4.3.3).

Source			N_2H^+(1–0)		
	T_{ex}	$FWHM^a$	v_{LSR}	τ	N_{tot}
	(K)	(km s^{-1})	(km s^{-1})		($\times 10^{13}$cm^{-2})
mm1	43	10.0±0.7	-14.8±0.4	0.061±0.006	9±2
mm3	18	9.9±0.6	-14.7±0.3	0.18±0.02	5.0±0.8

Source			$^{15}NNH^+$(1–0)					$N^{15}NH^+$(1–0)		
	T_{ex}	$FWHM$	v_{LSR}	τ^b	N_{tot}	T_{ex}	$FWHM$	v_{LSR}	τ^b	N_{tot}
	(K)	(km s^{-1})	(km s^{-1})		($\times 10^{11}$cm^{-2})	(K)	(km s^{-1})	(km s^{-1})		($\times 10^{11}$cm^{-2})
mm1	43	1.7±0.3	-16.1±0.1	0.0009±0.0001	4.1±0.7	43	2.1±0.4	-16.2±0.2	0.0008±0.0002	5±2
mm3	18	1.9±0.4	-15.8±0.1	0.0022±0.0004	2.3±0.4	18	1.8±0.3	-16.1±0.2	0.003±0.001	2.6±0.7

^{a} Note that these FWHM overestimate those obtained with the ^{15}N-isotopologues since N_2H^+ has a spectral resolution higher than the physical FWHM;
^{b} line opacity of the main hyperfine component;
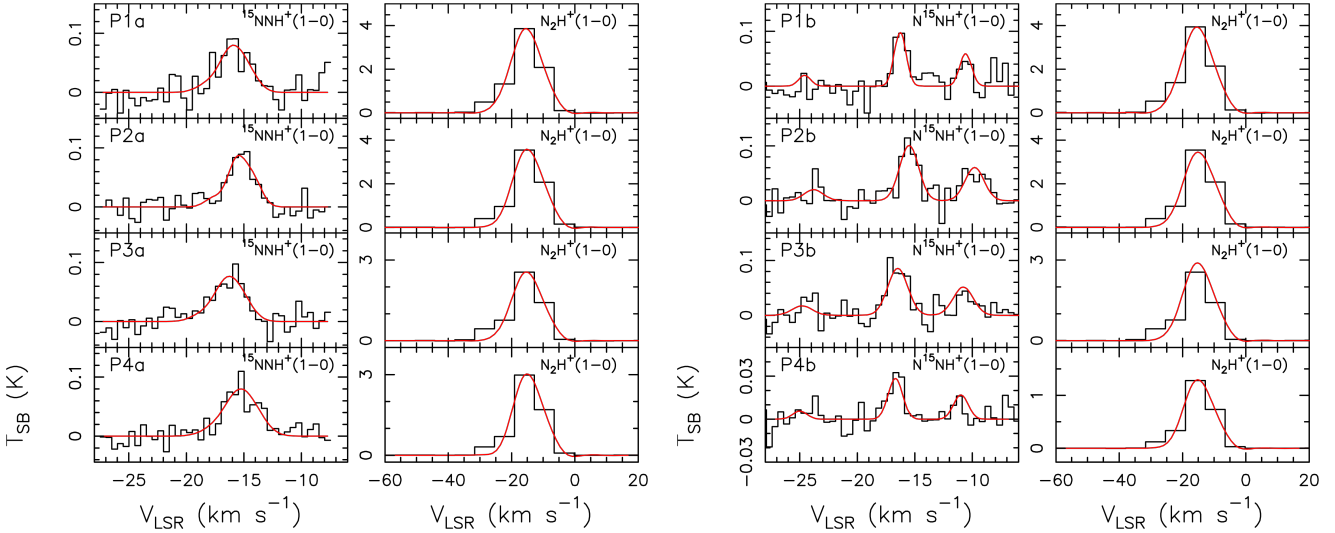
Fig. 4.7: *Left panels*: Spectra of the $^{15}NNH^+$(1–0) and N_2H^+(1-0) transitions (first and second column, respectively) obtained for the P1a, P2a, P3a, and P4a regions. *Right panels*: Spectra of the $N^{15}NH^+$(1–0) and N_2H^+(1-0) transitions (first and second column, respectively) obtained for the P1b, P2b, P3b and P4b regions. For each spectrum, in both panels, the x-axis represents the systematic velocity of the source, and the y-axis shows the line intensity in synthesised beam temperature scale. The red curves are the best Gaussian fits obtained with MADCUBA with a T_{ex}=30K.
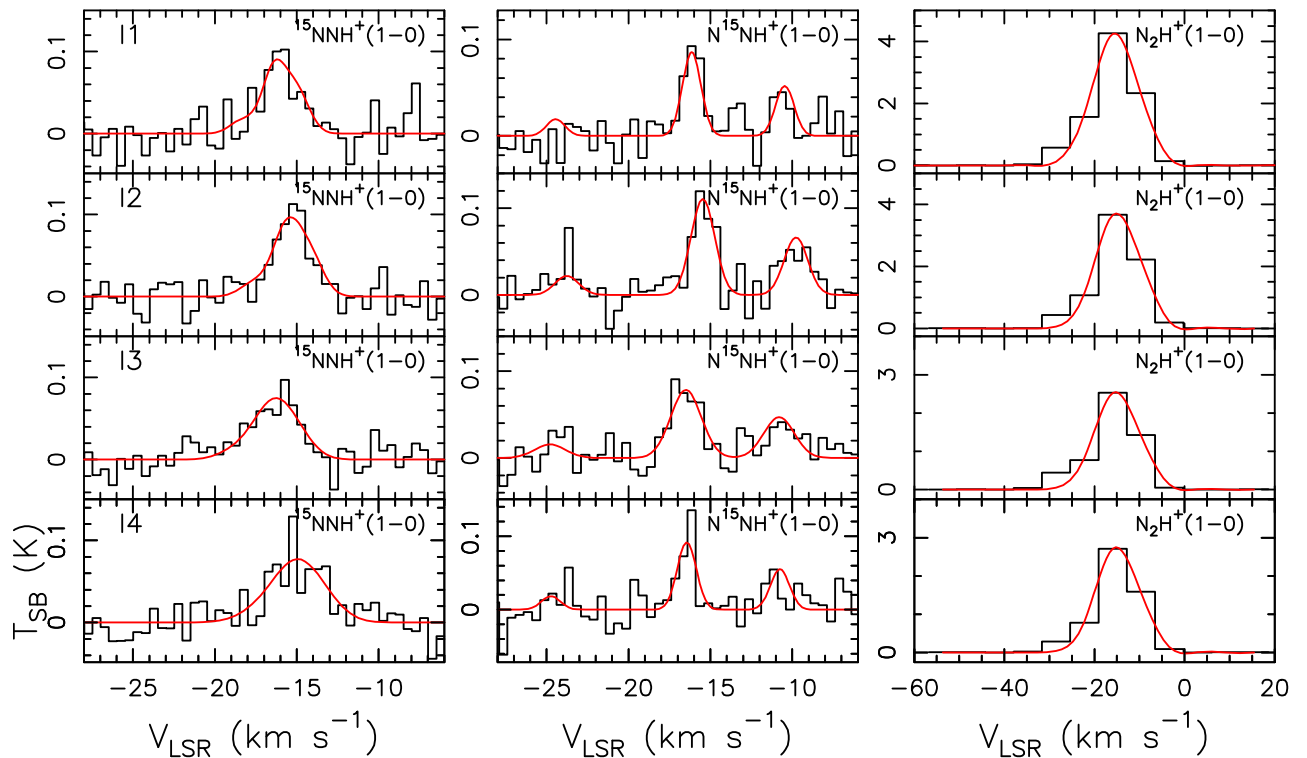
Fig. 4.8: Spectra of the $^{15}NNH^+(1–0)$, $N^{15}NH^+(1–0)$ and $N_2H^+(1-0)$ transitions (first, second and third column, respectively) obtained for the I1, I2, I3, and I4 regions (first, second, third and fourth line, respectively). For each spectrum the x-axis represents the systematic velocity of the source, and the y-axis shows the line intensity in synthesised beam temperature scale. The red curves are the best Gaussian fits obtained with MADCUBA with a $T_{ex}=30K$.
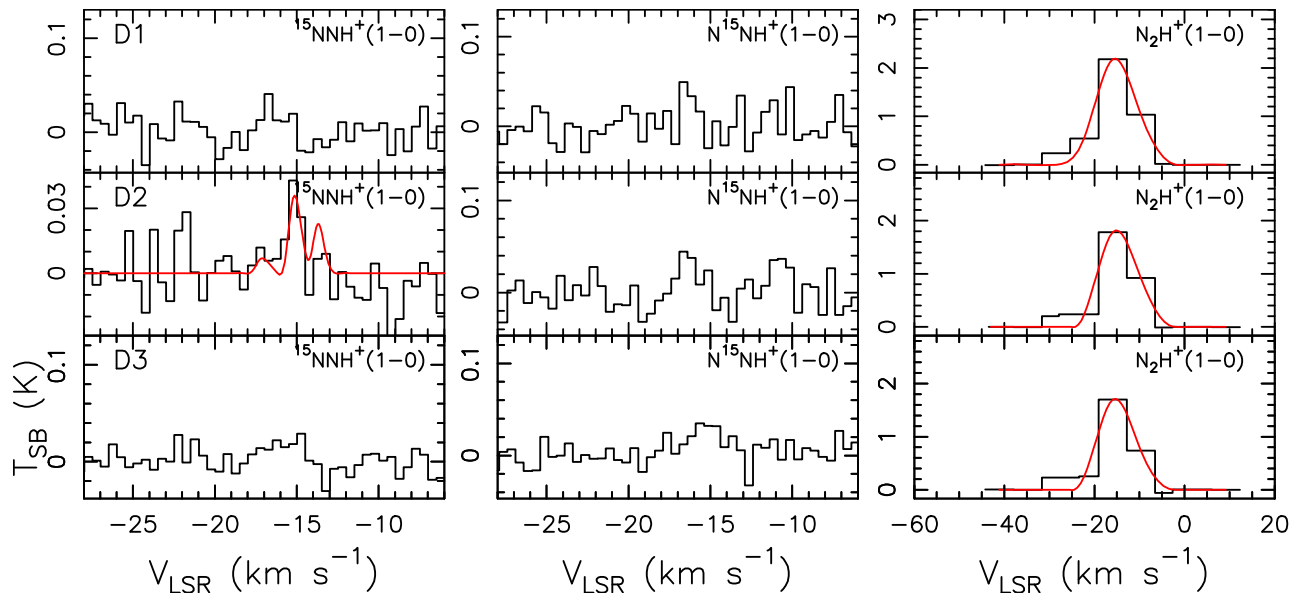
Fig. 4.9: Spectra of the $^{15}NNH^+(1–0)$, $N^{15}NH^+(1–0)$ and $N_2H^+(1-0)$ transitions (first, second and third column, respectively) obtained for the D1, D2, and D3 regions (first, second and third line, respectively). For each spectrum the x-axis represents the systematic velocity of the source, and the y-axis shows the line intensity in synthesised beam temperature scale. The red curves are the best Gaussian fits obtained with MADCUBA with a $T_{ex}=30K$.
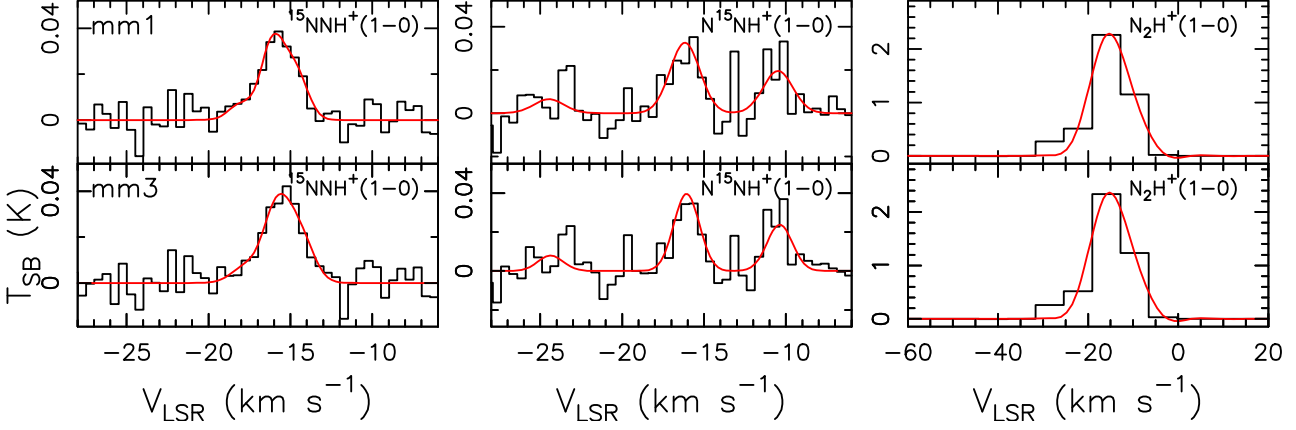
Fig. 4.10: Spectra of the ^{15}NNH$^+$(1–0), N^{15}NH$^+$(1–0) and N$_2$H$^+$(1-0) transitions (first, second and third column, respectively) obtained for the regions that correspond to the IRAM-30m beam around mm1 and mm3 (first and second line, respectively). For each spectrum the x-axis represents the systematic velocity of the source, and the y-axis shows the line intensity in synthesised beam temperature scale. The red curves are the best Gaussian fits obtained with MADCUBA with a T_{ex}=43 K for mm1 and a T_{ex}=18 K for mm3, obtained from Fontani et al. (2015b).

DIFFUSE REGIONS

The ^{15}NNH$^+$(1–0) and N^{15}NH$^+$(1–0) transitions are not detected in any of the diffuse N$_2$H$^+$emission regions D1, D2, and D3, except for ^{15}NNH$^+$(1–0) in D2 for which we have obtained a tentative detection (see Fig. 4.9). We have considered tentative detections the lines where the peak synthesized beam temperature ($T_{\text{SB}}^{\text{peak}}$) was between 2.5$\sigma$ and 3σ (2.5$\sigma \leq T_{\text{SB}}^{\text{peak}} < 3\sigma$) , where σ is the r.m.s noise of the spectrum. For the non detections we have computed upper limits for the column densities with MADCUBA. They have been derived from the formula $3\sigma \times \Delta v / \sqrt{N_{\text{chan}}}$, where N_{chan} is the number of channels covered by the line width Δv, as already described in Sect. 3.3.2. In particular, we have considered as Δv an average value of the FWHM derived from the same transitions towards P1a–P4a and P1b–P4b (Table 4.4): $\Delta v_{^{15}\text{NNH}^+} = 2.3 \pm 0.2$ km s^{-1} and $\Delta v_{\text{N}^{15}\text{NH}^+} = 1.7 \pm 0.4$ km s^{-1}. The upper limits and tentative detection fit results from diffuse N$_2$H$^+$emission regions are reported in Table 4.6.

EXTRACTED SPECTRA FROM IRAM-30M BEAM

In order to compare our results with those obtained by Fontani et al. (2015b) with IRAM-30m observations, we have also extracted spectra from regions that correspond to the IRAM-30m beam around the sources mm1 and mm3, as defined in Table 4.1 (considering mm1a and mm1b at the same coordinates). This was also done to show how much the ^{14}N/^{15}N ratios change going to smaller scales with respect to those observed with single-dish observations. The IRAM-30m beam at 93 GHz is ~27.6″. To be consistent with Fontani et al. (2015b), we have fitted our spectra fixing the T_{ex} equal to those used in their work: 43 K for mm1 and 18 K for mm3. We noted that even though the two main beams are partially overlapping, the dominant emission of each of the two is from the corresponding central source. The extracted spectra from regions equivalent to the IRAM-30m beam are shown in Fig. 4.10 and the results from the fit are listed in Table 4.7.

Table 4.8: ^{14}N/^{15}N ratios derived for ^{15}NNH$^+$ towards P1a, P2a, P3a, and P4a (left) and for N^{15}NH$^+$ towards P1b, P2b, P3b and P4b (right).

Source	T_{ex} (K)	$\frac{N_2H^+}{^{15}NNH^+}$	Source	T_{ex} (K)	$\frac{N_2H^+}{N^{15}NH^+}$
P1a	20	200±34	P1b	20	200±25
	30	186±31		30	217±29
	40	178±29		40	212±27
	50	173±27		50	222±30
P2a	20	180±18	P2b	20	129±17
	30	171±17		30	120±15
	40	156±16		40	108±13
	50	154±15		50	113±14
P3a	20	120±18	P3b	20	100±15
	30	114±17		30	100±16
	40	111±16		40	109±17
	50	109±15		50	100±15
P4a	20	117±14	P4b	20	187±33
	30	112±14		30	182±31
	40	120±15		40	185±33
	50	108±12		50	185±32

4.3.4. ^{14}N/^{15}N RATIOS

We have computed the ^{14}N/^{15}N ratios for N$_2$H$^+$, along with the uncertainties derived propagating the error on total column densities. In Tables 4.8, 4.9 and 4.10 the ^{14}N/^{15}N ratios for the different regions defined in Sect. 4.3.2 and 4.3.3 are given. Since the ratios are obtained from column density values obtained from observations at different spectral resolution, we have carefully evaluated the effects of this data inhomogeneity in Appendix A. There we show that the different spectral resolution does not affect significantly the column densities, and hence the ^{14}N/^{15}N ratios.

In general, we have found values that span from ~100 up to ~220, where the higher values are comparable with those observed with the IRAM-30m (Fontani et al. 2015b). Moreover, the assumption of different T_{ex} does not change the results, that are consistent within the errors. Therefore, in the next Section we will discuss the final results considering a single excitation temperature. Moreover, a different T_{ex} can change the column densities of each molecule, but does not influence their ratios, since the dependence on T_{ex} in the ratio is irrelevant when the two column densities are both computed from the (1–0) transition and the lines are not optically thick. This is supported by the fact that the ratios given in Table 4.8 are the same within the uncertainties, towards each region.

Table 4.9: ^{14}N/^{15}N ratios derived for ^{15}NNH$^+$ and N^{15}NH$^+$ towards I1, I2, I3, and I4.

Source	T_{ex} (K)	$\frac{N_2H^+}{^{15}NNH^+}$	$\frac{N_2H^+}{N^{15}NH^+}$
I1	20	220±32	275±50
	30	214±30	250±41
	40	200±27	257±46
	50	200±28	244±40
I2	20	167±17	143±18
	30	150±15	120±15
	40	136±13	125±16
	50	146±14	127±16
I3	20	100±13	86±12
	30	114±16	89±13
	40	111±15	91±14
	50	109±15	86±12
I4	20	100±14	140±24
	30	100±14	150±29
	40	100±15	137±25
	50	93±14	130±23

4.4. DISCUSSION OF THE RESULTS

4.4.1. COMPARISON BETWEEN LINE AND CONTINUUM EMISSION MAPS

The averaged emission map peaks of the J=1–0 transition of N$_2$H$^+$, ^{15}NNH$^+$ and N^{15}NH$^+$ (Fig. 4.4 and 4.5) present a shift of ~2-3$''$ to the south (for mm1 and mm2) and to the west (for mm3) with respect to the peak continuum sources. In particular, this effect is stronger for mm1, mm2, and mm3 than for mm4. The overall structure of the integrated N$_2$H$^+$(1–0) (and its ^{15}N-isotopologues) consists of three main cores. Two of these are located to the south of the mm1 and mm2 continuum sources, and to the west of the mm3 continuum sources, while the third is located exactly towards the mm4 source. Numerous studies have shown that during the collapse of a low-mass core, the CO desorbs from the grain mantles, because of the rising of the temperature, and this causes substantial destruction of N$_2$H$^+$ (e.g. Di Francesco et al. 2004). The chemical processes at work in high-mass star-forming regions are likely different from those in low-mass star-forming ones, but the destruction of N$_2$H$^+$ by CO should occur in both cases. Towards mm1 the presence of a young massive protostar is well-known (see Sect. 4.2) and the displacement between the dust and N$_2$H$^+$ peak suggests that the heating of the protostar, and probably of the molecular outflows associated with it (Beuther et al. 2002d), may have caused the desorption of CO from grain mantles and the subsequent destruction of N$_2$H$^+$. An evidence that the kinetic temperature is higher towards mm1 is given from the NH$_3$(1,1) observations performed
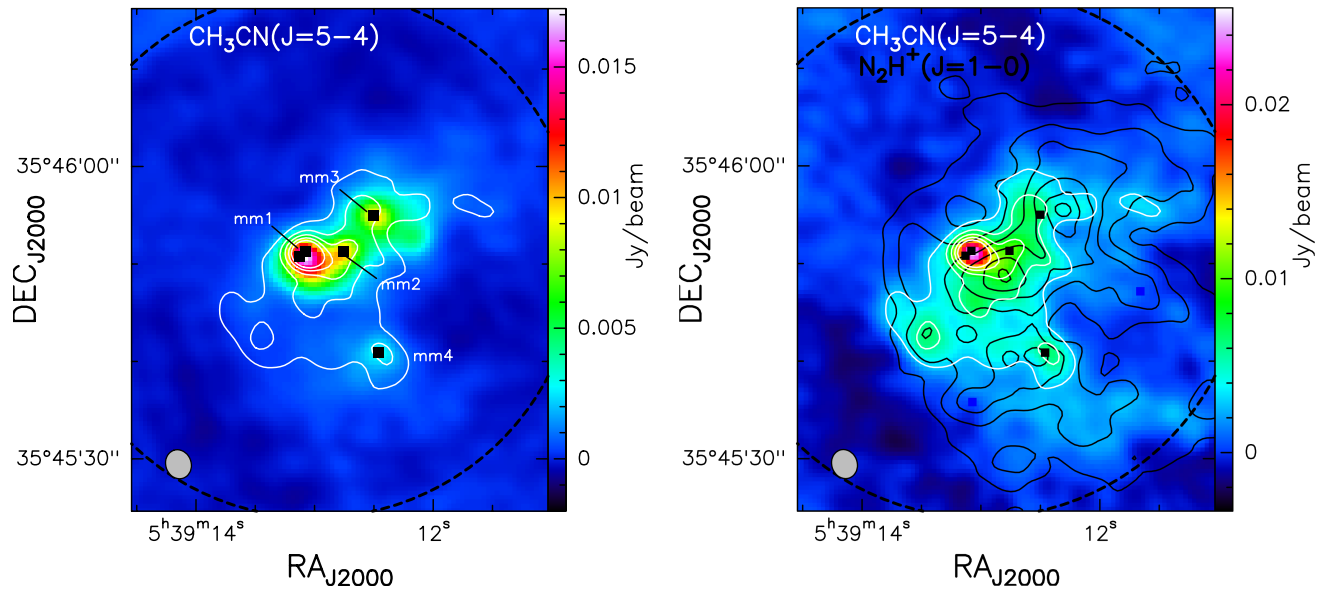
Fig. 4.11: *Left panel*: 3mm continuum intensity of 05358 in color scale (as in Fig. 4.3). The white contours are 5, 10, 15, 20 and 25 times the 1σ rms of the $CH_3CN(5–4)$ map, equal to 0.6 mJy/beam km s^{-1}. *Right panel*: Average emission of $CH_3CN(5–4)$ in color scale, the white contours are the same as in the left panel, and the black contours are those of $N_2H^+(1–0)$ (as in Fig. 4.4). In both panels the black squares indicate the positions of the continuum sources. The dashed circle represents the NOEMA field of view and the synthesized beam is the ellipse indicated in the lower left corner.

by Lu et al. (2014) towards 05358. In particular, they found that towards mm1 and mm2 the temperature is higher than towards the other sources. Probably something similar is happening also around mm3 although we do not have clear evidence that star formation already started. Moreover, the correspondence of the dust and N_2H^+ peak towards mm4 is an evidence that it is chemically less evolved and hence maybe starless. Something similar for high-mass star-forming regions has been reported towards IRAS 23033+5951 (Reid and Matthews 2008) and towards the massive protocluster AFGL 5142 (Busquet et al. 2011). To investigate better this situation we have searched in our spectral setup for other molecules that could better trace the continuum sources and the associated star formation activity. In particular, in Fig. 4.11 the averaged emission map of $CH_3CN(J=5–4, K=0,1)$ is shown. In the left panel the clear correspondence between the 3mm-continuum sources and CH_3CN can be noted; moreover, in the right panel it is evident that CH_3CN and N_2H^+ do not coincide towards mm1, mm2, and mm3, while the core-structure defined by the two different molecules corresponds towards mm4.

As already mentioned in Sect. 4.3.2, in the western and the south-eastern parts of the cluster, two other N_2H^+-emission zones are present. In particular, A corresponds to a core structure in the ^{15}N-isotopologues maps (P4a and P4b in Fig. 4.5) and corresponds also to one of the emission peaks of the high-density tracer $H^{13}CO^+$ defined in Fig. 8 of Beuther et al. (2002d), which is a high-density tracer. However, B presents a more complicated structure, probably related to the presence of multiple outflows in the whole region (outflow *A* in Beuther et al. 2002d). Leurini et al. (2011) discussed the $N_2H^+(1–0)$ emission towards the IRDC G351.77-0.51 and they found a velocity gradient on large scale, probably associated with outflows detected in CO. Although N_2H^+ is seldom associated with outflows, this

could be due to an in interaction of outflow shocks with the molecular envelope (traced also by N_2H^+). A similar situation was detected in the same transitions towards the class 0 object IRAM 04191+1522 by Lee et al. (2005). Moreover, Codella et al. (2013) present the first detection of N_2H^+ towards a low-mass protostellar outflow, L1157-B1, a bow-shock, at ~0.1 pc from the protostellar cocoon L1157.

4.4.2. Is N-fractionation a core-scale effect?

Fontani et al. (2015b) have derived, with the IRAM-30m radiotelescope, $^{14}N/^{15}N$ ratios of 190±20 for $^{15}NNH^+$ and of 180±23 for $N^{15}NH^+$ towards mm1, and of 210±12 for $^{15}NNH^+$ and of 180±13 for $N^{15}NH^+$ towards mm3. Extracting the spectra in regions equivalent to the IRAM-30m beam at 93 GHz, we have derived the $^{14}N/^{15}N$ ratios listed in the lower panel of Table 4.10. These are consistent with the results obtained with the single-dish telescope, within the errors. The comparison of these results with the $^{14}N/^{15}N$ ratios obtained towards P1a, P2a, P3a, and P4a and towards P1b, P2b, P3b and P4b is shown in Fig. 4.12. In particular, it is evident from the left panel of Fig. 4.12 that there is a ^{15}N-enrichment (i.e. a $^{14}N/^{15}N$ ratio significantly lower) towards P2a, P3a, and P4a. The same happens towards P2b and P3b (right panel of Fig. 4.12). This means that at higher angular resolution, where the core scales can be resolved, it is possible to reveal a different N-fractionation with respect to that observed with a single-dish telescope and more representative of the average $^{14}N/^{15}N$ between the cores and the envelope of the whole star-forming region. This suggests that the mechanisms that produce more ^{15}N with respect to ^{14}N in N_2H^+ can occur in smaller regions and could be a local effect. The fact that towards P1a and P1b, $^{14}N/^{15}N$ values consistent with IRAM-30m observations (~200) are found could be explained by the fact that these regions are near an evolved high-mass source (mm1) and the chemistry could be different toward hotter gas. Moreover, the different $^{14}N/^{15}N$ ratios between P4a and P4b, ~115 and ~185, respectively, could be due to a different behaviour of the two ^{15}N-isotopologues, but we will discuss this in the next section.

It should be noted that there is an enrichment in ^{15}N in all the sources compared to the PSN value. In general, the lower $^{14}N/^{15}N$ ratios of ~100–110, are similar to the values measured by Guzmán et al. (2017) towards protoplanetary discs in HCN, and they are also consistent with the low values measured in pristine Solar System materials. However, the N-fractionation of different molecules, like HCN and N_2H^+, could be different, as discussed in chapter 1. To investigate better this point, consistent measurements of N-fractionation from different species in the same sources are needed to understand the puzzle of nitrogen isotopic ratios. Moreover, high angular resolution observations towards other high-mass star-forming regions are needed to confirm these results. In fact, it is also important to gather more data in sources that are good candidates to represent the environment in which our Sun was born. In this respect, intermediate- and high-mass star-forming cores are interesting targets because the Sun was probably born in a rich cluster that also contained massive stars (see Sect. 1.2).

Unfortunately, none of the published chemical models up to now can reproduce the low $^{14}N/^{15}N$ observed in this work. Moreover, they are not able to reproduce observed values of N-fractionation in N_2H^+ in general, as already discussed in Sect. 1.4.4. However, they are models that feature only low-temperature exchange reactions as the only fractionation mechanism (e.g. Roueff et al. 2015; Wirström and Charnley 2018; Loison et al. 2019). Prob-

Table 4.10: ^{14}N/^{15}N ratios derived from ^{15}NNH$^+$ and N^{15}NH$^+$ for D1, D2, and D3 (upper panel). In the lower panel the ^{14}N/^{15}N ratios derived from both ^{15}NNH$^+$ and N^{15}NH$^+$ towards mm1 and mm3 in regions equivalent to the IRAM-30m beam are shown.

Source	T_{ex} (K)	$\frac{N_2H^+}{^{15}NNH^+}$	$\frac{N_2H^+}{N^{15}NH^+}$
D1	20	≥245	≥204
	30	≥231	≥188
	40	≥242	≥200
	50	≥250	≥204
D2	20	336±96	≥154
	30	327±91	≥148
	40	316±87	≥143
	50	292±77	≥140
D3	20	≥243	≥340
	30	≥250	≥321
	40	≥261	≥353
	50	≥250	≥333
Source	T_{ex} (K)	$\frac{N_2H^+}{^{15}NNH^+}$	$\frac{N_2H^+}{N^{15}NH^+}$
mm1	43	219±22	180±33
mm3	18	217±23	192±32
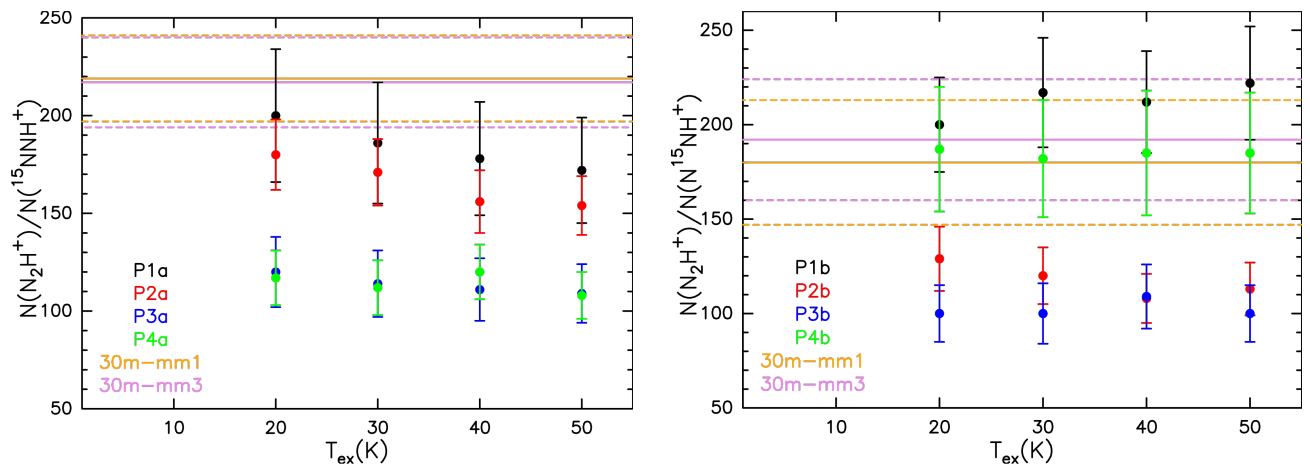
Fig. 4.12: *Left panel*: ^{14}N/^{15}N ratios obtained from ^{15}NNH$^+$, as a function of the different T_{ex} assumed, towards P1a (black points), P2a (red points), P3a (blue points) and P4a (green points). *Right panel*: same as in the left panel but for N^{15}NH$^+$ towards P1b (black points), P2b (red points), P3b (blue points) and P4b (green points). In both panels the orange solid line is the value obtained in a polygon equal to the IRAM-30m beam towards mm1 (the dashed lines correspond to the error bar) and the pink line is the same but towards mm3. The T_{ex} assumed to compute the ^{14}N/^{15}N ratios toward 30m-mm1 and 30m-mm3 are equal to those derived in Fontani et al. (2015b): 43 K for mm1 and 18 K for mm3.
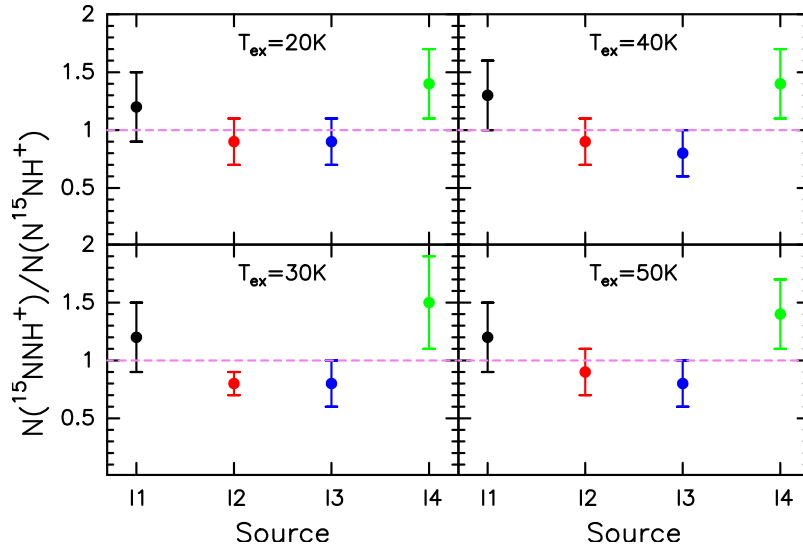
Fig. 4.13: $^{15}NNH^+/N^{15}NH^+$ ratios towards I1 (black points), I2 (red points), I3 (blue points) and I4 (green points). Different panels show the results with the different T_{ex} assumed. The pink solid line represents the locus of points where $^{15}NNH^+/N^{15}NH^+=1$.

ably other mechanisms must be taken into account, as the isotope selective photodissociation of N_2, as proposed by Furuya and Aikawa (2018). We will discuss this possibility more in detail in Sect. 4.4.4.

4.4.3. $^{15}NNH^+$ vs $N^{15}NH^+$

In this section, we will discuss the possible differences between the two ^{15}N-isotopologues of N_2H^+: $^{15}NNH^+$ and $N^{15}NH^+$. To do that, we have compared the $^{14}N/^{15}N$ ratios obtained for $^{15}NNH^+$ and $N^{15}NH^+$ towards I1, I2, I3, and I4, since the column densities of the two ^{15}N-isotopologues were derived from the same regions.

In Fig. 4.13 the $^{15}NNH^+/N^{15}NH^+$ column density ratios, for the different excitation temperatures assumed, are shown. In this case, the dependence on the T_{ex} is small because both the ^{15}N-isotopologues are almost optically thin. We have found that $^{15}NNH^+$ is more abundant (at 1σ level) with respect to $N^{15}NH^+$ towards I4, and the contrary towards I1, I2, and I3.

Concerning what happens towards I4, it is difficult to interpret our results from an evolutionary point of view, because the nature of this source is unknown (as already mentioned in Sect. 4.4.1). In this case, the ratio between the two ^{15}N-isotopologues is higher than one, also including the errorbar. This could be a clue that in some particular cases of densities and temperatures the two ^{15}N-isotopologues could form through different reaction pathways. This finding should also be confirmed by a higher statistics.

As already mentioned, the most recent chemical models are not able to reproduce a different behaviour between the two ^{15}N-isotopologues. Other works toward very different environments show a tentative trend of $^{15}NNH^+$ to be less abundant than $N^{15}NH^+$: Kahane et al. (2018) towards OMC-2 FIR4 ($^{15}NNH^+/N^{15}NH^+\sim 0.8$) and Redaelli et al. (2018) towards the prestellar cores L1544 and L694-2 ($^{15}NNH^+/N^{15}NH^+\sim 0.9$ and ~ 0.8, respectively).

4.4.4. ^{14}N/^{15}N RATIOS IN DIFFUSE REGIONS

In Tab. 4.10 the results obtained towards the more diffuse N_2H^+ emission regions D1, D2, and D3 are shown. All of these results are lower limits since the ^{15}N-isotopologues were not detected, except for ^{15}NNH$^+$ towards D2. The lower limit values obtained are, on average, higher than 200–250. These are also the maximum values obtained towards the peak-emission regions. Only the lower limits towards D2 from N^{15}NH$^+$ are smaller, but given that the detection from ^{15}NNH$^+$ confirms a ^{14}N/^{15}N ratio of ~320, and that we have found a maximum difference of ~1.5 (see the previous Section), we can confirm that this lower limits corresponds to ^{14}N/^{15}N ratios higher than 200. These results mean that ^{15}N tends to be less enriched in N_2H^+in the outer parts of a star-forming region. This could be a confirmation of the work of Furuya and Aikawa (2018). In fact, since N_2H^+ is a daughter molecule of N_2, the ^{14}N/^{15}N ratio of N_2H^+ should follow the behaviour of N_2 and increase towards the NI/N_2 transition zones. Here, the gas is less dense and the interstellar UV radiation field is not significantly attenuated (A_v<3 mag), the ^{15}N is frozen in NH_3 ice and there is a loss of ^{15}N from the gas phase.
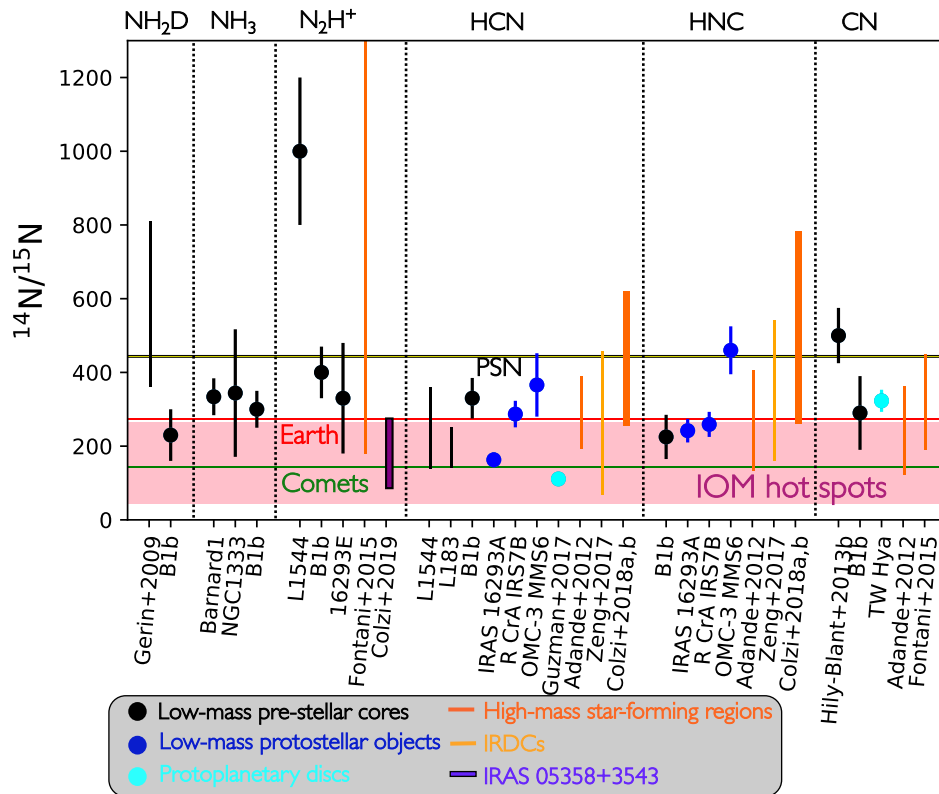
Fig. 4.14: Same as in the upper panel of Fig. 3.16 updated with values found by Colzi et al. (2019). For more details about the distribution of values found by Colzi et al. (2018a) and Colzi et al. (2018b) see lower panels of Fig. 3.16.

ENVELOPE
- Isotope selective photodissociation of N_2
- ^{15}N locked on grains

    $^{14}N/^{15}N$ ⬇

    $^{14}N^{14}N/^{14}N^{15}N$ ⬆

CORE
- Ice sublimation → desorption of ^{15}N in gas phase
- Photodissociation inefficient

    → Initial $^{14}N/^{15}N$

$N_2H^+/^{15}NNH^+ > 250$

$N_2H^+/^{15}NNH \sim 100$

$HCN/HC^{15}N = x$

$HCN/HC^{15}N < x$

Regarding the envelope...

N_2H^+ follows N_2
→ $N_2H^+/^{15}NNH^+$ ⬆

FUV

HCN follows N
→ $HCN/HC^{15}N$ should ⬇

5''

>15''
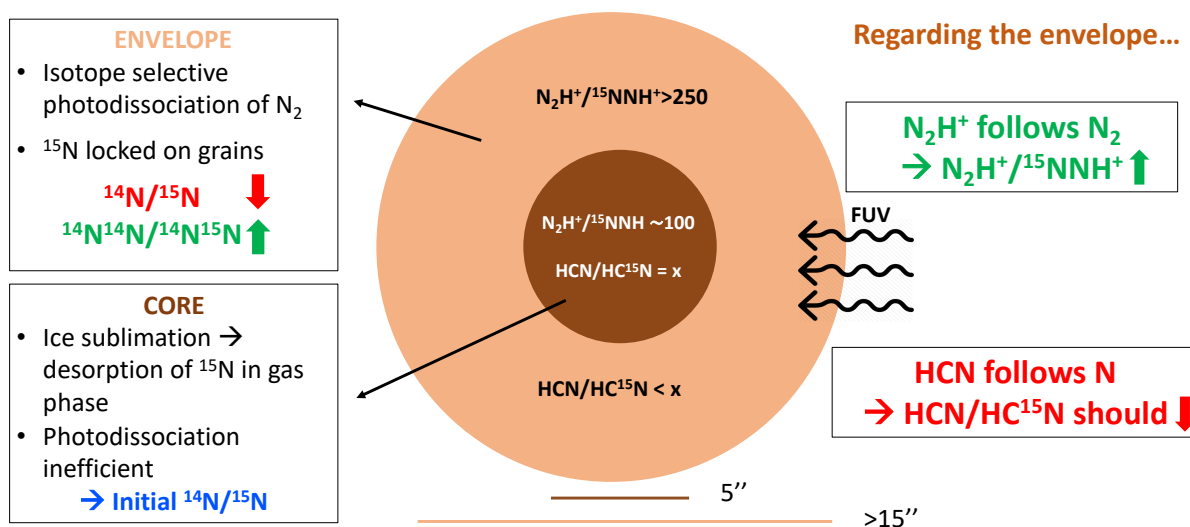
Fig. 4.15: Schematic view of the results obtained in this work (Colzi et al. 2019), with N_2H^+ and its ^{15}N-isotopologues interferometric observations, together with the possible explanation given by the model of Furuya et al. (2018). In particular, the light brown regions corresponds to the diffuse $N_2H^+(1-0)$ emission regions, in which isotope-selective photodissociation of N_2 is still important. Dark brown regions corresponds to regions in which photodissociation is not efficient and desorption of ice species could be important. Note that the extended light brown region could be detected only after the merging with zero spacing data provided by single-dish observations.

4.5. Conclusions

We used the IRAM NOEMA Interferometer to observe the emission of $N_2H^+(1-0)$ and its ^{15}N-isotopologues towards the high-mass star-forming protocluster IRAS 05358+3543. The N_2H^+ dense gas emission consists of three main cores, two of which are displaced with respect to the 3mm continuum sources, probably because of the star-formation activity that causes the N_2H^+ destruction by CO desorption from grain mantles. We have also discussed the presence of two other N_2H^+-emission zones: A and B. The first define a fourth core from the ^{15}N-isotopologues emission maps and corresponds to a $H^{13}CO^+$ peak observed in previous works. The second is probably associated with an outflow coming out from the more evolved region in the north.

The $^{14}N/^{15}N$ ratios derived toward regions that correspond to the IRAM-30m beam are higher than those from the cores of the cluster. This indicates the possibility that ^{15}N-enrichment in star-forming regions is a local effect. Fig. 3.16 was implemented with the range of values derived in this work (Fig. 4.14). The lower values of ~ 100 toward the cores are similar to some values measured in protoplanetary discs, and also to the low values measured in the pristine Solar System material. Moreover, the $^{14}N/^{15}N$ ratios derived from $^{15}NNH^+$ and $N^{15}NH^+$ show some differences. In particular, towards I1 and I4 $^{15}NNH^+$ is more abundant than $N^{15}NH^+$. However, the most recent chemical models are not able to reproduce the $^{14}N/^{15}N$ values found for N_2H^+ in this work and in other works.

Finally, the $^{14}N/^{15}N$ upper limits derived in the more diffuse N_2H^+ emission regions of the cluster, point to values higher than those derived in the cores. This confirms the conclusion that N-fractionation, measured from N_2H^+, seems to be a local effect, at least in this high-mass star-forming region.

However, more observations, also of different molecules, are needed to unveil which

physical parameters are affecting the N-fractionation, thus helping us to gain understanding on the chemistry involved. In fact, the findings described in this chapter are in agreement with the isotope-selective photodissociation of N_2 scenario proposed by Furuya and Aikawa (2018): the values of the $^{14}N/^{15}N$ ratios for N_2H^+ found in the diffuse clumps are higher than that measured in the central cores, where isotope-selective photodissociation is not efficient any more. Unlike N_2H^+, the proposed theoretical model predicts that nitriles (HCN and HNC) should have lower $^{14}N/^{15}N$ values in the diffuse envelope than in the central cores (Fig. 4.15). This proposed scenario seems to be in agreement with the results found by Adande and Ziurys (2012) and those described in chapter 3, which, as already explained in Sect. 3.4.2, trace different spatial scales. Adande and Ziurys (2012) found $^{14}N/^{15}N$ ratios for nitrile-bearing species on scales of ~1 pc that are lower than those derived in our work in smaller scales of ~0.4 pc. This could be explained if extended and less-dense gas contributes to lower the $^{14}N/^{15}N$ values. To fully probe the proposed model, higher angular resolution observations of N-fractionation of nitriles with interferometers are needed.

5

CARBON ISOTOPIC FRACTIONATION: A NEW DETAILED CHEMICAL STUDY

ABSTRACT

^{12}C/^{13}C ratio has been studied from a theoretical point of view introducing the two fundamental processes that could create a different isotopic ratio in molecules with respect to the initial elemental one: isotope-selective photodissociation and isotopic-exchange reactions. Recent chemical models predict that exchange reactions may lead to ^{13}CO enrichment. This leads to a dilution of ^{13}C in the other gas-phase molecular species, and ^{12}C/^{13}C ratios two times higher than those observed across the Galaxy. Since the carbon isotopic ratio is also used to evaluate the nitrogen isotopic ratio with the double isotope method, it is important to study carbon fractionation in detail.

In this work we implemented a gas+grain chemical model with new isotopic-exchange reactions and we have investigated their introduction in the context of the dense and cold molecular gas, where both low- and high-mass stars can form. We found that the isotopic-exchange reaction ^{13}C + ^{13}C → ^{12}C +^{13}CC$_2$ leads to ^{12}C/^{13}C ratios that tend to 68, or lower values, for molecules that are formed starting from atomic carbon. This effect is efficient in a range of time between the formation of CO and its freeze-out on grain surfaces. Moreover, we investigated a grid of models, with T=10–50 K and n(H)=2×10^3–2×10^7 cm^{-3}, showing that the ^{12}C/^{13}C ratios of the nitrile-bearing species HCN and HNC, are predicted to be a factor 0.8–1.7 different from the usually assumed value of 68. Finally, we are also able to reproduce some of the observed values towards low-mass star-forming regions for CN, HCN, and HNC.

5.1. INTRODUCTION

As already discussed in chapter 1, the variations in isotopic ratios may give important information about the link between Solar system objects and Galactic interstellar environments (e.g. Caselli and Ceccarelli 2012; Hily-Blant et al. 2013a; Hily-Blant et al. 2013b; Ceccarelli et al. 2014; Colzi et al. 2018a; Colzi et al. 2018b and Colzi et al. 2019).

One element for which fractionation is important is carbon. C-fractionation in dense interstellar clouds has been studied with different models of time-dependent chemistry.

Langer et al. (1984) introduced different isotopic exchange reactions in their model, as proposed by Watson et al. (1976). In particular, they proposed that C-fractionation in interstellar species is a result of the isotopic-exchange reaction

$$^{13}C^+ + {}^{12}CO \leftrightarrow {}^{13}CO + {}^{12}C^+ + 35 \text{ K}. \tag{5.1}$$
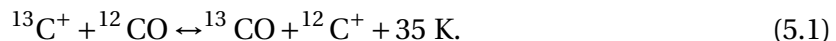
They concluded that the lower the temperature, the higher the chemical fractionation of C-bearing species. Smith and Adams (1980) introduced another isotopic exchange reaction:

$$HCO^+ + {}^{13}CO \leftrightarrow H^{13}CO^+ + CO + 9 \text{ K}, \tag{5.2}$$
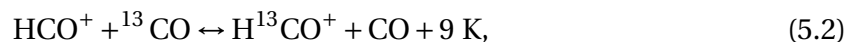
which was found to be important in a low temperature (~20 K) environment. However, more recently, this reaction has been revised and Mladenović and Roueff (2014) determined a new value of 17.4 K for the exothermicity. Subsequently, the photodissociation of CO by ultraviolet (UV) photons has been taken into account. This process is entirely governed by excitation in pre-dissociative states, which are quasi-bond excited states of molecules from which an internal conversion to an unstable excited state (without emission of radiation) takes place and leads to dissociation. Then, the photodissociation of CO is a line process and in the ISM the lines become saturated at a ^{12}CO column density of about 10^{15} cm^{-2} (self-shielding). At this point the photodissociation rate of ^{12}CO decreases and the ^{13}CO isotopologue is less abundant than ^{12}CO since its self-shielding becomes important deeper into the cloud. Reaction (5.1) is then interesting because in the outer regions of a molecular cloud ($0.5 < A_v < 2$ mag), where CO is effectively self-shielded, the $^{13}C^+$ abundance is very large, contrary to that of ^{13}CO. This difference leads to isotope-selective photodissociation. Given that the exact visual extinction values depend on the strength of the FUV field and on the density distribution, the selective photodissociation of ^{12}CO is expected to be dominant in low density ($n<10^2$ cm^3) environments, or denser regions with a strong radiation field (Röllig and Ossenkopf 2013). Moreover, where 2 mag $< A_v < 5$ mag, both ^{12}CO and ^{13}CO are protected from the radiation field and reaction (5.1) is now the only way to produce a difference between ^{12}CO and ^{13}CO. All of these processes are summarised in Fig. 5.1 (Szűcs et al. 2014).

Röllig and Ossenkopf (2013) found, with their photodissociation region (PDR) model, that $^{12}CO/^{13}CO$ is always the same as the $^{12}C/^{13}C$ elemental ratio (~68), while Visser et al. (2009), were able, with their PDR model, to reproduce both higher and lower values with respect to the elemental ratio, as a function of H$_2$ column density. In fact, Visser et al. introduce Alfvén waves in their code, that have the effect of replacing the kinetic temperatures (T_{kin}), in the rate equation of ion-neutral reactions, by an effective temperature (T_{eff})

$$T_{eff} = T_{kin} + \frac{\mu v_a^2}{3k} \tag{5.3}$$

where μ is the reduced mass of the reactants and v_A is the Alfvén velocity. In this sense, they demonstrated that non-thermal effects can take place and modify the $^{12}CO/^{13}CO$ ratio.

Observationally, numerous studies of the $^{12}C/^{13}C$ ratio have been conducted toward molecular clouds in the Galaxy, but most of them through observations of CO, H$_2$CO and HCO$^+$ that, as stated before, have the possible effects of isotopic-selective photodissociation and/or chemical fractionation (e.g. Wilson and Rood 1994; Langer and Penzias 1990 and Langer and Penzias 1993). To estimate the $^{12}C/^{13}C$ elemental ratio across the Galaxy,
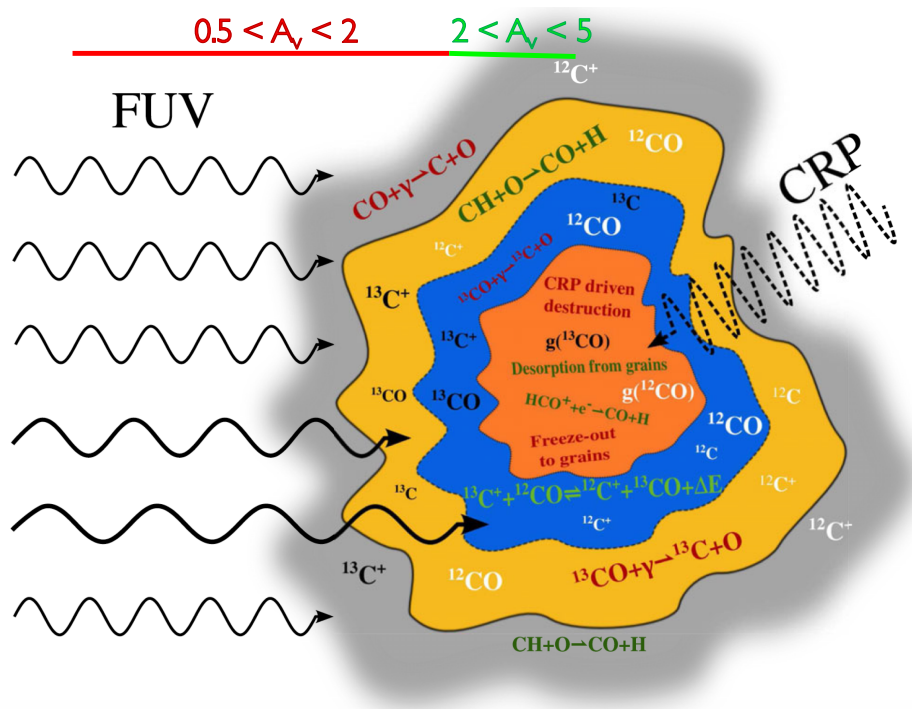
Fig. 5.1: Scheme of carbon isotopic chemistry in molecular clouds. The outer diffuse layer (grey) is followed by the translucent (yellow and blue) and the inner, dense regions (orange). In particular, the yellow and external blue zones are where $0.5 < A_v < 2$ mag and the inner blue and the orange regions are those where 2 mag < $A_v < 5$ mag. The font size of the chemical species relates to the abundance of the species in the region. The font size of chemical reactions indicates the importance of the reaction in the region, while the green and red colours represent reactions producing and destroying CO, respectively. Figure based on van Dishoeck and Black (1988) and taken from Szűcs et al. (2014).

Milam et al. (2005) observed ^{12}CN and ^{13}CN toward Galactic molecular clouds. They found the Galactocentric trend:

$$[^{12}\mathrm{C}/^{13}\mathrm{C}]_{\mathrm{CN}} = (6.01 \pm 1.19)\ \mathrm{kpc}^{-1} \times \mathrm{D_{GC}} + (12.28 \pm 9.33), \qquad (5.4)$$

and then the average local present-day ^{12}C/^{13}C is 68±15 (at a Sun distance D_{GC} = 7.9 kpc, as derived by Hunt et al. (2016) and Boehle et al. (2016)). More recently, Yan et al. (2019) presented $\mathrm{H_2CO}$ and $\mathrm{H_2^{13}CO}$ observations towards a sample of 112 sources from which they evaluated a new ^{12}C/^{13}C trend as a function of $\mathrm{D_{GC}}$. They obtained the following linear fit:

$$[^{12}\mathrm{C}/^{13}\mathrm{C}]_{\mathrm{H_2CO}} = (5.08 \pm 1.10)\ \mathrm{kpc}^{-1} \times \mathrm{D_{GC}} + (11.86 \pm 6.60), \qquad (5.5)$$

which is consistent within the errors with that found by Milam et al. (2005).

Daniel et al. (2013) performed a NON-LTE analysis of HCN, HNC and CN and their ^{13}C-isotopologues towards the pre-stellar core B1b. They found HNC/HN^{13}C=20^{+5}_{-4}, HCN/H^{13}CN=30^{+7}_{-4}, and CN/^{13}CN=50^{+19}_{-11}. More recently, Magalhães et al. (2018) obtained, towards the starless core L1498, a HCN/H^{13}CN ratio of 45±3, showing that HCN is enriched in ^{13}C with respect to the local ISM value (^{12}C/^{13}C = 68).

Knowing the exact value of the ^{12}C/^{13}C ratio is also important for computing ^{14}N/^{15}N ratio for nitrile-bearing species since most studies use the so-called double isotope method (e.g Wampfler et al. 2014, Zeng et al. 2017, Colzi et al. 2018a, Colzi et al. 2018b). This is

based on observations of optically thin species (with ^{13}C instead of ^{12}C, e.g. H^{13}CN, HN^{13}C), as done in the analysis of data in chapters 2 and 3. However, this method works only if the ^{13}C-fractionation effects remain small for the considered species. All of the observed ^{12}C/^{13}C abundance ratios listed in the previous paragraph are not consistent with the values predicted by chemical models for species like CN, HCN, and HNC. In fact, as already discussed in chapter 2, ^{13}C chemical fractionation may affect the abundances, and also the ^{14}N/^{15}N of nitrile-bearing species. This behaviour is typically not taken into account in chemical models inclusive of ^{15}N-bearing species. As shown in Fig. 5.2, the dilution of ^{13}C for nitriles and isonitriles is at most of a factor of 2 and it is derived from chemical models with a fixed kinetic temperature of 10 K. The predictions of this model must, therefore, be verified and new studies are needed. Moreover, Roueff et al. (2015) also studied C-fractionation for C, CH, CO and HCO$^+$ showing that the ^{12}C/^{13}C ratio is highly time-dependent (see Fig. 5.3). In fact, since the start of the simulation, ^{13}C$^+$ forms ^{13}CO through reaction (5.1). For a similar reason, CN is enriched in ^{13}C with similar time scales compared to ^{13}C-enrichment in CO, due to the reaction:

$$^{13}C^+ + CN \rightleftharpoons {}^{12}C^+ + {}^{13}CN. \tag{5.6}$$

Reaction (5.2) becomes important once ^{13}C$^+$ starts to disappear from the gas phase. HCO$^+$ is then enriched in ^{13}C until all the ^{13}CO that was in excess with respect to ^{12}CO is used (i.e. until CO/^{13}CO comes back to the initial value of 68). The chemical model of Roueff et al. (2015) reached a steady state at about 10^6 yr. At this time C, CH, HCN, HNC and CN are depleted in ^{13}C. This is related to reactions (5.1) and (5.2) that continue to be important and retain all the ^{13}C in HCO$^+$ and CO.
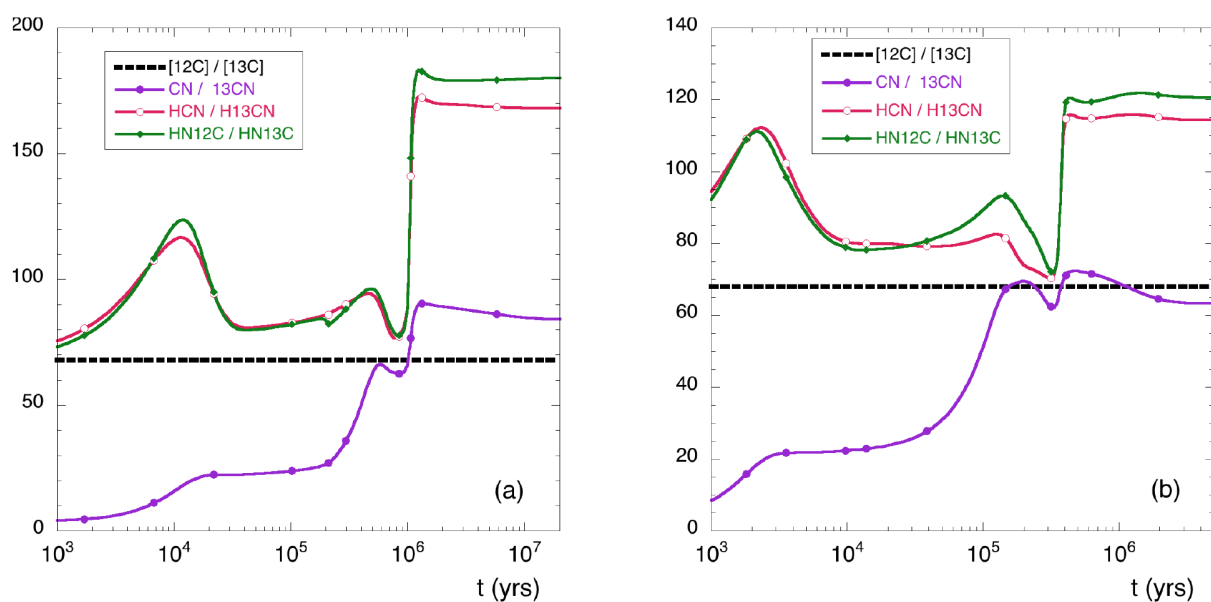
Fig. 5.2: Time evolution of ^{12}C/^{13}C ratios for CN, HCN and HNC as predicted by Roueff et al. (2015), for model (a) and (b) described in Sect. 1.4.4 (left and right panel, respectively). In both panels the black horizontal dashed line represents the initial ^{12}C/^{13}C ratio of 68. Taken from Roueff et al. (2015).

In this work we present a study of C-fractionation in different environments typical in astrochemical studies. A description of the chemical model used in this work is described in Sect. 5.2 and the results are presented in Sect. 5.3.
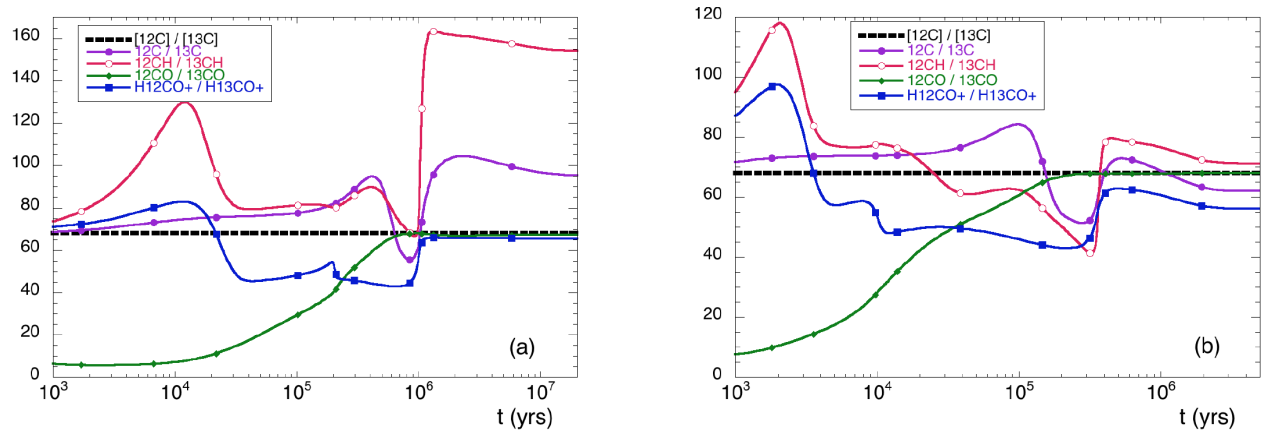
Fig. 5.3: Time evolution of $^{12}C/^{13}C$ ratios for C, CH, CO and HCO$^+$ as predicted by Roueff et al. (2015), for model (a) and (b) described in Sect. 1.4.4 (left and right panel, respectively). In both panels the black horizontal dashed line represents the initial $^{12}C/^{13}C$ ratio of 68. Taken from Roueff et al. (2015).

5.2. MODEL

5.2.1. CHEMICAL MODEL

Our chemical code is based on the one described in Sipilä et al. (2015a), recently updated to include several new chemical processes (Sipilä et al. 2019). The code solves rate equations for gas-phase and grain-surface chemistry.

GAS-PHASE REACTIONS

The reaction rate coefficients for neutral-neutral and ion-neutral reactions used in the model are already given in Sect. 1.3.2. Here we give the reaction rates for other processes not discussed before, such as photodissociation, cosmic-ray ionisation and so on. The photodissociation reactions, i.e. those where an external photon ionizes a neutral species, rate coefficient is:

$$k_{\text{photo}} = \alpha \exp\left(-\gamma_1 A_V\right), \tag{5.7}$$

where A_V is the visual extinction and γ_1 is an efficiency factor. Moreover, for direct cosmic-ray ionisation reactions the rate coefficient is:

$$k_{\text{CR}} = \gamma_2 \zeta, \tag{5.8}$$

where ζ is the H$_2$ cosmic-ray ionisation rate and γ_2 is again an efficiency factor. We have also taken into account cosmic-ray induced secondary photo-reactions (e.g. Gredel et al. 1989). In fact, the inner parts of a dense core are shielded from UV photons, that can only be created through H$_2$ ionisation induced by cosmic rays. The rate coefficient is defined as:

$$k_{\text{SEC–PHOT}} = \frac{\alpha_{sec}\beta_{sec}\zeta}{1-\omega}, \tag{5.9}$$

where α_{sec} is the branching ratio of the reaction, β_{sec} is the ionisation/dissociation probability, and ω is the grain albedo. We have used the list of reactions and efficiency factors in the current version of the KIDA network (Wakelam et al. 2015) applying the data given

by Heays et al. (2017). Moreover, we add a special subset of reactions in gas-phase that are those involving grains. In particular, negatively charged and neutral grains are important to neutralise atomic ions. In this case the rate coefficient is multiplied by the so-called J-factor that takes into account the increased efficiency of such a reaction due to the charge difference (see e.g Draine and Sutin 1987).

GAS AND GRAIN INTERACTIONS

Gas-phase and grain-surface chemistry are connected through adsorption and (non-) thermal desorption. Adsorption occurs when gas-phase species collide and stick onto grain surfaces[1]. The adsorption rate coefficient is given by:

$$k_i^{\mathrm{ads}} = v_i \sigma S, \tag{5.10}$$

where v_i is the thermal speed of species i, σ is the cross-section of grains and S is the sticking coefficient. For the latter we have assumed temperature-dependent sticking coefficients for H (Cuppen et al. 2010), H_2, N_2, CO, O_2 and CH_4 (He et al. 2016). Desorption from grain surfaces can occur thermally (thermal desorption). The rate coefficient is:

$$k_i^{\mathrm{des,th}} = v_i \exp\left(-E_i^{\mathrm{b}}/T_{\mathrm{dust}}\right), \tag{5.11}$$

where v_i is the characteristic vibration frequency and E_i^{b} is the binding energy of species i. The binding energies considered in this work, corresponding to a water-ice surface, are listed for some selected species in Table 5.1. In general, binding energies are taken from Garrod and Herbst (2006).

We have also considered non-thermal desorption reactions, due to cosmic-ray impacts with grains for which the rate coefficient is:

$$k_i^{\mathrm{des,CR}} = 3.16 \times 10^{-19} \times \left(f_{\mathrm{CR}}(\mathrm{s}^{-1})/1.3 \times 10^{-17}(\mathrm{s}^{-1})\right) k_i^{\mathrm{des,th}}(70\mathrm{K}), \tag{5.12}$$

where f_{CR} is the cosmic ray flux in s^{-1}, units of the cosmic-ray ionisation rate (Hasegawa and Herbst 1993). Another non-thermal desorption mechanism taken into account is the photodesorption, with a rate coefficient defined as:

$$k_i^{\mathrm{des,phot}} = F_{\mathrm{phot}} G_{\mathrm{CR}} \gamma_{\mathrm{phot}} \sigma, \tag{5.13}$$

where F_{phot} is the flux of interstellar UV photons (10^8 photon cm^{-2} s^{-1}, Mathis et al. 1983), G_{CR} is the efficiency of cosmic-ray production by the ultraviolet flux (fixed to be 10^{-3}) and γ_{phot} is the photodesorption yield. We considered the photodesorption of CO, H_2O, CO_2, N_2 and, NH_3, for which the photodesorption yields are 2.7×10^{-3}, 1×10^{-3}, 1.2×10^{-3}, 3×10^{-4} and 1×10^{-3}, respectively (Öberg et al. 2009a; Öberg et al. 2009b). Finally, we have also considered the so-called chemical desorption, that can occur when the excess energy from a grain-surface reaction is in part adsorbed by the dust grain and in part transformed in kinetic energy of the formed molecule. In this way the molecule does not dissociate and there is a certain probability that this molecule leaves the grain surface. The efficiency of this process could change depending on the reaction and on the type of surface; we have chosen a constant efficiency of 1%. For more detail see Garrod et al. (2007) and Vasyunin et al. (2017).

---

[1]   This is commonly called either depletion or freeze-out.

Table 5.1: Binding energies of some selected species. For comparison, the binding energies available in the KIDA database are shown in the third column.

Species	Binding energy (K)	
	This work	KIDA database
H	450^a	650±195
H_2	500^b	440±132
C	800^a	$10000±3000^d$
CH	925^a	–
CH_2	1050^a	1400±420
N	800^a	720±216
N_2	1000^a	1100±330
O_2	1000^c	1200±360
CO	1150^a	1300±390
O	1390^a	1600±480
NH	2378^a	2600±780
OH	2850^a	4600±1380
NH_2	3956^a	3200±960
NH_3	5534^a	5500±1650
H_2O	5700^a	5600±1680
HCN	2050^a	3700±1110
HNC	2050^a	3800±1140
CN	1600^a	2800±840
C_3	2400^a	2500±750
HC_3N	4580^a	–

[a] Garrod and Herbst (2006).
[b] Taquet et al. (2014).
[c] Bergeron et al. (2008).
[d] This value is significantly different to the one we use in our model. However, Das et al. (2018) derived a binding energy of 660, comparable with the value we use, taking into account a mantle made of water tetramer.

GRAIN SURFACE REACTIONS

For grain surface reactions we have considered the Langmuir-Hinshelwood mechanism (Langmuir 1922; Hinshelwood 1940), for which two physisorbed species[2] can react when they meet in a binding site. The rate coefficient for these reactions is given by:

$$k_{ij} = \alpha_g \kappa (D_i^{th} + D_j^{th})/n_g, \tag{5.14}$$

where n_g is the number density of grains, α_g is the branching ratio and D_i^{th} is the thermal diffusion rate of species i, defined as:

$$D_i^{th} = \frac{\nu_i}{N_s} \exp(-E_i^{diff}/T_{dust}), \tag{5.15}$$

---

[2] The physisorption is the mechanism with which a species is bound on the grain surface thanks to the Van der Waals force.

where N_s is the number of binding sites on a grain, assuming a spherical geometry and E_i^{diff} is the diffusion energy of species i, that is directly defined from its relation with the binding energy of species i, $E_i^{\text{diff}} = \epsilon E_i^{\text{b}}$. The parameter ϵ is a source of uncertainty in chemical models and is typically assumed to be from 0.3 up to 0.8 (e.g. Ruffle and Herbst 2000, Vasyunin et al. 2017). In this work we have assumed a value of 0.6. However, we have checked that assuming a lower value of 0.3 our results remain the same, and so are not dependent on this parameter. Moreover, the efficiency factor κ is 1 if the activation energy (E_a) is 0, while for reactions with non-zero activation energy we take into account quantum tunnelling effects, in which case κ becomes:

$$\kappa = \exp\left[-2(a/\hbar)\sqrt{(2\mu k_B E_a)}\right], \tag{5.16}$$

where μ is the reduced mass and a is the barrier width of quantum tunnelling (here defined to be 10^{-8} cm).

5.2.2. INTRODUCTION OF ^{13}C-FRACTIONATION IN THE CHEMICAL MODEL

In this work we have modelled the isotopic fractionation of carbon by introducing the isotope ^{13}C to the KIDA gas-phase network (Wakelam et al. 2015) using a procedure similar to that used for generating deuterated networks (Sipilä et al. 2013; Sipilä et al. 2015b).

As an example of the fractionation-generation procedure, let us consider the reaction

$$H + CCN \longrightarrow C + HCN. \tag{5.17}$$

Here, the ^{13}C atom can be introduced in CCN in two positions that are considered equivalent. From a chemical standpoint, the position of the ^{13}C atom is important and may impact the reactivity of the molecule, but here we make the simplifying assumption that the order of carbon atoms is not tracked. Even if we do not consider the position of ^{13}C in molecules with multiple carbon atoms, significant differences in abundances have been observed. For example, Sakai et al. (2010) observed the N=1–0 lines of CCH and its ^{13}C-isotopic species towards the dark cloud TMC-1 and the star-forming region L1527. They investigated the ^{13}C-species abundances and the possible different formation pathways. They found a C^{13}CH/^{13}CCH ratio of 1.6±0.4 and 1.6±0.1 towards TMC-1 and L1527, respectively. They proposed that the reaction

$$CH_2 + C \rightarrow C_2H + H \tag{5.18}$$

could make a difference between the formation of the two ^{13}C-isotopic species of C$_2$H. Recently, Taniguchi et al. (2019) found similar results towards L1521B and L134N. However, to test this result is beyond the aims of this work and we will reconsider to track the position of ^{13}C in future studies. In this way the number of reactions that we have obtained remains tractable.

Then, the following branches will be generated once ^{13}C is substituted in reaction (5.17):

$$H + C^{13}CN \xrightarrow{1/2} C + H^{13}CN \tag{5.19}$$

$$H + C^{13}CN \xrightarrow{1/2} {}^{13}C + HCN \tag{5.20}$$

$$H + {}^{13}C^{13}CN \xrightarrow{1} {}^{13}C + H^{13}CN, \tag{5.21}$$

where the branching ratio is displayed above the arrow. Essentially, we calculate the probability of a given branch based on the positions that the ^{13}C atom can appear in the *product* side of the reaction. The same rule is applied to most reactions, i.e., the inherent assumption is that the reactions proceed via full scrambling, which is not universally true. Notable exceptions to the full-scrambling rule are charge-exchange reactions and proton-donation reactions, for which we consider that carbon atoms cannot be interchanged in the reaction. Mass and/or energy corrections to the rate coefficients of the reactions due to isotopic effects are not made in general, except for selected important exchange reactions discussed in Sect. 5.2.3. The same fractionation procedure is applied to our grain-surface network (Sipilä et al. 2019).

We do not consider fractionation for all carbon-containing reactions included in KIDA, or in our surface network, to maintain relative simplicity while still including the chemistry that is essential for modeling carbon fractionation properly. First, we discard all reactions that contain molecules with more than five atoms. So, for example, cyanoacetylene (HC_3N) is included in our models while methanol (CH_3OH) is not. Second, we only perform the fractionation procedure for reactions that contain molecules with up to three carbon atoms, and so our final networks do not contain species like $C_3{}^{13}CH$. With these restrictions our final networks (gas-phase and grain-surface) contain a combined total of ~11500 reactions.

5.2.3. ISOTOPIC EXCHANGE REACTIONS

In this work we have examined the behaviour of C-fractionation in a low-temperature environment ($T_{gas} \leq 50$ K). Isotopic-exchange reactions are very important in these cold environments and could differentiate the behaviour of the ^{12}C/^{13}C ratio in different molecules. As already discussed in Sect. 5.1, Roueff et al. (2015) studied the ^{12}C/^{13}C ratio of some molecules introducing some isotopic-exchange reactions. For this work we have updated the list of exchange reactions. The considered reactions are listed in Table 5.2.

As noticed in Roueff et al. (2015), these reactions are taken into account when no other exothermic channel is available. We now discuss the reactions showed in the bottom panel of Table 5.2. To quantify the efficiency of these possible exchange reactions, we have computed the variation of the involved Zero point Energies (ZPEs) assuming that the reactions take place via an intermediate complex (e.g. type of reaction B as described in Sect. 1.4.4). Since no experimental data is available, we have assumed a pre-exponential factor. As already discussed in Sect. 1.3.2, for ion-neutral reactions we could use the rate given by the Langevin formula (eq. (1.20)). However, this value highly depends on the assumption that only the long-range part of the interatomic potential plays a role in the reaction and then they are very uncertain. Thus, we have decided to use guesses depending on the reaction. In particular, for reactions (6), (7), and (9) of Table 5.2 we have used the Langevin rate. For reaction (11) we have used a rate of 9.5×10^{-10} cm^3 s^{-1}, that is of the same order of the Langevin rate (1.7×10^{-09} cm^3 s^{-1}) with a reduction factor of about 2 to account for the two different possible positions of the ^{13}C nucleus in C_3 (e.g. ^{12}C ^{13}C^{12}C or ^{13}C^{12}C^{12}C). We have done this assumption since in this work we consider only one position (^{13}C^{12}C$_2$). Therefore, we have decided to use as a guess this lower value. Exchange reactions may occur in neutral-neutral reactions but these cases often involve small activation barriers. In absence of more detailed theoretical investigations, for reactions (8) and (10) we assumed as pre-exponential factor the same of reaction (5) in Table 5.2. Moreover, for the new reactions

Table 5.2: Carbon isotopic exchange reactions used in this work. In the top panel the reactions already used by Roueff et al. (2015) and in the bottom panel the new ones.

Label	Reaction	$k_{\rm f}$ (cm^3 s^{-1})	$f(B,m)^a$	ΔE^b (K)
(1) B	$^{13}C^+ + CO \rightleftharpoons {}^{12}C^+ + {}^{13}CO$	$6.6\times10^{-10} \times (\frac{T}{300})^{-0.45} \times$ $\exp(-6.5/T) \times \frac{1}{1+\exp(-34.7/T)}$	1	34.7
(2) A	$^{13}CO + HCO^+ \rightleftharpoons CO + H^{13}CO^+$	$2.6\times10^{-12} \times (\frac{T}{300})^{-0.4}$	1	17.4
(3) B	$^{13}C^+ + CN \rightleftharpoons {}^{12}C^+ + {}^{13}CN$	$3.82\times10^{-9} \times$ $(\frac{T}{300})^{-0.4} \times \frac{1}{1+\exp(-31.1/T)}$	1	31.1
(4) B	$^{13}C + CN \rightleftharpoons {}^{12}C + {}^{13}CN$	$3.0\times10^{-10} \times \frac{1}{1+\exp(-31.1/T)}$	1	31.1
(5) B	$^{13}C + C_2 \rightleftharpoons {}^{12}C + {}^{13}CC$	$3.0\times10^{-10} \times \frac{2}{2+\exp(-26.4/T)}$	2	26.4
(6) B	$^{13}C^+ + C_2 \rightleftharpoons {}^{12}C^+ + {}^{13}CC$	$1.86\times10^{-09} \times \frac{2}{2+\exp(-25.9/T)}$	2	25.9
(7) B	$^{13}C^+ + {}^{13}CC \rightleftharpoons {}^{12}C^+ + {}^{13}C_2$	$1.86\times10^{-09} \times \frac{0.5}{0.5+\exp(-26.3/T)}$	0.5	26.3
(8) B	$^{13}C + {}^{13}CC \rightleftharpoons {}^{12}C + {}^{13}C_2$	$3.0\times10^{-10} \times \frac{0.5}{0.5+\exp(-26.3/T)}$	0.5	26.3
(9) B	$^{13}C^+ + CS \rightleftharpoons {}^{12}C^+ + {}^{13}CS$	$1.86\times10^{-09} \times \frac{1}{1+\exp(-25.9/T)}$	1	25.9
(10) B	$^{13}C + C_3 \rightleftharpoons {}^{12}C + {}^{13}CC_2$	$3.0\times10^{-10} \times \frac{2}{2+\exp(-27/T)}$	2	27
(11) B	$^{13}C^+ + C_3 \rightleftharpoons {}^{12}C^+ + {}^{13}CC_2$	$9.5\times10^{-10} \times \frac{2}{2+\exp(-27/T)}$	2	27

^{a} $f(B,m)$ is a probability factor that depends on the rotational constant, mass, and symmetry values of the reactants and products. In reactions involving ^{15}N and ^{13}C, the mass ratio of reactants and products are very close, and $f(B,m) \simeq \sigma_{\rm entrance\ channel} = \sigma_{\rm exit\ channels}$. The symmetry number σ is equal to the number of pathways.
^{b} ΔE is the exoergicity of the reaction.

studied in this work, the equilibrium symmetry factor f is near unity unless C_2 appears, in which case it is near 2.0 if C_2 is a reactant, and near 0.5 if C_2 is a product.

The factor that multiplied the pre-exponential factor in the rate and in the reverse (endothermic) reaction requires the knowledge of the energy defect (ΔZPE) which is defined by the difference of the zero-point energies of the products and the reactants. In Table 5.3 we give the values found in the literature for C_2, CS, and C_3.

5.3. RESULTS AND DISCUSSION

In this Section we discuss the main results obtained through the simulation at different densities and temperatures. The main physical parameters that the code requires are the total number density of H nuclei ($n_{\rm H}$), the dust temperature ($T_{\rm dust}$), the gas temperature ($T_{\rm gas}$), the cosmic-ray ionisation rate (ζ), the visual extinction ($A_{\rm V}$), the grain albedo (ω), the grain radius ($a_{\rm g}$) and the grain material density ($\rho_{\rm g}$). Apart from densities and temperatures, we have fixed all of the other initial parameters as described in Table 5.4.

After all the reactions and associated rate coefficients have been evaluated, the program calculates all the formation and destruction rates for each species. Finally, it computes the chemical evolution by solving a system of first-order differential equations. For a detailed

Table 5.3: Values of the ZPEs for molecules related to the isotopic-exchange reactions used in our model. The related references are also given in the fourth column.

Molecule	ZPE (cm^{-1})	ΔZPE (K)	Reference
C_2	924.13	–	Zhang et al. (2011)
^{13}CC	906.1	25.9	Zhang et al. (2011)
$^{13}C_2$	887.8	52.3	Zhang et al. (2011)
$^{13}C_2$		26.4	Zhang et al. (2011)
CS	640.9	–	Bergeman and Cossart (1981)
^{13}CS	622.7	26.3	Huber and Herzberg (1979)
C_3	1705.06	–	Schröder and Sebald (2016)
$^{13}CC_2$	1686.44	27	Schröder and Sebald (2016)
$C^{13}CC$	1675.54	43	Schröder and Sebald (2016)

Table 5.4: Values of the physical parameters fixed in each model.

Parameter	Value
ζ	1.3×10^{-17} s^{-1}
A_V	10 mag
ω	0.6
a_g	10^{-5} cm
ρ_g	3 g cm^{-3}
$\epsilon = E_{diff}/E_b$	0.6
R_d= dust-to-gas mass ratio	0.01

explanation of how the code works see Sipilä (2013).

We have assumed that the gas is initially atomic except H_2. The adopted initial abundances are presented in Table 5.5 and are used for all of the models presented in this chapter. Note that we have assumed an initial $^{12}C/^{13}C$ ratio of 68. In this Section we will present the fiducial model that we have chosen to describe the main characteristics and new results about C-fractionation of this chemical model. Then, we will present a parameter space exploration showing how the C-fractionation of some specific models varies with the density and the temperature.

5.3.1. THE FIDUCIAL MODEL

First of all, we have analysed the behaviour of abundances and $^{12}C/^{13}C$ ratios of different species for a particular model with a fixed temperature and density. We have chosen as "fiducial-model" that with a T_{gas}=10 K and a n_H of 2×10^4 cm^{-3}. Note that we have always assumed that the gas and dust are thermally coupled, and then T_{gas}=T_{dust}.

Table 5.5: Initial abundances with respect to n_H. Adapted from Semenov et al. (2010).

Species	Initial abundance
H_2	0.5
He	9.00×10^{-2}
C^+	1.20×10^{-4}
$^{13}C^+$	1.76×10^{-6}
N	7.60×10^{-5}
O	2.56×10^{-4}
S^+	8.00×10^{-8}
Si^+	8.00×10^{-9}
Na^+	2.00×10^{-9}
Mg^+	7.00×10^{-9}
Fe^+	3.00×10^{-9}
P^+	2.00×10^{-10}
Cl^+	1.00×10^{-9}
F	2.00×10^{-9}

ONLY GAS-PHASE MODEL

In Fig. 5.4 the time-dependence of C^+, C, CO, CH, HCO^+, CN, HCN and HNC abundances, for a model with only gas-phase chemistry at work, is shown. As in Roueff et al. (2015), the steady-state is reached at $\sim 10^6$ yr. At the beginning, all the carbon is in ionised form, and after 10^2 yr it starts to be converted into atomic carbon until all the atomic carbon is quickly transformed into CO (in a timescale of $\sim 10^5$ yr). Meanwhile, CH follows the behaviour of atomic carbon, and HCO^+ that of CO, as expected. In Fig. 5.5 the related $^{12}C/^{13}C$ ratios
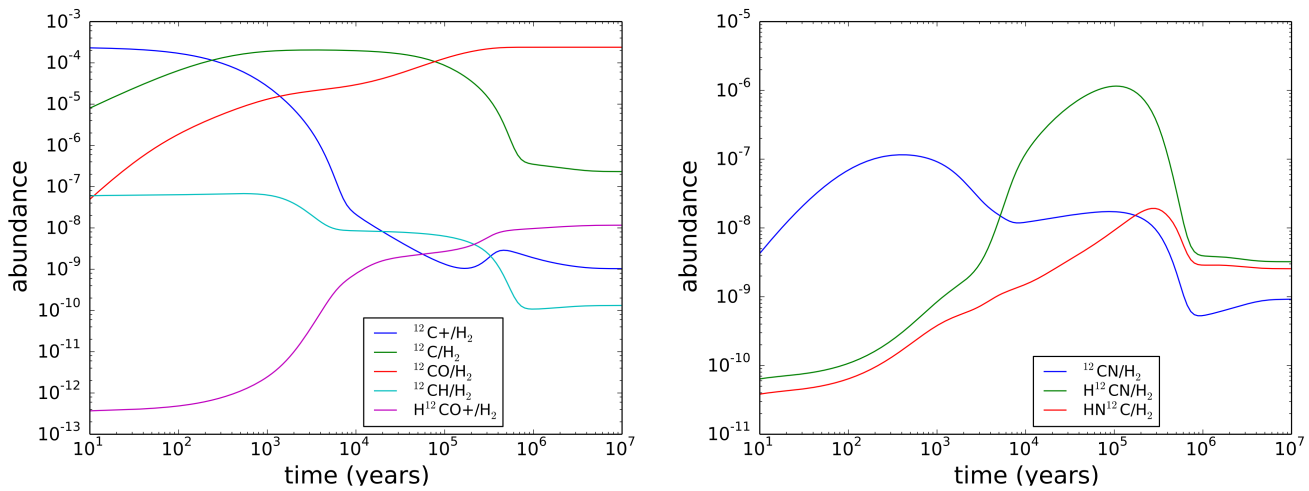
Fig. 5.4: Time evolution of C, C^+, CO, CH and HCO^+ (*left panel*) and of CN, HCN and HNC (*right panel*) abundances with respect to H_2 for the fiducial model with only gas-phase chemistry at work.

are shown. As already explained in the introduction of this chapter, the $^{12}C/^{13}C$ ratios of
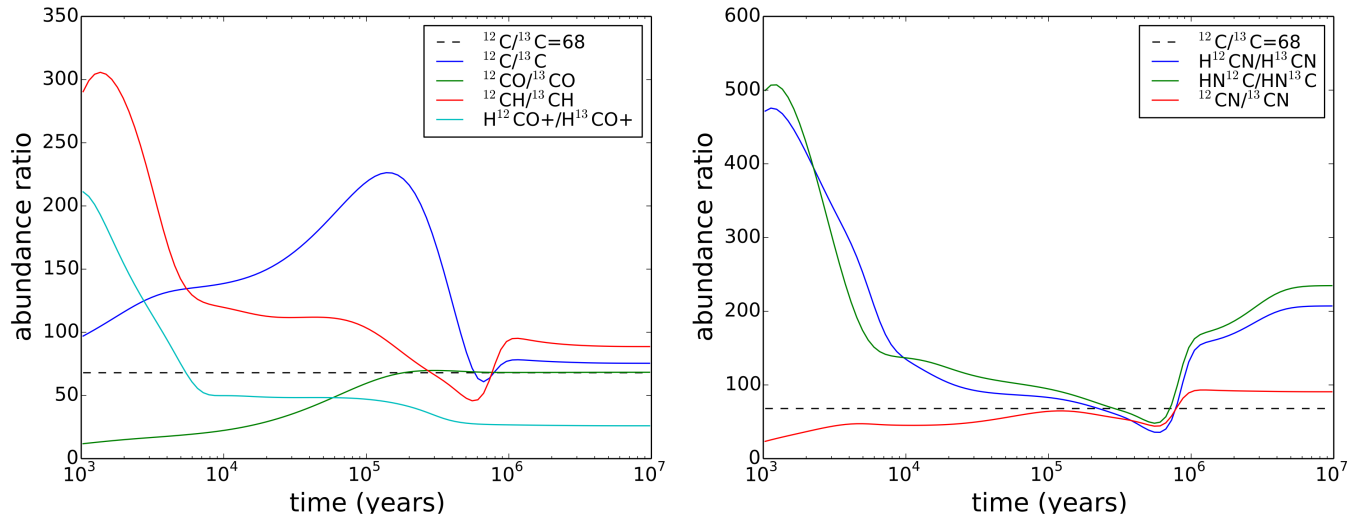
Fig. 5.5: Time evolution of $^{12}C/^{13}C$ ratio for C, CO, CH and HCO^+ (*left panel*) and for CN, HCN and HNC (*right panel*) for the fiducial model with only gas-phase chemistry at work. In both panels the black horizontal dashed line represents the initial $^{12}C/^{13}C$ ratio of 68.

these molecules are mainly governed by the isotopic-exchange reactions (1), (2) and (3) shown in Table 5.2. This model already shows differences between the results of Roueff et al. (2015) and this work. In fact, there is a range of time in which the $^{12}C/^{13}C$ ratio for nitrile bearing species is consistent between the different species, and lower than 68. These values for HCN and HNC were different and higher than 68 in previous chemical models that simulated similar physical conditions, as we have already discussed in Sect. 5.1 (see e.g. left panel of Fig. 5.2).

GAS+GRAIN MODEL

The time-dependence of C^+, C, CO, CH, HCO^+, CN, HCN and HNC abundances, for the complete model, with both gas-phase and grain surface reactions, is shown in Fig. 5.6. In addition to what was shown in Fig. 5.4, after 2×10^5 yr the CO starts to freeze-out on grain surfaces and the abundance drops from the gas phase. Moreover, when most of the CO is depleted, the abundance of He^+ increases because of cosmic-ray ionization reactions and destroys further CO molecules, increasing the abundance of C. As a consequence, the abundances of C_2, C_3, CH, HCN, HNC and CN increase as well (Fig. 5.7). This behaviour was already predicted by Ruffle et al. (1997), and carbon-chains such as HC_3N can be used as depletion indicators in late-type chemistry (after CO freeze-out). Fig. 5.8 displays the time dependence of the $^{12}C/^{13}C$ ratios of the same molecules studied in Fig. 5.5. For $t<10^5$ yr, the inclusion of gas-grain interactions does not affect the C-isotopic ratio of molecules. In fact, adsorption rates (eq. 5.10) depend on v_i that is inversely proportional to the mass of species i. Since typical differences in mass between ^{12}C-containing species and ^{13}C-containing species are less than 4%, they do not have a significant effect. At around 10^6 yr[3], a peak is present on the $^{12}C/^{13}C$ ratios. The peak appears because of the interaction between gas

---

[3] This time is the "steady-state time" in a model where only gas-phase reactions are included.
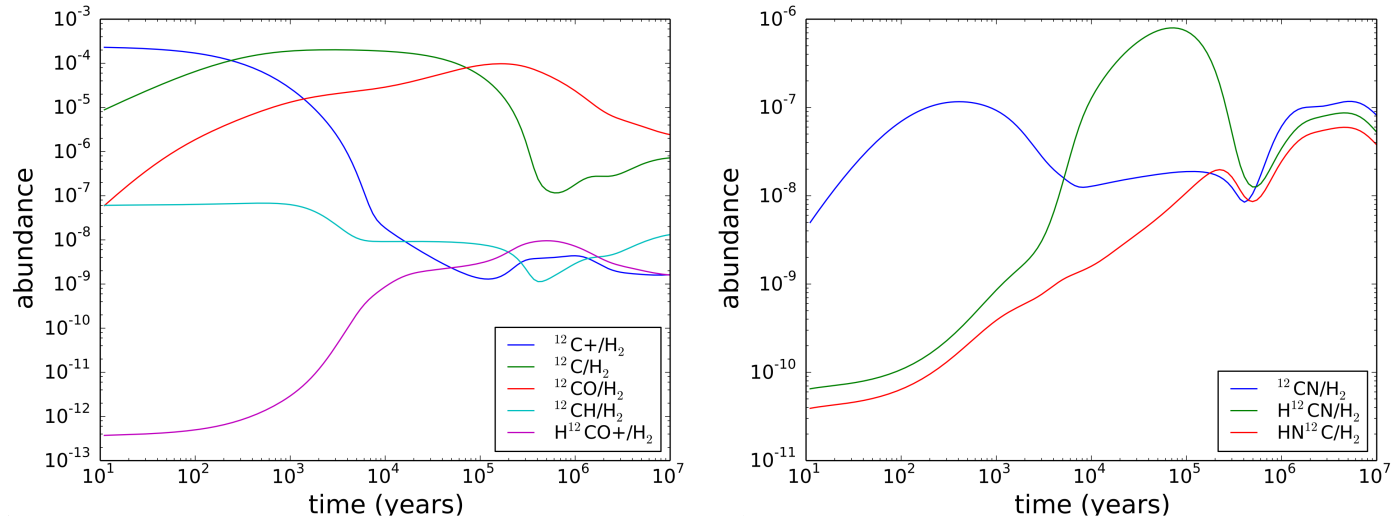
Fig. 5.6: Time evolution of C, C^+, CO, CH and HCO^+ (*left panel*) and of CN, HCN and HNC (*right panel*) abundances with respect to H_2 for the fiducial model with both gas-phase and grain-surface chemistries at work.
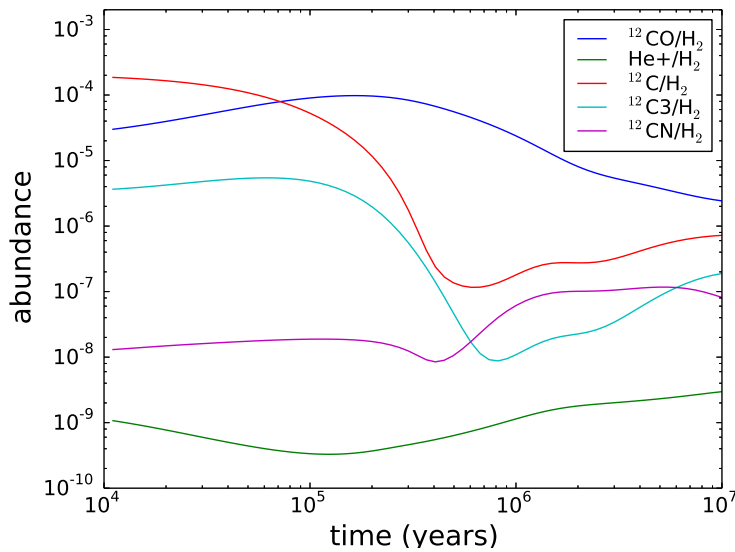

Fig. 5.7: Time evolution of CO, He^+, C, C_3 and CN abundances for the fiducial model with both gas-phase and grain-surface chemistries at work. In this case we have zoomed the time scale from 10^4 yr and 10^7 yr. When CO starts to freeze out on grain surfaces, He^+ abundance increases, and as a consequence the abundances of C, C_3, CN increase as well.

and grains. In fact, the fast early chemistry transforms most of the atomic carbon into CO. In this fast range of time, most of the ^{13}C is in HCO^+ and then, it is missed in other species. Then, after 10^6 yr the $^{12}C/^{13}C$ ratios tend to decrease again because of the CO freeze-out that drives again atomic C to be a significant sink of gas-phase carbon. Moreover, there is a short-range of time where the $^{12}C/^{13}C$ ratios tend to decrease to a value lower than 68, and after that time scale the ratios tend to increase again. We will discuss in next Sections why
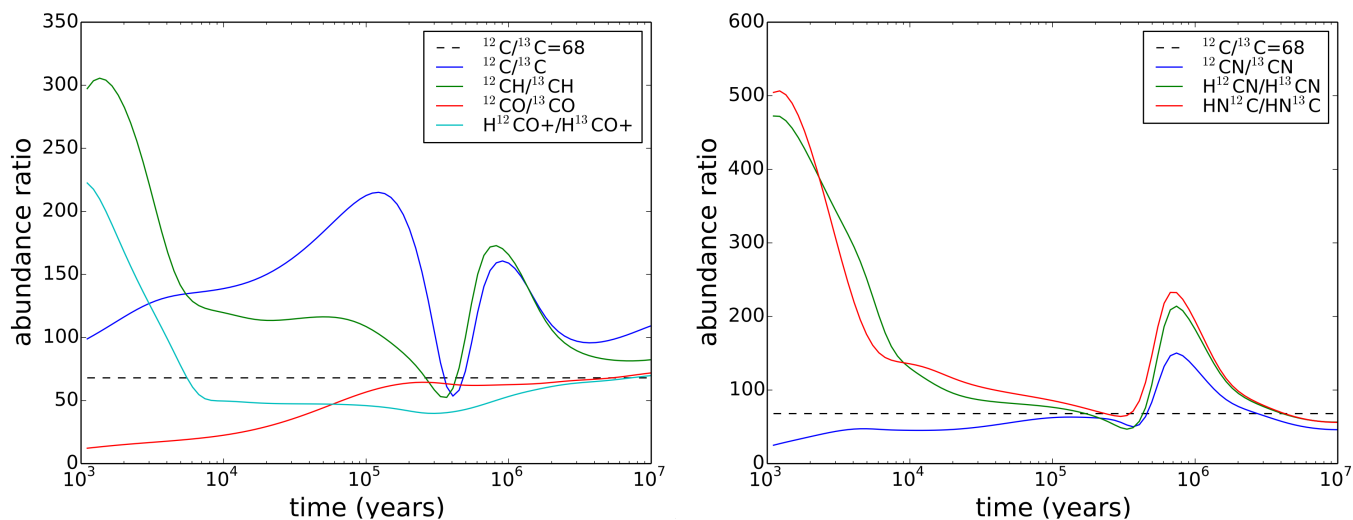
Fig. 5.8: Time evolution of ^{12}C/^{13}C ratio for C, CO, CH and HCO$^+$ (*left panel*) and for CN, HCN and HNC (*right panel*) for the fiducial model with both gas-phase and grain-surface chemistries at work. In both panels the black horizontal dashed line represents the initial ^{12}C/^{13}C ratio of 68.

this feature in the time dependence of ^{12}C/^{13}C is present, and its consequences at different densities and temperatures.

COMPARISON WITH THE PREVIOUS MODEL OF FURUYA ET AL. (2011)

Furuya et al. (2011) studied the behaviour of ^{12}C/^{13}C for CCH and CCS with a gas-grain chemical model. In particular, their work was based on the study of isotopomer fractionation, that is the abundance ratio between the variants of a given species with ^{13}C in a different position. They introduced as isotopic-exchange reactions only (1) and (2) of Table 5.2. Interestingly, their results are similar to what we found with our chemical model using the same density (10^5 cm^{-3}) and temperature (10 K). The differences could be due to the dissimilar species considered, namely: we cut our chemistry to molecules containing 5 atoms, while they introduce also methanol (CH$_3$OH), and because we have introduced new possible isotopic-exchange reactions that are efficient at low temperatures (like those for CN, C$_2$, CS, and C$_3$). The comparison between the two chemical models is shown in Fig. 5.9.

5.3.2. THE IMPORTANCE OF C$_3$ ISOTOPIC-EXCHANGE REACTION

Observations of atomic carbon, and simple molecules containing more than one carbon atom, are important to put constraints into the processes that form larger molecules. The linear molecule C$_3$ is one of these species. It was observed for the first time in the ISM by Haffner and Meyer (1995), that reported a tentative detection, and clearly by Maier et al. (2001). Later Roueff et al. (2002) studied this molecule towards the diffuse molecular cloud HD 210121. In this environment it forms mainly from the recombination of C$_3$H$^+$, and is destroyed by photodissociation. Roueff et al. (2002) found an abundance relative to H$_2$ of 6.75×10^{-9}. In our chemical model this abundance can be found, for a density of 2×10^3
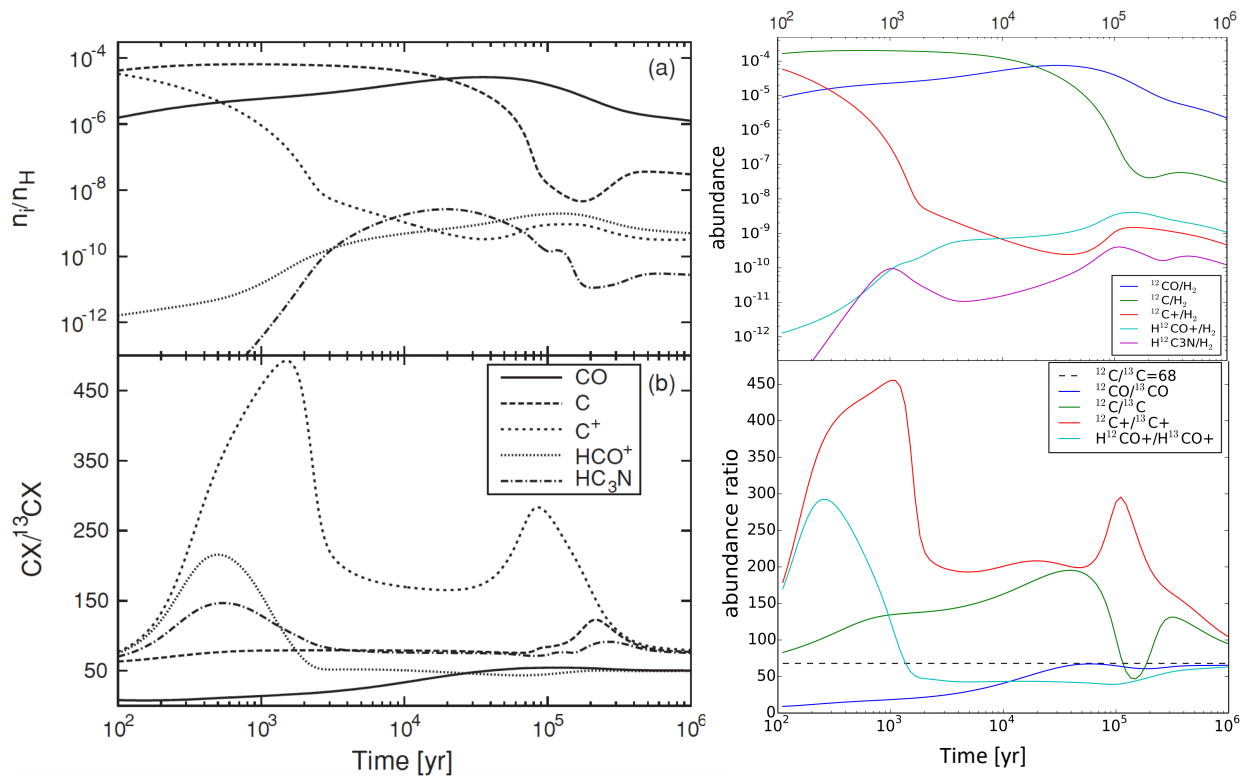
Fig. 5.9: *Left panels*: results by Furuya et al. (2011). *Right panels*: results from our chemical model using a density of 10^5 cm^{-3} and temperature of 10 K (same as Furuya et al. 2011). Note that we have excluded HC$_3$N in our ^{12}C/^{13}C ratio since we cut the chemistry to 5 atoms-containing molecules and the results for HC$_3$N are biased by this assumption.

cm^{-3} and a T_{gas}=10 K, at around 60 yr when the atomic carbon is still mainly in its ionised form. Other detections were made later by Galazutdinov et al. (2002) towards stars surrounded by molecular clouds, Ádámkovics et al. (2003) and Oka et al. (2003). Moreover, Wakelam et al. (2009) pointed out the interest of the reaction C + C$_3$ → C$_4$ for the formation of CO. In fact, later, C$_4$ reacts with O forming CO and again C$_3$.

Mookerjea et al. (2012) observed four ro-vibrational far-infrared transitions of C3 towards the high-mass star-forming region DR21(OH) with HIFI (*Herschel* instrument). They found an abundance of C3 in the envelope of 6.3×10^{-10}, that they are able to reproduce with a chemical model with n_{H_2}=5×10^6 cm^{-3} and a T_{max} of 30 K and at a time of ~10^6 yr. The T_{max} that they fixed is the one that the model reaches after a gradual temperature increase that starts from 10 K (Garrod and Herbst 2006). With our chemical model, assuming a density n_H=10^7 cm^{-3} and a fixed T=30 K, we are able to reproduce their observed abundance in a range of time ~7.5~10^5–7×10^6 yr (left panel of Fig. 5.10). This time is consistent with the one found by Mookerjea et al. (2012) and with the dynamical timescale of 2 Myr derived for the source (Schneider et al. 2010). They discussed the abundance of C$_3$ in dense clouds via warming-up of grain mantels to release CH$_4$ and C$_3$H$_2$ that are the first step for the formation of C$_3$. Moreover, Mookerjea et al. (2014) observed along the line of sight of the UC HII region W51e2, with *Herschel*, detecting an absorption feature probably tracing a cold external envelope. They evaluated the abundance of C3 with respect to CCH to be 1.2

and found that the best chemical model that reproduces the observations is the one with $n_{H_2}=5\times10^6$ cm^{-3} and a T_{max} of 30 K. Plotting the calculated abundances from our chemical model, assuming a $n_H=10^6$ cm^{-3} and a fixed $T=30$ K, relative to their observed column density of CCH and assuming a filament of 1 pc, we found agreement with their observations at a time of 1.6×10^6 yr and 1.6×10^7 yr (right panel of Fig. 5.10). Even if we did not introduce an evolution of the temperature with time, our predictions are consistent with the post-warm-up chemistry that occurs after the early chemistry stages, as described by Mookerjea et al. (2012).
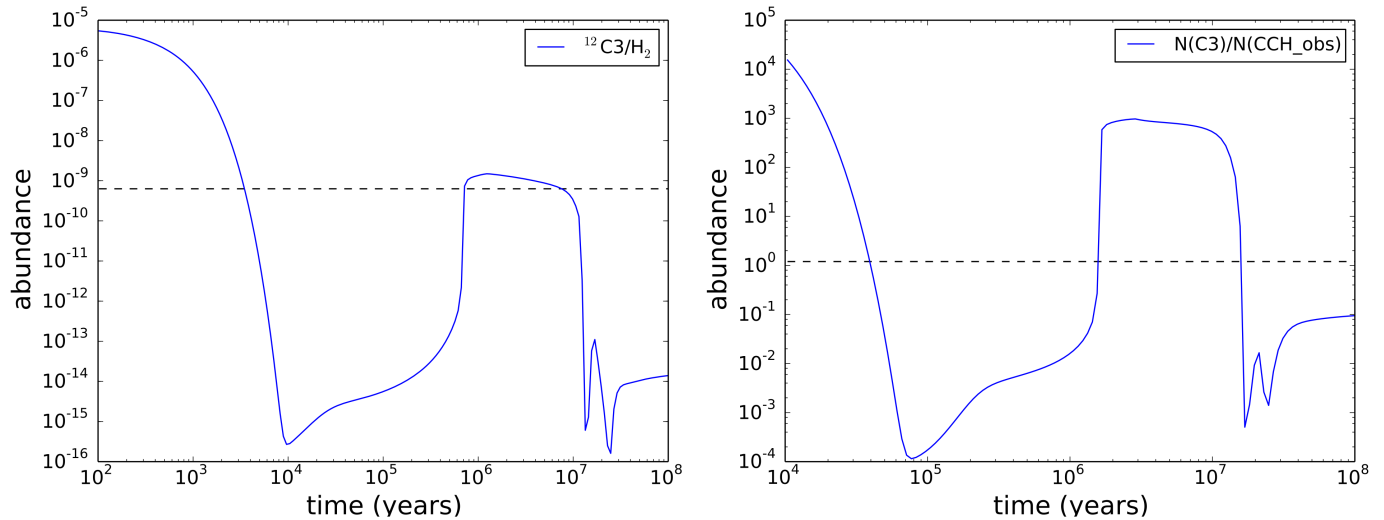
Fig. 5.10: *Left panel*: C3 abundance modeled with a $n_H=10^7$ cm^{-3} and a fixed $T=30$ K. The black dashed line corresponds to the observed abundance by Mookerjea et al. (2012) of 6.3×10^{-10}. *Right panel:* C3 abundance modelled with $n_H=10^6$ cm^{-3} and a fixed $T=30$ K, with respect to the observed column density of CCH. The black dashed line corresponds to the observed abundance of C$_3$ by Mookerjea et al. (2012), with respect to CCH, of 1.2.

The importance of the carbon isotopic-exchange reaction of C$_3$ in our chemical model was already mentioned in the discussion of the results shown in Figs. 5.5 and 5.8. In this Section we will investigate what the contribution of this species is in the ^{12}C/^{13}C ratio of different molecules. To do this, we have studied in detail what are the main reactions that form or destroy C$_3$ at two precise times in the fiducial model: 3×10^4 yr and 3×10^5 yr. These two times are before and after the "first early chemistry time" (t_1), that we have defined to be:

Definition. t_1 is the time at which the abundance of atomic carbon drops by one order magnitude while it is transformed into CO.

In the fiducial model, $t_1=1.7\times10^5$ yr, and it is shown in Fig. 5.11 as the vertical purple line. In Fig. 5.11 the predicted abundances (left panel) and ^{12}C/^{13}C ratio (right panel) for C$_2$, C$_3$, CN, C, and CO are shown. The abundance of C$_3$ is two orders of magnitude higher than that of CN until the late-chemistry time in which CO starts to freeze-out onto grain surfaces (∼2–4×10^5 yr). The main reactions for the two times are summarised in Fig. 5.12 and are explained below in detail. Moreover, the ^{12}C/^{13}C ratio for some important molecules at the three times (3×10^4 yr, 1.7×10^5 yr and 3×10^5 yr) are summarised in Table 5.6.
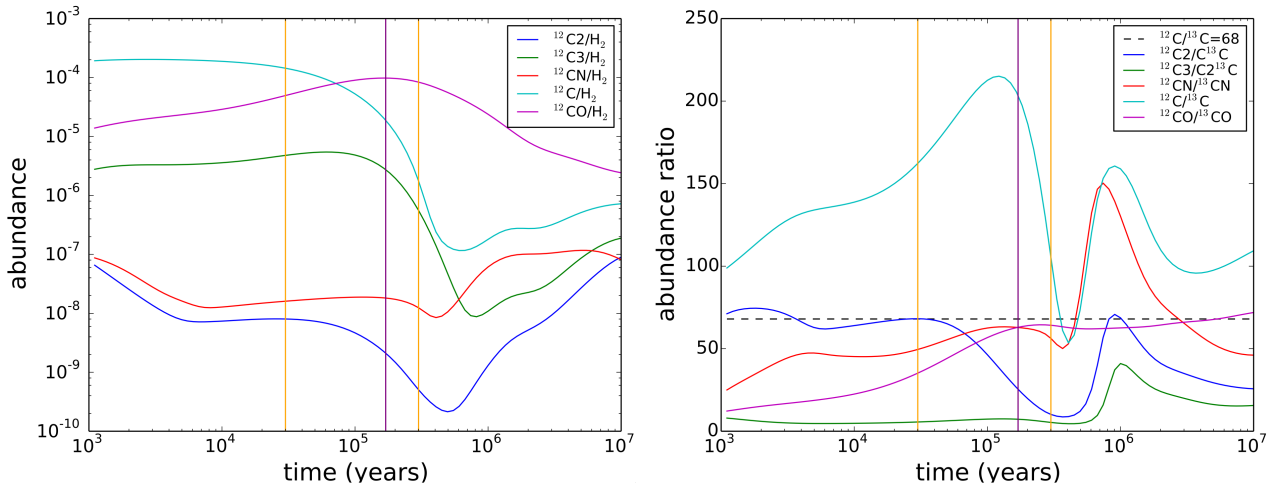
Fig. 5.11: *Left panel:* Time evolution of C_2, C_3, CN, C and CO abundances with respect to H_2 for the fiducial model. *Right panel:* Time evolution of $^{12}C/^{13}C$ for C_2, C_3, CN, C and CO for the fiducial model. In both panels, the vertical purple solid line represents the "first early chemistry" time as defined in the text, while the two vertical orange solid lines represent the two times (3×10^4 yr, and 3×10^5 yr) that we have analysed and discussed in the text.

- For t< t_1 most of the atomic ^{12}C is formed through the cycle:

$$C_2 \xrightarrow{O} C \xrightarrow{C_4/CH} C_2. \tag{5.22}$$

Conversely, ^{13}C is mainly in the form of $^{13}CC_2$, thanks to the forward reaction (10) of Table 5.2. As a consequence, the $C_3/^{13}CC_2$ ratio is lower than the elemental, initial, value of 68, and the atomic $^{12}C/^{13}C$ is higher than 68. Even if reaction (4) has a similar exothermicity, reaction (10) is more efficient since $C_3/H_2 >$CN$/H_2$. This means that the $C_3/^{13}CC_2$ ratio is lower than the CN$/^{13}$CN ratio and it stays low for a longer time than CN (CN$/^{13}$CN=68 at t_1). Moreover, $C_2/^{13}CC\simeq 68$ since it reaches an equilibrium between the efficient formation of C_2 from the very abundant ^{12}C and the main formation of ^{13}CC from $^{13}CC_2$.

- For t> t_1, when most atomic carbon is already transformed into CO, the cycle of reactions (5.22) is not efficient any more. C_2 is now mainly formed from C_3 that reacts with secondary photons. C_2 then reacts with the remaining O forming new atomic carbon. At this time, the main reactions that form atomic carbon starting from C_3 are the same for ^{12}C and ^{13}C (red reactions in the right panel of Fig. 5.12), and then the $^{12}C/^{13}C$ ratios of molecules, like that of carbon-chains and nitrile-bearing species tend to be as low as that of C_3. This behaviour lasts until the isotopic-exchange reaction of C_3 is efficient, and all of these $^{12}C/^{13}C$ ratios rise again.

Recently, Giesen et al. (2019) have reported the first detection of the ^{13}C-isotopologues of C_3, ^{13}CCC and C^{13}CC, towards the massive star-forming region SgrB2(M), near the Galactic Center. They derived an average $^{12}C/^{13}C$ abundance ratio of 20.5±4.2, in agreement with the local value of 20 as derived from the Galactocentric trend by Milam et al. (2005) for CN, CO and H_2CO, taking into account the three molecules:

$$[^{12}C/^{13}C]_{\text{all molecules}} = (6.21 \pm 1.00)\, \text{kpc}^{-1} \times D_{GC} + (18.71 \pm 10.88). \tag{5.23}$$

Thus, it seems that no ^{13}C-fractionation is detected in SgrB2. However, our chemical model is not appropriate to reproduce the physical conditions and the chemistry towards this source. Furthermore, other observational studies towards the Galactic Center are needed to improve the reliability of the ^{12}C/^{13}C estimated from the Galactocentric trend. Moreover, the authors found a N(^{13}CCC)/N(C^{13}CC) ratio of 1.2±0.1, different from the statistically expected value (2)[4]. This discrepancy could be explained by a difference of 16 K in zero-point energy between the two species with respect to the main species C$_3$, as shown in Table 5.3. The different position of the ^{13}C in carbon chains would probably bring to an higher abundance of C^{13}CC with respect to ^{13}CCC for 27 K < T < 43 K because of the reaction C$_3$ + ^{13}C → C^{13}CC + C + 43 K. One of the next upgrade of our chemical network will be to track the position of ^{13}C in molecules and study the possible role of different ZPE.

Table 5.6: ^{12}C/^{13}C ratios for different molecules (C$_3$, C, CO, CN, HCN and HNC) for three different times: the "early-chemistry" time (second row), t_1, as defined in the text, and the times before and after t_1 that we have discussed in the text. (first and third row, respectively).

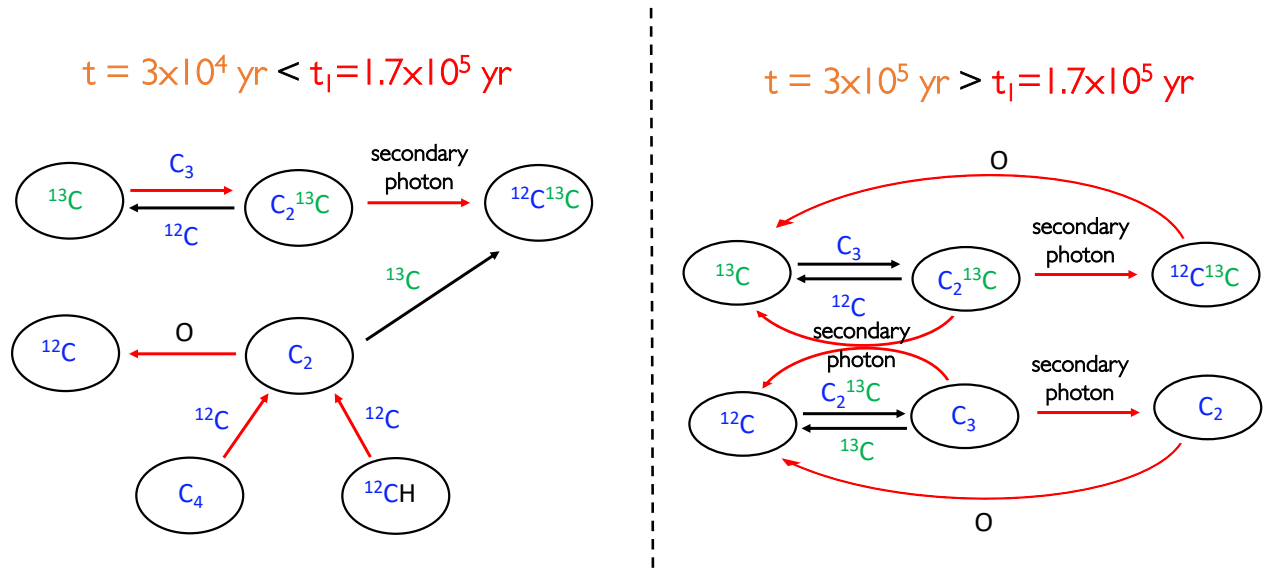| Time	^{12}C/^{13}C					
	C$_3$	C	CO	CN	HCN	HNC
3×10^4 yr	6	162	35	50	87	105
$t_1=1.7\times10^5$ yr	7	197	63	63	66	74
3×10^5 yr	5	105	64	56	49	64

Fig. 5.12: Chemical pathways that distribute the two carbon isotopes in atomic carbon, C$_2$ and C$_3$ at 3×10^4 yr (*left panel*) and 3×10^5 yr (*right panel*), for the fiducial model. Main creation and destruction reactions are highlighted in red, ^{12}C is represented in blue and ^{13}C is represented in green.

---

[4] Assuming a statistical distribution of ^{13}C in C$_3$, there are two options to place it at the ends of the carbon chain and only one to be at the center of the molecule.

5.3.3. PARAMETER SPACE EXPLORATION

In this Section we focus the analysis only on the nitrile-bearing species CN, HCN and HNC, since those are studied in the first two works of this thesis (chapters 2 and 3), and in order to give an estimate of how much we can be wrong in deriving the ^{14}N/^{15}N ratio assuming a canonical ^{12}C/^{13}C ratio of 68.

We have analysed the ^{12}C/^{13}C ratio for different temperatures and densities in three well defined fixed times: the "first early chemistry" time t_1, t_2=2×t_1 and t_3=10×t_1. The densities we have analysed are between $2×10^3$ cm^{-3} and $2×10^7$ cm^{-3}, and the temperatures are 10, 20, 30, 40 and 50 K. Figs. 5.13, 5.14 and 5.15 show the behaviour of HN^{12}C/HN^{13}C, H^{12}CN/H^{13}CN and ^{12}CN/^{13}CN, respectively, as a function of hydrogen density and for different temperatures. In particular, it can be noted that for t_1 and t_2 and for densities higher than 10^6 cm^{-3}, the ^{12}C/^{13}C ratios tend to be higher for 10 K with respect to higher temperatures. This is because forward reaction (5.2) is efficient until T<17.4 K, and most of the ^{13}C is in HCO$^+$. Moreover, it should be noted that this behaviour is different depending on the density. This is because of the definition of t_1: for a density of 10^6 cm^{-3} t_1 is the time just before reaching the dip of carbon isotopic ratios that directly follows C$_3$, while for a density of 10^5 cm^{-3} t_1 is the time when the dip in ^{12}C/^{13}C is present and follows that of C$_3$. The higher the density, the later the dip of lower ^{12}C/^{13}C with respect to t_1 when most of the atomic C is in the form of CO. The most probable explanation, following also what was described in Sect. 5.3.2, is that there is a competition between the O atoms transformed in CO and frozen out on ice mantles, and those that are still available to take part in the reactions shown in the right panel of Fig. 5.12.

LOW-MASS STAR-FORMING REGIONS

As already discussed in the introduction of this chapter, Daniel et al. (2013) found towards B1b HNC/HN^{13}C=20$^{+5}_{-4}$, HCN/H^{13}CN=30$^{+7}_{-4}$, and CN/^{13}CN=50$^{+19}_{-11}$, and Magalhães et al. (2018) towards the pre-stellar core L1498 obtained a HCN/H^{13}CN ratio of 45±3. Note that the results found by Daniel et al. (2013) for HCN and HNC cannot be accurate because the HCN and HNC lines are heavily saturated. Since both of these works studied the observed sources, modelling also the temperature and density profiles, we were able to simulate the chemistry of these two sources with our chemical model. Daniel et al. (2013) found an average hydrogen density, towards the center of the core, of $6×10^6$ cm^{-3} and a temperature of 11–18 K. Thus, we have decided to take this density and, indicatively, a temperature of 11 K. Moreover, Magalhães et al. (2018) found for the center of the core an average hydrogen density of $2×10^5$ cm^{-3} and a temperature of 10 K. For HNC and HCN we reproduce with the model the values observed by Daniel et al. (2013) at time t_3, while for CN the value we found with our model is slightly lower. Moreover, we can reproduce the value observed for HCN by Magalhães et al. (2018) at time t_2. This behaviour is also shown in Fig. 5.16, which represents the time evolution of the ^{12}C/^{13}C ratio for the two models corresponding to the two observed low-mass star-forming regions. Note that since the model is not simulating also the dynamical evolution, the fact that different observations could be reproduced at different times can not conclude anything about the chemical age of the simulated star-forming region.
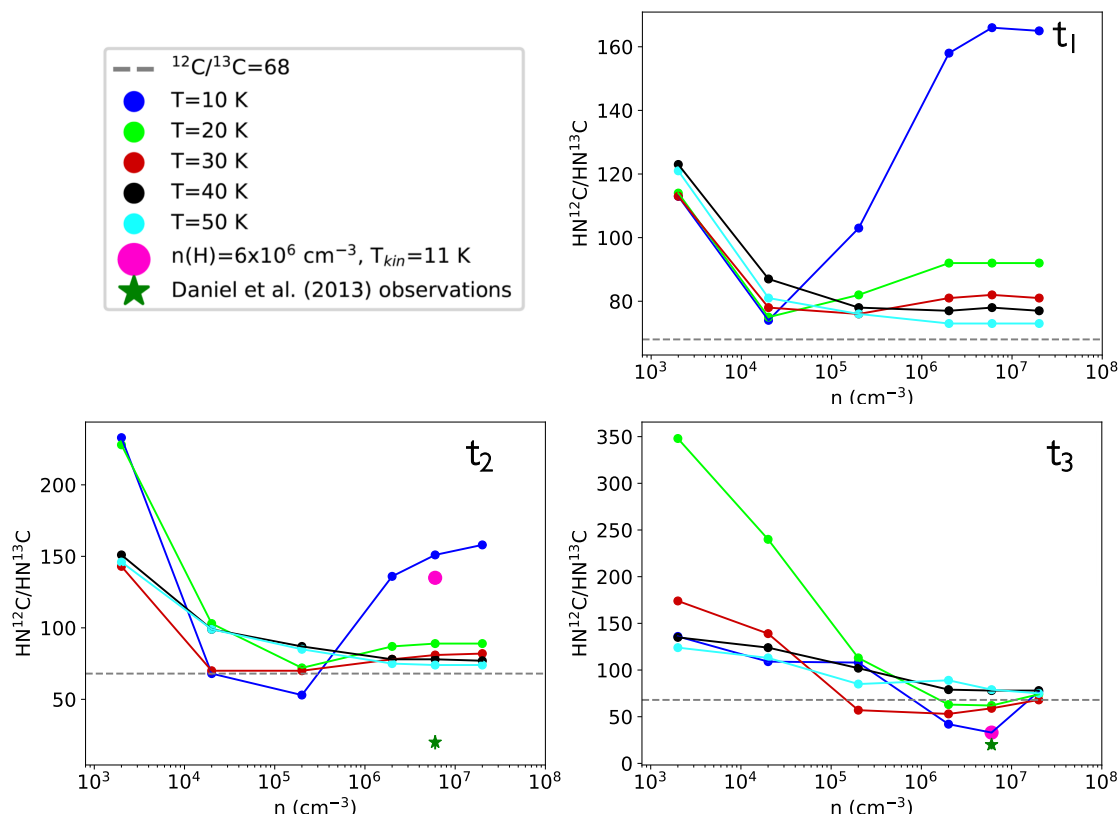
Fig. 5.13: HN^{12}C/HN^{13}C ratio as a function of hydrogen density, for different temperatures, at t_1 (top right panel), t_2 (bottom left panel) and t_3 (bottom right panel). The large pink circles in the bottom panels represent the result of the model that simulates the physical conditions in the pre-stellar core B1b observed by Daniel et al. (2013). The HN^{12}C/HN^{13}C ratio observed by Daniel et al. (2013) is represented by the dark green star.

HIGH-MASS STAR-FORMING REGIONS SAMPLE

Finally, we have used our grid of models to give an estimate of the ^{12}C/^{13}C ratio for HCN, HNC and CN towards the high-mass star-forming regions sample described in chapter 2. In particular, we have used the H$_2$ column densities computed by Fontani et al. (2018b), and listed in Table 2.1, to derive the H$_2$ densities towards the region described by the SCUBA or APEX effective beam[5]. The average range of densities of the sources is from 1.5×10^4 cm^{-3} up to 3×10^5 cm^{-3}. The range of kinetic temperatures, given in Table 2.8, is from 14 up to 47 K, and it is similar to the range of values used in the grid of models performed in this Section. With this information we can constrain the ^{12}C/^{13}C predicted by our models that could be used to compute N-fractionation from ^{13}C-isotopologue observations. In Figs. 5.17, 5.18 and 5.19 the HN^{12}C/HN^{13}C and H^{12}CN/H^{13}CN ratios, for the three analysed times, are shown, together with the observed volume density range.

The ^{12}C/^{13}C ratios derived for t_1, t_2 and t_3, and the errors made to derive the ^{14}N/^{15}N ratios assuming a ^{12}C/^{13}C ratio of 68, for HNC and HCN, are listed in Table 5.7. Taking, for example, one of the sources with the highest H$_2$ density, 19410+2336 with

---

[5] The effective beam of the continuum observations is 22″ for SCUBA and 15″ for APEX. The instrument used for each source is given in Table 2.1.
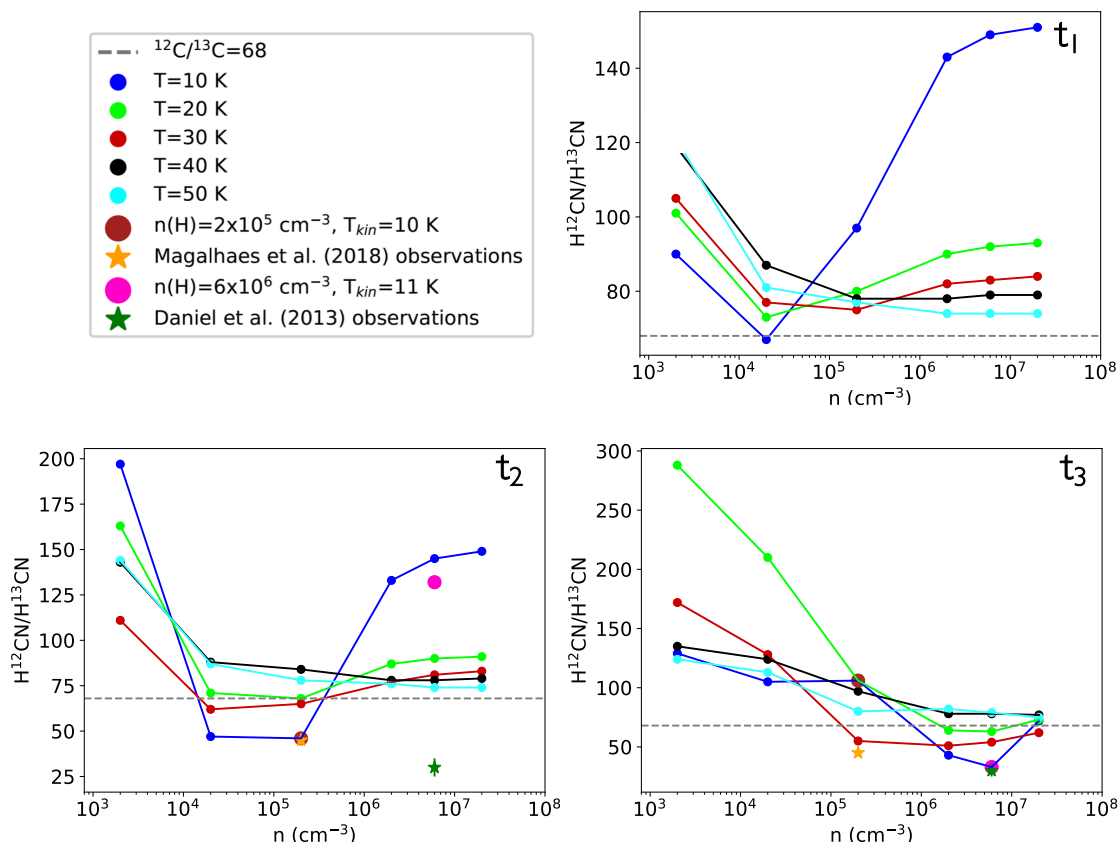
Fig. 5.14: $H^{12}CN/H^{13}CN$ ratio as a function of hydrogen density, for different temperatures, at t_1 (top right panel), t_2 (bottom left panel) and t_3 (bottom right panel). The large pink and brown circles in the bottom panels represent the result of the model that simulates the physical conditions in the pre-stellar core B1b observed by Daniel et al. (2013) and L1498 observed by Magalhães et al. (2018), respectively. The $H^{12}CN/H^{13}CN$ ratios observed by Daniel et al. (2013) and Magalhães et al. (2018) are the dark green and orange stars, respectively.

$n=2.9\times10^5$ cm^{-3} and $T_{kin}=21$ K, Colzi et al. (2018a) derived a HNC/H^{15}NC ratio of 431±24. For the first early chemistry time this is translated in a HNC/H^{15}NC of ~530. For t_2 the ratio is 470 (similar to the one that they obtained), and for t_3 it rises up to ~660. This is evidence that our results are time-dependent, and it should be noted that the times that we are using are only chemical times that may not represent the dynamical age of the object. So, a more accurate model including also the evolution of physical parameters is necessary to constrain better the time scales. Moreover, the H_2 column densities are derived from regions (15″ or 22″) that probably correspond to the more diffuse gas that surrounds the denser cores in which star-formation occurs. As an example, Beuther et al. (2007b) derived an H_2 column density of ~10^{23}–10^{24} cm^{-2} in regions of ~2″ towards the denser cores of 05358. These column densities correspond to H_2 densities of ~10^6–10^7 cm^{-3} that are one or two orders of magnitude higher than those used in this Section to compare with the model. Thus, detailed continuum observations and a description of the structures of these regions are needed to create more complete chemical and physical models.
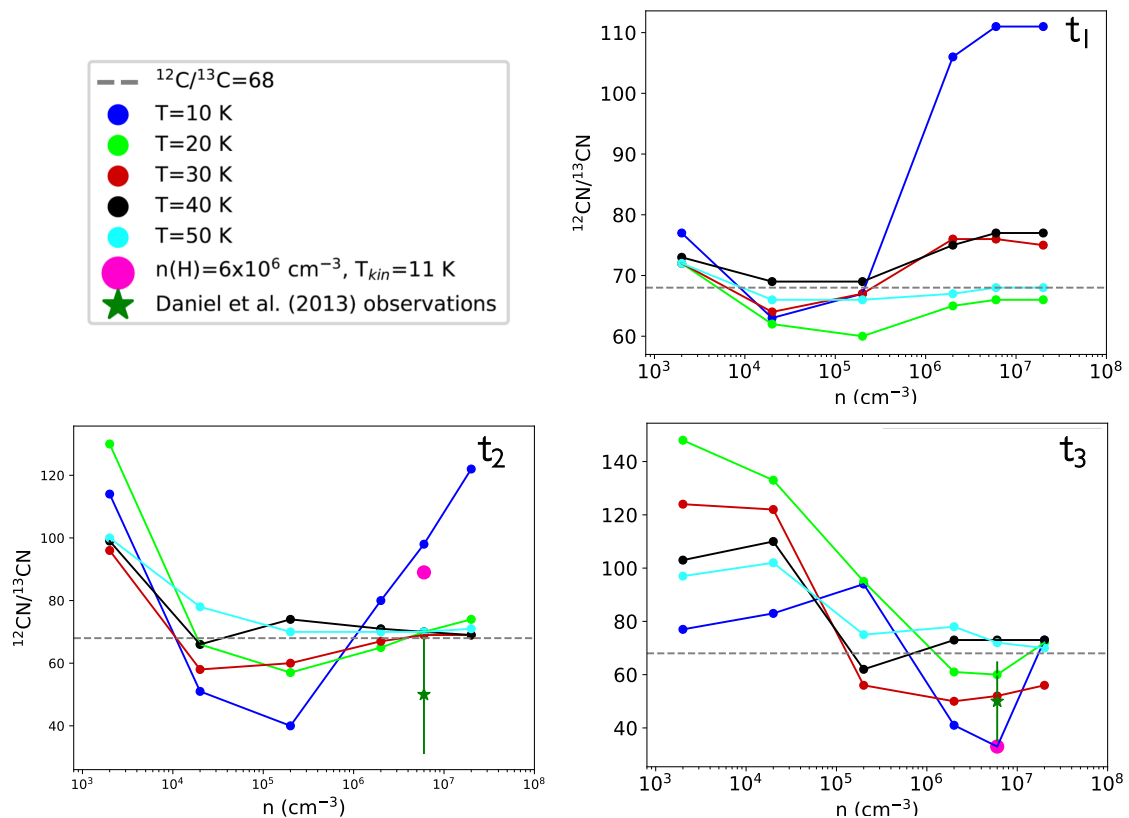
Fig. 5.15: ^{12}CN/^{13}CN ratio as a function of hydrogen density, for different temperatures, at t_1 (top right panel), t_2 (bottom left panel) and t_3 (bottom right panel). The large pink circles in the bottom panels represent the result of the model that simulates the physical conditions in the pre-stellar core B1b observed by Daniel et al. (2013). The ^{12}CN/^{13}CN ratio observed by Daniel et al. (2013) is represented by the green star.

Table 5.7: ^{12}C/^{13}C ratios derived for HNC and HCN in the range of temperatures and densities of the high-mass star-forming regions sample described in chapter 2 (Cols. 2 and 3). The fourth and fifth columns present the error factor made when deriving ^{14}N/^{15}N ratios assuming a ^{12}C/^{13}C ratio of 68.

Time	$R_1 = \frac{\text{HN}^{12}\text{C}}{\text{HN}^{13}\text{C}}$	$R_2 = \frac{\text{H}^{12}\text{CN}}{\text{H}^{13}\text{CN}}$	$R_1/68$	$R_2/68$
t_1	74–112	69–105	1.1–1.6	1–1.5
t_2	67–119	61–94	1–1.7	0.9–1.4
t_3	55–252	54–218	0.8–3.7	0.8–3.2

5.4. CONCLUSIONS

We have upgraded a comprehensive gas-grain chemical model to study in detail how important isotopic-exchange reactions are in the cold temperature (10–50 K) gas of different star-forming regions (with $n_{\text{H}}=2\times10^3$–2×10^7 cm^{-3}). Thus we were able to study how much column density ratios of species containing ^{13}C are affected by assuming a canonical ^{12}C/^{13}C ratio. In particular, we have investigated in detail the importance of the reaction:

$$^{13}\text{C} + \text{C}_3 \rightleftharpoons \text{C} + ^{13}\text{CC}_2, \tag{5.24}$$
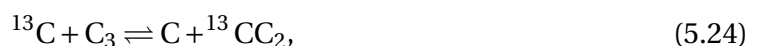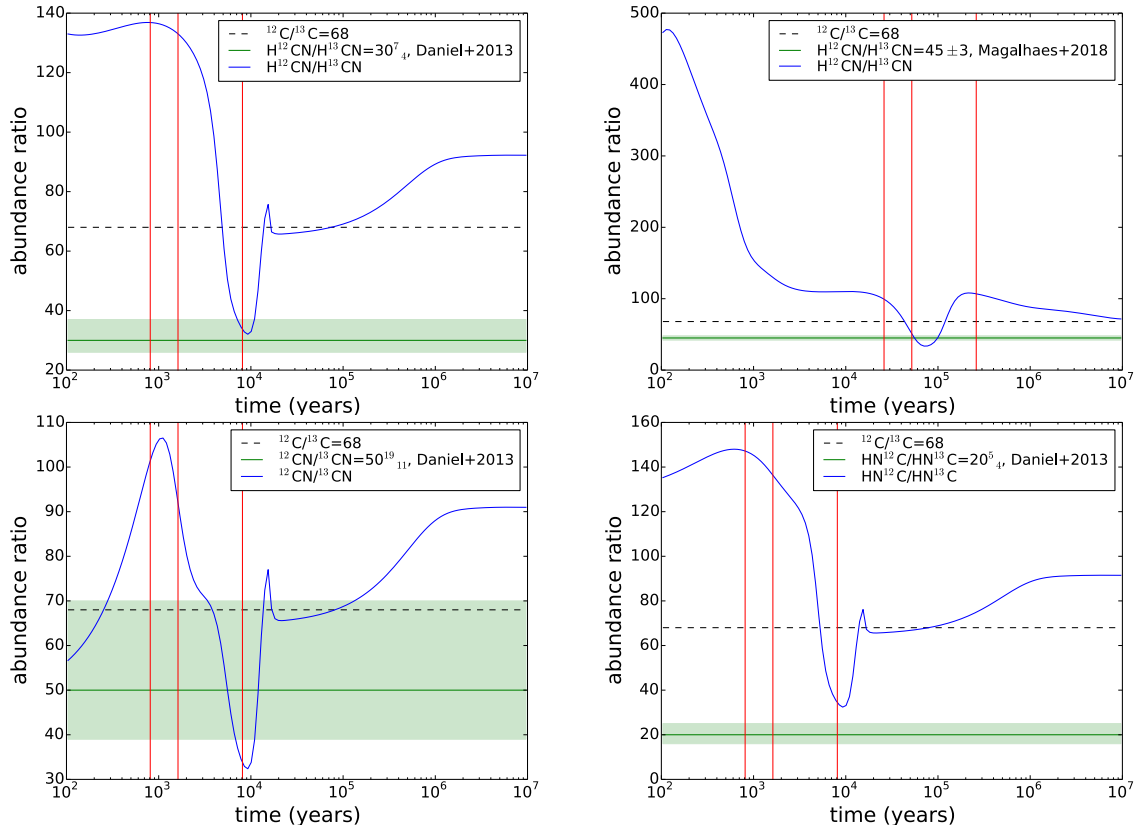
Fig. 5.16: *Top right panel:* time evolution of $^{12}C/^{13}C$ for HCN for the model that simulates L1498 observed by Magalhães et al. (2018). *Top left panel and bottom panels:* time evolution of $^{12}C/^{13}C$ for HCN, CN and HNC for the model that simulates the pre-stellar core B1b observed by Daniel et al. (2013). In all the panels the green horizon line indicates the observed ratio, with the associated uncertainty as green area. The three red vertical lines represent t_1, t_2 and t_3. The black horizontal dashed line represent the initial $^{12}C/^{13}C$ ratio of 68

Fig. 5.17: Same as Fig. 5.13 for HNC (*left*) and HCN (*right*) at t_1. In both panels the two vertical purple dashed lines represent the range of densities of the sample of high-mass star-forming region described in chapter 2.
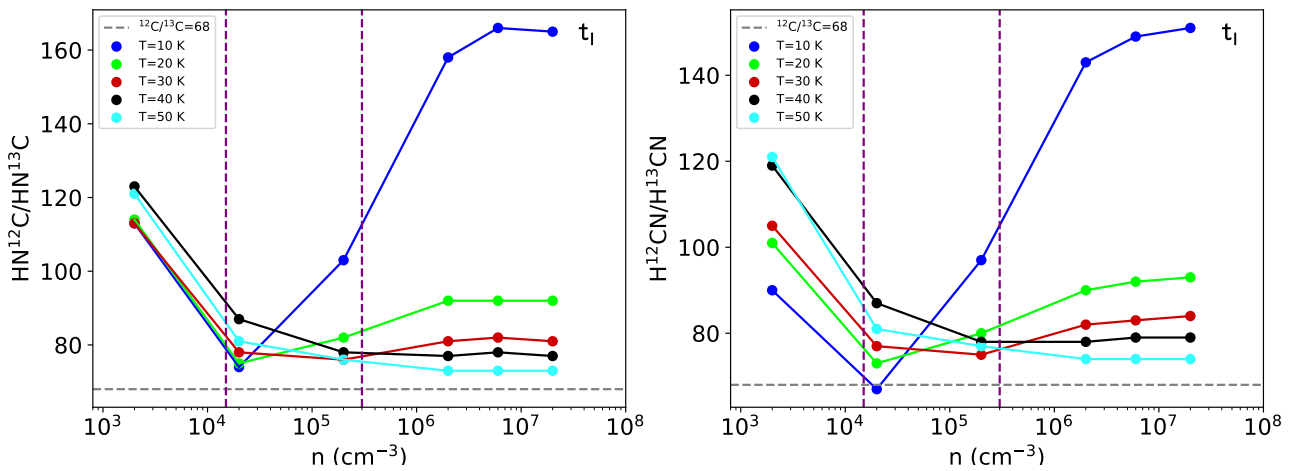
Fig. 5.18: Same as Fig. 5.13 for HNC (*left*) and HCN (*right*) at t_2. In both panels the two vertical purple dashed lines represent the range of densities of the sample of high-mass star-forming region described in chapter 2.

Fig. 5.19: Same as Fig. 5.13 for HNC (*left*) and HCN (*right*) at t_3. In both panels the two vertical purple dashed lines represent the range of densities of the sample of high-mass star-forming region described in chapter 2.
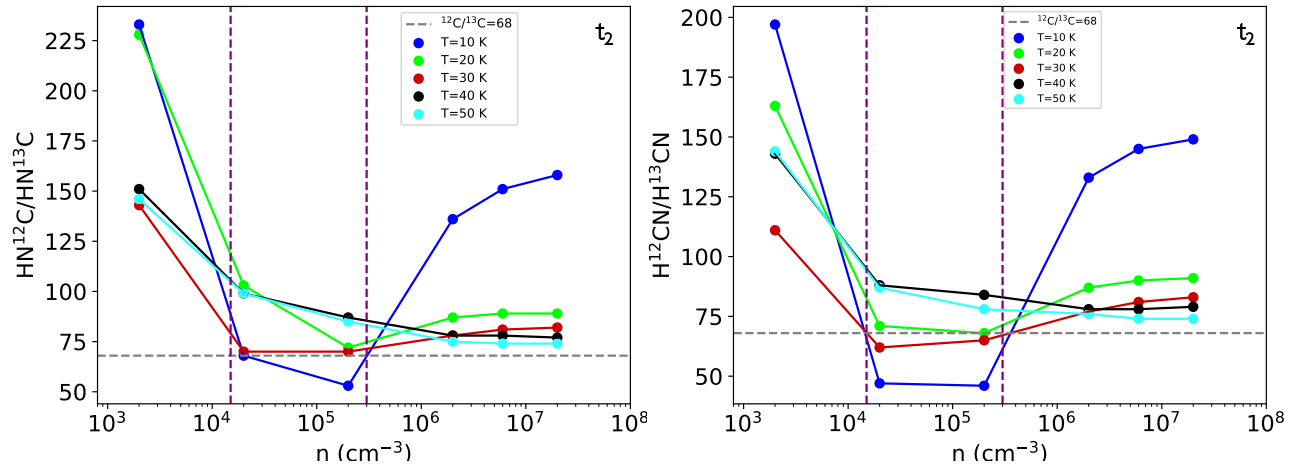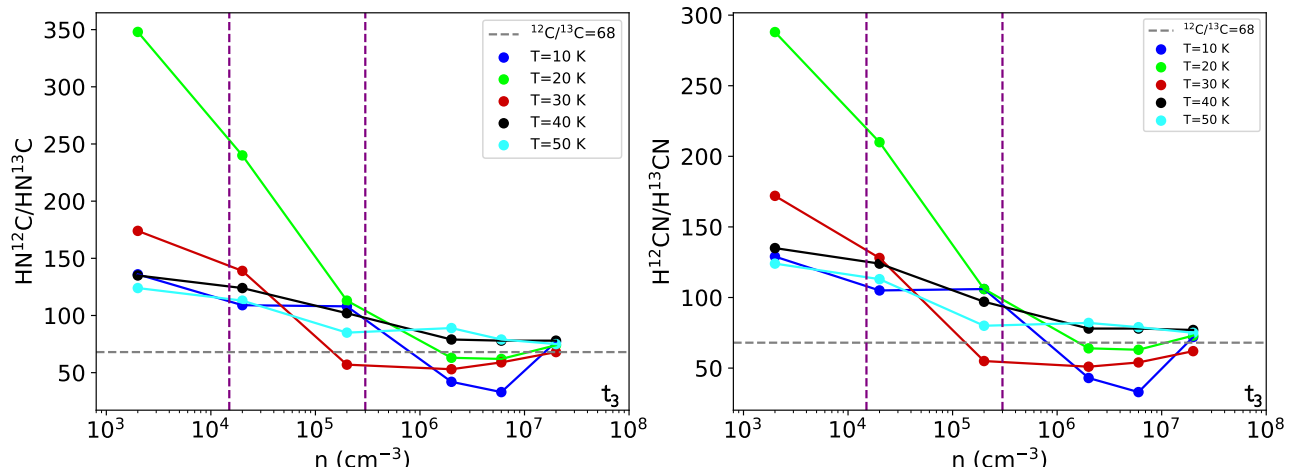
never investigated before in chemical models. This reaction is mainly important for T_{gas} <27 K (owing to its exothermicity), and leads to $^{12}C/^{13}C$<68 for molecules that form from atomic carbon. This behaviour is in between the early-chemistry time, defined as the time when most of the carbon is part of CO, and the late-chemistry time, that is when the CO almost totally freezes out on dust surfaces.

Furthermore, we have performed a detailed study of $^{12}C/^{13}C$ for the nitrile-bearing species HCN, HNC and CN, as a function of density and for different temperatures. To do this analysis we have identified three times, the first early-chemistry time (t_1, defined as the time when the abundance of atomic carbon decreases by one order magnitude when transformed in CO), $2 \times t_1$ and $10 \times t_1$. Interestingly, some of the $^{12}C/^{13}C$ <68, obtained thanks to reaction (5.24), could reproduce the carbon isotopic ratio derived by Daniel et al. (2013) and Magalhães et al. (2018) from observations towards low-mass star-forming regions.

Finally, we have used our grid of models to evaluate how far we are from the correct $^{12}C/^{13}C$ ratio assuming it to be 68 to derive the $^{14}N/^{15}N$ ratios in the sample observed and described in chapter 2. Our chemical model predicts that we are underestimating the assumed $^{12}C/^{13}C$ ratios by factors ~0.8–1.7, even up to ~3.7, depending on the time that we choose for the analysis. Considering these factors, the averaged nitrogen fractionation value of ~330 derived in chapters 2 and 3 for HCN and HNC, could become 260–1221. This range would include both the low values measured in comets (e.g. 250), and the high values found in low-mass pre-stellar cores (e.g. 1000 for N_2H^+ Bizzocchi et al. 2013). This highlights the importance of knowing the precise $^{12}C/^{13}C$ ratios to study nitrogen fractionation with the double-isotope method.

In a second work in preparation we will upgrade the chemical network to work on the ^{15}N in molecules and how carbon chemical fractionation could influence nitrogen fractionation.

6

SUMMARY AND MAIN CONCLUSIONS

High-mass star-forming regions, i.e. regions where massive stars ($M > 8$ M$_\odot$) can form, are raising interest for astrochemical studies since there is growing evidence that the environment in which our Sun was born contained also massive stars. Thus, the study of the chemical content of massive star-forming regions can give us important information about the chemical heritage of our Solar system.

One of the most important tools to perform this kind of study is the isotopic fractionation, which is the process that distributes different isotopes of an element in different molecular species. In particular, deuterium and ^{15}N turn out to be very enriched, with respect to hydrogen and ^{14}N, in pristine Solar system material, like comets and carbonaceous chondrites. The latter presents ^{14}N/^{15}N ratio~50–250 and D/H~10^{-4}, while for the proto-Solar nebula are estimated to be ~441 and 2×10^{-5}, respectively.

Nowadays there is a general theoretical consensus in explaining the observed D/H ratios towards both low- and high-mass star-forming regions: the cold and dense molecular gas is enriched in deuterium, as a consequence of the CO freeze-out. However, how and when the enrichment of ^{15}N in pristine Solar system material happened, during the Sun formation process, is still a highly debated topic. In fact, chemical models are still not able to reproduce all the observed ^{14}N/^{15}N ratios for the different kinds of molecules, like nitrile-bearing species (e.g. CN, HCN, HNC) and nitrogen hydrogenated species (e.g. NH$_3$, N$_2$H$^+$).

This thesis work is focused on the observational study of the ^{14}N/^{15}N ratio towards massive star-forming regions. I have studied it from a statistical point of view in a large sample of 87 sources, and then I have analysed in detail one of them with interferometric observations at high angular resolution. I have also studied theoretically the carbon fractionation (i.e. ^{12}C/^{13}C ratio) with the implementation of a new chemical network. With the introduction of new low-temperature isotopic-exchange reactions, I have studied its role in the derivation of ^{14}N/^{15}N when a canonical ^{12}C/^{13}C ratio is assumed.

The main objectives of this work were:

i) To investigate a possible relation between hydrogen and nitrogen fractionation of HCN and HNC, and a possible trend between different stages of high-mass star-forming regions.

ii) To derive the $^{14}N/^{15}N$ ratios, for HCN and HNC, as a function of the Galactocentric distance (in a large sample of 87 sources), and to compare with the predictions of a Galactic chemical evolution model.

iii) To study in detail the morphological distribution of ^{15}N-isotopologues of N_2H^+ towards the star-forming region IRAS 05358+3543 at high angular resolution, and to evaluate if there are local effects in the fractionation of nitrogen.

iv) To study carbon fractionation with a newly implemented gas-grain chemical network, simulating different gas densities and temperatures and comparing with available observations.

The main results and conclusions of this thesis are the following:

- **Hydrogen and nitrogen fractionation of HNC are independent.**
  The H/D and $^{14}N/^{15}N$ ratios for HNC in a sample of 27 high-mass star-forming regions have been studied. I have used single-dish IRAM 30m observations of the rotational transition (1–0) to evaluate, assuming LTE, both the HNC/DNC and HNC/H^{15}NC column density ratios towards the sample. The independence of the two isotopic fractionation ratios was found with a statistical test. This is in agreement with the possible anti-correlation found by Fontani et al. (2015b) for N_2H^+ towards the same sample of sources, and with the results of the chemical model performed by Wirström et al. (2012).

- **Nitrogen fractionation is not dependent on the evolutionary stage.**
  I have studied the HNC/H^{15}NC and HCN/HC^{15}N ratios in the sample of 27 massive star-forming regions, as a function of the evolutionary stage (high-mass starless cores, high-mass protostellar objects, and ultra compact HII regions). I have derived for both molecules no large spread of values around the proto-Solar nebula one (441), and no trend with the evolutionary stage. In fact, the $^{14}N/^{15}N$ ratios were consistent, within the errors, between the different evolutionary categories. I have also checked this last trend searching for a correlation between the $^{14}N/^{15}N$ ratios and the kinetic temperatures of the sources or the line width of the different observed lines since these parameters are good evolutionary indicators. Consistently, I did not find a trend with either temperature and line width. A similar result was already found also by Fontani et al. (2015b) for N_2H^+ towards the same sample of sources. Thus, it seems that N-fractionation for all the kind of molecules is not dependent on the kinetic temperatures, as already shown by the chemical model of Roueff et al. (2015). Our findings support that most of the important low-temperature isotopic-exchange reactions present a barrier and could not occur, maintaining the $^{14}N/^{15}N$ ratios basically unchanged with respect to the initial value assumed ($^{14}N/^{15}N$=441).

- **$^{14}N/^{15}N$ ratios distribution for HCN and HNC in massive star-forming regions.**
  The first sample was implemented with 60 new sources. The distributions of $^{14}N/^{15}N$ ratio for HCN and HNC present a peak in the bin defined between 310 and 350, namely below the PSN value (441) and above that measured in the terrestrial atmosphere (270). The two distributions are very similar and asymmetric, with a long tail at high $^{14}N/^{15}N$ values (up to ~780 and 1305 for HNC and HCN, respectively),

and a shorter one to lower values (~100). The asymmetric behaviour suggests that most of the values are in between 100–350, and only a few sources present anti-fractionated values (^{14}N/^{15}N>440).

- **^{14}N/^{15}N Galactocentric behaviour and its consistency with GCE models.**
  A new ^{14}N/^{15}N Galactocentric trend has been derived, and for the first time with a large statistical sample of 87 massive star-forming regions. First, I have performed a linear regression fit to the data that has provided results similar to those previously obtained by Adande and Ziurys (2012) based on a smaller sample. Then, I have performed a new fit with a Bayesian method that takes into account also the error bars of the derived ^{14}N/^{15}N. This result is in agreement with the linear regression fit. Both analyses suggest a linear positive trend, which is consistent with the prediction of Galactic chemical evolution models up to 8 kpc. These models predict a linear positive trend up to 8 kpc because of the introduction of novae outbursts as the main mechanism to produce ^{15}N. Then, after 8 kpc they predict a flattening trend because of the stellar yields that they assume for low-metallicity massive stars. Thus, I have performed a different analysis taking into account that to evaluate the ^{14}N/^{15}N for nitrile-bearing species I did not observe the main isotopologue, but the one with the ^{13}C isotope (H^{13}CN and HN^{13}C). This strategy needed to assume a certain ^{12}C/^{13}C ratio, and I have used the one derived as a function of the Galactocentric distance obtained by Milam et al. (2005). Taking into account this Galactocentric behaviour and that of our observations (H^{13}CN/HC^{15}N and HN^{13}C/H^{15}NC ratios) I have found a parabolic trend, that grows up to 8 kpc and flattens for higher distances. This behaviour is consistent with the GCE model of Romano et al. (2017) in the trend but not in the absolute values. More recently, Romano et al. (2019) have updated the low-metallicity massive stellar yields and the ejected mass in the form of ^{15}N from a novae outburst. In this way they can reproduce both our observed trend and absolute values.

- **The new local ISM ^{14}N/^{15}N ratio.**
  The new linear positive trend allow us to find a new local ISM ^{14}N/^{15}N value: 375±60. This was evaluated from the linear regression fit at a Sun distance from the Galactic center of ~8.4 kpc, as derived by Reid et al. (2014). This new value approaches the PSN ^{14}N/^{15}N of 441, with respect to previous estimates, and is consistent with the nowadays local value predicted by GCE models.

- **N-fractionation of N$_2$H$^+$ is a local effect in the high-mass star-forming region IRAS 05358+3543.**
  Interferometric observations allow us to investigate in detail the morphological distribution of different isotopologues. Moreover, they are needed to search if ^{15}N-enrichment in molecules is a local effect. In this context, I have studied the spatial distribution of ^{15}N-isopologues of N$_2$H$^+$ towards the high-mass star-forming region IRAS 05358+3543, with NOEMA Interferometer observations. The high angular resolution of 3″ allowed us to resolve spatial scales of ~0.03 pc given the distance of the source (1.8 kpc). The continuum emission is resolved in four cores: a high-mass protostellar object, a starless core, a core in an evolutionary stage intermediate between starless and protostellar, and a core (detected for the first time in this work) whose

nature is not clear yet. The overall structure of the integrated N_2H^+(1–0) emission, and that of $^{15}NNH^+$(1–0) and $N^{15}NH^+$(1–0) consists of three main cores, in agreement with each other. These cores are shifted with respect to the continuum peak, mainly towards mm1, likely because the star-formation activity destroys N_2H^+. The main results of this work is that N-fractionation of N_2H^+ seems to be a local effect. I have found $^{14}N/^{15}N$ ratios that are about 100-200 towards the dense cores, and higher values (>250) towards the diffuse envelope in which the cores are embedded. The model proposed by Furuya and Aikawa (2018) is in agreement with these results. They predict that isotope-selective photodissociation of N_2 leads to higher values of $^{14}N/^{15}N$ for N_2H^+, with respect to the initial one. The predictions of the model are also in agreement with the results obtained for nitrile-bearing species described in the points above. In fact, the $^{14}N/^{15}N$ ratios I have obtained for HCN and HNC with the IRAM 30m radiotelescope on scales of ~0.4 pc are higher than those obtained by Adande and Ziurys (2012) on scales of ~1 pc. Higher angular resolution observations of HCN and HNC are needed to firmly confirm this scenario, and explain the $^{14}N/^{15}N$ values observed.

- **Carbon fractionation: the importance of new low-temperature isotopic-exchange reactions.**
  Since some of the results on N-fractionation strongly depend on the assumed $^{12}C/^{13}C$ ratio, I have studied in detail carbon fractionation with the implementation of a chemical model. A gas-grain chemical model has been implemented with new carbon fractionation reactions. I have also included the same low-temperature isotopic-exchange reactions already included by Roueff et al. (2015). The reaction

$$^{13}C + {}^{12}C_3 \rightleftharpoons C + {}^{13}CC_2, \tag{6.1}$$

  is found to be important for gas temperatures <27 K, creating $^{12}C/^{13}C$ ratios lower than the nominal initial value of 68. This result is a consequence of the time scales when this reaction is still efficient and when most of the atomic carbon is already transformed in CO.

- **Carbon fractionation: density and temperature space exploration.**
  I have performed a detailed analysis of C-fractionation for the nitrile-bearing species CN, HCN and HNC, for different densities and temperatures. The analysis has been performed identifying 3 times: t_1 the one in which the abundance of atomic carbon drops by one order magnitude when transformed in CO, $2 \times t_1$, and $10 \times t_1$. With this analysis I could reproduce some of the $^{12}C/^{13}C$ ratios observed towards low-mass star-forming regions, which are lower than 68 (the local ISM value and assumed initial condition in the model). Finally, I have used the parameter space exploration to search for the predicted $^{12}C/^{13}C$ in regions with densities and kinetic temperatures similar to those observed in the first sample of 27 high-mass star-forming regions. I have derived $^{12}C/^{13}C$ for HCN and HNC that differ by factors between 0.8 and 3.7 compared to the one usually assumed of 68, in the local ISM, just using the Galactocentric dependence. This result highlights the importance of a proper derivation of the $^{12}C/^{13}C$ ratio to study the $^{14}N/^{15}N$ ratio.

BIBLIOGRAPHY

Máté Ádámkovics, Geoffrey A. Blake, and Benjamin J. McCall. Observations of Rotationally Resolved C_3 in Translucent Sight Lines. ApJ, 595(1):235–246, Sep 2003. doi: 10.1086/377305.

Fred C. Adams. The Birth Environment of the Solar System. ARA&A, 48:47–85, Sep 2010. doi: 10.1146/annurev-astro-081309-130830.

N. G. Adams and D. Smith. N-14/N-15 isotope fractionation in the reaction N2H/+/ + N2 - Interstellar significance. ApJ, 247:L123–L125, Aug 1981. doi: 10.1086/183604.

G. R. Adande and L. M. Ziurys. Millimeter-wave Observations of CN and HNC and Their ^{15}N Isotopologues: A New Evaluation of the $^{14}N/^{15}N$ Ratio across the Galaxy. ApJ, 744(2): 194, Jan 2012. doi: 10.1088/0004-637X/744/2/194.

Alfredo Aguado, Octavio Roncero, Alexandre Zanchet, Marcelino Agúndez, and José Cernicharo. The Photodissociation of HCN and HNC: Effects on the HNC/HCN Abundance Ratio in the Interstellar Medium. ApJ, 838(1):33, Mar 2017. doi: 10.3847/1538-4357/aa63ee.

Jérôme Aléon, François Robert, Marc Chaussidon, and Bernard Marty. Nitrogen isotopic composition of macromolecular organic matter in interplanetary dust particles. Geochim. Cosmochim. Acta, 67(19):3773–3783, Oct 2003. doi: 10.1016/S0016-7037(03)00170-4.

K. Altwegg, H. Balsiger, A. Bar-Nun, J. J. Berthelier, A. Bieler, P. Bochsler, C. Briois, U. Calmonte, M. Combi, and J. De Keyser. 67P/Churyumov-Gerasimenko, a Jupiter family comet with a high D/H ratio. *Science*, 347(6220):1261952, Jan 2015. doi: 10.1126/science.1261952.

Esteban Araya, Peter Hofner, Stan Kurtz, Leonardo Bronfman, and Simon DeDeo. CH_3CN Observations toward Southern Massive Star-forming Regions. *The Astrophysical Journal Supplement Series*, 157(2):279–301, Apr 2005. doi: 10.1086/427187.

A. Bacmann, V. Taquet, A. Faure, C. Kahane, and C. Ceccarelli. Detection of complex organic molecules in a prestellar core: a new challenge for astrochemical models. A&A, 541:L12, May 2012. doi: 10.1051/0004-6361/201219207.

Hans A. Bechtel, Adam H. Steeves, and Robert W. Field. Laboratory Measurements of the Hyperfine Structure of $H^{14}N^{12}C$ and $D^{14}N^{12}C$. ApJ, 649(1):L53–L56, Sep 2006. doi: 10.1086/508272.

M. T. Beltrán and W. J. de Wit. Accretion disks in luminous young stellar objects. *Astronomy and Astrophysics Review*, 24:6, Jan 2016. doi: 10.1007/s00159-015-0089-z.

M. T. Beltrán, R. Cesaroni, R. Neri, C. Codella, R. S. Furuya, L. Testi, and L. Olmi. Rotating Disks in High-Mass Young Stellar Objects. *The Astrophysical Journal*, 601(2):L187–L190, Feb 2004. doi: 10.1086/382150.

M. T. Beltrán, R. Cesaroni, R. Neri, C. Codella, R. S. Furuya, L. Testi, and L. Olmi. A detailed study of the rotating toroids in G31.41+0.31 and G24.78+0.08. *Astronomy and Astrophysics*, 435(3):901–925, Jun 2005. doi: 10.1051/0004-6361:20042381.

M. T. Beltrán, R. Cesaroni, V. M. Rivilla, Á. Sánchez-Monge, L. Moscadelli, A. Ahmadi, V. Allen, H. Beuther, S. Etoka, D. Galli, R. Galván-Madrid, C. Goddi, K. G. Johnston, P. D. Klaassen, A. Kölligan, R. Kuiper, M. S. N. Kumar, L. T. Maud, J. C. Mottram, T. Peters, P. Schilke, L. Testi, F. van der Tak, and C. M. Walmsley. Accelerating infall and rotational spin-up in the hot molecular core G31.41+0.31. *Astronomy and Astrophysics*, 615:A141, Jul 2018. doi: 10.1051/0004-6361/201832811.

T. Bergeman and D. Cossart. The lower excited states of CS: A study of extensive spin-orbit perturbations. *Journal of Molecular Spectroscopy*, 87(1):119–195, May 1981. doi: 10.1016/0022-2852(81)90088-6.

H. Bergeron, N. Rougeau, V. Sidis, M. Sizun, D. Teillet-Billy, and F. Aguillon. OH Formation from O and H Atoms Physisorbed on a Graphitic Surface through the Langmuir-Hinshelwood Mechanism: A Quasi-Classical Approach. *Journal of Physical Chemistry A*, 112:11921–11930, Oct 2008. doi: 10.1021/jp8050966.

Edwin A. Bergin and Mario Tafalla. Cold Dark Clouds: The Initial Conditions for Star Formation. ARA&A, 45(1):339–396, Sep 2007. doi: 10.1146/annurev.astro.45.071206.100404.

H. Beuther, P. Schilke, K. M. Menten, F. Motte, T. K. Sridharan, and F. Wyrowski. High-Mass Protostellar Candidates. II. Density Structure from Dust Continuum and CS Emission. *The Astrophysical Journal*, 566(2):945–965, Feb 2002a. doi: 10.1086/338334.

H. Beuther, P. Schilke, T. K. Sridharan, K. M. Menten, C. M. Walmsley, and F. Wyrowski. Massive molecular outflows. A&A, 383:892–904, Mar 2002b. doi: 10.1051/0004-6361: 20011808.

H. Beuther, A. Walsh, P. Schilke, T. K. Sridharan, K. M. Menten, and F. Wyrowski. CH_3OH and H_2O masers in high-mass star-forming regions. A&A, 390:289–298, Jul 2002c. doi: 10.1051/0004-6361:20020710.

H. Beuther, P. Schilke, F. Gueth, M. McCaughrean, M. Andersen, T. K. Sridharan, and K. M. Menten. IRAS 05358+3543: Multiple outflows at the earliest stages of massive star formation. A&A, 387:931–943, Jun 2002d. doi: 10.1051/0004-6361:20020319.

H. Beuther, E. B. Churchwell, C. F. McKee, and J. C. Tan. The Formation of Massive Stars. In Bo Reipurth, David Jewitt, and Klaus Keil, editors, *Protostars and Planets V*, page 165, Jan 2007a.

H. Beuther, S. Leurini, P. Schilke, F. Wyrowski, K. M. Menten, and Q. Zhang. Interferometric multi-wavelength (sub)millimeter continuum study of the young high-mass protocluster IRAS 05358+3543. A&A, 466(3):1065–1076, May 2007b. doi: 10.1051/0004-6361:20066742.

H. Beuther, Q. Zhang, E. A. Bergin, and T. K. Sridharan. Chemical Diversity in High-Mass Star Formation. AJ, 137(1):406–418, Jan 2009. doi: 10.1088/0004-6256/137/1/406.

A. Bieler, K. Altwegg, H. Balsiger, A. Bar-Nun, J. J. Berthelier, P. Bochsler, C. Briois, U. Calmonte, M. Combi, and J. de Keyser. Abundant molecular oxygen in the coma of comet 67P/Churyumov-Gerasimenko. Nature, 526(7575):678–681, Oct 2015. doi: 10.1038/nature15707.

S. E. Bisschop, J. K. Jørgensen, E. F. van Dishoeck, and E. B. M. de Wachter. Testing grain-surface chemistry in massive hot-core regions. A&A, 465(3):913–929, Apr 2007. doi: 10.1051/0004-6361:20065963.

L. Bizzocchi, P. Caselli, and L. Dore. Detection of $N^{15}NH^+$ in L1544. A&A, 510:L5, Feb 2010. doi: 10.1051/0004-6361/200913835.

L. Bizzocchi, P. Caselli, E. Leonardo, and L. Dore. Detection of $^{15}NNH^+$ in L1544: non-LTE modelling of dyazenilium hyperfine line emission and accurate $^{14}N/^{15}N$ values. A&A, 555:A109, Jul 2013. doi: 10.1051/0004-6361/201321276.

D. Bockelée-Morvan, D. Gautier, D. C. Lis, K. Young, J. Keene, T. Phillips, T. Owen, J. Crovisier, P. F. Goldsmith, and E. A. Bergin. Deuterated Water in Comet C/1996 B2 (Hyakutake) and Its Implications for the Origin of Comets. Icarus, 133(1):147–162, May 1998. doi: 10.1006/icar.1998.5916.

D. Bockelée-Morvan, N. Biver, E. Jehin, A. L. Cochran, H. Wiesemeyer, J. Manfroid, D. Hutsemékers, C. Arpigny, J. Boissier, and W. Cochran. Large Excess of Heavy Nitrogen in Both Hydrogen Cyanide and Cyanogen from Comet 17P/Holmes. ApJ, 679(1):L49, May 2008. doi: 10.1086/588781.

D. Bockelée-Morvan, N. Biver, B. Swinyard, M. de Val-Borro, J. Crovisier, P. Hartogh, D. C. Lis, R. Moreno, S. Szutowicz, and E. Lellouch. Herschel measurements of the D/H and $^{16}O/^{18}O$ ratios in water in the Oort-cloud comet C/2009 P1 (Garradd). A&A, 544:L15, Aug 2012. doi: 10.1051/0004-6361/201219744.

A. Boehle, A. M. Ghez, R. Schödel, L. Meyer, S. Yelda, S. Albers, G. D. Martinez, E. E. Becklin, T. Do, J. R. Lu, K. Matthews, M. R. Morris, B. Sitarski, and G. Witzel. An Improved Distance and Mass Estimate for Sgr A* from a Multistar Orbit Analysis. ApJ, 830(1):17, Oct 2016. doi: 10.3847/0004-637X/830/1/17.

Eva G. Bøgelund, Brett A. McGuire, Niels F. W. Ligterink, Vianney Taquet, Crystal L. Brogan, Todd R. Hunter, John C. Pearson, Michiel R. Hogerheijde, and Ewine F. van Dishoeck. Low levels of methanol deuteration in the high-mass star-forming region NGC 6334I. A&A, 615:A88, Jul 2018. doi: 10.1051/0004-6361/201832757.

Ian A. Bonnell, Stephen G. Vine, and Matthew R. Bate. Massive star formation: nurture, not nature. MNRAS, 349(2):735–741, Apr 2004. doi: 10.1111/j.1365-2966.2004.07543.x.

Henner Busemann, Andrea F. Young, Conel M. O'D. Alexand er, Peter Hoppe, Sujoy Mukhopadhyay, and Larry R. Nittler. Interstellar Chemistry Recorded in Organic Matter from Primitive Meteorites. Science, 312(5774):727–730, May 2006. doi: 10.1126/science.1123878.

G. Busquet, R. Estalella, Q. Zhang, S. Viti, A. Palau, P. T. P. Ho, and Á. Sánchez-Monge. N_2H^+ depletion in the massive protostellar cluster AFGL 5142. A&A, 525:A141, Jan 2011. doi: 10.1051/0004-6361/201014152.

Michael J. Butler and Jonathan C. Tan. Mid-Infrared Extinction Mapping of Infrared Dark Clouds: Probing the Initial Conditions for Massive Stars and Star Clusters. ApJ, 696(1): 484–497, May 2009. doi: 10.1088/0004-637X/696/1/484.

P. Caselli, C. M. Walmsley, M. Tafalla, L. Dore, and P. C. Myers. CO Depletion in the Starless Cloud Core L1544. ApJ, 523(2):L165–L169, Oct 1999. doi: 10.1086/312280.

P. Caselli, C. M. Walmsley, A. Zucconi, M. Tafalla, L. Dore, and P. C. Myers. Molecular Ions in L1544. II. The Ionization Degree. ApJ, 565(1):344–358, Jan 2002. doi: 10.1086/324302.

P. Caselli, F. F. S. van der Tak, C. Ceccarelli, and A. Bacmann. Abundant H_2D^+ in the pre-stellar core L1544. A&A, 403:L37–L41, May 2003. doi: 10.1051/0004-6361:20030526.

P. Caselli, C. Vastel, C. Ceccarelli, F. F. S. van der Tak, A. Crapsi, and A. Bacmann. Survey of ortho-H_2D^+ ($1_{1,0}$-$1_{1,1}$) in dense cloud cores. A&A, 492(3):703–718, Dec 2008. doi: 10. 1051/0004-6361:20079009.

Paola Caselli and Cecilia Ceccarelli. Our astrochemical heritage. A&A Rev., 20:56, Oct 2012. doi: 10.1007/s00159-012-0056-x.

S. Cazaux, P. Caselli, and M. Spaans. Interstellar Ices as Witnesses of Star Formation: Selective Deuteration of Water and Organic Molecules Unveiled. ApJ, 741(2):L34, Nov 2011. doi: 10.1088/2041-8205/741/2/L34.

Gabriele Cazzoli and Cristina Puzzarini. The Lamb-dip spectrum of the J + 1 ← J (J = 0, 1, 3-8) transitions of H ^{13}CN: The nuclear hyperfine structure due to H, ^{13}C, and ^{14}N. *Journal of Molecular Spectroscopy*, 233(2):280–289, Oct 2005b. doi: 10.1016/j.jms.2005.07.009.

Gabriele Cazzoli and Cristina Puzzarini. The Lamb-dip spectrum of methylcyanide: Precise rotational transition frequencies and improved ground-state rotational parameters. *Journal of Molecular Spectroscopy*, 240(2):153–163, Dec 2006. doi: 10.1016/j.jms.2006.09. 013.

Gabriele Cazzoli, Cristina Puzzarini, and Jürgen Gauss. The Rare Isotopomers of HCN: HC^{15}N and DC^{15}N. Rotational Spectrum and Resolved Nuclear Hyperfine Structures due to ^{15}N and D. ApJS, 159(1):181–188, Jul 2005a. doi: 10.1086/430209.

Gabriele Cazzoli, Lino Cludi, Giovanni Buffa, and Cristina Puzzarini. Precise THz Measurements of HCO$^+$, N_2H^+, and CF$^+$ for Astrophysical Observations. ApJS, 203(1):11, Nov 2012. doi: 10.1088/0067-0049/203/1/11.

C. Ceccarelli, P. Caselli, D. Bockelée-Morvan, O. Mousis, S. Pizzarello, F. Robert, and D. Semenov. Deuterium Fractionation: The Ariadne's Thread from the Precollapse Phase to Meteorites and Comets Today. In Henrik Beuther, Ralf S. Klessen, Cornelis P. Dullemond, and Thomas Henning, editors, *Protostars and Planets VI*, page 859, Jan 2014. doi: 10.2458/azu_uapress_9780816531240-ch037.

R. Cesaroni, M. T. Beltrán, Q. Zhang, H. Beuther, and C. Fallscheer. Dissecting a hot molecular core: the case of G31.41+0.31. *Astronomy and Astrophysics*, 533:A73, Sep 2011. doi: 10.1051/0004-6361/201117206.

R. Cesaroni, Á. Sánchez-Monge, M. T. Beltrán, K. G. Johnston, L. T. Maud, L. Moscadelli, J. C. Mottram, A. Ahmadi, V. Allen, H. Beuther, T. Csengeri, S. Etoka, G. A. Fuller, D. Galli, R. Galván-Madrid, C. Goddi, T. Henning, M. G. Hoare, P. D. Klaassen, R. Kuiper, M. S. N. Kumar, S. Lumsden, T. Peters, V. M. Rivilla, P. Schilke, L. Testi, F. van der Tak, S. Vig, C. M. Walmsley, and H. Zinnecker. Chasing discs around O-type (proto)stars: Evidence from ALMA observations. *Astronomy and Astrophysics*, 602:A59, Jun 2017. doi: 10.1051/0004-6361/201630184.

A. Chacón-Tanarro, P. Caselli, L. Bizzocchi, J. E. Pineda, O. Sipilä, A. Vasyunin, S. Spezzano, A. Punanova, B. M. Giuliano, and V. Lattanzi. Mapping deuterated methanol toward L1544. I. Deuterium fraction and comparison with modeling. A&A, 622:A141, Feb 2019. doi: 10.1051/0004-6361/201832703.

S. B. Charnley and S. D. Rodgers. The End of Interstellar Chemistry as the Origin of Nitrogen in Comets and Meteorites. ApJ, 569(2):L133–L137, Apr 2002. doi: 10.1086/340484.

Yi-nan Chin, Christian Henkel, Norbert Langer, and Rainer Mauersberger. The Detection of Extragalactic ^{15}N: Consequences for NitrogenNucleosynthesis and Chemical Evolution. ApJ, 512(2):L143–L146, Feb 1999. doi: 10.1086/311875.

Donald Clayton. *Handbook of Isotopes in the Cosmos.* 2003.

C. Codella, S. Viti, C. Ceccarelli, B. Lefloch, M. Benedettini, G. Busquet, P. Caselli, F. Fontani, A. Gómez-Ruiz, L. Podio, and M. Vasta. Broad N_2H^+ Emission toward the Protostellar Shock L1157-B1. ApJ, 776(1):52, Oct 2013. doi: 10.1088/0004-637X/776/1/52.

C. Codella, F. Fontani, C. Ceccarelli, L. Podio, S. Viti, R. Bachiller, M. Benedettini, and B. Lefloch. Astrochemistry at work in the L1157-B1 shock: acetaldehyde formation. MNRAS, 449:L11–L15, Apr 2015. doi: 10.1093/mnrasl/slu204.

L. Colzi, F. Fontani, P. Caselli, C. Ceccarelli, P. Hily-Blant, and L. Bizzocchi. Nitrogen and hydrogen fractionation in high-mass star-forming cores from observations of HCN and HNC. *Astronomy and Astrophysics*, 609:A129, Feb 2018a. doi: 10.1051/0004-6361/201730576.

L. Colzi, F. Fontani, V. M. Rivilla, A. Sánchez-Monge, L. Testi, M. T. Beltrán, and P. Caselli. Nitrogen fractionation in high-mass star-forming cores across the Galaxy. *Monthly Notices of the Royal Astronomical Society*, 478(3):3693–3720, Aug 2018b. doi: 10.1093/mnras/sty1027.

L. Colzi, F. Fontani, P. Caselli, S. Leurini, L. Bizzocchi, and G. Quaia. First interferometric study of enhanced N-fractionation in N_2H^+: the high-mass star-forming region IRAS 05358+3543. MNRAS, 485(4):5543–5558, Jun 2019. doi: 10.1093/mnras/stz794.

A. Crapsi, P. Caselli, C. M. Walmsley, P. C. Myers, M. Tafalla, C. W. Lee, and T. L. Bourke. Probing the Evolutionary Status of Starless Cores through N_2H^+ and N_2D^+ Observations. ApJ, 619(1):379–406, Jan 2005. doi: 10.1086/426472.

A. Crapsi, P. Caselli, M. C. Walmsley, and M. Tafalla. Observing the gas temperature drop in the high-density nucleus of L 1544. A&A, 470(1):221–230, Jul 2007. doi: 10.1051/0004-6361:20077613.

H. M. Cuppen, L. E. Kristensen, and E. Gavardi. H_2 reformation in post-shock regions. MNRAS, 406(1):L11–L15, Jul 2010. doi: 10.1111/j.1745-3933.2010.00871.x.

C. J. Cyganowski, C. L. Brogan, T. R. Hunter, D. Graninger, K. I. Öberg, A. Vasyunin, Q. Zhang, R. Friesen, and S. Schnee. G11.92-0.61-MM2: A Bonafide Massive Prestellar Core? ApJ, 796(1):L2, Nov 2014. doi: 10.1088/2041-8205/796/1/L2.

F. Daniel, M. Gérin, E. Roueff, J. Cernicharo, N. Marcelino, F. Lique, D. C. Lis, D. Teyssier, N. Biver, and D. Bockelée-Morvan. Nitrogen isotopic ratios in Barnard 1: a consistent study of the N_2H^+, NH_3, CN, HCN, and HNC isotopologues. A&A, 560:A3, Dec 2013. doi: 10.1051/0004-6361/201321939.

F. Daniel, A. Faure, L. Pagani, F. Lique, M. Gérin, D. Lis, P. Hily-Blant, A. Bacmann, and E. Roueff. N_2H^+ and $N^{15}NH^+$ toward the prestellar core 16293E in L1689N. A&A, 592: A45, Jul 2016. doi: 10.1051/0004-6361/201628192.

J. Daranlot, U. Hincelin, A. Bergeat, M. Costes, J. C. Loison, V. Wakelam, and K. M. Hickson. Elemental nitrogen partitioning in dense interstellar clouds. *Proceedings of the National Academy of Science*, 109(26):10233–10238, Jun 2012. doi: 10.1073/pnas.1200017109.

Ankan Das, Milan Sil, Prasanta Gorai, Sand ip K. Chakrabarti, and J. C. Loison. An Approach to Estimate the Binding Energy of Interstellar Species. ApJS, 237(1):9, Jul 2018. doi: 10.3847/1538-4365/aac886.

James Di Francesco, Philippe André, and Philip C. Myers. Quiescent Dense Gas in Protostellar Clusters: The Ophiuchus A Core. ApJ, 617(1):425–438, Dec 2004. doi: 10.1086/425264.

P. Didelon, F. Motte, P. Tremblin, T. Hill, S. Hony, M. Hennemann, P. Hennebelle, L. D. Anderson, F. Galliano, and N. Schneider. From forced collapse to H ii region expansion in Mon R2: Envelope density structure and age determination with Herschel⋆. A&A, 584: A4, Dec 2015. doi: 10.1051/0004-6361/201526239.

V. Dislaire, P. Hily-Blant, A. Faure, S. Maret, A. Bacmann, and G. Pineau Des Forêts. Nitrogen hydrides and the H_2 ortho-to-para ratio in dark clouds. A&A, 537:A20, Jan 2012. doi: 10.1051/0004-6361/201117765.

L. Dore, L. Bizzocchi, C. Degli Esposti, and F. Tinti. Accurate rest frequencies for the submillimetre-wave lines of the ^{15}{N}-containing isotopologues of N_2H^+ and N_2D^+. A&A, 496(1):275–279, Mar 2009. doi: 10.1051/0004-6361/200811235.

B. T. Draine and Brian Sutin. Collisional Charging of Interstellar Grains. ApJ, 320:803, Sep 1987. doi: 10.1086/165596.

Maria N. Drozdovskaya, Ewine F. van Dishoeck, Jes K. Jørgensen, Ursina Calmonte, Matthijs H. D. van der Wiel, Audrey Coutens, Hannah Calcutt, Holger S. P. Müller, Per Bjerkeli,

and Magnus V. Persson. The ALMA-PILS survey: the sulphur connection between protostars and comets: IRAS 16293-2422 B and 67P/Churyumov-Gerasimenko. MNRAS, 476 (4):4949–4964, Jun 2018. doi: 10.1093/mnras/sty462.

A. Duarte-Cabral, S. Bontemps, F. Motte, M. Hennemann, N. Schneider, and Ph. André. CO outflows from high-mass Class 0 protostars in Cygnus-X. A&A, 558:A125, Oct 2013. doi: 10.1051/0004-6361/201321393.

W. W. Duley and D. A. Williams. Book-Review - Interstellar Chemistry. Nature, 311:685, Oct 1984.

M. Emprechtinger, P. Caselli, N. H. Volgenau, J. Stutzki, and M. C. Wiedner. The N_2D^+/N_2H^+ ratio as an evolutionary tracer of Class 0 protostars. A&A, 493(1):89–105, Jan 2009. doi: 10.1051/0004-6361:200810324.

Christian P. Endres, Stephan Schlemmer, Peter Schilke, Jürgen Stutzki, and Holger S. P. Müller. The Cologne Database for Molecular Spectroscopy, CDMS, in the Virtual Atomic and Molecular Data Centre, VAMDC. *Journal of Molecular Spectroscopy*, 327:95–104, Sep 2016. doi: 10.1016/j.jms.2016.03.005.

A. Faure, M. Faure, P. Theulé, E. Quirico, and B. Schmitt. Hydrogen isotope exchanges between water and methanol in interstellar ices. A&A, 584:A98, Dec 2015. doi: 10.1051/0004-6361/201526499.

F. Fontani, P. Caselli, A. Crapsi, R. Cesaroni, S. Molinari, L. Testi, and J. Brand. Searching for massive pre-stellar cores through observations of N2H$^+$ and N2D$^+$. A&A, 460(3):709–720, Dec 2006. doi: 10.1051/0004-6361:20066105.

F. Fontani, I. Pascucci, P. Caselli, F. Wyrowski, R. Cesaroni, and C. M. Walmsley. Comparative study of complex N- and O-bearing molecules in hot molecular cores. A&A, 470(2):639–652, Aug 2007. doi: 10.1051/0004-6361:20077485.

F. Fontani, A. Palau, P. Caselli, Á. Sánchez-Monge, M. J. Butler, J. C. Tan, I. Jiménez-Serra, G. Busquet, S. Leurini, and M. Audard. Deuteration as an evolutionary tracer in massive-star formation. A&A, 529:L7, May 2011. doi: 10.1051/0004-6361/201116631.

F. Fontani, A. Giannetti, M. T. Beltrán, R. Dodson, M. Rioja, J. Brand, P. Caselli, and R. Cesaroni. High CO depletion in southern infrared dark clouds. MNRAS, 423(3):2342–2358, Jul 2012. doi: 10.1111/j.1365-2966.2012.21043.x.

F. Fontani, T. Sakai, K. Furuya, N. Sakai, Y. Aikawa, and S. Yamamoto. DNC/HNC and N_2D^+/N_2H^+ ratios in high-mass star-forming cores. MNRAS, 440(1):448–456, May 2014. doi: 10.1093/mnras/stu298.

F. Fontani, G. Busquet, Aina Palau, P. Caselli, Á. Sánchez-Monge, J. C. Tan, and M. Audard. Deuteration and evolution in the massive star formation process. The role of surface chemistry. A&A, 575:A87, Mar 2015a. doi: 10.1051/0004-6361/201424753.

F. Fontani, P. Caselli, A. Palau, L. Bizzocchi, and C. Ceccarelli. First Measurements of ^{15}N Fractionation in N_2H^+ toward High-mass Star-forming Cores. ApJ, 808(2):L46, Aug 2015b. doi: 10.1088/2041-8205/808/2/L46.

F. Fontani, B. Commerçon, A. Giannetti, M. T. Beltrán, A. Sánchez-Monge, L. Testi, J. Brand, P. Caselli, R. Cesaroni, R. Dodson, S. Longmore, M. Rioja, J. C. Tan, and C. M. Walmsley. Magnetically regulated fragmentation of a massive, dense, and turbulent clump. A&A, 593:L14, Sep 2016. doi: 10.1051/0004-6361/201629442.

F. Fontani, B. Commerçon, A. Giannetti, M. T. Beltrán, Á. Sánchez-Monge, L. Testi, J. Brand, and J. C. Tan. Fragmentation properties of massive protocluster gas clumps: an ALMA study. A&A, 615:A94, Jul 2018a. doi: 10.1051/0004-6361/201832672.

F. Fontani, A. Vagnoli, M. Padovani, L. Colzi, P. Caselli, and V. M. Rivilla. Protonated CO_2 in massive star-forming clumps. MNRAS, 481(1):79–83, Nov 2018b. doi: 10.1093/mnrasl/sly160.

Wilfred Frieswijk. *Early stages of clustered star formation: massive dark clouds throughout the Galaxy.* PhD thesis, Kapteyn Astronomical Institute, Mar 2008.

Kenji Furuya and Yuri Aikawa. Depletion of Heavy Nitrogen in the Cold Gas of Star-forming Regions. ApJ, 857(2):105, Apr 2018. doi: 10.3847/1538-4357/aab768.

Kenji Furuya, Yuri Aikawa, Nami Sakai, and Satoshi Yamamoto. Carbon Isotope and Isotopomer Fractionation in Cold Dense Cloud Cores. ApJ, 731(1):38, Apr 2011. doi: 10.1088/0004-637X/731/1/38.

G. Galazutdinov, A. Pětlewski, F. Musaev, C. Moutou, G. Lo Curto, and J. Krelowski. The interstellar C_3 chain molecule in different interstellar environments. A&A, 395:969–974, Dec 2002. doi: 10.1051/0004-6361:20021324.

R. T. Garrod and E. Herbst. Formation of methyl formate and other organic species in the warm-up phase of hot molecular cores. A&A, 457(3):927–936, Oct 2006. doi: 10.1051/0004-6361:20065560.

R. T. Garrod, V. Wakelam, and E. Herbst. Non-thermal desorption from interstellar dust grains via exothermic surface reactions. A&A, 467(3):1103–1115, Jun 2007. doi: 10.1051/0004-6361:20066704.

J. Geiss and G. Gloeckler. Abundances of Deuterium and Helium-3 in the Protosolar Cloud. Space Sci. Rev., 84:239–250, Apr 1998.

Y. M. Georgelin. PhD thesis, -, Jan 1975.

Yuri Georgievskii and J. Klippenstein, Stephen. Long-range transition state theory. *The Journal of Chemical Physics*, 122:194103, 2005. doi: 10.1063/1.1899603.

M. Gerin, D. C. Lis, S. Philipp, R. Güsten, E. Roueff, and V. Reveret. The distribution of ND_2H in LDN 1689N. A&A, 454(2):L63–L66, Aug 2006. doi: 10.1051/0004-6361:20065401.

M. Gerin, N. Marcelino, N. Biver, E. Roueff, L. H. Coudert, M. Elkeurti, D. C. Lis, and D. Bockelée-Morvan. Detection of $^{15}NH\{2\}D$ in dense cores: a new tool for measuring the $^{14}N/^{15}N$ ratio in the cold ISM. A&A, 498(2):L9–L12, May 2009. doi: 10.1051/0004-6361/200911759.

A. Giannetti, F. Wyrowski, J. Brand, T. Csengeri, F. Fontani, C. M. Walmsley, Q. Nguyen Lu-ong, H. Beuther, F. Schuller, R. Güsten, and K. M. Menten. ATLASGAL-selected massive clumps in the inner Galaxy. I. CO depletion and isotopic ratios. A&A, 570:A65, Oct 2014. doi: 10.1051/0004-6361/201423692.

Thomas F. Giesen, Bhaswati Mookerjea, Guido W. Fuchs, Alexander A. Breier, Daniel Witsch, Robert Simon, and Jürgen Stutzki. First detection of the carbon chain molecules 13CCC and C13CC towards SgrB2(M). *arXiv e-prints*, art. arXiv:1911.09751, Nov 2019.

Adam G. Ginsburg, John Bally, Chi-Hung Yan, and Jonathan P. Williams. Outflows and Massive Stars in the Protocluster IRAS 05358+3543. ApJ, 707(1):310–327, Dec 2009. doi: 10.1088/0004-637X/707/1/310.

R. Gomes, H. F. Levison, K. Tsiganis, and A. Morbidelli. Origin of the cataclysmic Late Heavy Bombardment period of the terrestrial planets. Nature, 435(7041):466–469, May 2005. doi: 10.1038/nature03676.

M. Gounelle and G. Meynet. Solar system genealogy revealed by extinct short-lived radionuclides in meteorites. A&A, 545:A4, Sep 2012. doi: 10.1051/0004-6361/201219031.

Matthieu Gounelle, Frank H. Shu, Hsien Shang, A. E. Glassgold, K. E. Rehm, and Typhoon Lee. Extinct Radioactivities and Protosolar Cosmic Rays: Self-Shielding and Light Elements. ApJ, 548(2):1051–1070, Feb 2001. doi: 10.1086/319019.

Didier Gourier, Francois Robert, Olivier Delpoux, Laurent Binet, Herve Vezin, Alain Moissette, and Sylvie Derenne. Extreme deuterium enrichment of organic radicals in the Orgueil meteorite: Revisiting the interstellar interpretation? Geochim. Cosmochim. Acta, 72(7):1914–1923, Apr 2008. doi: 10.1016/j.gca.2008.01.017.

Gravity Collaboration, R. Abuter, A. Amorim, M. Bauböck, J. P. Berger, H. Bonnet, W. Brandner, Y. Clénet, V. Coudé Du Foresto, P. T. de Zeeuw, J. Dexter, G. Duvert, A. Eckart, F. Eisenhauer, N. M. Förster Schreiber, P. Garcia, F. Gao, E. Gendron, R. Genzel, O. Gerhard, S. Gillessen, M. Habibi, X. Haubois, T. Henning, S. Hippler, M. Horrobin, A. Jiménez-Rosales, L. Jocou, P. Kervella, S. Lacour, V. Lapeyrère, J. B. Le Bouquin, P. Léna, T. Ott, T. Paumard, K. Perraut, G. Perrin, O. Pfuhl, S. Rabien, G. Rodriguez Coira, G. Rousset, S. Scheithauer, A. Sternberg, O. Straub, C. Straubmeier, E. Sturm, L. J. Tacconi, F. Vincent, S. von Fellenberg, I. Waisberg, F. Widmann, E. Wieprecht, E. Wiezorrek, J. Woillez, and S. Yazici. A geometric distance measurement to the Galactic center black hole with 0.3% uncertainty. A&A, 625:L10, May 2019. doi: 10.1051/0004-6361/201935656.

R. Gredel, S. Lepp, A. Dalgarno, and E. Herbst. Cosmic-Ray–induced Photodissociation and Photoionization Rates of Interstellar Molecules. ApJ, 347:289, Dec 1989. doi: 10.1086/168117.

V. V. Guzmán, K. I. Öberg, R. Loomis, and C. Qi. Cyanide Photochemistry and Nitrogen Fractionation in the MWC 480 Disk. ApJ, 814(1):53, Nov 2015. doi: 10.1088/0004-637X/814/1/53.

V. V. Guzmán, K. I. Öberg, J. Huang, R. Loomis, and C. Qi. Nitrogen Fractionation in Protoplanetary Disks from the $H^{13}CN/HC^{15}N$ Ratio. ApJ, 836(1):30, Feb 2017. doi: 10.3847/1538-4357/836/1/30.

H. J. Habing. The interstellar radiation density between 912 A and 2400 A. Bull. As-
    tron. Inst. Netherlands, 19:421, Jan 1968.

L. Matthew Haffner and David M. Meyer. A Search for Interstellar C 3 in the Translucent
    Cloud toward HD 147889. ApJ, 453:450, Nov 1995. doi: 10.1086/176406.

Paul Hartogh, Dariusz C. Lis, Dominique Bockelée-Morvan, Miguel de Val-Borro, Nicolas
    Biver, Michael Küppers, Martin Emprechtinger, Edwin A. Bergin, Jacques Crovisier, and
    Miriam Rengel. Ocean-like water in the Jupiter-family comet 103P/Hartley 2. Nature,
    478(7368):218–220, Oct 2011. doi: 10.1038/nature10519.

Tatsuhiko I. Hasegawa and Eric Herbst. New gas-grain chemical models of quiscent dense
    interstellar clouds :the effects of H2 tunnelling reactions and cosmic ray induced desorp-
    tion. MNRAS, 261:83–102, Mar 1993. doi: 10.1093/mnras/261.1.83.

Jiao He, Kinsuk Acharyya, and Gianfranco Vidali. Sticking of Molecules on Nonporous
    Amorphous Water Ice. ApJ, 823(1):56, May 2016. doi: 10.3847/0004-637X/823/1/56.

A. N. Heays, A. D. Bosman, and E. F. van Dishoeck. Photodissociation and photoionisation
    of atoms and molecules of astrophysical interest. A&A, 602:A105, Jun 2017. doi: 10.1051/
    0004-6361/201628742.

Alan N. Heays, Ruud Visser, Roland Gredel, Wim Ubachs, Brenton R. Lewis, Stephen T. Gib-
    son, and Ewine F. van Dishoeck. Isotope selective photodissociation of N_2 by the inter-
    stellar radiation field and cosmic rays. A&A, 562:A61, Feb 2014. doi: 10.1051/0004-6361/
    201322832.

Eric Herbst. Isotopic Fractionation by Ion-Molecule Reactions. Space Sci. Rev., 106(1):293–
    304, Apr 2003. doi: 10.1023/A:1024654108167.

Mark H. Heyer, John M. Carpenter, and E. F. Ladd. Giant Molecular Cloud Complexes with
    Optical H II Regions: 12CO and 13CO Observations and Global Cloud Properties. ApJ,
    463:630, Jun 1996. doi: 10.1086/177277.

P. Hily-Blant, M. Walmsley, G. Pineau Des Forêts, and D. Flower. CN in prestellar cores.
    A&A, 480(1):L5–L8, Mar 2008. doi: 10.1051/0004-6361:20079296.

P. Hily-Blant, L. Bonal, A. Faure, and E. Quirico. The ^{15}N-enrichment in dark clouds and
    Solar System objects. Icarus, 223(1):582–590, Mar 2013a. doi: 10.1016/j.icarus.2012.12.
    015.

P. Hily-Blant, G. Pineau des Forêts, A. Faure, R. Le Gal, and M. Padovani. The CN/C^{15}N
    isotopic ratio towards dark clouds. A&A, 557:A65, Sep 2013b. doi: 10.1051/0004-6361/
    201321364.

P. Hily-Blant, V. Magalhaes, J. Kastner, A. Faure, T. Forveille, and C. Qi. Direct evidence of
    multiple reservoirs of volatile nitrogen in a protosolar nebula analogue. A&A, 603:L6, Jul
    2017. doi: 10.1051/0004-6361/201730524.

C. N. Hinshelwood. *The Kinetics of Chemical Change (The Clarendon Press)*, 1940.

Tomoya Hirota, Satoshi Yamamoto, Hitomi Mikami, and Masatoshi Ohishi. Abundances of HCN and HNC in Dark Cloud Cores. ApJ, 503(2):717–728, Aug 1998. doi: 10.1086/306032.

J. G. Hosking and A. P. Whitworth. Fragmentation of magnetized cloud cores. MNRAS, 347 (3):1001–1010, Jan 2004. doi: 10.1111/j.1365-2966.2004.07274.x.

B. Hu, K. M. Menten, Y. Wu, A. Bartkiewicz, K. Rygl, M. J. Reid, J. S. Urquhart, and X. Zheng. On the Relationship of UC HII Regions and Class II Methanol Masers. I. Source Catalogs. ApJ, 833(1):18, Dec 2016. doi: 10.3847/0004-637X/833/1/18.

Jane Huang, Karin I. Öberg, Chunhua Qi, Yuri Aikawa, Sean M. Andrews, Kenji Furuya, Viviana V. Guzmán, Ryan A. Loomis, Ewine F. van Dishoeck, and David J. Wilner. An ALMA Survey of DCN/H^{13}CN and DCO$^+$/H^{13}CO$^+$ in Protoplanetary Disks. ApJ, 835(2):231, Feb 2017. doi: 10.3847/1538-4357/835/2/231.

K.P Huber and G. Herzberg. *Molecular Spectra and Molecular Structure - IV. Constants of diatomic molecules.* 1979.

Jason A. S. Hunt, Jo Bovy, and Raymond G. Carlberg. Detection of a Dearth of Stars with Zero Angular Momentum in the Solar Neighborhood. ApJ, 832(2):L25, Dec 2016. doi: 10.3847/2041-8205/832/2/L25.

Muneaki Imai, Nami Sakai, Ana López-Sepulcre, Aya E. Higuchi, Yichen Zhang, Yoko Oya, Yoshimasa Watanabe, Takeshi Sakai, Cecilia Ceccarelli, Bertrand Lefloch, and Satoshi Yamamoto. Deuterium Fractionation Survey Toward Protostellar Sources in the Perseus Molecular Cloud: HNC Case. ApJ, 869(1):51, Dec 2018. doi: 10.3847/1538-4357/aaeb21.

Shun Ishii, Fumitaka Nakamura, Yoshito Shimajiri, Ryohei Kawabe, Takashi Tsukagoshi, Kazuhito Dobashi, and Tomomi Shimoikura. Nobeyama 45 m mapping observations toward Orion A. II. Classification of cloud structures and variation of the ^{13}CO/C^{18}O abundance ratio due to far-UV radiation. PASJ, page 87, Jul 2019. doi: 10.1093/pasj/psz065.

Robert G. Izzard, Christopher A. Tout, Amanda I. Karakas, and Onno R. Pols. A new synthetic model for asymptotic giant branch stars. *Monthly Notices of the Royal Astronomical Society*, 350(2):407–426, May 2004. doi: 10.1111/j.1365-2966.2004.07446.x.

A. Jacobs, M. Wahl, R. Weller, and J. Wolfrum. Kinetic studies of the reaction of CN with H $_2$O from 518 to 1027 K. *Chemical Physics Letters*, 144(2):203–207, Feb 1988. doi: 10.1016/0009-2614(88)87118-5.

Izaskun Jiménez-Serra, Anton I. Vasyunin, Paola Caselli, Nuria Marcelino, Nicolas Billot, Serena Viti, Leonardo Testi, Charlotte Vastel, Bertrand Lefloch, and Rafael Bachiller. The Spatial Distribution of Complex Organic Molecules in the L1544 Pre-stellar Core. ApJ, 830(1):L6, Oct 2016. doi: 10.3847/2041-8205/830/1/L6.

Mihwa Jin, Jeong-Eun Lee, and Kee-Tae Kim. The HCN/HNC Abundance Ratio Toward Different Evolutionary Phases of Massive Star Formation. ApJS, 219(1):2, Jul 2015. doi: 10.1088/0067-0049/219/1/2.

Claudine Kahane, Ali Jaber Al-Edhari, Cecilia Ceccarelli, Ana López-Sepulcre, Francesco Fontani, and Mihkel Kama. First Measurement of the $^{14}N/^{15}N$ Ratio in the Analog of the Sun Progenitor OMC-2 FIR4. ApJ, 852(2):130, Jan 2018. doi: 10.3847/1538-4357/aa9e88.

Brandon C. Kelly. Some Aspects of Measurement Error in Linear Regression of Astronomical Data. ApJ, 665(2):1489–1506, Aug 2007. doi: 10.1086/519947.

Robert C. Kennicutt. The role of massive stars in astrophysics. In R. Cesaroni, M. Felli, E. Churchwell, and M. Walmsley, editors, *Massive Star Birth: A Crossroads of Astrophysics*, volume 227 of *IAU Symposium*, pages 3–11, Jan 2005. doi: 10.1017/S1743921305004308.

Eric Keto and Paola Caselli. Dynamics and depletion in thermally supercritical starless cores. MNRAS, 402(3):1625–1634, Mar 2010. doi: 10.1111/j.1365-2966.2009.16033.x.

B. Klein, S. Hochgürtel, I. Krämer, A. Bell, K. Meyer, and R. Güsten. High-resolution wideband fast Fourier transform spectrometers. *Astronomy and Astrophysics*, 542:L3, Jun 2012. doi: 10.1051/0004-6361/201218864.

Pavel Kroupa. On the variation of the initial mass function. MNRAS, 322(2):231–246, Apr 2001. doi: 10.1046/j.1365-8711.2001.04022.x.

M. L. Kutner and B. L. Ulich. Recommendations for calibration of millimeter-wavelength spectral line data. ApJ, 250:341–348, Nov 1981. doi: 10.1086/159380.

Charles J. Lada and Elizabeth A. Lada. Embedded Clusters in Molecular Clouds. ARA&A, 41:57–115, Jan 2003. doi: 10.1146/annurev.astro.41.011802.094844.

Kenneth R. Lang. *Astrophysical Data I. Planets and Stars.* 1992.

W. D. Langer, T. E. Graedel, M. A. Frerking, and P. B. Armentrout. Carbon and oxygen isotope fractionation in dense interstellar clouds. ApJ, 277:581–604, Feb 1984. doi: 10.1086/161730.

William D. Langer and Arno A. Penzias. 12C/ 13C Isotope Ratio across the Galaxy from Observations of 13C 18O in Molecular Clouds. ApJ, 357:477, Jul 1990. doi: 10.1086/168935.

William D. Langer and Arno A. Penzias. 12C/ 13C Isotope Ratio in the Local Interstellar Medium from Observations of 13C 18O in Molecular Clouds. ApJ, 408:539, May 1993. doi: 10.1086/172611.

I. Langmuir. *Transactions of the Faraday Society*, 17:621, 1922.

Patrick A. Lawson, Jr. Osborne, David, and Nigel G. Adams. Effect of isotopic content on the rate constants for the dissociative electron-ion recombination of N2H+. *International Journal of Mass Spectrometry*, 304(1):41–44, Jun 2011. doi: 10.1016/j.ijms.2011.03.013.

J. Le Bourlot. Ammonia formation and the ortho-to-para ratio of H2 in dark clouds. A&A, 242:235, Feb 1991.

Chin-Fei Lee, Paul T. P. Ho, and Stephen M. White. Molecular Line Observations of IRAM 04191+1522. ApJ, 619(2):948–958, Feb 2005. doi: 10.1086/426780.

S. Leurini, H. Beuther, P. Schilke, F. Wyrowski, Q. Zhang, and K. M. Menten. Multi-line (sub)millimetre observations of the high-mass proto cluster IRAS 05358+3543. A&A, 475 (3):925–939, Dec 2007. doi: 10.1051/0004-6361:20077977.

S. Leurini, T. Pillai, T. Stanke, F. Wyrowski, L. Testi, F. Schuller, K. M. Menten, and S. Thorwirth. The molecular distribution of the IRDC G351.77-0.51. A&A, 533:A85, Sep 2011. doi: 10.1051/0004-6361/201016380.

Mao-Chang Liang, Alan N. Heays, Brenton R. Lewis, Stephen T. Gibson, and Yuk L. Yung. Source of Nitrogen Isotope Anomaly in HCN in the Atmosphere of Titan. ApJ, 664(2): L115–L118, Aug 2007. doi: 10.1086/520881.

Tim Lichtenberg, Gregor J. Golabek, Remo Burn, Michael R. Meyer, Yann Alibert, Taras V. Gerya, and Christoph Mordasini. A water budget dichotomy of rocky protoplanets from ^{26}Al-heating. *Nature Astronomy*, 3:307–313, Feb 2019. doi: 10.1038/s41550-018-0688-5.

Marco Limongi and Alessandro Chieffi. Presupernova Evolution and Explosive Nucleosynthesis of Rotating Massive Stars in the Metallicity Range $-3 \leq [\mathrm{Fe/H}] \leq 0$. ApJS, 237(1):13, Jul 2018. doi: 10.3847/1538-4365/aacb24.

D. C. Lis, A. Wootten, M. Gerin, and E. Roueff. Nitrogen Isotopic Fractionation in Interstellar Ammonia. ApJ, 710(1):L49–L52, Feb 2010. doi: 10.1088/2041-8205/710/1/L49.

Ming-Chang Liu, Marc Chaussidon, Christa Göpel, and Typhoon Lee. A heterogeneous solar nebula as sampled by CM hibonite grains. *Earth and Planetary Science Letters*, 327: 75–83, Apr 2012. doi: 10.1016/j.epsl.2012.02.016.

Jean-Christophe Loison, Valentine Wakelam, and Kevin M. Hickson. The interstellar gas-phase chemistry of HCN and HNC. MNRAS, 443(1):398–410, Sep 2014. doi: 10.1093/mnras/stu1089.

Jean-Christophe Loison, Valentine Wakelam, Pierre Gratier, and Kevin M. Hickson. Chemical nitrogen fractionation in dense molecular clouds. MNRAS, 484(2):2747–2756, Apr 2019. doi: 10.1093/mnras/sty3293.

Xing Lu, Qizhou Zhang, Hauyu Baobab Liu, Junzhi Wang, and Qiusheng Gu. Very Large Array Observations of Ammonia in High-mass Star Formation Regions. ApJ, 790(2):84, Aug 2014. doi: 10.1088/0004-637X/790/2/84.

W. J. Maciel and R. D. D. Costa. Abundance gradients in the galactic disk: Space and time variations. In Johannes Andersen, Nordströara, Birgitta m, and Joss Bland - Hawthorn, editors, *The Galaxy Disk in Cosmological Context*, volume 254 of *IAU Symposium*, page 38, Mar 2009.

V. S. Magalhães, P. Hily-Blant, A. Faure, M. Hernand ez-Vera, and F. Lique. Abundance of HCN and its C and N isotopologues in L1498. A&A, 615:A52, Jul 2018. doi: 10.1051/0004-6361/201832622.

John P. Maier, Nicholas M. Lakin, Gordon A. H. Walker, and David A. Bohlender. Detection of C_3 in Diffuse Interstellar Clouds. ApJ, 553(1):267–273, May 2001. doi: 10.1086/320668.

J. Manfroid, E. Jehin, D. Hutsemékers, A. Cochran, J. M. Zucconi, C. Arpigny, R. Schulz, J. A. Stüwe, and I. Ilyin. The CN isotopic ratios in comets. A&A, 503(2):613–624, Aug 2009. doi: 10.1051/0004-6361/200911859.

S. Martín, J. Martín-Pintado, C. Blanco-Sánchez, V. M. Rivilla, A. Rodríguez-Franco, and F. Rico-Villas. Spectral Line Identification and Modelling (SLIM) in the MAdrid Data CUBe Analysis (MADCUBA) package: An interactive software for data cube analysis. *arXiv e-prints*, art. arXiv:1909.02147, Sep 2019.

Bernard Marty, Laurent Zimmermann, and Peter G. Burnard. Large scale nitrogen isotope variation in the solar system. *Geochimica et Cosmochimica Acta Supplement*, 73:A842, Jun 2009.

Bernard Marty, Laurent Zimmermann, Peter G. Burnard, Rainer Wieler, Veronika S. Heber, Donald L. Burnett, Roger C. Wiens, and Peter Bochsler. Nitrogen isotopes in the recent solar wind from the analysis of Genesis targets: Evidence for large scale isotope heterogeneity in the early solar system. Geochim. Cosmochim. Acta, 74(1):340–355, Jan 2010. doi: 10.1016/j.gca.2009.09.007.

J. S. Mathis, P. G. Mezger, and N. Panagia. Interstellar radiation field and dust temperatures in the diffuse interstellar matter and in giant molecular clouds. A&A, 500:259–276, Nov 1983.

D. A. McQuarrie. *Statistical Mechanics. Harper & Row, New York.* 1976.

Anders Meibom, Alexander N. Krot, François Robert, Smail Mostefaoui, Sara S. Russell, Michael I. Petaev, and Matthieu Gounelle. Nitrogen and Carbon Isotopic Composition of the Sun Inferred from a High-Temperature Solar Nebular Condensate. ApJ, 656(1): L33–L36, Feb 2007. doi: 10.1086/512052.

Roland Meier, Tobias C. Owen, David C. Jewitt, Henry E. Matthews, Matthew Senay, Nicolas Biver, Dominique Bockelee-Morvan, Jacques Crovisier, and Daniel Gautier. Deuterium in Comet C/1995 O1 (Hale-Bopp): Detection of DCN. *Science*, 279:1707, Mar 1998. doi: 10.1126/science.279.5357.1707.

G. Meynet and A. Maeder. Stellar evolution with rotation. VIII. Models at $Z = 10^{-5}$ and CNO yields for early galactic evolution. A&A, 390:561–583, Aug 2002. doi: 10.1051/0004-6361: 20020755.

S. N. Milam, C. Savage, M. A. Brewster, L. M. Ziurys, and S. Wyckoff. The $^{12}C/^{13}C$ Isotope Gradient Derived from Millimeter Transitions of CN: The Case for Galactic Chemical Evolution. ApJ, 634(2):1126–1132, Dec 2005. doi: 10.1086/497123.

V. Minier, R. S. Booth, and J. E. Conway. VLBI observations of 6.7 and 12.2 GHz methanol masers toward high mass star-forming regions. I. Observational results: protostellar disks or outflows? A&A, 362:1093–1108, Oct 2000.

M. Mladenović and E. Roueff. Ion-molecule reactions involving HCO^+ and N_2H^+: Isotopologue equilibria from new theoretical calculations and consequences for interstellar isotope fractionation. A&A, 566:A144, Jun 2014. doi: 10.1051/0004-6361/201423733.

C. D. Molek, J. L. McLain, V. Poterya, and N. G. Adams. A Remeasurement of the Products for Electron Recombination of N2H+Using a New Technique: No Significant NH + N Production†. *Journal of Physical Chemistry A*, 111(29):6760–6765, Jul 2007. doi: 10.1021/jp068965d.

S. Molinari, J. Brand, R. Cesaroni, and F. Palla. A search for precursors of ultracompact HII regions in a sample of luminous IRAS sources. I. Association with ammonia cores. A&A, 308:573–587, Apr 1996.

B. Mookerjea, G. E. Hassel, M. Gerin, T. Giesen, J. Stutzki, E. Herbst, J. H. Black, P. F. Goldsmith, K. M. Menten, J. Krełowski, M. De Luca, T. Csengeri, C. Joblin, M. Kaźmierczak, M. Schmidt, J. R. Goicoechea, and J. Cernicharo. Chemistry of C_3 and carbon chain molecules in DR21(OH). A&A, 546:A75, Oct 2012. doi: 10.1051/0004-6361/201219287.

B. Mookerjea, C. Vastel, G. E. Hassel, M. Gerin, J. Pety, P. F. Goldsmith, J. H. Black, T. Giesen, T. Harrison, C. M. Persson, and J. Stutzki. Detection of a dense clump in a filament interacting with W51e2. A&A, 566:A61, Jun 2014. doi: 10.1051/0004-6361/201323131.

A. Morbidelli, J. Chambers, J. I. Lunine, J. M. Petit, F. Robert, G. B. Valsecchi, and K. E. Cyr. Source regions and time scales for the delivery of water to Earth. *Meteoritics and Planetary Science*, 35(6):1309–1320, Nov 2000. doi: 10.1111/j.1945-5100.2000.tb01518.x.

L. Moscadelli, A. Sanna, C. Goddi, M. C. Walmsley, R. Cesaroni, A. Caratti o Garatti, B. Stecklum, K. M. Menten, and A. Kraus. Extended CH_3OH maser flare excited by a bursting massive YSO. A&A, 600:L8, Apr 2017. doi: 10.1051/0004-6361/201730659.

Frédérique Motte, Sylvain Bontemps, and Fabien Louvet. High-Mass Star and Massive Cluster Formation in the Milky Way. ARA&A, 56:41–82, Sep 2018. doi: 10.1146/annurev-astro-091916-055235.

H. S. P. Müller, S. Thorwirth, D. A. Roth, and G. Winnewisser. The Cologne Database for Molecular Spectroscopy, CDMS. A&A, 370:L49–L52, Apr 2001. doi: 10.1051/0004-6361:20010367.

Holger S. P. Müller, Frank Schlöder, Jürgen Stutzki, and Gisbert Winnewisser. The Cologne Database for Molecular Spectroscopy, CDMS: a useful tool for astronomers and spectroscopists. *Journal of Molecular Structure*, 742(1-3):215–227, May 2005. doi: 10.1016/j.molstruc.2005.01.027.

S. Muller, A. Beelen, M. Guélin, S. Aalto, J. H. Black, F. Combes, S. J. Curran, P. Theule, and S. N. Longmore. Molecules at z = 0.89. A 4-mm-rest-frame absorption-line survey toward PKS 1830-211. A&A, 535:A103, Nov 2011. doi: 10.1051/0004-6361/201117096.

Norman Murray. Star Formation Efficiencies and Lifetimes of Giant Molecular Clouds in the Milky Way. ApJ, 729(2):133, Mar 2011. doi: 10.1088/0004-637X/729/2/133.

Fumitaka Nakamura, Shuri Oyamada, Sachiko Okumura, Shun Ishii, Yoshito Shimajiri, Yoshihiro Tanabe, Takashi Tsukagoshi, Ryohei Kawabe, Mumetake Momose, Yumiko Urasawa, Ryoichi Nishi, Shen-Jun Lin, Shih-Ping Lai, Kazuhito Dobashi, Tomomi Shimoikura, and Koji Sugitani. Nobeyama 45 m mapping observations toward Orion A. III.

Multi-line observations toward an outflow-shocked region, Orion Molecular Cloud 2 FIR 4. PASJ, page 32, Mar 2019. doi: 10.1093/pasj/psz001.

Q. Nguyen-Lu'o'ng, F. Motte, P. Carlhoff, F. Louvet, P. Lesaffre, P. Schilke, T. Hill, M. Hennemann, A. Gusdorf, and P. Didelon. Low-velocity Shocks Traced by Extended SiO Emission along the W43 Ridges: Witnessing the Formation of Young Massive Clusters. ApJ, 775(2): 88, Oct 2013. doi: 10.1088/0004-637X/775/2/88.

Ken'ichi Nomoto, Chiaki Kobayashi, and Nozomu Tominaga. Nucleosynthesis in Stars and the Chemical Enrichment of Galaxies. ARA&A, 51(1):457–509, Aug 2013. doi: 10.1146/annurev-astro-082812-140956.

T. Nony, F. Louvet, F. Motte, J. Molet, K. Marsh, E. Chapillon, A. Gusdorf, N. Brouillet, S. Bontemps, T. Csengeri, D. Despois, Q. Nguyen Luong, A. Duarte-Cabral, and A. Maury. Detection of a high-mass prestellar core candidate in W43-MM1. A&A, 618:L5, Oct 2018. doi: 10.1051/0004-6361/201833863.

K. I. Öberg, E. F. van Dishoeck, and H. Linnartz. Photodesorption of ices I: CO, N_2, and CO_2. A&A, 496(1):281–293, Mar 2009a. doi: 10.1051/0004-6361/200810207.

Karin I. Öberg, Harold Linnartz, Ruud Visser, and Ewine F. van Dishoeck. Photodesorption of Ices. II. H_2O and D_2O. ApJ, 693(2):1209–1218, Mar 2009b. doi: 10.1088/0004-637X/693/2/1209.

Takeshi Oka, Julie A. Thorburn, Benjamin J. McCall, Scott D. Friedman, Lewis M. Hobbs, Paule Sonnentrucker, Daniel E. Welty, and Donald G. York. Observations of C_3 in Translucent Sight Lines. ApJ, 582(2):823–829, Jan 2003. doi: 10.1086/344726.

J. Ospina-Zamudio, C. Favre, M. Kounkel, L. H. Xu, J. Neill, B. Lefloch, A. Faure, E. Bergin, D. Fedele, and L. Hartmann. Deuterated methanol toward NGC 7538-IRS1. A&A, 627: A80, Jul 2019. doi: 10.1051/0004-6361/201834948.

L. Pagani, M. Salez, and P. G. Wannier. The chemistry of H2D+ in cold clouds. A&A, 258: 479–488, May 1992.

Aina Palau, Asunción Fuente, Josep M. Girart, Robert Estalella, Paul T. P. Ho, Álvaro Sánchez-Monge, Francesco Fontani, Gemma Busquet, Benoit Commerçon, and Patrick Hennebelle. Early Stages of Cluster Formation: Fragmentation of Massive Dense Cores down to <‿1000 AU. ApJ, 762(2):120, Jan 2013. doi: 10.1088/0004-637X/762/2/120.

E. F. Pearson, R. A. Creswell, M. Winnewisser, and G. Winnewisser. The molecular structure of HNC and HCN derived from the eight stable isotopic species. *Zeitschrift Naturforschung Teil A*, 31:1394–1397, Jan 1976. doi: 10.1515/zna-1976-1119.

J. Pety. Successes of and Challenges to GILDAS, a State-of-the-Art Radioastronomy Toolkit. In F. Casoli, T. Contini, J. M. Hameury, and L. Pagani, editors, *SF2A-2005: Semaine de l'Astrophysique Francaise*, page 721, Dec 2005.

T. Pillai, J. Kauffmann, F. Wyrowski, J. Hatchell, A. G. Gibb, and M. A. Thompson. Probing the initial conditions of high-mass star formation. II. Fragmentation, stability, and chemistry

towards high-mass star-forming regions G29.96-0.02 and G35.20-1.74. A&A, 530:A118, Jun 2011. doi: 10.1051/0004-6361/201015899.

S. Portegies Zwart. The formation of solar-system analogs in young star clusters. A&A, 622: A69, Feb 2019. doi: 10.1051/0004-6361/201833974.

C. R. Purcell, R. Balasubramanyam, M. G. Burton, A. J. Walsh, V. Minier, M. R. Hunt-Cunningham, L. L. Kedziora-Chudczer, S. N. Longmore, T. Hill, I. Bains, P. J. Barnes, A. L. Busfield, P. Calisse, N. H. M. Crighton, S. J. Curran, T. M. Davis, J. T. Dempsey, G. Derragopian, B. Fulton, M. G. Hidas, M. G. Hoare, J. K. Lee, E. F. Ladd, S. L. Lumsden, T. J. T. Moore, M. T. Murphy, R. D. Oudmaijer, M. B. Pracy, J. Rathborne, S. Robertson, A. S. B. Schultz, J. Shobbrook, P. A. Sparks, J. Storey, and T. Travouillion. A CH$_3$CN and HCO$^+$ survey towards southern methanol masers associated with star formation. *Monthly Notices of the Royal Astronomical Society*, 367(2):553–576, Apr 2006. doi: 10.1111/j.1365-2966.2005.09921.x.

Sarah E. Ragan, Edwin A. Bergin, and Robert A. Gutermuth. Detection of Structure in Infrared-Dark Clouds with Spitzer: Characterizing Star Formation in the Molecular Ring. ApJ, 698(1):324–349, Jun 2009. doi: 10.1088/0004-637X/698/1/324.

J. M. Rathborne, J. M. Jackson, and R. Simon. Infrared Dark Clouds: Precursors to Star Clusters. ApJ, 641(1):389–405, Apr 2006. doi: 10.1086/500423.

E. Redaelli, L. Bizzocchi, P. Caselli, J. Harju, A. Chacón-Tanarro, E. Leonardo, and L. Dore. ^{14}N/^{15}N ratio measurements in prestellar cores with N$_2$H$^+$: new evidence of ^{15}N-antifractionation. A&A, 617:A7, Sep 2018. doi: 10.1051/0004-6361/201833065.

Elena Redaelli, Luca Bizzocchi, Paola Caselli, Olli Sipilä, Valerio Lattanzi, Barbara Michela Giuliano, and Silvia Spezzano. High sensitivity maps of molecular ions in L1544: I. Deuteration of N2H+ and HCO+ and first evidence of N2D+ depletion. *arXiv e-prints*, art. arXiv:1907.08217, Jul 2019.

M. J. Reid, K. M. Menten, A. Brunthaler, X. W. Zheng, T. M. Dame, Y. Xu, Y. Wu, B. Zhang, A. Sanna, M. Sato, K. Hachisuka, Y. K. Choi, K. Immer, L. Moscadelli, K. L. J. Rygl, and A. Bartkiewicz. Trigonometric Parallaxes of High Mass Star Forming Regions: The Structure and Kinematics of the Milky Way. ApJ, 783(2):130, Mar 2014. doi: 10.1088/0004-637X/783/2/130.

Michael A. Reid and Brenda C. Matthews. Deconstructing the High-Mass Star-Forming Region IRAS 23033+5951. ApJ, 675(2):1343–1351, Mar 2008. doi: 10.1086/527408.

Laurent Remusat, François Robert, Anders Meibom, Smail Mostefaoui, Olivier Delpoux, Laurent Binet, Didier Gourier, and Sylvie Derenne. Proto-Planetary Disk Chemistry Recorded by D-Rich Organic Radicals in Carbonaceous Chondrites. ApJ, 698(2):2087–2092, Jun 2009. doi: 10.1088/0004-637X/698/2/2087.

Claire Rist, Alexandre Faure, Pierre Hily-Blant, and Romane Le Gal. Nuclear-Spin Selection Rules in the Chemistry of Interstellar Nitrogen Hydrides. *Journal of Physical Chemistry A*, 117(39):9800–9806, Oct 2013. doi: 10.1021/jp312640a.

V. M. Rivilla, F. Fontani, M. T. Beltrán, A. Vasyunin, P. Caselli, J. Martín-Pintado, and R. Cesaroni. The First Detections of the Key Prebiotic Molecule PO in Star-forming Regions. *The Astrophysical Journal*, 826(2):161, Aug 2016. doi: 10.3847/0004-637X/826/2/161.

V. M. Rivilla, M. T. Beltrán, R. Cesaroni, F. Fontani, C. Codella, and Q. Zhang. Formation of ethylene glycol and other complex organic molecules in star-forming regions. *Astronomy and Astrophysics*, 598:A59, Feb 2017. doi: 10.1051/0004-6361/201628373.

François Robert. The D/H Ratio in Chondrites. Space Sci. Rev., 106(1):87–101, Apr 2003. doi: 10.1023/A:1024629402715.

S. D. Rodgers and S. B. Charnley. Nitrogen superfractionation in dense cloud cores. MNRAS, 385(1):L48–L52, Mar 2008a. doi: 10.1111/j.1745-3933.2008.00431.x.

S. D. Rodgers and S. B. Charnley. Nitrogen Isotopic Fractionation of Interstellar Nitriles. ApJ, 689(2):1448–1455, Dec 2008b. doi: 10.1086/592195.

M. Röllig and V. Ossenkopf. Carbon fractionation in photo-dissociation regions. A&A, 550: A56, Feb 2013. doi: 10.1051/0004-6361/201220130.

D. Romano, F. Matteucci, Z. Y. Zhang, P. P. Papadopoulos, and R. J. Ivison. The evolution of CNO isotopes: a new window on cosmic star formation history and the stellar IMF in the age of ALMA. *Monthly Notices of the Royal Astronomical Society*, 470(1):401–415, Sep 2017. doi: 10.1093/mnras/stx1197.

Donatella Romano and Francesca Matteucci. Nova nucleosynthesis and Galactic evolution of the CNO isotopes. *Monthly Notices of the Royal Astronomical Society*, 342(1):185–198, Jun 2003. doi: 10.1046/j.1365-8711.2003.06526.x.

Donatella Romano, Francesca Matteucci, Zhi-Yu Zhang, Rob J. Ivison, and Paolo Ventura. The evolution of CNO isotopes: the impact of massive stellar rotators. *arXiv e-prints*, art. arXiv:1907.09476, Jul 2019.

E. Roueff, P. Felenbok, J. H. Black, and C. Gry. Interstellar C_3 toward HD 210121. A&A, 384: 629–637, Mar 2002. doi: 10.1051/0004-6361:20020067.

E. Roueff, D. C. Lis, F. F. S. van der Tak, M. Gerin, and P. F. Goldsmith. Interstellar deuterated ammonia: from NH_3 to ND_3. A&A, 438(2):585–598, Aug 2005. doi: 10.1051/0004-6361: 20052724.

E. Roueff, J. C. Loison, and K. M. Hickson. Isotopic fractionation of carbon, deuterium, and nitrogen: a full chemical study. A&A, 576:A99, Apr 2015. doi: 10.1051/0004-6361/201425113.

D. P. Ruffle, T. W. Hartquist, S. D. Taylor, and D. A. Williams. Cyanopolyynes as indicators of late-time chemistry and depletion in star-forming regions. MNRAS, 291(1):235–240, Oct 1997. doi: 10.1093/mnras/291.1.235.

Deborah P. Ruffle and Eric Herbst. New models of interstellar gas-grain chemistry - I. Surface diffusion rates. MNRAS, 319(3):837–850, Dec 2000. doi: 10.1046/j.1365-8711.2000. 03911.x.

G. Sabatini, A. Giannetti, S. Bovino, J. Brand, S. Leurini, E. Schisano, T. Pillai, and K. M. Menten. On the size of the CO-depletion radius in the IRDC G351.77-0.51. MNRAS, 490 (4):4489–4501, Dec 2019. doi: 10.1093/mnras/stz2818.

N. Sakai, O. Saruwatari, T. Sakai, S. Takano, and S. Yamamoto. Abundance anomaly of the ^{13}C species of CCH. A&A, 512:A31, Mar 2010. doi: 10.1051/0004-6361/200913098.

Takeshi Sakai, Nami Sakai, Kenji Furuya, Yuri Aikawa, Tomoya Hirota, and Satoshi Yamamoto. DNC/HNC Ratio of Massive Clumps in Early Evolutionary Stages of High-mass Star Formation. ApJ, 747(2):140, Mar 2012. doi: 10.1088/0004-637X/747/2/140.

A. Sanna, L. Moscadelli, C. Goddi, V. Krishnan, and F. Massi. Protostellar Outflows at the EarliesT Stages (POETS). I. Radio thermal jets at high resolution nearby H_2O maser sources. A&A, 619:A107, Nov 2018. doi: 10.1051/0004-6361/201833573.

P. Schilke, C. M. Walmsley, G. Pineau Des Forets, E. Roueff, D. R. Flower, and S. Guilloteau. A study of HCN, HNC and their isotopomers in OMC-1. I. Abundances and chemistry. A&A, 256:595–612, Mar 1992.

J. H. M. M. Schmitt and J. U. Ness. Carbon and nitrogen abundances in the coronae of Algol B and other evolved stars: Evidence for CNO-cycle processed material. *Astronomy and Astrophysics*, 388:L13–L16, Jun 2002. doi: 10.1051/0004-6361:20020558.

N. Schneider, T. Csengeri, S. Bontemps, F. Motte, R. Simon, P. Hennebelle, C. Federrath, and R. Klessen. Dynamic star formation in the massive DR21 filament. A&A, 520:A49, Sep 2010. doi: 10.1051/0004-6361/201014481.

Benjamin Schröder and Peter Sebald. High-level theoretical rovibrational spectroscopy beyond fc-CCSD(T): The C_3 molecule. J. Chem. Phys., 144(4):044307, Jan 2016. doi: 10.1063/1.4940780.

D. Semenov, F. Hersant, V. Wakelam, A. Dutrey, E. Chapillon, S. Guilloteau, T. Henning, R. Launhardt, V. Piétu, and K. Schreyer. Chemistry in disks. IV. Benchmarking gas-grain chemical models with surface reactions. A&A, 522:A42, nov 2010. doi: 10.1051/0004-6361/201015149.

Frank Shu, Joan Najita, Daniele Galli, Eve Ostriker, and Susana Lizano. The Collapse of Clouds and the Formation and Evolution of Stars and Disks. In Eugene H. Levy and Jonathan I. Lunine, editors, *Protostars and Planets III*, page 3, Jan 1993.

Frank H. Shu. The Formation of Low Mass Stars: Theory. In Charles J. Lada and Nikolaos D. Kylafis, editors, *NATO Advanced Science Institutes (ASI) Series C*, volume 342, page 365, Jan 1991.

Frank H. Shu, Fred C. Adams, and Susana Lizano. Star formation in molecular clouds: observation and theory. ARA&A, 25:23–81, Jan 1987. doi: 10.1146/annurev.aa.25.090187.000323.

O. Sipilä, P. Caselli, and J. Harju. HD depletion in starless cores. A&A, 554:A92, jun 2013. doi: 10.1051/0004-6361/201220922.

O. Sipilä, P. Caselli, and J. Harju. Benchmarking spin-state chemistry in starless core models. A&A, 578:A55, jun 2015a. doi: 10.1051/0004-6361/201424364.

O. Sipilä, J. Harju, P. Caselli, and S. Schlemmer. Spin-state chemistry of deuterated ammonia. A&A, 581:A122, sep 2015b. doi: 10.1051/0004-6361/201526468.

O. Sipilä, P. Caselli, E. Redaelli, M. Juvela, and L. Bizzocchi. Why does ammonia not freeze out in the centre of pre-stellar cores? MNRAS, 487(1):1269–1282, Jul 2019. doi: 10.1093/mnras/stz1344.

Olli Sipilä. *Studies of the chemistry and physics of starless and prestellar cores.* PhD thesis, University of Helsinki, 2013.

D. Smith and N. G. Adams. Laboratory studies of isotope fractionation in the reactions of C/+/ and HCO/+/ with CO - Interstellar implications. ApJ, 242:424–431, Nov 1980. doi: 10.1086/158476.

Ronald L. Snell, Robert L. Dickman, and Y. L. Huang. Molecular Outflows Associated with a Flux-limited Sample of Bright Far-Infrared Sources. ApJ, 352:139, Mar 1990. doi: 10.1086/168521.

T. K. Sridharan, H. Beuther, P. Schilke, K. M. Menten, and F. Wyrowski. High-Mass Protostellar Candidates. I. The Sample and Initial Results. ApJ, 566(2):931–944, Feb 2002. doi: 10.1086/338332.

László Szűcs, Simon C. O. Glover, and Ralf S. Klessen. The ^{12}CO/^{13}CO ratio in turbulent molecular clouds. MNRAS, 445(4):4055–4072, Dec 2014. doi: 10.1093/mnras/stu2013.

M. Tafalla, P. C. Myers, P. Caselli, and C. M. Walmsley. On the internal structure of starless cores. I. Physical conditions and the distribution of CO, CS, N_2H^+, and NH_3 in L1498 and L1517B. A&A, 416:191–212, Mar 2004. doi: 10.1051/0004-6361:20031704.

J. C. Tan, M. T. Beltrán, P. Caselli, F. Fontani, A. Fuente, M. R. Krumholz, C. F. McKee, and A. Stolte. Massive Star Formation. In Henrik Beuther, Ralf S. Klessen, Cornelis P. Dullemond, and Thomas Henning, editors, *Protostars and Planets VI*, page 149, Jan 2014. doi: 10.2458/azu_uapress_9780816531240-ch007.

Jonathan C. Tan, Mengyao Liu, James De Buizer, Yichen Zhang, Viviana Rosero, Kei Tanaka, Yara Yousef, Maria T. Beltrán, and Joshua Marvil. The SOFIA Massive (SOMA) Star Formation Survey - Latest Results. In *American Astronomical Society Meeting Abstracts #233*, volume 233 of *American Astronomical Society Meeting Abstracts*, page 208.01, Jan 2019.

Kotomi Taniguchi, Eric Herbst, Hiroyuki Ozeki, and Masao Saito. ^{13}C Isotopic Fractionation of CCH in Two Starless Cores: L1521B and L134N. *arXiv e-prints*, art. arXiv:1908.09983, Aug 2019.

V. Taquet, C. Ceccarelli, and C. Kahane. Formaldehyde and Methanol Deuteration in Protostars: Fossils from a Past Fast High-density Pre-collapse Phase. ApJ, 748(1):L3, Mar 2012. doi: 10.1088/2041-8205/748/1/L3.

V. Taquet, K. Furuya, C. Walsh, and E. F. van Dishoeck. A primordial origin for molecular oxygen in comets: a chemical kinetics study of the formation and survival of O_2 ice from clouds to discs. MNRAS, 462:S99–S115, Nov 2016. doi: 10.1093/mnras/stw2176.

Vianney Taquet, Steven B. Charnley, and Olli Sipilä. Multilayer Formation and Evaporation of Deuterated Ices in Prestellar and Protostellar Cores. ApJ, 791(1):1, Aug 2014. doi: 10.1088/0004-637X/791/1/1.

R. Terzieva and Eric Herbst. The possibility of nitrogen isotopic fractionation in interstellar clouds. MNRAS, 317(3):563–568, Sep 2000. doi: 10.1046/j.1365-8711.2000.03618.x.

D. Teyssier, P. Hennebelle, and M. Pérault. Radio-millimetre investigation of galactic infrared dark clouds. A&A, 382:624–638, Feb 2002. doi: 10.1051/0004-6361:20011646.

A. G. G. M. Tielens. *The Physics and Chemistry of the Interstellar Medium.* 2005.

F. F. S. van der Tak, H. S. P. Müller, M. E. Harding, and J. Gauss. Hyperfine structure in the J = 1-0 transitions of DCO⁺, DNC, and $HN^{13}C$: astronomical observations and quantum-chemical calculations. A&A, 507(1):347–354, Nov 2009. doi: 10.1051/0004-6361/200912912.

Ewine F. van Dishoeck and John H. Black. The Photodissociation and Chemistry of Interstellar CO. ApJ, 334:771, Nov 1988. doi: 10.1086/166877.

Elishevah M. M. E. van Kooten, Kazuhide Nagashima, Takeshi Kasama, Susanne F. Wampfler, Jon P. Ramsey, Søren Frimann, Zoltan I. Balogh, Martin Schiller, Daniel P. Wielandt, and Ian A. Franchi. A divergent heritage for complex organics in Isheyevo lithic clasts. Geochim. Cosmochim. Acta, 205:119–148, May 2017. doi: 10.1016/j.gca.2017.02.002.

C. Vastel, T. G. Phillips, and H. Yoshida. Detection of D_2H^+ in the Dense Interstellar Medium. ApJ, 606(2):L127–L130, May 2004. doi: 10.1086/421265.

C. Vastel, C. Ceccarelli, B. Lefloch, and R. Bachiller. The Origin of Complex Organic Molecules in Prestellar Cores. ApJ, 795(1):L2, Nov 2014. doi: 10.1088/2041-8205/795/1/L2.

A. I. Vasyunin, P. Caselli, F. Dulieu, and I. Jiménez-Serra. Formation of Complex Molecules in Prestellar Cores: A Multilayer Approach. ApJ, 842(1):33, Jun 2017. doi: 10.3847/1538-4357/aa72ec.

G. L. Villanueva, M. J. Mumma, B. P. Bonev, M. A. Di Santi, E. L. Gibb, H. Böhnhardt, and M. Lippi. A Sensitive Search for Deuterated Water in Comet 8p/Tuttle. ApJ, 690(1):L5–L9, Jan 2009. doi: 10.1088/0004-637X/690/1/L5.

R. Visser, E. F. van Dishoeck, and J. H. Black. The photodissociation and chemistry of CO isotopologues: applications to interstellar clouds and circumstellar disks. A&A, 503(2):323–343, Aug 2009. doi: 10.1051/0004-6361/200912129.

Ruud Visser, Simon Bruderer, Paolo Cazzoletti, Stefano Facchini, Alan N. Heays, and Ewine F. van Dishoeck. Nitrogen isotope fractionation in protoplanetary disks. A&A, 615:A75, Jul 2018. doi: 10.1051/0004-6361/201731898.

Serena Viti, Francesco Fontani, Izaskun Jiménez-Serra, and Jonathan Holdship. Nitrogen fractionation in external galaxies. MNRAS, 486(4):4805–4812, Jul 2019. doi: 10.1093/mnras/stz1172.

V. Wakelam, J. C. Loison, E. Herbst, D. Talbi, D. Quan, and F. Caralp. A sensitivity study of the neutral-neutral reactions C + C{3} and C + C{5} in cold dense interstellar clouds. A&A, 495(2):513–521, Feb 2009. doi: 10.1051/0004-6361:200810967.

V. Wakelam, E. Herbst, J. C. Loison, I. W. M. Smith, V. Chandrasekaran, B. Pavone, N. G. Adams, M. C. Bacchus-Montabonel, A. Bergeat, K. Béroff, V. M. Bierbaum, M. Chabot, A. Dalgarno, E. F. van Dishoeck, A. Faure, W. D. Geppert, D. Gerlich, D. Galli, E. Hébrard, F. Hersant, K. M. Hickson, P. Honvault, S. J. Klippenstein, S. Le Picard, G. Nyman, P. Pernot, S. Schlemmer, F. Selsis, I. R. Sims, D. Talbi, J. Tennyson, J. Troe, R. Wester, and L. Wiesenfeld. A KInetic Database for Astrochemistry (KIDA). ApJS, 199(1):21, Mar 2012. doi: 10.1088/0067-0049/199/1/21.

V. Wakelam, I. W. M. Smith, J. C. Loison, D. Talbi, S. J. Klippenstein, A. Bergeat, W. D. Geppert, and K. M. Hickson. Review of important reactions for the nitrogen chemistry in the interstellar medium. *arXiv e-prints*, art. arXiv:1310.4350, Oct 2013.

V. Wakelam, J. C. Loison, E. Herbst, B. Pavone, A. Bergeat, K. Béroff, M. Chabot, A. Faure, D. Galli, W. D. Geppert, D. Gerlich, P. Gratier, N. Harada, K. M. Hickson, P. Honvault, S. J. Klippenstein, S. D. Le Picard, G. Nyman, M. Ruaud, S. Schlemmer, I. R. Sims, D. Talbi, J. Tennyson, and R. Wester. The 2014 KIDA Network for Interstellar Chemistry. ApJS, 217 (2):20, Apr 2015. doi: 10.1088/0067-0049/217/2/20.

S. H. J. Wallström, S. Muller, and M. Guélin. Isotopic ratios at z = 0.68 from molecular absorption lines toward B 0218+357. A&A, 595:A96, Nov 2016. doi: 10.1051/0004-6361/201628615.

C. M. Walmsley, D. R. Flower, and G. Pineau des Forêts. Complete depletion in prestellar cores. A&A, 418:1035–1043, May 2004. doi: 10.1051/0004-6361:20035718.

S. F. Wampfler, J. K. Jørgensen, M. Bizzarro, and S. E. Bisschop. Observations of nitrogen isotope fractionation in deeply embedded protostars. A&A, 572:A24, Dec 2014. doi: 10.1051/0004-6361/201423773.

Junzhi Wang, Zhi-Yu Zhang, Jianjie Qiu, Yong Shi, Jiangshui Zhang, and Min Fang. Isotopologues of Dense Gas Tracers in NGC 1068. ApJ, 796(1):57, Nov 2014. doi: 10.1088/0004-637X/796/1/57.

D. Ward-Thompson, F. Motte, and P. Andre. The initial conditions of isolated star formation - III. Millimetre continuum mapping of pre-stellar cores. MNRAS, 305(1):143–150, May 1999. doi: 10.1046/j.1365-8711.1999.02412.x.

W. D. Watson, V. G. Anicich, and Jr. Huntress, W. T. Measurement and significance of the reaction $^{13}C^+ + ^{12}CO$ ü $^{12}C^+ + ^{13}CO$ for alteration of the $^{13}C/^{12}C$ ratio in interstellar molecules. ApJ, 205:L165–L168, May 1976. doi: 10.1086/182115.

J. P. Williams, L. Blitz, and C. F. McKee. The Structure and Evolution of Molecular Clouds: from Clumps to Cores to the IMF. In V. Mannings, A. P. Boss, and S. S. Russell, editors, *Protostars and Planets IV*, page 97, May 2000.

T. L. Wilson and R. Rood. Abundances in the Interstellar Medium. ARA&A, 32:191–226, Jan 1994. doi: 10.1146/annurev.aa.32.090194.001203.

E. S. Wirström and S. B. Charnley. Revised models of interstellar nitrogen isotopic fractionation. MNRAS, 474(3):3720–3726, Mar 2018. doi: 10.1093/mnras/stx3030.

Eva S. Wirström, Steven B. Charnley, Martin A. Cordiner, and Stefanie N. Milam. Isotopic Anomalies in Primitive Solar System Matter: Spin-state-dependent Fractionation of Nitrogen and Deuterium in Interstellar Clouds. ApJ, 757(1):L11, Sep 2012. doi: 10.1088/2041-8205/757/1/L11.

Mark G. Wolfire and Joseph P. Cassinelli. Conditions for the Formation of Massive Stars. ApJ, 319:850, Aug 1987. doi: 10.1086/165503.

David E. Woon and Eric Herbst. Quantum Chemical Predictions of the Properties of Known and Postulated Neutral Interstellar Molecules. ApJS, 185(2):273–288, Dec 2009. doi: 10.1088/0067-0049/185/2/273.

J. G. A. Wouterloot, J. Brand, and K. Fiegle. IRAS sources beyond the solar circle. III. Observations of H2O, OH, CH3OH and CO. *Astronomy and Astrophysics Supplement Series*, 98: 589–636, May 1993.

J. G. A. Wouterloot, C. Henkel, J. Brand, and G. R. Davis. Galactic interstellar $^{18}O/\{î7\}O$ ratios - a radial gradient? A&A, 487(1):237–246, Aug 2008. doi: 10.1051/0004-6361: 20078156.

Satoshi Yamamoto. *Introduction to Astrochemistry: Chemical Evolution from Interstellar Clouds to Star and Planet Formation*. 2017. doi: 10.1007/978-4-431-54171-4.

Y. T. Yan, J. S. Zhang, C. Henkel, T. Mufakharov, L. W. Jia, X. D. Tang, Y. J. Wu, J. Li, Z. A. Zeng, Y. X. Wang, Y. Q. Li, J. Huang, and J. M. Jian. A Systematic TMRT Observational Study of Galactic $^{12}C/^{13}C$ Ratios from Formaldehyde. ApJ, 877(2):154, Jun 2019. doi: 10.3847/1538-4357/ab17d6.

H. W. Yorke. Theory of Formation of Massive Stars via Accretion. In Michael G. Burton, Ray Jayawardhana, and Tyler L. Bourke, editors, *Star Formation at High Angular Resolution*, volume 221 of *IAU Symposium*, page 141, Sep 2004.

Edward D. Young, Matthieu Gounelle, Rachel L. Smith, Mark R. Morris, and Klaus M. Pontoppidan. Astronomical Oxygen Isotopic Evidence for Supernova Enrichment of the Solar System Birth Environment by Propagating Star Formation. ApJ, 729(1):43, Mar 2011. doi: 10.1088/0004-637X/729/1/43.

Luis A. Zapata, Laurent Loinard, Luis F. Rodríguez, Vicente Hernández-Hernández, Satoko Takahashi, Alfonso Trejo, and Bérengère Parise. ALMA 690 GHz Observations of IRAS 16293-2422B: Infall in a Highly Optically Thick Disk. *The Astrophysical Journal*, 764(1): L14, Feb 2013. doi: 10.1088/2041-8205/764/1/L14.

S. Zeng, I. Jiménez-Serra, G. Cosentino, S. Viti, A. T. Barnes, J. D. Henshaw, P. Caselli, F. Fontani, and P. Hily-Blant. ^{15}N fractionation in infrared-dark cloud cores. A&A, 603: A22, Jul 2017. doi: 10.1051/0004-6361/201630210.

Qizhou Zhang, Todd R. Hunter, T. K. Sridharan, and Paul T. P. Ho. A Disk/Jet System toward the High-Mass Young Star in AFGL 5142. ApJ, 566(2):982–992, Feb 2002. doi: 10.1086/338278.

Xiao-Niu Zhang, De-Heng Shi, Jin-Feng Sun, and Zun-Lue Zhu. MRCI study of spectroscopic and molecular properties of $X^1\Sigma^+_g$ and $A^1\Pi_u$ electronic states of the C_2 radical. *Chinese Physics B*, 20(4):043105, Apr 2011. doi: 10.1088/1674-1056/20/4/043105.

Hans Zinnecker and Harold W. Yorke. Toward Understanding Massive Star Formation. ARA&A, 45(1):481–563, Sep 2007. doi: 10.1146/annurev.astro.44.051905.092549.

<div align="right">

A

</div>

<div align="center">

SPECTRA SIMULATION TESTS

</div>

In this appendix we have estimated how much our results towards 05358 are influenced by the different spectral resolution between the main isotopologue (N_2H^+, of about 6.45 km s^{-1}), and the ^{15}N-isotopologues (^{15}NNH$^+$ and N^{15}NH$^+$, of about 0.5 km s^{-1}) in the work described in chapter 4 and published by Colzi et al. (2019). For this test we have taken into account the spectra extracted from P1a and P1b, and the corresponding fit results with a T_{ex}=20 K, in Sect. A.1 and A.2. Moreover, in Sect. A.3 we have tested how a moderately optically thick N_2H^+ line can be distinguished from a heavily saturated line. For this test we have taken into account the spectra extracted from I1 and the corresponding fit results with a T_{ex}=20 K, 30 K, 40 K and 50 K.

A.1. ^{15}N-ISOTOPOLOGUES AT LOWER SPECTRAL RESO-LUTION

We have smoothed the ^{15}NNH$^+$(1–0) transition to a 6.5 km s^{-1} resolution. In Fig. A.1, the black spectrum is the observed one, the blue solid line is the fit to the observed spectrum, and the red line is the smoothed one. The integrated intensity ($A=\int T_{MB}\,dv$) of the observed spectrum is (0.27±0.04) K km s^{-1} (relative error $\Delta A/A\simeq$15%), while the integrated intensity of the smoothed spectrum is (0.31±0.06) K km s^{-1}, 13% higher than the observed one. This error is comparable to the error given from the fit. We have done the same analysis with N^{15}NH$^+$(1–0) (Fig. A.2), for which we have obtained, for the smoothed spectrum, an integrated intensity of (0.26±0.08) K km s^{-1}, 12% higher than the observed one (0.23±0.03 K km s^{-1}), that again is comparable with the relative error given by the fit of the observed spectrum ($\Delta A/A\simeq$13%). The test hence shows that the integrated intensity of the ^{15}N-isotopologues, and thus their column densities, are not affected by changing the resolution from 0.5 to 6.5 km s^{-1}.

A.2. N_2H^+ AT HIGHER SPECTRAL RESOLUTION

We have simulated the spectrum of N_2H^+(1–0) with a resolution of 0.5 km s^{-1} using the results of the fit obtained for a T_{ex}=20 K, towards P1a, but with a line width of 2.3 km s^{-1}
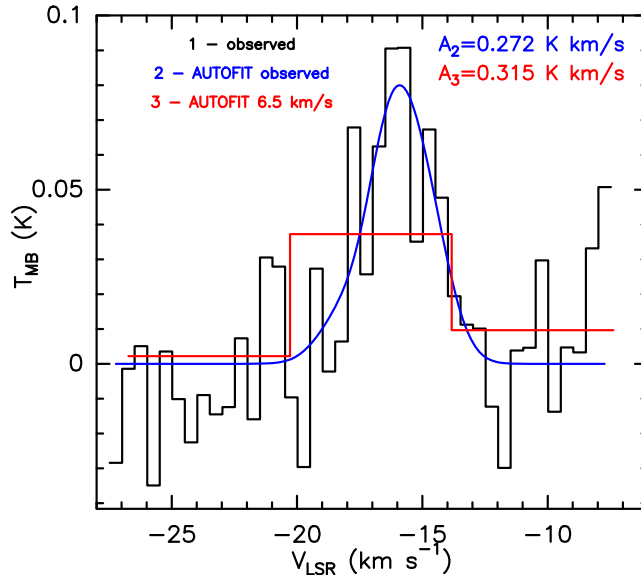
Fig. A.1: $^{15}NNH^+$(1–0) spectra. The black histogram indicates the $^{15}NNH^+$(1–0) spectrum, observed with the NOEMA interferometer towards 05358. The best fit to the observed spectrum is the blue solid line. The red histogram indicates the spectrum smoothed to 6.5 km s^{-1}.
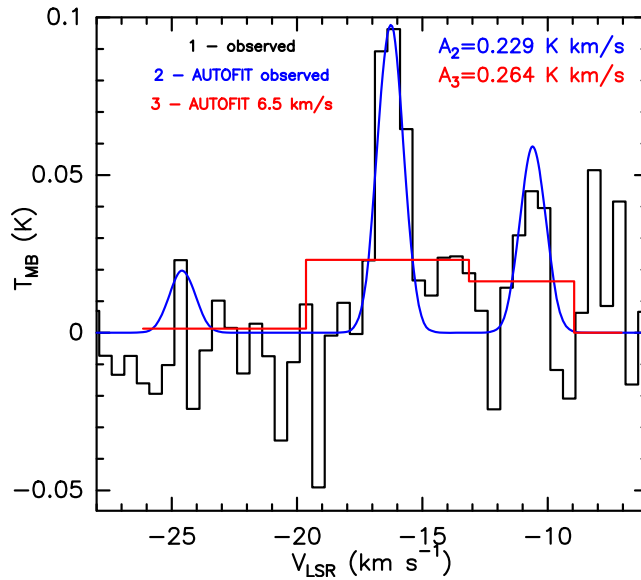

Fig. A.2: $N^{15}NH^+$(1–0) spectra. The black histogram indicates the $N^{15}NH^+$(1–0) spectrum, observed with the NOEMA interferometer towards 05358. The best fit to the observed spectrum is the blue solid line. The red histogram indicates the spectrum smoothed to 6.5 km s^{-1}.

(which is the average value measured from $^{15}NNH^+$). The obtained spectrum is the blue in Fig. A.3, with an integrated intensity of (44 ± 2) K km s^{-1}. Then, we have smoothed this simulated spectrum to 6.45 km s^{-1} obtaining the red one in the same figure. The integrated intensity of this latter is the same as that at higher spectral resolution. We can also note that the smoothed simulated spectrum is comparable with the observed one (black) that has an integrated intensity of (48 ± 2) K km s^{-1} ($\Delta A/A \simeq 4\%$), 8% higher than the simulated one. We can conclude that, even if we cannot resolve the hyperfine structure of N_2H^+(1–0), with our analysis we have obtained an accurate integrated intensity, with at most 4%
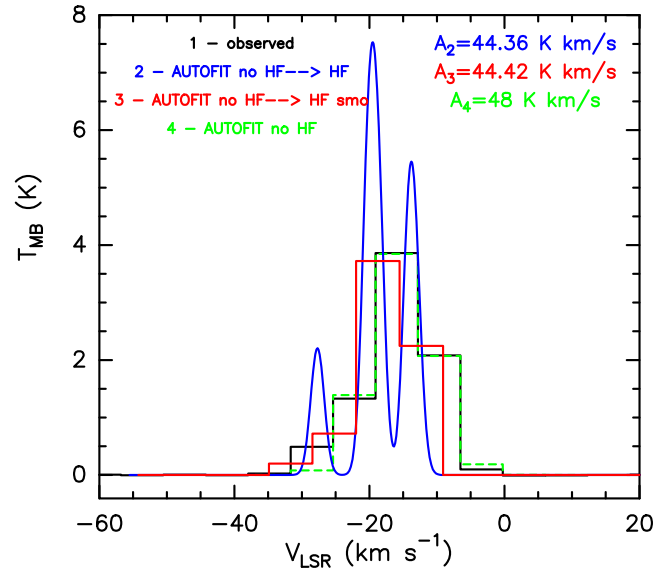
Fig. A.3: N$_2$H$^+$(1–0) spectra. The black histogram indicates the N$_2$H$^+$(1–0) spectrum, observed with the NOEMA interferometer towards 05358. The best fit to the observed spectrum is the green dashed line. The blue solid line is the simulated spectrum at high spectral resolution (0.5 km s^{-1}) with a line width of 2.3 km s^{-1}. The red histogram indicates the blue simulated spectrum smoothed to 6.5 km s^{-1}.

overestimation.

A.3. THE EFFECT OF A POSSIBLE N$_2$H$^+$ LINE SATURATION

We have simulated the spectra of N$_2$H$^+$(1–0) with a resolution of 0.5 km s^{-1}, a line width of 2.3 km s^{-1}, and a fixed temperature (trying the different cases analysed in the main work, between 20 and 50 K). As column density we fixed it to the one that corresponded to a line opacity of the main hyperfine component τ_{main}=1. The obtained simulated spectra are the blue in the right panels of Fig. A.4. Then, we have smoothed the simulated spectra to a resolution of 6.5 km s^{-1} obtaining the red spectra superimposed to the blue ones. The left panels of Fig. A.4 show the spectra observed towards I1, with the best fit found at different temperatures. Comparing the observations to the simulation, it is shown that the low spectral resolution of N$_2$H$^+$ emission is not hiding heavily saturated line profiles, since the peak of the simulated spectra is always higher than the observed ones. We also tried to simulate a spectra, with a fixed T=20 K to obtain a τ_{main}=5, and we found the same results: the simulated spectra at low spectral resolution has a peak higher than the observed one (see Fig. A.5).
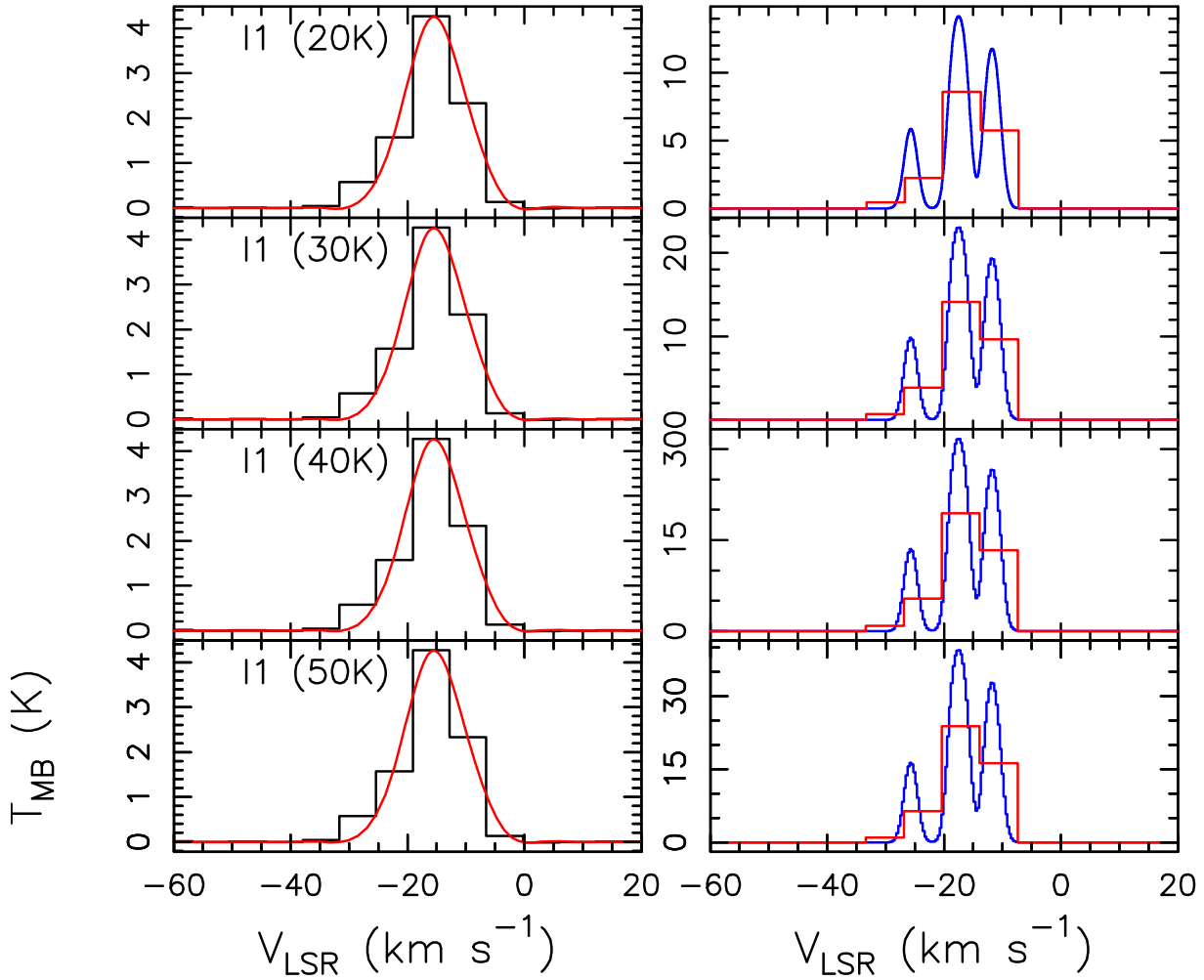
Fig. A.4: N_2H^+(1–0) spectra. *Left panels*: The black histograms indicatesthe N_2H^+(1–0) spectrum, observed with the NOEMA interferometer towards 05358 (I1 region). The best fit to the observed spectrum are the red solid line, obtained with a fixed T_{ex} from 20 K up to 50 K (from top to the bottom panel) and a τ_{main}=1. *Right panels*: The blue solid line are the simulated spectrum at high spectral resolution (0.5 km s^{-1}) with a line width of 2.3 km s^{-1} and a T_{ex} from 20 K up to 50 K (from top to the bottom panel). The red histograms indicate the blue simulated spectra smoothed to 6.5 km s^{-1}.

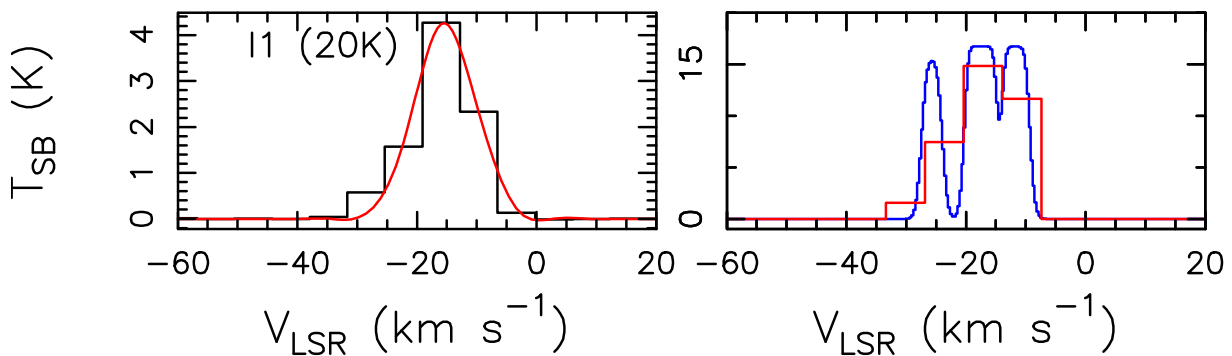Fig. A.5: N_2H^+(1–0) spectra. *Left panel*: The black histogram indicates the N_2H^+(1–0) spectrum, observed with the NOEMA interferometer towards 05358 (I1 region). The best fit to the observed spectrum is the red solid line, obtained with a fixed T_{ex} of 20 K and a τ_{main}=5. *Right panel*: The blue solid line is the simulated spectrum at high spectral resolution (0.5 km s^{-1}) with a line width of 2.3 km s^{-1} and a T_{ex} of 20 K. The red histogram indicates the blue simulated spectra smoothed to 6.5 km s^{-1}.